NAT'L INST. OF STAND & TECH R.I.C.
A11105 047594
NIST
PUBLICATIONS

NIST
United States Department of Commerce
Technology Administration
National Institute of Standards and Technology

NIST Special Publication 905

Technical Digest Symposium on Optical Fiber Measurements, 1996

Sponsored by the National Institute of Standards and Technology in cooperation with the IEEE Lasers and Electro-Optics Society and the Optical Society of America

QC
100
U57
NO.905
1996
AUTHENTICATED
U.S. GOVERNMENT
INFORMATION
GPO

NIST Special Publication 905

Technical Digest—Symposium on Optical Fiber Measurements, 1996

Digest of a symposium sponsored by the
National Institute of Standards and Technology
in cooperation with the
IEEE Lasers and Electro-Optics Society
and the Optical Society of America

Edited by

G.W. Day
D.L. Franzen
P.A. Williams

Optoelectronics Division
Electronics and Electrical Engineering Laboratory
National Institute of Standards and Technology
Boulder, Colorado 80303-3328

October 1996

U.S. DEPARTMENT OF COMMERCE, Michael Kantor, Secretary
TECHNOLOGY ADMINISTRATION, Mary L. Good, Under Secretary for Technology
NATIONAL INSTITUTE OF STANDARDS AND TECHNOLOGY, Arati Prabhakar, Director

National Institute of Standards
and Technology
Special Publication 905
Natl. Inst. Stand. Technol.
Spec. Publ. 905
220 pages (October 1996)
CODEN: NSPUE2

U.S. Government Printing Office
Washington: 1996

For sale by the Superintendent of
Documents
U.S. Government Printing Office
Washington, DC 20402-9325

PREFACE

Measurements of polarization mode dispersion (PMD) and nonlinear processes in optical fibers are two of the major topics in this digest of papers presented at the ninth Symposium on Optical Fiber Measurements, held October 1-3, 1996, at the laboratories of the National Institute of Standards and Technology in Boulder, CO. Summaries of all the papers presented at the Symposium–10 invited and 39 contributed–are included.

The statistical nature of PMD complicates its measurement and makes verification of accuracy difficult. This is reflected in the content of the papers, many of which focus on comparisons of measurement techniques. In wavelength division multiplexed systems employing optical amplification, high powers can lead to problems from nonlinear processes such as Brillouin scattering and four-wave mixing. The importance of these issues is seen by the inclusion of several papers regarding the measurement of nonlinear coefficients and effective area.

The Symposium continues to be a prime gathering place for specialists in the characterization of optical fiber and related components. Strong international participation has been maintained, as about two thirds of the papers in this digest originated outside of the United States.

G.W. Day
D.L. Franzen
P.A. Williams
Boulder, Colorado
October 1996

Except where attributed to NIST authors, the content of individual sections of this volume has not been reviewed or edited by the National Institute of Standards and Technology. NIST therefore accepts no responsibility for comments or recommendations therein. The mention of trade names in this volume is in no sense an endorsement or recommendation by the National Institute of Standards and Technology.

SYMPOSIUM COMMITTEE

D.L. Franzen, NIST, General Chair

G.W. Day, NIST, Program Chair

M. Artiglia, CSELT

A. Barlow, EG&G

S. Fleming, University of Sydney

T.A. Hanson, Corning

B.L. Heffner, Hewlett-Packard

R.K. Hickernell, NIST

R.B. Kummer, Lucent Technologies

P.S. Lovely, Photon Kinetics

S. Pollitt, NPL

W.A. Reed, Lucent Technologies

P.R. Reitz, AMP

C. Saravanos, Siecor

P.A. Williams, NIST

H. Yajima, Electrotechnical Laboratory

H.H. Yuce, Bellcore

CONTENTS

PREFACE iii
SYMPOSIUM COMMITTEE iv

Characterization of optical components for D-WDM applications (invited)
J. Dupre, Hewlett-Packard Company 1

Design and measurement of optical fibre gratings (invited)
Raman Kashyap, BT Laboratories 7

Chirp determination of fiber Bragg gratings with interferometric autocorrelation measurements
M. Fuss, University of Kaiserslautern 13

Optical amplifier characterization (invited)
F.W. Willems, Lucent Technologies, The Netherlands 17

Fiber amplifiers for the second telecommunication window: development and characterisation
Marcello Potenza, Tiziana Tambosso, CSELT 23

All-fiber superfluorescent light source at 1.06 μm
V. Reichel, A. Ertmer, M. Rothhardt, H.-R. Müller, H. Bartelt, Institut für Physikalische Hochtechnologie e.V. Jena 27

Results of COST 241 EDFA round-robin on gain and noise figure
F.W. Willems, Lucent Technologies, The Netherlands; M. Artiglia, CSELT; C. Larsen, Lycom; C. Soccolich, Lucent Technologies, USA; B. Heens, FPM 31

A general method for measuring the electric-field-dependent absorption coefficient in quantum confined structures
J.F. Siliquini, M.G. Xu, J.M. Dell, The University of Western Australia 35

Measuring the reliability of fiber optic components (invited)
L.A. Reith, Bellcore 39

Opto-mechanical method for measurement of ferrule concentricity and roundness error
Paul Townley-Smith, Costas Saravanos, Siecor Corp. 45

Errors due to connectors in optical fiber power meters
Igor Vayshenker, Xiaoyu Li, Darryl A. Keenan, Thomas R. Scott, NIST 49

MU-type PANDA fiber connector
R. Nagase, S. Mitachi, NTT Opto-electronics Laboratories 53

High performance single-mode wavelength independent all-fiber build-out attenuator
Shin-Lo Chia, AMP 57

Nonlinear coefficient of optical fibers at 1550 nm (invited)
Valéria L. da Silva, Y. Liu, A.J. Antos, G.E. Berkey, M.A. Newhouse, Corning. 61

Polarization independent nonlinear refractive index measurement in optical fiber
Andrea Melloni, Mario Martinelli, Politecnico di Milano; Andrea Del Core, Andrea Fellegara, ITALTEL, BUTR 67

Interferometric determination of the nonlinear refractive index n_2 of optical fibers
F. Wittl, Techn. Univ. Darmstadt; J. Vobian, G. Herchenröder, W. Dultz, Deutsche Telekom 71

Inverse method for systematic investigations of linear and nonlinear properties of dispersion-shifted and dispersion-compensating fibers
R. Boness, TU Dresden; S. Unger, J. Kirchhof, IPHT Jena; F. Wittl, J. Vobian, FTZ Darmstadt, K.-F. Klein, FH Giessen-Friedberg 75

Effective area measurement comparison between direct far field scan and variable aperture method in the far field
Michael J. Hackert, M. Ajaaz Zainul, Corning 79

Characterizing components for high speed data interconnects (invited)
David Smith, Honeywell 83

Modal optical coupling efficiency measurements and modeling for fiber interconnections
J. Sutherland, G. George, J.P. Krusius, Cornell University 89

Dispersion-compensating fibers with high birefringence
J. Vobian, G. Herchenröder, FTZ Darmstadt; K. Mörl, IPHT Jena 93

Accurate wavelength calibration for optical spectrum analysers
D. A. Humphreys, National Physical Laboratory 97

Nonlinearity of optical fiber power meters
Igor Vayshenker, NIST; Shao Yang, Ohmeda Medical Systems; Xiaoyu Li, Thomas R. Scott, NIST 101

Methods of suppressing stimulated Brillouin scattering in optical fibers by manipulation of the fiber properties (invited)
Clifford Headley, J.B. Clayton, W.A. Reed, Lucent Technologies 105

Local analysis of stimulated Brillouin interaction in installed fiber optics cables
Marc Niklès, Luc Thévenaz, Swiss Federal Institute of Technology; Pascal Salina, Swiss Telecom PTT; Philippe A. Robert, Swiss Federal Institute of Technology 111

Non-invasive mapping of dispersion in optical fibers (invited)
R.M. Jopson, Lucent Technologies; M. Eiselt, Heinrich Hertz Institut 115

Determination of zero-dispersion wavelength in optical fiber using four-wave mixing
J.B. Schlager, S.E. Mechels, D.L. Franzen, NIST 121

Accuracy issues in comparisons of time- and frequency-domain polarization mode dispersion measurements (invited)
P.A. Williams, NIST 125

How accurately can one measure a statistical quantity like Polarization Mode Dispersion?
N. Gisin, B. Gisin, University of Geneva; J.P. Von der Weid, R. Passy, Pontifícia Universidade Católica do Rio de Janeiro 131

Compensation formula for noise threshold bias of interferometric PMD measurement
B.L. Heffner, Hewlett-Packard Laboratories 135

A practical comparison between two different PMD measurement methods
Bertil Arvidsson, Hans Mickelsson, Ericsson Cables AB; Kim Brising, TELIA 139

Interferometric polarization mode dispersion measurements with femtoseconds sensitivity
Ph. Oberson, K. Julliard, N. Gisin, University of Geneva; R. Passy, J.P. Von der Weid, Pontifícia Universidade Católica do Rio de Janeiro 143

A novel PMD estimation technique with wavelength stepsize optimization
Osamu Aso, Haruki Ogoshi, Furukawa Electric 147

First report of ITU-T PMD round robin measurements for optical fibers and component
Y. Namihira, KDD R&D Laboratories; ITU-T PMD Round Robin Group 151

TIA round robin for the measurement of PMD
P.A. Williams, NIST 155

Measurement of SOP evolution along a linear birefringent fibre with twist using polarisation OTDR
R.E. Schuh, A.S. Siddiqui, University of Essex 159

Polarisation dependent loss of concatenated passive optical components
A. Elamari, N. Gisin, University of Geneva; B. Perny, Swiss Telecom PTT; H. Zbinden, University of Geneva; Ch. Zimmer, Swiss Telecom PTT 163

Novel method for polarization-maintaining fiber launch
Bernhard Scholl, Jens Rasmussen, Aachen University of Technology 167

Characterization of high-speed and low-loss polymer optical fibers (invited)
Yasuhiro Koike, Eisuke Nihei, Takaaki Ishigure, Keio University 171

A single device for both accurate measurements of λ_c and w_0 in single-mode fibers
D. Pagnoux, J.-M. Blondy, P. Roy, P. Facq, Institut de Recherche en Communications Optiques et Microondes 175

Wavelength dependence of correction factor of effective area (A*eff*) and mode field diameter (MFD) in various optical fibers
Yoshinori Namihira, KDD R&D Laboratories 179

Fiber cutoff wavelength measurement by modal spectrum modulation
P. Di Bin, C. Simos, D. Pagnoux, P. Faugeras, P. Facq, Institut de Recherche en Communications Optiques et Microondes 183

A simple, fast and accurate measurement of the mode field-radius: The axial gap method
J.L. Auguste, J.-M. Blondy, D. Pagnoux, M. Clapeau, P. Facq, Institut de Recherche en Communications Optiques et Microondes 187

Calibrated test fiber for optical time-domain reflectometers
Duwayne Anderson, Tektronix 191

A method for the localisation and quantization of faults in passive tree-structured optical networks using the OTDR technique
L. Wuilmart, V. Moeyaert, D. Daniaux, P. Mégret, M. Blondel, Faculté Polytechnique de Mons 195

A coarse ranging measurement method for access systems using passive optical networks
A. Fellegara, ITALTEL 199

Spatial-resolution improvement in coherent optical frequency domain reflectometry for long optical fibers by reducing frequency-sweep nonlinearity
K. Tsuji, K. Shimizu, T. Horiguchi, Y. Koyamada, NTT Access Network Systems Laboratories 203

A new wide scan range high resolution optical low coherence reflectometer
Mauro Bottanelli, SIRTI S.p.A. 207

Interferometric noise in fiber transmission systems incorporating birefringent substances
Michael A. Bukhshtab, Corning 211

Author Index 215

Characterization of optical components for D-WDM applications

J. Dupre
Hewlett-Packard Co.
Santa Rosa, CA

1 Introduction

Dense wavelength-division-multiplexed (D-WDM) transmission systems at 1550 nm have become commonplace for increasing the capacity of point-to-point terrestrial links. In the near future, this technology will be employed as well for undersea systems [1]. In addition, the all-optical network, providing flexible high capacity through wavelength routing, will soon be a reality [2]. In both cases, the optical components utilized in these systems require more sophisticated characterization than those intended for single channel applications. Simply stated, the wavelength dependencies of the optical parameters of the transmitter, amplifier, passive, and receiver components, while only of secondary importance in single-channel applications, become critical to the performance of D-WDM systems. The laser sources comprising the WDM transmitter must be selected and maintained precisely to the wavelengths required by the particular channel plan. The passive components such as multiplexers, demultiplexers, isolators, and couplers must have their parameters, including polarization dependence, measured versus wavelength. The erbium-doped fiber amplifiers (EDFAs) must have their gain and noise figure characterized for the multi-signal environment in which they are used because the spectral gain dynamics can have a particularly adverse effect on system performance [3].

This paper addresses measurement issues on two important components of D-WDM systems: the demultiplexer and the EDFA.

2 Characterizing demultiplexers

Fig. 1 shows a simplified diagram of a D-WDM system for point-to-point transport. The outputs of N laser sources at the prescribed wavelengths are combined and applied to the

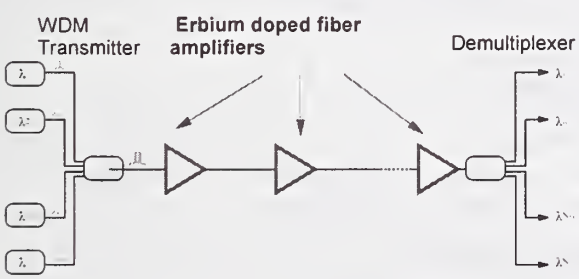

Fig. 1. A D-WDM system for point to point transmission.

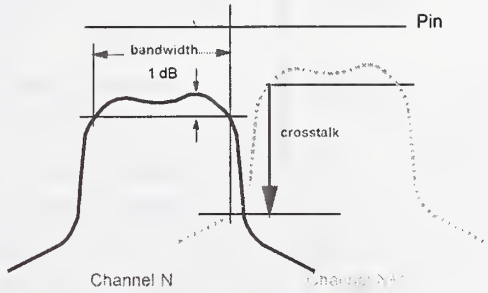

Fig. 2. Some typical demultiplexer charateristics. In general, all parameters are a function of input state-of-polarization.

transmission fiber. EDFAs are typically used in booster, line, and preamplifier configurations. At the far end of the system, the demultiplexer separates the N channels and routes each one to an optical receiver. The perfect demultiplexer would have a rectangular bandpass at each channel just wide enough to accommodate source laser drift, have minimal insertion loss, high rejection of other channels, and no polarization dependence. In practice, these parameters must all be carefully characterized as indicated in Fig. 2. There are two basic setups that can be utilized to make these measurements and each has particular advantages. The first, as shown in Fig. 3(a), is a narrow linewidth tunable laser in combination with an optical power meter or optical spectrum analyzer (OSA). The second, Fig. 3(b), uses a source of broadband noise and an OSA. In both configurations, a polarization controller is necessary to probe the device with all states of polarization. Which setup to use is determined by the required amplitude and wavelength measurement ranges, wavelength resolution, and measurement speed. The tunable laser/power meter setup has excellent wavelength resolution, limited by its

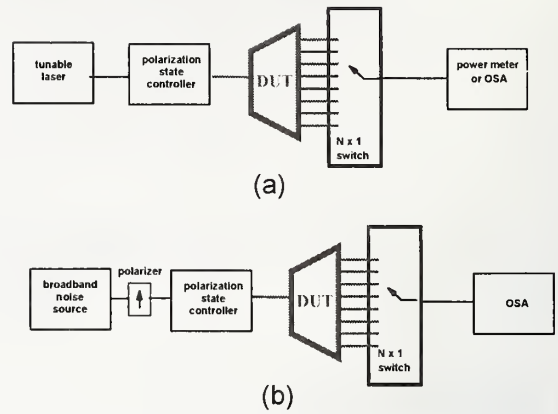

Fig. 3 Two alternative setups for measuring demultiplexers: (a) narrow linewidth source and power meter or optical spectrum analyzer (OSA) and (b) broadband noise source and OSA.

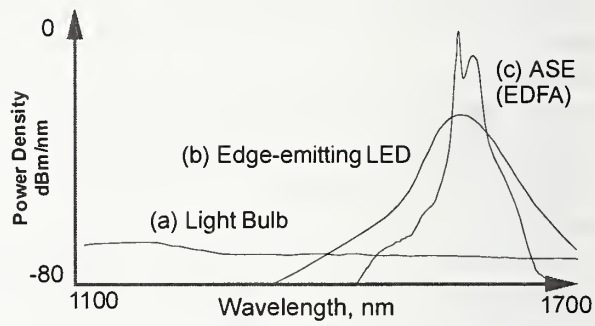

Fig. 4. The spectral power density for three types of broadband noise source. The edge-emitting LED and ASE sources have sufficient power to adequately characterize demultiplexers.

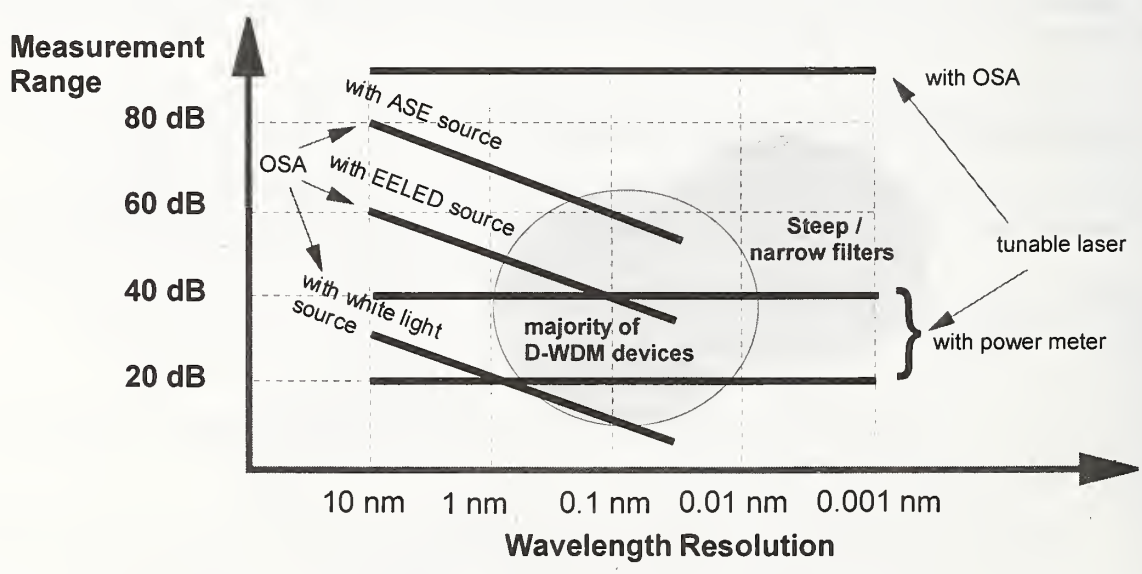

Fig. 5. Comparison of measurement methods

incremental wavelength linearity to about 0.001 nm. The measurement range is limited by the tunable laser's spontaneous emission level and the filter characteristics of the DUT. A narrow (1-nm) bandpass filter, for example, can be measured with 40-dB range while a band reject filter would be limited to about 20-dB. Replacing the power meter with an OSA or adding a tunable filter on the source will increase the measurement range significantly.

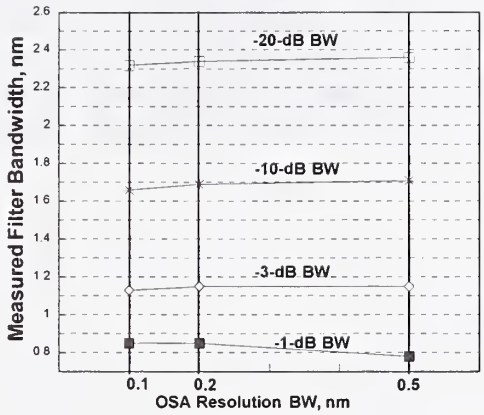

Fig. 6. Filter bandwidth measurement results using an EELED source and three settings of resolution bandwidth.

The key advantage of the second alternative -- the broadband noise source and OSA -- is measurement speed which is determined by the OSA's sweep speed. There are several options for the broadband sources shown in Fig. 4 [4]. An incandescent light bulb, while very broadband, does not have sufficient power spectral density to measure the out-of-band characteristics of demultiplexer filters. An edge-emitting LED (EELED) or the amplified spontaneous emission (ASE) from an EDFA with no input signal can provide useful measurement range over the bandwidths required for demultiplexer characterization. Fig. 5 shows the measurement range and resolution possible from the alternative test setups. The majority of D-WDM devices can take advantage of the faster measurement time of broadband noise techniques while for very narrow filters (<0.2-nm 3-dB width) , a setup with a tunable laser is required.

The resolution of a filter measurement made with a broadband noise source and OSA is limited by the OSA's resolution bandwidth. The actual measured result is the convolution of the OSA's filter characteristic with that of the DUT filter. To gauge the impact of this effect on the measurement of a typical D-WDM filter, a measurement of a filter's -1, -3, -10, and -20 dB bandwidths were made with three settings of the OSA's resolution bandwidth (Fig. 6). The maximum bandwidth error was 8% when the OSA resolution bandwidth was set to about one-half of the filter's 3-dB bandwidth. This error can be significantly reduced by measuring the OSA's filter spectral shape with a narrow source and deconvolving it from the measured result.

3 Characterizing optical amplifiers

Measurements on EDFAs in compression are generally made with a *single* saturating signal. Gain is simply the output signal power divided by the input signal power. Noise figure is calculated from the amplified spontaneous emission (ASE) measured at the amplifier output either at or near the signal wavelength. The signal wavelength is tuned across the band of interest to obtain the noise figure and gain as a function of wavelength. This method is quite adequate for single wavelength systems but, for WDM applications, the resulting gain and noise figure results are not an accurate predictor of system performance. In multi-channel systems (Fig. 7), all of the signals contribute to EDFA gain compression. Each signal amplitude affects

the gain at all wavelengths. That is, a change in the λ_1 signal power causes a gain change not only at λ_1 but also at λ_2 through λ_n. Similarly, ASE changes at all wavelengths for a signal level change at any wavelength. The problem is compounded in the more common situation for point-to-point transport in which there are multiple EDFAs or in a wavelength routing situation where channels are added and dropped. Clearly, characterization techniques are required that can

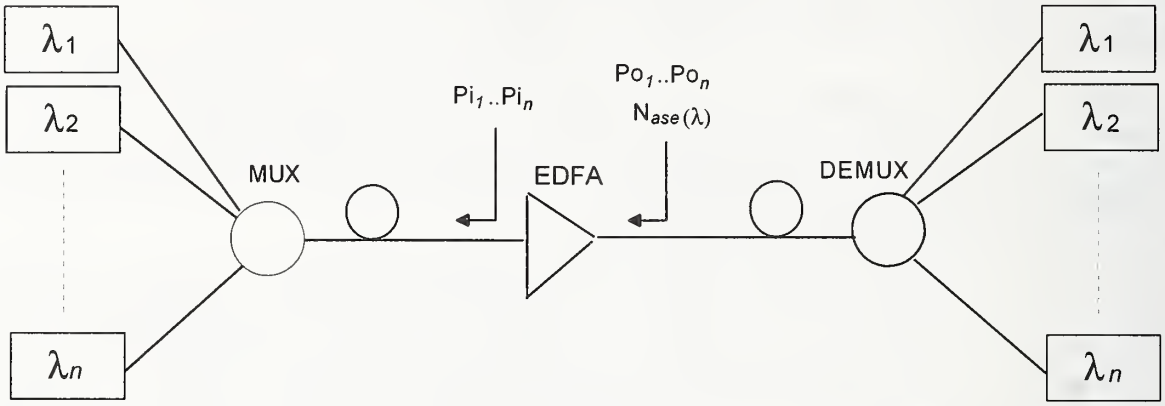

Figure 7. An EDFA in a multi-signal environment.

predict and assure system performance in spite of the complex gain dynamics in the EDFA.

There are two ways to approach this characterization. The most direct is to utilize a multi-channel source setup with the exact wavelengths in a particular channel plan. Gain is derived by measuring the signal power with the EDFA bypassed, then with the EDFA in place, and carefully excluding the effect of source spontaneous emission and amplified spontaneous emission. Multi-channel noise figures can be obtained by estimating the ASE at each channel wavelength by interpolating between channels and subtracting the effect for source noise. For narrow channel spacings, this is difficult due to the OSA resolution. Alternatively, *time-domain extinction* [5][6] that takes advantage of the slow time dynamics of the EDFA can be used to estimate the ASE. The cumbersome feature of this multiple source approach is that a large number of lasers at specific wavelengths must be assembled. If characterization is required for multiple channel plans (differing wavelengths, number of channels, and channel spacings) then the setup needs to be reconfigured for each characterization.

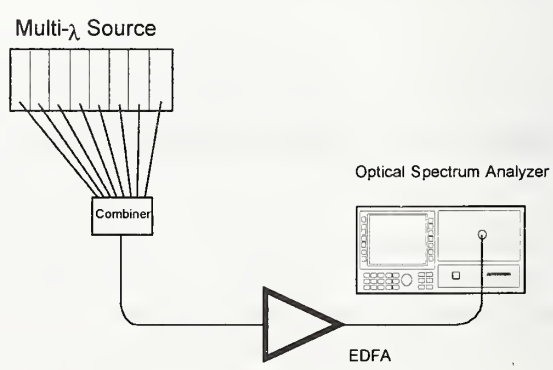

Fig. 8. The direct approach to multi-channel gain and noise figure measurement.

Another approach that takes advantage of the largely homogeneous saturation property of the EDFA utilizes a reduced number of saturating lasers and broadband small-signal probe to measure gain continuously across a wavelength range [6].

The concept of reducing the number of saturating lasers is explained in Fig. 9. The full complement of signals for the multi-wavelength plan is divided into regions (a). For each region, a single saturating source replicates the saturating effect of all the channels(b). The number of saturating sources required depends upon the significance of inhomogeneous effects, namely spectral hole burning. For erbium doping, at room temperature, one laser can accurately replicate multiple channels over about 15-nm of spectral width.

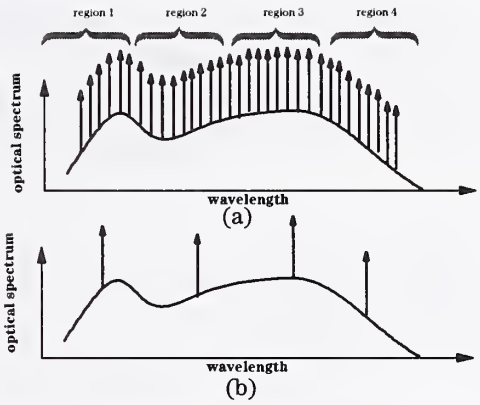

Fig. 9. A simplified test scheme results from replacing the n D-WDM channels with a reduced number of sources and using *noise gain profile*.

A setup for making gain measurements with a broadband noise probe, called *noise gain profile* is shown in Fig. 10. An edge-emitting LED (EELED) is combined with a tunable laser and applied to the test device. In order to obtain the value of the wavelength, λ_{sat}, and optical power, P_{sat}, of the single saturating laser that accurately replicates the saturation of a number of channels, a recursive algorithm is used that sets the *population inversion* equal for the two cases [7]. The algorithm makes an initial estimate of λ_{sat} and P_{sat}, and measures the noise gain at the channel wavelengths. Then, a new estimate is made using the following equations until convergence is achieved.

$$\lambda_{sat} = \sum_n \frac{P_n}{P_{sat}} \lambda_n$$

$$P_{sat} = \frac{1}{\lambda_{sat} G_{sat}} \sum_n \lambda_n G_n P_n$$

where P_{sat}, G_{sat}, λ_{sat} are the power, gain, and wavelength of the single input signal.

P_n, G_n, P_n are the power, gain, and wavelength of the n channel signals

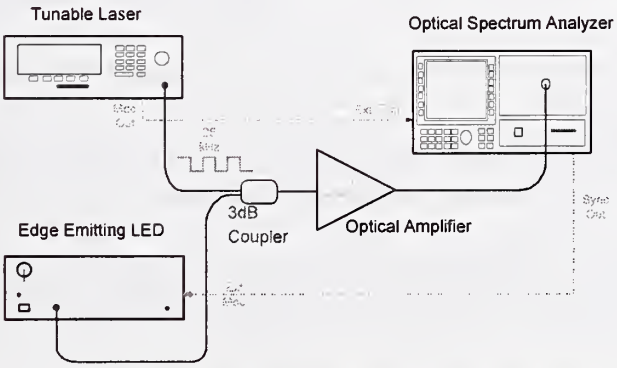

Fig. 10. The noise gain profile technique is implemented with one or more tunable lasers and an EELED probe.

An experiment was set up to compare gain measurements for a four channel system using the direct method with four lasers of Fig. 8 and the noise gain profile method with a single saturating source of Fig. 10 using the convergence algorithm described above. The results, as shown in Fig. 11, agree to within 0.2 dB which is within the measurement uncertainty of the two methods.

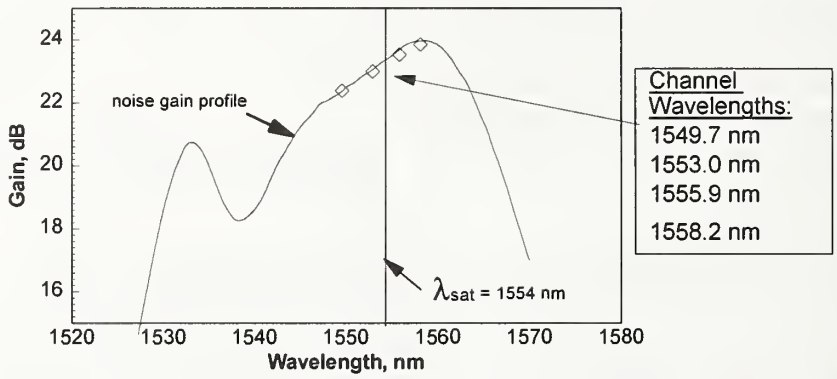

Fig. 11. Comparison of direct gain measurement and noise gain profile.

Acknowledgments

The author would like to thank Douglas Baney, Walter Benger, Jim Stimple, and Joachim Vobis for contributing material for this paper.

References

[1] Neal Bergano, *et al.*,"100 Gb/s Transmission of Twenty 5 Gb/s NRZ Data Channels Over Transoceanic Distances Using a Gain Flattened Amplifier Chain," ECOC'95, post deadline paper, 1995.

[2] Paul E. Green, Jr., "Optical Networking Update," *Selected Areas in Communications*, vol. 14, no. 5, June 1996, pp. 764-769.

[3] B. Clesca, D. Bayart, and J.L. Beylet, "1.5-μm Fluoride-Based Fiber Amplifiers for Wideband Multichannel Transport Networks," *Optical Fiber Technology 1*, 1995, pp. 135-157.

[4] Dennis Derickson, "Measuring ASE in Fiber Optic Systems," *Communication System Design*, January 1996, pp. 36-41

[5] D.M. Baney and J. Dupre, "Pulsed-Source technique for optical amplifier noise figure measurement," European Conference on Communications, ECOC'92, paper WeP2.11, Berlin, 1992.

[6] H. Chou and J. Stimple, "Inhomogeneous Gain Saturation of Erbium-Doped Fiber Amplifiers," Optical Amplifiers and Their Applications Technical Digest, vol. 18, paper ThE1-1, 1995.

[7] D.M. Baney and J. Stimple, "WDM EDFA Gain Characterization with a Reduced Set of Saturating Channels," To be published.

INVITED PAPER

Design and measurement of optical fibre gratings

Raman Kashyap
BT Laboratories, Martlesham Heath, Ipswich IP5 7RE
United Kingdom

Abstract

Optical fibre gratings for application in telecommunication are now routinely produced. Recent developments have been in the area of specialist gratings for band-pass, ultra-narrow-band filters with either excellent side mode suppression or particular phase-characteristics, and also chirped gratings for dispersion management in optical fibre transmission systems. This paper introduces some of these recent developments and address the problems associated with design, fabrication and measurement of the transfer functions for specific applications.

Introduction:

Fibre Bragg gratings were discovered by Ken Hill *et al*[1] in 1978 during the course of experiments with a line narrowed argon ion laser operating at 514 nm and a germania doped silica optical fibre. It was noticed that the transmitted power continued to reduce with time and upon investigation it was realised that the power was being reflected. The proposed reason for this phenomenon was the inscription of a refractive index Bragg grating within the core of the fibre. The propagating wave interfered with a counter-propagating wave due to a weak reflection from the far end of the fibre to form a spatially periodic intensity pattern which modified the refractive index of the core. As more light was reflected, so did the refractive index perturbation grow in concert, with nearly 100% of the light being reflected after some minutes. This was the beginning of the field of photosensitive optical fibres. The Bragg grating had the correct period for reflection at the wavelength of the inscribing wavelength only and was restricted to the visible part of the spectrum. Research was slow to pick up in this field because of difficulties in making measurements and the belief that there was something magical about the original fibre. Stone[2], however, showed that most germania doped silica fibres demonstrated photosensitivity and following the interesting discovery of second harmonic generation from germania doped silica fibres[3] as well, worldwide activity in optical fibre photosensitive behavior began.

The next major step was taken by Meltz et al[4], who demonstrated that by applying standard holographic techniques with UV radiation at 248nm, the Bragg wavelength could be shifted to more useful longer wavelengths in the near IR at 850nm. By a further modification, gratings at telecommunications wavelengths in the 1500nm window were reported, opening the area of photosensitive optical fibre Bragg grating devices[5].

Optical Fibre Bragg Gratings:

Bragg reflection in a waveguide:

Figure 1 shows a refractive index perturbation in a waveguide. A reflection occurs if the period of the perturbation is:

$$\Lambda = N\lambda / 2n_{eff} \qquad (1)$$

where n_{eff} is the effective index of the mode in the waveguide, λ is the Bragg wavelength, and N is the order of the interaction[6]. N is one for a first order interaction.

For synchronous coupling into the backward propagating radiation modes, satisfying the phase-matching condition, Equation (1) alone, is not sufficient. The second important parameter for efficient interaction is the overlap integral of the forward traveling guided-mode with the backward wave and the perturbation profile. This may be computed from simple integrals assuming a uniform index-perturbation across the core. For a guided wave reflection, the overlap decreases with either inclination of the Bragg planes for shallow angles, or asymmetry of the perturbation across the core. On the other hand, counter-propagating radiation mode coupling increases with either asymmetry or inclination of the Bragg planes[7,8], also for shallow angles. Forward propagating radiation mode coupling requires no asymmetry of the grating across the core; the mode only requires additional momentum equivalent to $2\pi\Delta n/\lambda$, where Δn is the core-cladding index difference[9].

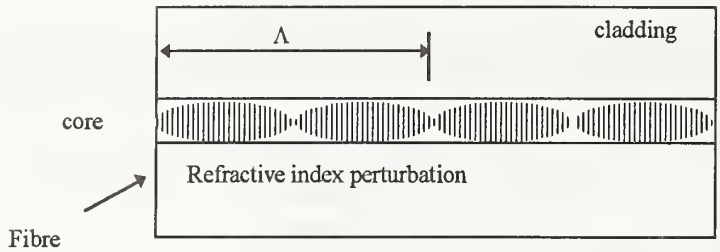

Figure 1. Optical fibre with periodic refractive index modulation in core.

Methods of Fibre Grating Inscription:

Figure 2 shows one of the methods of inscribing Bragg gratings in an optical fibre. The interferometer is based around a beam-splitter[4] or a phase-mask[10,11,12]. The latter is a phase relief grating made in UV-transmitting silica which acts as a diffraction grating. In Figure 1, the phase-mask is used as a beam-splitter with two mirrors to recombine the beams at the fibre. The advantage of the phase-mask is that it allows the easy replication of the Bragg grating at the desired wavelength without re-course to the measurement of the mirror angles. The phase-mask may be used in contact with the fibre[10], and the UV beam scanned along the phase-mask to write a long grating[13]. Variations have also been reported[5], including a method to project a magnified amplitude mask on the fibre to write a higher order grating[14].

Another method writes the grating point by point[15]. In this scheme, the index modulation is induced by focusing a UV laser spot at a point in the fibre and then moving the fibre by a period before the second point is written. Although this method allows long gratings to be written, the positional control required for the integrity of first order grating period, limits this technique to higher orders, or long period gratings[9].

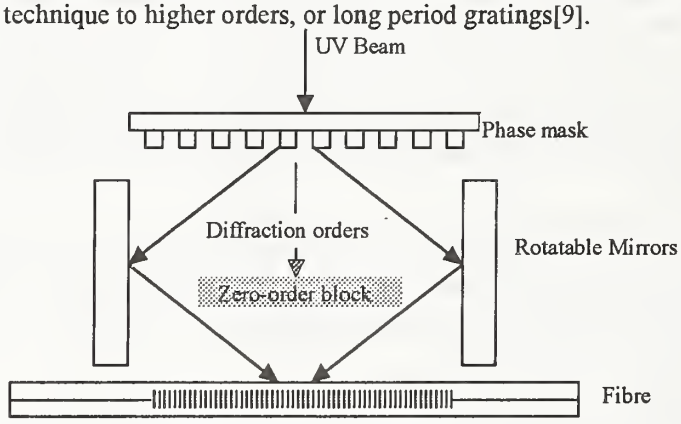

Figure 2. Interferometer used for inscription of gratings, with the phase-mask as a beam splitter.

Simple Fibre Bragg Gratings:

A spatially uniform index modulation along the propagation direction produces a reflection spectrum shown in Figure 3, with side-lobes which decrease with de-tuning from the Bragg wavelength. Basically, the optical fibre Bragg grating is a reflecting band-stop filter. This fact alone limits the usefulness of the simple fibre grating as a device. However, the technology of fibres and Bragg gratings are such that the quality of the perturbation may be maintained over tens of thousands of periods, producing responses close to those theoretically predicted, so that it has been possible to use the amplitude and phase characteristics of a single grating to shape the spectrum of a pulse[16]. The side-lobes shown in Figure 3 are undesirable and may be modified by a number of apodisation schemes[17,18,19]and will be discussed later in the article.

Method of Analysis:

Coupled mode theory[20] may be used to calculate the reflectivity of a uniform grating of length, L and dielectric constant peak modulation of $\Delta\varepsilon$ as:

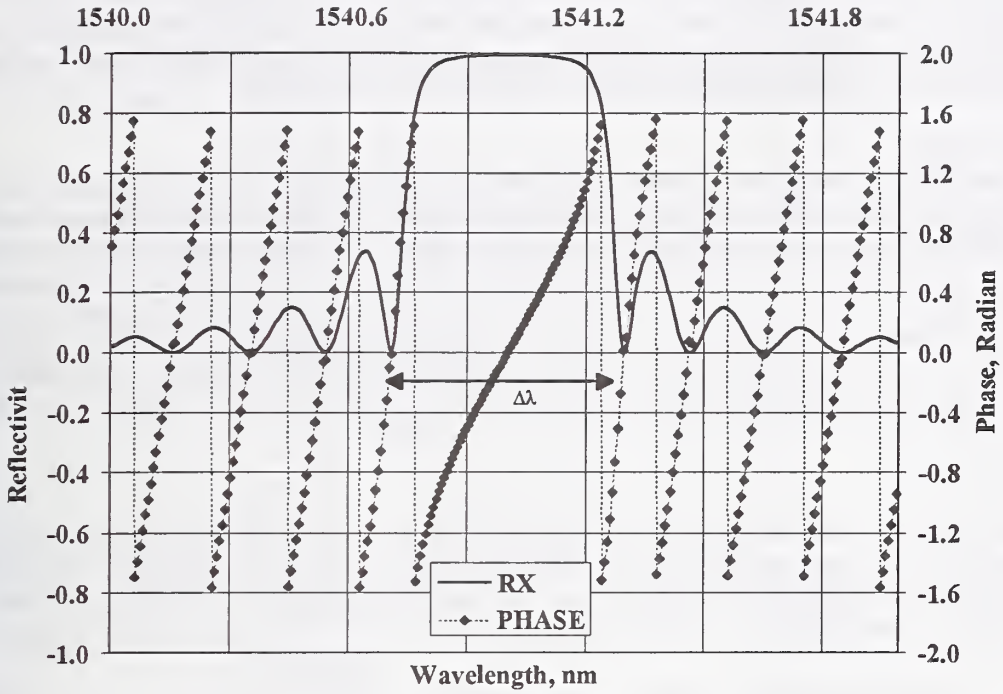

Figure 3. Reflection and phase spectrum of a 4mm long Bragg grating with Δn = 4e-4.

$$R = \frac{\kappa^2 \sinh^2(\Omega L)}{\Omega^2 \cosh^2(\Omega L) + (\Delta k/2)^2 \sinh^2(\Omega L)} \tag{2}$$

where,

$$\kappa = \frac{\pi n_{eff} \Delta\varepsilon}{\lambda n_0^2} \tag{3}$$

is the coupling constant, and $\Omega = \left[\kappa^2 - (\Delta k/2)^2\right]^{1/2}$ is the de-tuning parameter, n_0 is the average fibre refractive index and $\Delta k = \frac{4\pi}{\lambda} - \frac{2N\pi}{\Lambda}$ is the mismatch between the momentum of the mode and the index perturbation.

For the special case of zero mismatch, the reflectivity, R at the Bragg wavelength is

$$R = \tanh^2(kL) \tag{4}$$

Bandwidth, Reflectivity and Modulation Index Relationships and Measurement:

The bandwidth and the reflectivity are the only parameters required to characterise a uniform grating. The bandwidth of the grating which is defined as the difference in wavelengths between the first two minima (See Figure 3) is given as

$$\Delta\lambda = \frac{\lambda^2}{\pi n_{eff} L}\left[(\kappa L)^2 + \pi^2\right]^{1/2} \tag{5}$$

In making measurements or in the design of fibre gratings, the first parameter of interest is the required reflectivity at the Bragg wavelength. Given this value, the argument of Equation (4) may be calculated. From Equation (5), the length of the grating can be calculated for the required bandwidth. The modulation index is then calculated from

Equation (3), with $\Delta n = \Delta\varepsilon/2n_0$. Measurement of a fibre Bragg grating requires a tunable laser or a broadband ASE source, a circulator or coupler and a spectrum analyser. For long uniform gratings, or gratings of high reflectivity ($\Delta\lambda < 0.2$nm or R > 30dB), the transmission spectrum can be difficult to resolve, owing to the resolution of the spectrum analyser, and require refined spectroscopic techniques for measurement[21].

Numerical Method of Analysis:
Gratings of a more complicated nature such as linearly, quadratically chirped or multiple section gratings can be easily analysed by numerical schemes, for example by Rouard's method[22]. This was first applied to optical multi-layer waveguide problems by Weller-Borphy and Hall[23]. This matrix approach allows gratings of arbitrary periods and refractive index modulation to be accurately modeled, and has been used successfully to analyse both linearly and quadratically chirped gratings[19]. The grating is broken up into M sections, each of distinct constant period. Each period is also sub-divided into sufficient sections to mimic the contour of the sinusoidal modulation. The total response of the grating is then computed by summing the fields over the length of the M gratings. The flexibility of this method makes it highly attractive and reasonably fast for purposes of modeling, producing excellent correlation with experimental results.

Band-Pass Filters:
The reflection band-stop filter may be transformed interferometrically into a band-pass filter by using two identical Bragg gratings located on output ports of a 50:50 fibre coupler, equidistant from the coupling region[24]. Balancing of the interferometer can be performed using UV radiation and the photosensitivity of the core dopant in one arm of the coupler. Figure 4 shows a schematic of this device.

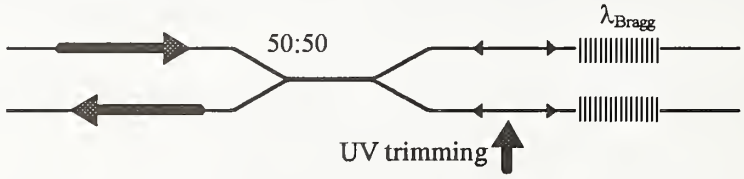

Figure 4. The fibre Bragg grating Michelson interferometer band-pass filter.

The important parameter for such a device is the de-tuning from zero-path length difference for identical unapodised gratings. For a 45dB rejection of the peak, the paths need to be equalised to within $\sim 0.002\lambda_{Bragg}$ [25].

Apodisation of fibre Gratings:
Apodisation reduces side-lobes of a uniform grating so that cross-talk can be reduced in fine grain WDM channels[26]. There are several methods of apodising Bragg gratings. The choice of the type of Hanning function is dependent on the application. However, a simple form of apodisation is the cosine apodisation, in which the amplitude of the modulation index of the grating varies as a cosine function around the centre of the grating. Apodisation requires the Bragg-wavelength to be kept a constant by varying the only the visibility of the fringes at constant UV flux[17,18,19]. An easy and universal scheme for cosine envelope apodisation requires that the fibre be stretched in opposite direction in a way that the edges of the grating experiences a half-period stretch, while the centre see no change[19]. Periodic stretching while writing the grating automatically gives rise to a cosine envelope of the visibility function, at constant flux.

Chirped Bragg Gratings:
Ouellette[27] proposed the use of chirped gratings for dispersion compensation. The principle of operation is simple: the point of reflection varies linearly with wavelength, causing a propagation delay which is also a function of wavelength. Since the propagation delay in a fibre is ~10ns/m in reflection, a compact device is possible; a 100mm long grating with a chirp of 0.1nm is capable of compensating for dispersion of ~700km of standard telecommunications fibre at a bit-rate of 10Gb/s[28]. However, dispersion compensation is in reflection, requiring a circulator or a band-pass configuration for the grating to be used[29, 30].
The design of chirped gratings for dispersion compensation requires some form of apodisation[17] if the coherence-length of the signal wavelength is a few percent of the length of the grating[19]. There are several methods of fabricating a chirped grating. The simplest is to introduce a known strain profile along the length of the grating[31,32], or to replicate a grating from a chirped phase-mask[33]. This method is by far the most reproducible

and mechanically robust method. The step-chirped phase-mask is designed to have n sections, each of a different but constant period. A relatively few steps are needed for a grating of a given chirp bandwidth, $\Delta\lambda_{chirp}$ (in nm) and length (in mm) to approximate to a continuously chirped grating[34]. The minimum bandwidth of each section may be calculated as[34]

$$\delta\lambda \approx 12 \times \Delta\lambda_{chirp} \qquad (4)$$

Without apodisation, the reflection spectrum has steep sides and the delay characteristics display a periodic ripple around an average linear slope; the calculated data of a near continuously chirped grating (200 sections) are shown in Figure 5[19]. With a cosine apodisation envelope of the refractive index modulation, both the reflection and the delay characteristics are smoothed, shown in Figure 6.

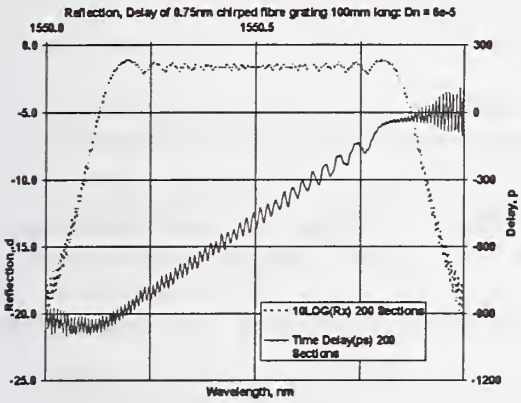

Figure 5

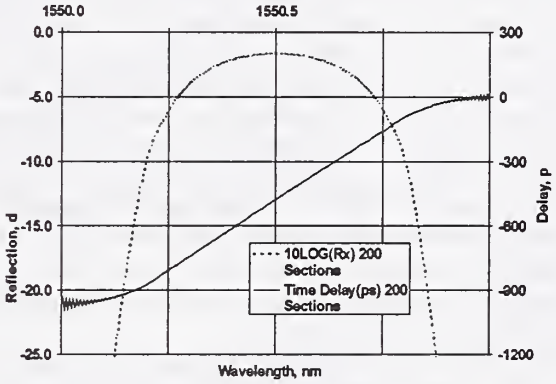

Figure 6

Figures 5 & 6. Theoretical reflection and delay spectrum of 0.75nm bandwidth, 100mm long step-chirped Bragg-grating without (Fig. 5) and with apodisation (Fig. 6).

The delay and reflection characteristics may be measured by using the scheme shown in Figure 7. A tunable external-cavity laser is modulated by a external modulator and coupled to a circulator. The grating is spliced to the second port of the circulator, while the reflected signal is detected by a photo-diode and compared with the modulation signal using a vector-voltmeter. As the laser is tuned the reflected signal and delay can be measured simultaneously. Low coherence reflectometry[35] may also be used to characterise the grating.

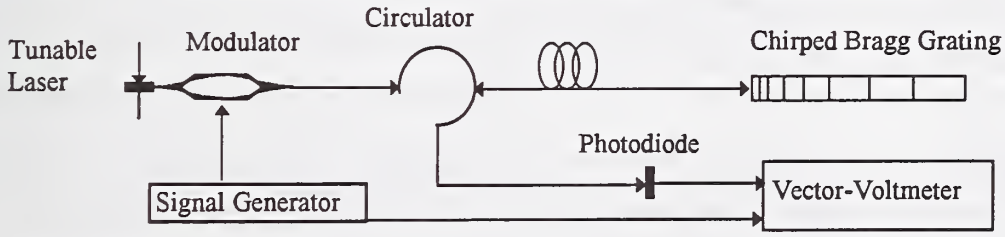

Figure 7. Measurement setup for delay and reflectivity measurement.

The paper will discuss some of the issues relating to the design, measurement and application of fibre Bragg gratings.

References:

1 Hill K O, Fujii F, Johnson D C, Kawasaki B S, 'Photosensitivity in optical waveguides: Application to reflection filter fabrication', *Appl. Phys. Lett. 32*(10), 647, 1978.

2 Stone J, 'Photorefractivity in GeO_2 doped silica fibres', *J. of Appl. Phys. 62*, 4371, 1987.

3 Osterberg U and Margulis W, *Opts. Lett. 11*, 516, 1987.

4 Meltz G, Morey W W & Glenn W H, 'Formation of Bragg gratings in optical fibre by transverse holographic method', *Opts. Lett. 14*(15), 823, 1989.

5 Kashyap R, Armitage J R, Wyatt R, Davey S T, Williams D L, 'All fibre narrowband reflection gratings at 1500nm', *Eectron. Lett. 26*(11), 730, 1990.
6 Kashyap R, 'Photosensitive optical fibres: devices and applications', *Optical Fiber Tech. 1*(1), 17, 1994.
7 Kashyap R, Wyatt R & Campbell R J, 'Wideband gain flattened erbium doped amplifier using a photosensitive fibre-blazed grating', *Electron. Lett. 29*(2), 154, 1993.
8 Erdogan T & Sipe J E, 'Radiation-mode coupling loss in tilted fibre phase gratings', *Opts. Lett. 20*(18), 1838-1840, 1995.
9 Bhatia V & Vengsarkar A, 'Optical fiber long-period grating sensor', *Opt. Lett. 21*(9), 692-694, 1996.
10 Hill K O, Malo B, Bilodeau F, Johnson D C, & Albert J, 'Bragg grating fabricated in monomode photosensitive optical fibres by UV exposure through a phase mask', *Appl. Phys. Lett. 62*(10), 1035, 1993.
11 Anderson D Z, Mizrahi V, Erdogan T & White E A,, 'Phase mask method for volume manufacturing of fiber phase gratings', *Proc. Conf. On Opt. Fiber Comm., OFC '93,* Tech. Digest., p68., Postdeadline Paper P16, 1993.
12 Kashyap R, Armitage J R, Campbell R J, Williams D L, Maxwell G D, Ainslie B J & Millar C A, 'Light-sensitive optical fibre and planar waveguides', *BT Technol. J. 11*(2), 1993.
13 Martin J & Ouellette F, 'Novel writing technique for long highly reflective in fibre', *Electron. Lett. 30*, 811, 1994
14 Rizvi N H, Gower M C, Goodall F C, Arthur G & Herman P, 'Excimer laser writing of submicrometre period fibre Bragg gratings using phase-shifting mask projection', *Electron. Lett. 31*(11), 901-902, 1995.
15 Hill K O, Malo B, Vineberg K A, Bilodeau F & Johnson D C, 'point by point', *Electron. Lett. 26*, 1270-72, 1990.
16 Kashyap R, de Lathouwer M, Emplit Ph., Haelterman M, Campbell R J & Armes D J, 'Optical Dark soliton generation using a fibre Bragg grating', *Topical meeting on Photosensitivity and Quadratic Nonlinearity in Glass Waveguides: Fundamentals and Applications, OSA Technical Digest No. 301, 1995.*
17 Malo B, Theriault S, Johnson D C, Bilodeau F & Hill K O, 'Apodised in-fibre Bragg grating reflectors photoimprinted using a phase mask', *Electron. Lett.31*(3), 223, 1995.
18 Cole M J, *et al.*, 'Moving fibre/phase mask-scanning beam technique for enhanced flexibility in producing fibre gratings with a uniform phase mask', *Electron. Lett.31*(17), 92, 1995.
19 Kashyap R, Swanton A, & Armes D J, 'A novel technique for apodisation of chirped and unchirped Bragg gratings', *Electron. Lett. 32*(13), June 1996.
20 Yariv A, & Yeh P, In *'Optical waves in crystals', Ch. 11, Publ. J. Wiley & Sons, 1984.*
21 Kashyap R McKee P F, Armes D J, Shabeer M & Cotter D, 'Measurement of ultra-steep edge, high rejection fibre Bragg grating filters', *Electron.Lett. 31*(15), 1282-1283, 1995.
22 Rouard M P, 'Etudes des proprietes optiques des lammes metaliques tres mince', *Annal. Phys. II, 7*(20), 1937.
23 Weller-Borphy L A & Hall D G, 'Analysis of waveguide gratings: application of Rouard'd method', *J. Opt. Soc. Am. B. 2*(6), 863-871, 1985.
24 Bilodeau F, Hill K O, Johnson D C & Albert J, 'High-return-loss narrowband all-fiber bandpass Bragg transmission filter', *IEEE. Photon. Technol. Lett. 6*(1), 80, 1994.
25 Kashyap R, 'Design of fibre grating band-pass filters', *In preparation.*
26 Malo B, Theriault S, Johnson D C, Bilodeau F, Albert J & Hill K O, 'Apodised in-fibre Bragg grating reflectors photoimprinted using a phase mask', *Electron. Lett. 31*(3), 223-225, 1995.
27 Ouellette F, 'Dispersion cancellation using linearly chirped Bragg grating filters in optical waveguides', *Opts. Lett. 12*(10), 847, 1987.
28 Loh W H, Laming R, Ellis A D & Atkinson D, '10Gb/s transmission over 700km of standard single mode fibre with 10cm chirped fibre grating compensator and duobinary transmitter', *Submitted to : Photon. Tech. Lett.*
29 Hill K O, Bilodeau F, Malo B, Kitagawa T, Theriault S, Johnson D C & Albert J, 'Aperiodic in-fiber Bragg gratings for optical fiber dispersion compensation, *OFC'94, Postdeadline paper, PD2, pp. 17-20, 1994.*
30 Chernikov S V, Taylor J R & Kashyap R, 'All-fiber dispersive transmission filters based on fiber grating reflectors', *Opts. Lett. 20*(14), 1586-1588, 1995.
31 Laming R I, Robinson N, Scrivener P L, Zervas M N, Barcelos S, Reekie L & Tucknott J A, 'A dispersion tunable grating in a 10-Gb/s 100-200km step index fibre link', *IEE Photon. Technol. Lett. 8*(3), 428-430, 1996.
32 Krug P A, Stephens T, Yoffe G, Ouellette F, Hill P & Doshi G, 'Dispersion compensation over 270 km at 10Gb/s using an offset-core chirped Bragg grating', *Electron. Lett. 31*(13), 1091-1092, 1995.
33 Kashyap R, McKee P F, Campbell R J & Williams D L, 'A novel method of writing photo-induced chirped Bragg gratings in optical fibres', *Electron. Lett. 30*(12), 996, 1994.
34 Kashyap R, 'Design of step-chirped gratings', *Submitted to Opts. Comm.*
35 Lambert P, Fonjallaz P Y, Limberger H G, Salathe R P, Zimmer Ch & Gilgen H H, 'Bragg grating characterisation by optical low coherence reflectometry', *IEEE Photon. Technol. Lett. 5*, 565-567, 1993.

Chirp Determination of Fiber Bragg Gratings with Interferometric Autocorrelation Measurements

M. Fuss, University of Kaiserslautern, Germany

Abstract: The possibility of in-fiber Bragg gratings characterization by analyzing of the first and second order interferometric autocorrelation functions of ps-pulses from a fiber laser and that ones reflected from the fiber grating has been investigated. The initial pulses were almost unchirped but the reflected ones obtained a significantly nonlinear phase shift induced by the fiber grating. Pulses nonlinear phase is dependent on gratings chirp and can be evaluated by means of interferometric autocorrelation measurements.

I. Introduction

In optical fiber transmission systems with high bit rates up to 10 Gbit/s and more dispersion has to be compensated to minimize pulse broadening for error-free detection. Especially at 1.55µm used in already-installed fiber links the compensation of fibers chromatic dispersion is of great importance. Several methods for achieving this are already known but linearly chirped fiber Bragg gratings are a promising method due to their constant dispersion over a bandwidth, sufficient to support ultrashort pulses [2][3][6][9]. Otherwise chirped fiber gratings specified by customers can find application as frequency selective components. Chirp determination with the heat-scan technique [7] or by external Bragg reflection [4] have been investigated, however, they require special equipment. If an interferometric autocorrelation measurement device for ultrashort optical pulses is available it can be used for fiber grating characterization as well.

II. Experimental setup

A measurement configuration consisting of an opto-mechanical autocorrelation apparatus with an electronic control unit and fringe-counting determination of displacement with digital data acquisition was constructed [1]. The experimental setup of the autocorrelator is shown in Fig.1.

The light to be measured entered the autocorrelator in a fiber collimator and passed a Michelson-interferometer with the moving retroreflector mounted on a translatory electrodynamic unit.

Two kinds of interferometric signals were measured simultaneously, with a photodetector (PD1) the fundamental harmonic light interferogram $S_1(\tau)$ as field autocorrelation function $G_1(\tau)$ and with a photomultiplier tube (PMT) the Frequency Resolved Second Harmonic Generation (FRSHG) signal $S_2(\tau)$ containing the intensity autocorrelation $G_2(\tau)$, a portion $F_1(\tau)$ at light frequency and the second harmonic light interferogram $F_2(\tau)$ at doubled frequency. As nonlinear medium a 3mm thick $LiIO_3$-crystal was used. It was cut for the center wavelength of 1475nm in order to enable phase-matching for 1550nm and 1300nm only by rotating a few degrees left or right on its axis.

To scan the signals with sufficient accuracy the linearly polarized light of a Helium-Neon-laser was directed into the Michelson-interferometer likewise with changing the polarization circularly by using a quarter wave plate. The two resulting orthogonally polarized interference signals dependent on the movement of one retroreflector were separated with a polarization beamsplitter and detected with two separated photodetectors. An electronic processing unit generated clock pulses for the analogous/digital-converter each $\frac{1}{2}\cdot\lambda_{HeNe}$=316,4nm displacement of the retroreflector.

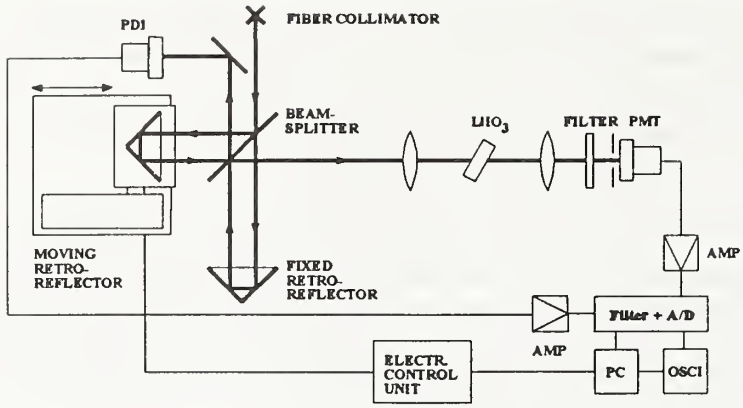

Fig. 1: Experimental setup of the collinear optical interferometric autocorrelator with signal processing electronics

Designating pulse electric field as $E(t)=E_o(t)e^{j\omega t}$ the measured autocorrelation signals $S_1(\tau)$ and $S_2(\tau)$ can be written normalized as functions of the time delay τ between the two beams in the Michelson-interferometer:

$$(1) \qquad S_1(\tau) \propto \int_{-\infty}^{+\infty} |E(t) + E(t+\tau)|^2 \, dt \propto 1 + Re[G_1(\tau)\, e^{j\omega\tau}]$$

$$(2) \qquad S_2(\tau) \propto \int_{-\infty}^{+\infty} |[E(t) + E(t+\tau)]^2|^2 \, dt \propto 1 + 2G_2(\tau) + 4Re[F_1(\tau)\, e^{j\omega\tau}] + Re[F_2(\tau)\, e^{2j\omega\tau}]$$

Pulse intensity and nonlinear phase particularly can be evaluated without equidistant scanning by comparing autocorrelation traces with simulated ones assuming physically well founded intensity profile and nonlinear phase behavior. A simulation program was developed executing this task.

The Fourier transforms of the two with interferometric accuracy digitized autocorrelation signals can be calculated by using Fast Fourier Transformation (FFT). From $S_1(\tau)$ the spectrum $|E(\omega)|^2$ at the fundamental frequency and from $S_2(\tau)$ the Fourier transforms $|I(\omega)|^2$ at zero frequency and $|U(\omega)|$ at the doubled frequency are deduced. Following relations are valid:

$$(3) \qquad |E(\omega)|^2 = \mathscr{F}\{G_1(\tau)\} \qquad |I(\omega)|^2 = \mathscr{F}\{G_2(\tau)\} \qquad |U(\omega)|^2 = \mathscr{F}\{F_2(\tau)\}$$

Another way of obtaining information about pulses intensity and phase is to reconstruct them with an iterative loop algorithm using the three Fourier moduli above [5]. The main idea is to approximate the electric field E(t) by replacing the Fourier moduli in frequency domain by calculated ones and applying the relations $I(t)=|E(t)|^2$ and $U(t)=E^2(t)$ in time domain.

III. Method for chirp determination of fiber Bragg gratings

The two autocorrelation signals $S_1(\tau)$ and $S_2(\tau)$ of 10ps absolutely unchirped pulses were simulated with 1024 points each. In Fig.2 and Fig.3 the resulting traces are shown used as references in comparison with those of the reflected pulses.

The axial distribution of the index modulation affecting an appropriate Bragg reflection condition regarding wavelength causes different optical pathes for different frequencies if the reflected pulses

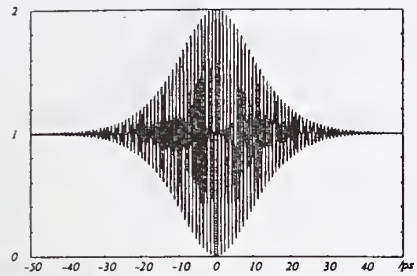

Fig. 2: $S_1(\tau)$ of unchirped pulses

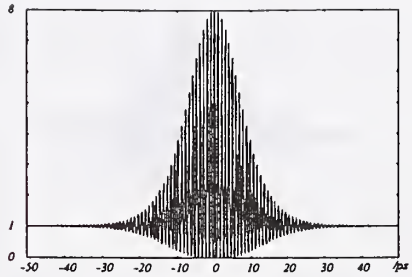

Fig. 3: $S_2(\tau)$ of unchirped pulses

are containing these optical frequencies. Therefore the measurement of pulses nonlinear phase behavior allows information about fiber gratings chirp distribution.

Assuming as example a linearly chirped fiber grating extended in z-direction with the length L and a Bragg wavelength distribution $\Lambda(z/L)$ around the center wavelength Λ_0 as follows:

$$\Lambda\left(\frac{t}{\Delta T}\right) = \Lambda\left(\frac{z}{L}\right) = \Lambda_0 + \Delta\Lambda\,\frac{z}{L} = \Lambda_0 + \Delta\Lambda\,\frac{t}{\Delta T} \tag{4}$$

ΔT stands for the difference in transit time and is equal to $2Ln_{eff}/c$. If the optical bandwidth $\Delta\lambda$ of the pulse signal is matched to the bandwidth of the fiber grating for a fiber length S the dispersion D can be compensated with $\Delta T = D\Delta\lambda S$.

Equation (5) for the pulses nonlinear phase $\Phi(t)$ is based on the linear chirp of formula (4):

$$\phi(t) = \int f\left(\frac{t}{\Delta T}\right)dt = \frac{c\,\Delta T}{\Delta\Lambda}\ln\left(1+\frac{\Delta\Lambda}{\Lambda_0}\frac{t}{\Delta T}\right) \Rightarrow \Phi_{nl}(t) \approx \frac{c\,\Delta\Lambda\,t^2}{2\,\Lambda_0^2\,\Delta T} \tag{5}$$

In accordance to this temporal nonlinear phase shift $S_1(\tau)$ and $S_2(\tau)$ result, shown in Fig.4 and Fig.5. Comparing the simulated envelopes with the measured signals with attention to the number and shape of extrem values admits sufficient conclusion to fiber gratings chirp.

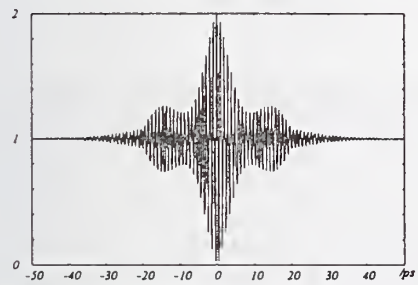

Fig. 4: Simulation of $S_1(\tau)$

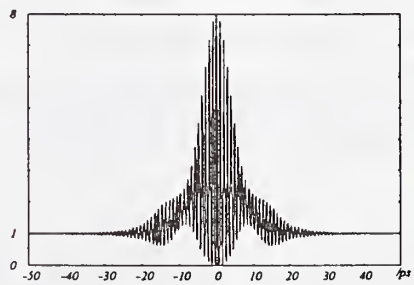

Fig. 5: Simulation of $S_2(\tau)$

Parameters for the simulation of $S_1(\tau)$ and $S_2(\tau)$:
Λ_0=1.55 µm, $\Delta\lambda$=0.5 nm,
L=10 mm, n_{eff}=1.5

IV. Measurement results

First confirmation of the measurement principle above was carried out with an unchirped fiber grating. First order autocorrelation function $S_1(\tau)$ of the unchirped fiber laser pulses is shown in Fig.6. The laser signal had to be amplified strongly with an Erbium Doped Fiber Amplifier (EDFA) before entering the grating, resulted autocorrelation trace in Fig.7. Slight Self Phase Modulation (SPM) causes the trace to appear little compressed. Due to the short pulse duration of approximately 5ps and gratings narrow bandwidth of about 0.1nm significant pulse broadening up to a factor of 10 could be obtained. of both of gratings input and output pulses, shown in Fig.8. Side maxima illustrate the initial SPM but the basic shape of the envelope has not changed. In this case a further detailed analysis of the measurement results was not necessary.

In a next step a customer specified chirped fiber grating ordered by Deutsche Telekom AG is to be characterized and the results will be presented at the conference.

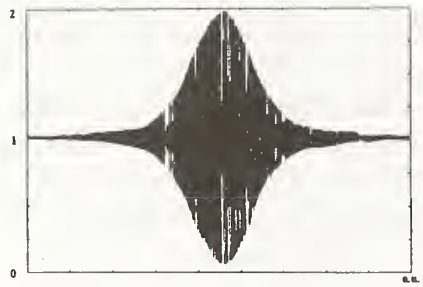

Fig. 6: $S_1(\tau)$ of fiber laser pulses

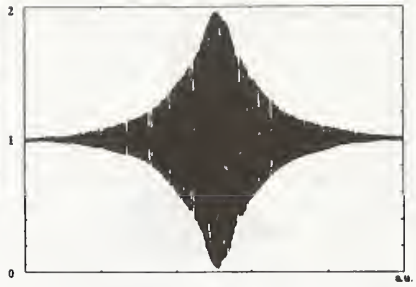

Fig. 7: $S_1(\tau)$ of fiber laser pulses, strongly amplified with EDFA

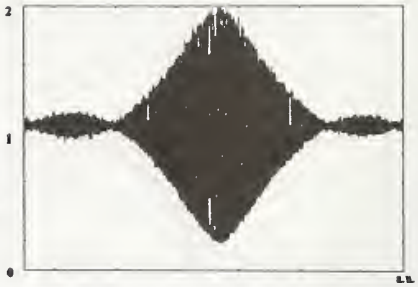

Fig. 8: $S_1(\tau)$ of reflected pulses by the fiber Bragg grating

V. Conclusions

An optical autocorrelator was developed for measuring both intensity and interferometric autocorrelation functions to determine shape and nonlinear phase, especially, of ultrashort pulses. By comparison or iterative processing of the autocorrelation data aquired with appropriate accuracy, especially, pulses can be calculated sufficiently. The measurement procedure is suited for characterization of wavelength distribution in chirped fiber Bragg gratings. In the case of a linearly chirped grating the two measurable autocorrelation signals were simulated and significant envelopes of the traces resulted. An unchirped fiber grating was available up to now in experimental work. The amplified but nearly unchirped pulses of a fiber laser were fed into the grating and the reflected ones obtained broadening due to the small bandwidth of the grating but no nonlinear phase change occured.

VI. Acknoledgements

This work was supported by the Deutsche Telekom AG. The author wish to thank Prof. W.E.Heinlein for constant encouraging and helpful discussions.

VII. References

[1] M. Fuss and W. Heinlein.: Characterization of fibre amplifiers influence on the nonlinear phase of ps-pulses. Optical Amplifier and Their Applications conference, Monterey, July 10-13, 1996

[2] K.O. Hill, F. Bilodeau, B. Malo, T. Kitagawa, S. Thériault, D.C. Johnson, J. Albert: Chirped in-fiber Bragg gratings for compensation of optical-fiber dispersion. Optics Letters, Vol. 19, No. 17, 1994

[3] R. Kashyap, S.V. Chernikov, R.J. Campbell, P.F. McKee, D.L. Williams, J.R. Taylor: Demonstration of dispersion compensation in all-fibre photoinduced chirped gratings. Pure Applied Optics, No. 4, 1995

[4] P.A. Krug, R. Stolte, R. Ulrich: Measurement of index modulation along an optical fiber Bragg grating. Optics Letters, Vol. 20, No. 17, 1995

[5] K. Naganuma, K. Mogi, H. Yamada: General method for ultrashort light pulse chirp measurement. IEEE Journal of Quantum Electronics, vol. 25, no. 6, 1989

[6] F. Oulette, J.-F. Cliche, S. Gagnon: All-Fiber Devices for Chromatic Dispersion Compensation Based on Chirped Distributed Resonant Coupling. Journal of Lightwave Technology, Vol. 12, No. 10, 1994

[7] S. Sandgren, B. Sahlgren, A. Asseh, W. Margulis, F. Laurell, R. Stubbe, A. Lidgard: Characterisation of Bragg gratings in fibres with the heat-scan technique. Electronics Letters, Vol. 31, No. 8, 1995

[8] D. Taverner, D.J. Richardson, J.-L. Archambault, L. Reekie, P.St.J. Russell, D.N. Payne: Experimental investigation of picosecond pulse reflection from fiber gratings. Optics Letters, Vol. 20, No. 3, 1995

[9] J.A.R. Williams, I. Bennion, K. Sugden, N.J. Doran: Fibre dispersion compensation using a chirped in-fibre Bragg grating. Electronics Letters, Vol. 30, No. 12, 1994

Optical Amplifier Characterization

F. W. Willems
Lucent Technologies
Network Systems Nederland
P.O. Box 18, 1270 AA Huizen, The Netherlands

Abstract: We present an overview of black-box measurement issues for optical amplifiers for analog and multi-wavelength characterization. In addition, we propose figures-of-merit for Erbium doped fibers used for those applications.

1 Introduction

This paper is divided in two major parts, the first one dealing with definitions and measurement methods for optical amplifiers treated as a black box, the second one dealing with characterisation of the main components in this black box: the Erbium doped fiber.

2 Black-box characterization

2.1 Single wavelength "Digital" Amplifiers

For these "simple"amplifiers, measurement methods exist for optical output power, gain, noise figure and reflectance. Basically they can be devided into Optical and Electrical methods. Typical examples for both are the the noise figure measurement by polarization nulling [1] using an Optical Spectrum Analyzer (OSA), and the one by RIN subtraction [2] for the ESA method.

2.2 "Analog" Amplifiers

Non-linear distortion and in particular second order distortion, is typically associated with amplifiers used in analog CATV systems. Several sources can be identified for this second order distortion:

1. *Signal induced carrier-density modulation* [3, 4]. The gain of an optical amplifier will be modulated by the signal if the product of the carrier lifetime τ_c and the signal modulation angular frequency of subcarrier i, ω_i, is below a certain value, since the second order harmonic distortion is given by Eq.(1).

$$HD_2^{cdm} = \left(\frac{mP_{out}}{P_{sat}} \frac{1}{\sqrt{1+(\omega_i \tau_c)^2}} \right)^2 \qquad (1)$$

with m the optical modulation index per channel, P_{out} the optical amplifier's output power and P_{sat} the optical amplifier's saturation output power. For an EDFA we have $\tau_c = 10$ms and $\omega_i = 50$ MHz, and therefore $\omega_i \tau_c = 5 \cdot 10^5$, which leads to negligible contribution to the second order distortion. However, note that for a semiconductor amplifier, typically $\tau_c = 300$ps, leading to a value 0.015 for the lifetime-frequency product, which is low enough to cause a large amount of distortion. THe carrier lifetime of Praseodymium doped amplifiers is around 300 μs which is also long enough to avoid carrier-density modulation. Therefore it is expected that for fiber amplifier modules, it is not necessary to measure this effect.

2. *Interaction of transmitter wavelength chirp with the gain-slope at the signal wavelength* [5, 6]. A gain profile around a saturating signal which is not flat, converts the frequency shift by direct modulation of a semiconductor laser to a spurious intensity modulation, causing second order distortions that can calculated with equation Eq.(2)

$$HD_2^{gsl} = \left(\frac{\ln 10}{20} \frac{\lambda^2}{c} \delta\nu_o \frac{dG}{d\lambda} \right)^2 \qquad (2)$$

with $\delta\nu_o$ the frequency chirp amplitude in Hz, and $\frac{dG}{d\lambda}$, the gain-slope of the EDFA at the signal wavelength. For directly modulated systems, the chirp amplitude can be calculated with $\delta\nu_o = m\eta_{FM}(I_{bias} - I_{th})$, with η_{FM} the FM-response of the laser diode, I_{bias} the bias current and I_{th} the laser threshold current. This distortion source is always present in principle.

3. *Interaction of transmitter wavelength chirp with dispersion of the Dispersion Compensating Fibre (DCF, if present)* [7]. Optical frequency chirp by direct modulation of the laser current, causes different propagation delays in a dispersive medium for different parts of the information signal, resulting in a distorted receiver input signal. If an optical amplifier is equipped with Dispersion Compensating Fibre (DCF), to

compensate for the dispersion in the feeder section in the network, the second order distortion will be very huge, if no precautions are taken to "compensate for the compensation". The resulting second order distortion would be:

$$HD_2^{disp} = \left(\frac{\pi}{2}\frac{\lambda^2}{c} f_d \delta\nu_o DL\right)^2 \quad (3)$$

with f_d the subcarrier frequency for which the distortion is calculated, D the fibre dispersion, and L the fiber length. If the dipsersion compensator (DCF, chirped grating) is integrated in the optical amplifier, large values for CSO will result if no proper precautions are taken to compensate the compensator.

4. *Interaction of Polarization-Mode-Dispersion (PMD) and Polarization Dependent Loss (PDL)* [8]. Polarization modulation caused by interaction of laser frequency chirp and PMD of a section just in front of the optical amplifier, is converted into intensity modulation if the amplifier exhibits PDL. Since polarization mode coupling is a time dependent phenomenon, the distortion fluctuated in time an only the time averaged second order distortion can be calculated:

$$HD_2^{pdl} = \left(\sqrt{\frac{\pi^3}{12}}\delta\nu_o \Delta T < \Delta\tau >\right)^2 \quad (4)$$

with ΔT the PDL, and $< \Delta\tau >$ the PMD. This effect can occur if an element that exhibits PMD (e.g. the Erbium Doped Fiber or the DCF) preceeds an element that has PDL (e.g. a WDM or an isolator). A separate PMD and PDL measurement might be needed to resolve this effect.

5. *Interaction of Self-Phase-Modulation induced frequency chirp with dispersion of DCF (if present)* [7, 9]. SPM results in a frequency chirp that can interact with the fibre dispersion, resulting in second order distortion. The distortion is by

$$HD_2^{disp} = \left(2m\pi^2 \frac{\lambda}{c}\frac{N_2}{A_{eff}} P_o f_d^2 D \frac{1}{\alpha}\left(L - \frac{1}{\alpha}\left(1 - e^{-\alpha L}\right)\right)\right)^2 \quad (5)$$

with N_2 the fiber's nonlinear index of refraction, A_{eff} the effective core area, P_o the average optical power entering the fiber, and α the loss of the fiber. If the optical amplifier contains dispersion compensating fibre at a location such that high optical power is injected in the DCF, SPM can cause frequency chirp and the same situation as with chirp-dispersion interaction exists.

6. *Coherent interference of multiple discrete reflections* [10, 11]. Mixing of the signal with a delayed fraction of itself, distorts the signal and generates second and third order distortions. The delayed fraction results from multiple reflections (MPI). The second order distortion magnitude is given by

$$HD_2^{mpi} = \left(4\frac{R_{eff}}{m} J_2(z_j) \prod_{i \neq j}^{N} J_0(z_i)\right)^2 \quad (6)$$

with R_{eff} the effective reflection coefficient, J_n the n-th order Bessel function, and $z_i = 2\frac{\delta\nu_o}{f_i}\sin(\omega_i\tau/2)$, and τ the cavity roundtrip time. Occurence if more than one discrete optical reflection exists, that have a distance less than the coherence length of the transmitter laser.

7. *Stimulated Brillouin scattering induced intensity modulation* [12] No simple equation to calculate this distortion exists. Occurence:The linewidth of the transmitter is not well above the SBS linewidth; DCF is used inside the optical amplifier.

Most of the distortion mechanisms described above can not be solely attributed to the optical amplifier, but arise in conjunction with non-idealities from elsewhere in the system. Ideally an OFA parameter can be measured without having to do a system measurement. Currently, it seems that the only candidate for system independent measurement is the gain slope:
Definition: We define the *gain-slope under single wavelength operation* as, "in the presence of a signal at given wavelength and optical input power, the derivative of the gain of a small probe, versus the wavelength, at the signal wavelength". The probe total time averaged power shall be at least 30 dB below the input signal level, to minimize the gain at the signal wavelength.

2.3 "WDM" Amplifiers

The field of application of optical amplifiers in multi-wavelength system is becoming larger every day, as is the growth in terminology that is used to address typical WDM parameters. We will therefore first present a set of definitions that follow the, still continuing discussion, within IEC.

2.3.1 Definitions

- *Multi-channel gain:* The gain for each channel of a multi-channnel input spectrum for a given input power configuration, expressed in dB.
- *Multi-channel gain flatness:* The maximum channel gain deviation over specified range of channel input power combinations.
- *Gain cross saturation:* The change in gain of one channel due to a given input signal change on any of the other channels for given input power combinations, expressed in dB/dB.
- *Gain tilt* the ration of gain change at any channel to the gain change at a selected reference channel due to a change of input condition, expressed in dB/dB.
- *Channel addition/removel response:* the maximum change in any remaining channel's output power following the addition/removel of input channel(s) after a specified time, expressed in dB.
- *Channel noise figure:* For each optical channel, the increase in signal-to-noise ratio at the output of an optical detector with unity quantum efficiency that follows an ideal (zero insertion loss) demultiplexer due to the propagation of a shot noise limited signal, expressed in dB. It is assumed that all signals are applied at individually specified power levels.
- *Channel signal-spontaneous noise :* Same as the previous definition, but only includes the signal-spontaneous beat-noise contribution to channel noise figure, expressed in dB.

2.3.2 Measurement Methods

Within IEC, no measurement methods for multi-wavelength application have been defined yet. However the most logical way to analyze WDM behavior of an optical amplifier is to subject the amplifier to the complete wavelength packet and to measure the gain and noise figure at each individual wavelength with one of the methods described above. From a practical point of view this has the disadvantage that multiwavelength transmitter, or at least a number of tunable DFB lasers must be available, which is very costly.
Considering that the spectral gain behaviour in a homogeneously broadened medium is determined solely by the average Erbium ion inversion, one can try to simulate the amplifier's response on a multi-wavelength signal, with a single wavelength that generates the same inversion level. The gain spectrum of a broadband light source consequently gives the multi wavelength gain spectrum [13].
It has been shown, however, that even at room temperature spectral hole burning can occur [14]. In this case the method above can not be used. However, currently it seems that errors in a measurement that uses the noise gain profile method for an amplifier that exhibits room temperature spectral hole burning, do not exceed 0.2 dB.

3 Erbium Doped Fiber Characterization

3.1 FOM for analog applications

The CSO (Composite Second Order) distortion caused by the interaction of laser chirp and gain-slope of an EDFA is given by the product of the number of distortion products that generate second order distortions, N_{CSO} (determined by frequency channel allocation for a particular CATV system), and harmonic distortion from one of those products. We found, using Giles modeling [15], that the total second order harmonic distortion caused by gain-slope is given by

$$CSO_{gsl,edfa} = N_{CSO} \cdot \left(\frac{1}{2}\beta L\left[\frac{\partial\alpha(\nu)}{\partial\nu}(\overline{\bar{n}_2(z)}-1)+\frac{\partial g^*(\nu)}{\partial\nu}\overline{\bar{n}_2(z)}\right]\right)^2 \quad (7)$$

with β the laser chirp in Hz/mA, L the fibre length, α the absorption in Np/m, ν the optical frequency, g^* the stimulated emission in Np/m and $\overline{\bar{n}_2(z)}$ the averaged (time and location z) Erbium ion inversion level. This equation tells us that the distortion can be minimized by three parameters: the Erbium doped fiber length, the average inversion, and the emission and absorption profiles. These parameters also determine the noise figure and output power, and therefore a balance must be found between them to make the EDFA fulfill the specification. Note that the harmonic distortion vanishes if we zero the term between square brackets in eq.8, i.e. if

$$\frac{\partial g^*(\nu)}{\partial\nu} = \left(\frac{1}{\overline{\bar{n}_2(z)}}-1\right)\frac{\partial\alpha(\nu)}{\partial\nu} \quad (8)$$

Therefore, each wavelength requires its particular inversion to have zero gain-slope. This inversion is given by:

$$\overline{\bar{n}_2(z)} = \frac{1}{1+\frac{\frac{dg^*(\lambda)}{d\lambda}}{\frac{d\alpha(\lambda)}{d\lambda}}} \quad (9)$$

For the best LOFA EDF, $\bar{n}(\lambda)_{D2=0}$ does not depend on wavelength and is as small as possible in the analog wavelength range (1545-1560 nm). Therefore, we introduce the following EDF figure of merit Λ to quickly assess the suitability for LOFA application:

$$\Lambda = \left(\bar{n}(\lambda)^{max}_{D2=0} - \bar{n}(\lambda)^{min}_{D2=0}\right) \cdot \left(\bar{n}(\lambda)^{max}_{D2=0} + \bar{n}(\lambda)^{min}_{D2=0}\right) = \left(\bar{n}(\lambda)^{max}_{D2=0}\right)^2 - \left(\bar{n}(\lambda)^{min}_{D2=0}\right)^2 \tag{10}$$

where $\bar{n}(\lambda)^{max}_{D2=0}$ is the maximum and $\bar{n}(\lambda)^{min}_{D2=0}$ is the minimum value of $\bar{n}(\lambda)_{D2=0}$ in the 1545-1560 nm wavelength range.

3.2 FOM for WDM applications

According to Giles modeling we have,

$$\frac{dP(z,\lambda)}{dz} = \gamma(z,\lambda)P(z,\lambda) \tag{11}$$

where

$$\gamma(\lambda, z) = [\alpha(\lambda) + g^*(\lambda)]\,\bar{n}_2(z) - [\alpha(\lambda) + \delta(\lambda)] \tag{12}$$

with α the absorption in Np/m, g^* the stimulated emission in Np/m, $\bar{n}_2$ the time averaged inversion coefficient, and δ the background loss (Rayleigh backscatter and impurity absorption in Np/m). If we define the time and location averaged inversion $\overline{\bar{n}_2(z)} = \frac{1}{L}\int_0^L \bar{n}_2(z)dz$, with L the Erbium doped fiber length, we arrive, expressing all parameters in dB, at the following expression for the gain G

$$G(\lambda) = L[(\alpha(\lambda) + g^*(\lambda))\overline{\bar{n}_2(z)} - (\alpha(\lambda) + \delta)] \tag{13}$$

The required length for a certain gain and inversion is given by

$$L = \frac{G}{(\alpha + g^*)\overline{\bar{n}_2(z)} - (\alpha + \delta)} \tag{14}$$

The difference in required gain at wavelength λ_0 and the gain at any wavelength λ, $G_0 - G(\lambda)$, can be calculated with equation 13 combined with equation 14:

$$\Delta G = G \cdot \frac{[\alpha(\lambda) - \alpha_0)](\overline{\bar{n}_2(z)} - 1) + \overline{\bar{n}_2(z)}[g^*(\lambda) - g_0^*]}{(\alpha_0 + g_0^*)\overline{\bar{n}_2(z)} - (\alpha_0 + \delta)} \tag{15}$$

Of course, one can rewrite Eq.(15) to resemble the gain-ripple relative to a certain gain-level. The choice must still be made to base the FOM to be defined lateron on the relative Γ figure or on absolute gain and ripple figures.

$$\Gamma = \frac{\Delta G}{G} = \frac{[\alpha(\lambda) - \alpha_0)](\overline{\bar{n}_2(z)} - 1) + \overline{\bar{n}_2(z)}[g^*(\lambda) - g_0^*]}{(\alpha_0 + g_0^*)\overline{\bar{n}_2(z)} - (\alpha_0 + \delta)} \tag{16}$$

We will use equation 15 to analyze how well different fibers perform with respect to the two criteria mentioned in the introduction.

A flat noise-gain profile for a certain input power/gain requirement. The required gain, which we will denote by G_0, is determined by the fiber length L and the inversion n_2 (see Eq.(13)), the profile ΔG can be tuned by n_2(see Eq.(15)). Therefore we must find for a certain gain, the value for n_2 that gives the best gain-flatness. With this value we can calculate the required fiber length with Eq.(14)), and we "only" have to provide enough pump power to generate the required inversion level.

Easy adjustment for new input power arrangement by changing the pump power Consider next a change in total signal input power. If we want that the gain is not affected by this, we must adjust the pump power such that the inversion level does not change. Since the length L is fixed, also the gain profile does not change if we succeed in providing the right amount of pump power.

Now, the lower the required n_2 is, as determined in the previous step, the "easier" a pump power adjustment will lead to a new optimum situation.

Therefore, to summarize, for certain Erbium doped fiber, we have to look for the inversion level that leads to the flattest noise-gain profile. The lower this inversion level is, the higher the change is that we can design a WDM EDFA that can cope with input power changes.

A good WDM fiber has a flat noise-gain profile over a large range of wavelength for low average inversion. A figure of merit incorporates those parameters. Therefore, we propose the following FOM for WDM applications:

$$FOM_{wdm} = \left(\Delta\lambda(1 - \overline{\bar{n}_2(z)}_{opt})\right)^{-1} \tag{17}$$

with $\Delta\lambda$ the wavelength range for which the gain profile stays within ± 0.5dB, and $\overline{\bar{n}_2(z)}_{opt}$ the inversion level that leads to a maximum gain flatness.

We will show during the presentation data for FOM analog and WDM and indicate the correlation between the two.

4 Conclusions

Measurement methods for single channel "digital" optical amplifiers are close to standardization. Both the ESA and OSA methods can be used to get comparable data in principle. Currently under development are measurement methods that address the specific parameters for analog and multi-wavelength digital OFAs. Figures of merit for "analog" and "WDM" Erbium doped fibre, have been presented, and a correlation between the two has been identified.

References

[1] J. Aspell, J. F. Federici, B. M. Nyman, D. L. Wilson, and D. S. Shenk, "Accurate noise figure measurements of erbium doped fiber amplifiers in saturation conditions," in *Digest of Conference on Optical Fiber Communications '92, San Jose*, pp. 189–190, Feb. 1992. paper ThA4.

[2] F. W. Willems, J. C. van der Plaats, C. Hentschel, and E. Leckel, "Optical amplifier noise figure determination by signal RIN subtraction," in *Symposium on optical fiber measurements, Boulder*, pp. 7–9, Sept. 1994.

[3] A. A. M. Saleh, T. D. Darcie, and R. M. Jopson, "Nonlinear distortion due to optical amplifiers in subcarrier-multiplexed lightwave communications systems," *IEE Electronics Letters*, vol. 25, pp. 79–80, Jan. 1989.

[4] L. K. Chen, K. Y. Lau, and D. R. Huber, "Fundamental distortion charactersitics of the Erbium fiber amplifier," in *Digest of Conference on Optical Fiber Communications '95, San Diego*, Feb. 1995. paper WL6.

[5] C. Y. Kuo and E. E. Bergmann, "Erbium-doped fiber amplifier second order distortion in analog links and electronic compensation," *IEEE Photonics Technology Letters*, vol. 3, pp. 829–831, Sept. 1991.

[6] S. L. Hansen, P. Thorsen, K. Dybdal, and S. B. Andreasen, "Gain tilt of Erbium-doped fiber amplifiers due to signal-induced inversion locking," *IEEE Photonics Technology Letters*, vol. 4, pp. 409–411, Apr. 1993.

[7] M. R. Phillips, T. E. Darcie, D. Marcuse, G. E. Bodeep, and N. J. Frigo, "Nonlinear Distortion Generated by Dispersive Transmission of Chirped Intensity-Modulated Signals," *IEEE Photonics Technology Letters*, vol. 3, pp. 481–483, May 1991.

[8] C. D. Poole and T. E. Darcie, "Distorsion related to Polarization-Mode Dispersion in Analog Lightwave Systems," *IEEE Journal of Lightwave Technology*, vol. 11, pp. 1749–1759, Nov. 1993.

[9] C. Desem, "Composite second order distortion due to self-phase modulation in externally modulated optical AM-SCM systems operating at 1550 nm," *IEE Electronics Letters*, vol. 30, pp. 2055–2056, Nov. 1994.

[10] F. W. Willems and A. M. J. Koonen, "The influence of multiple path interference in optical fibre amplifiers on RIN, CSO and CTB in AM-SCM lightwave systems," in *Proc. of European Conference on Optical Communications 1992, Berlin*, Sept. 1992. paper TuA4.5.

[11] J. H. Angenent, I. P. D. Ubbens, and P. J. de Waard, "Distortion of a multicarrier signal due to optical reflections," in *Proc. of European Conference on Optical Communications 1991, Paris*, pp. 569–572, Sept. 1991. paper WeC8-4.

[12] H. Yoshinaga, "Influence of stimulated Brillouin scattering on nonlinear distortion in SCM video transmission," *IEE Electronics Letters*, vol. 29, pp. 1707–1708, Sept. 1993.

[13] H. Chou and J. Stimple, "Inhomogeneous gain saturation of Erbium doped feber amplifiers," in *Optical Amplifiers and Their Applications, OAA '95, Davos*, pp. 92–95, June 1995. Paper ThE1.

[14] A. K. Srivastava, J. L. Zyskind, J. W. Sulhoff, and J. D. Evankow, "Room temperature spectral hole burning in Erbium-doped fiber amplifiers," in *Digest of Conference on Optical Fiber Communications '96, San Jose*, pp. 33–34, Feb. 1996. paper TuG7.

[15] C. R. Giles and E. Desurvire, "Modeling Erbium-Doped Fibre Amplfiers," *IEEE Journal of Lightwave Technology*, vol. 9, pp. 271–283, Feb. 1991.

FIBER AMPLIFIERS FOR THE SECOND TELECOMMUNICATION WINDOW: DEVELOPMENT AND CHARACTERISATION

Marcello POTENZA, Tiziana TAMBOSSO
CSELT - Via G. Reiss Romoli, 278, I-10148 Torino (ITALY)

Abstract *Optical amplification in the 1300 nm range is attracting much interest in the field of Telecommunications today. The present work discusses the realization and the characterization of a 1300 nm amplifier based on a praseodymium doped fluoride active fibre.*

1. Introduction The evolution of transport and access networks would be positively influenced by the development of Optical Amplifiers (OAs) for the second telecom window. Even though attenuation is higher at 1300 nm, OAs for the second window would allow the upgrading of presently installed systems on G.652 optical fibers as an alternative to the use of third window systems with Erbium-Doped Fiber Amplifiers (EDFAs), which require narrow linewidth optical sources and dispersion compensation techniques. The availability of efficient 1300 nm OAs would also be interesting for subcarrier analogue and digital video signal systems and other broadband services in the future assessment of the access network. Semiconductor optical amplifiers (SOAs) are available since several years for application around 1300 nm. Both bulk and Multi-Quantum Well active layer devices with very good characteristics have been developed [1, 2]. However, the high coupling losses to the transmission line affecting SOAs and their marked nonlinearities have prevented a widespread use of these devices to compensate for propagation or branching losses in optical networks. On the other hand, neodymium-doped fiber OAs have been investigated since ten years, but up to now they have shown rather poor gain characteristics. Since 1991, a new type of OA for the 1300 nm spectral region, i.e., the Praseodymium-Doped Fluoride Fiber Amplifier (PDFFA) [3, 4, 5] has been studied and developed. It has been demonstrated to reach small-signal gains of 30 dB with noise figures around 6-7 dB: a first generation of these devices is already on the market.

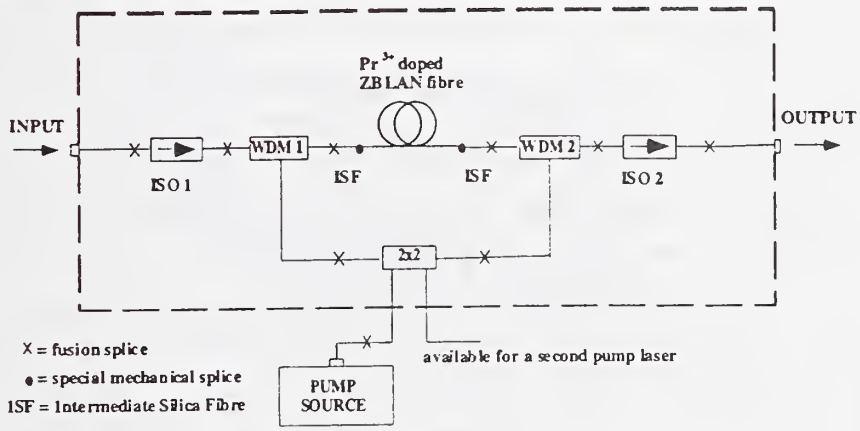

Fig. 1 - Set-up of the Praseodymium-Doped Fluoride Fiber Amplifier.

This paper briefly discusses the development of a PDFFA and the system characterization of the amplifier in terms of a transmission experiment and of an evaluation of possible impairments due to non linear effects. Results obtained so far confirm that such OAs can represent a viable solution to upgrade presently installed G.652 optical links.

2. Realization of a second window optical fiber amplifier Our laboratories have set a research project for the investigation and development of optical amplifiers in the second telecommunication window. In the framework of this project, called SWORD (Second

Window Optical Repeater Devices), a first result has been the realization of a portable, rack-sized PDFFA, the set-up of which is shown in Fig. 1. As described elsewhere [5], the PDFFA

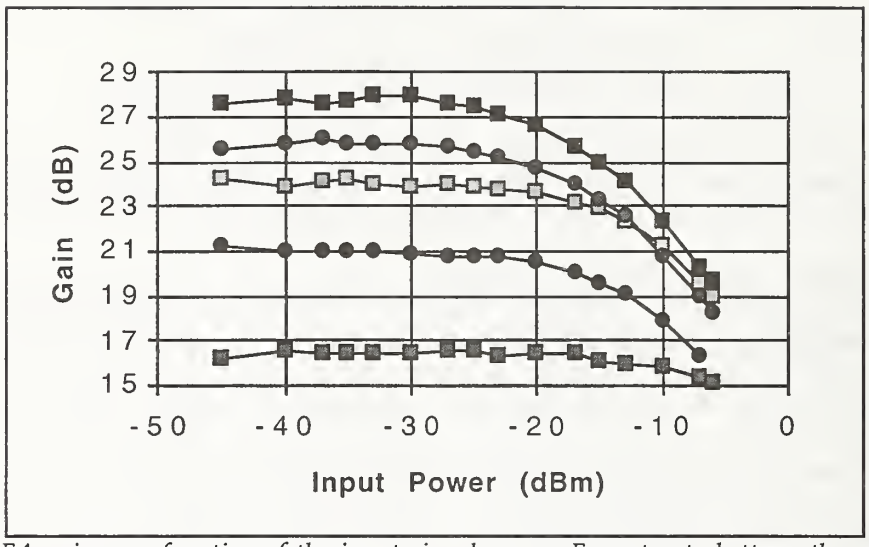

Fig. 2 - PDFFA gain as a function of the input signal power. From top to bottom, the curves refer to the following signal wavelengths: 1300, 1310, 1290, 1320 and 1280 nm.

uses a high-NA (0.4), small core (<2 μm diameter) fluoride active fiber. Silica glasses cannot be used as Pr^{3+} hosts because of their high mean phonon energy which makes non radiative relaxation dominant over radiative processes. The optimum cut-off wavelength is around 840 nm and the Pr^{3+}- ion concentration ranges between 500 and 1000 ppmw in order to minimize the incidence of cooperative relaxation events. The jointing of the fluoride fiber to standard fibers is critical as the difference in the glass phase transition temperature between

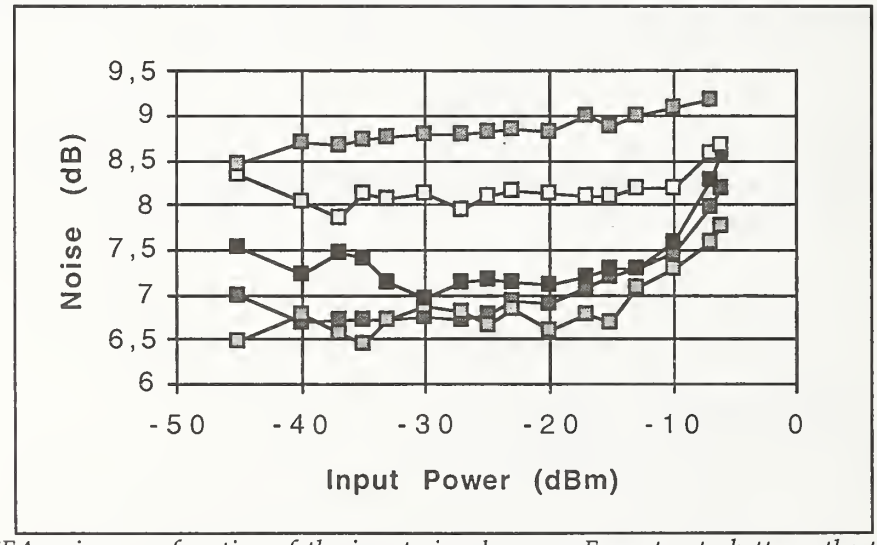

Fig. 3- PDFFA noise as a function of the input signal power. From top to bottom, the traces refer to the following signal wavelengths: 1320, 1310, 1300, 1280, and 1290 nm.

the two matrices makes fusion splicing not viable. The problem can be approached using an Intermediate Silica Fibre (ISF) having geometrical and optical parameters as close as possible to those of the fluoride active fibre [5]. The mechanical coupling ISF/active fibre is made by gluing the two fibers with UV-curing resin into a quartz capillary tube. Angle-cleaved cuts (around 25°) are needed in order to prevent the onset of laser oscillations, since internal

gains higher than 36 dB are easily obtainable: robustness and reliability of such a joint are satisfactory. Finally the joint ISF/standard fibre is optimized by means of the multiple arc technique. Unfortunately, the efficiency of PDFFAs is much lower than that of EDFAs: a 30 dB gain amplifier requires 300 mW pump power around 1017 nm, which is the Pr^{3+}-ion peak absorption wavelength. However, such a power cannot be easily reached with presently available semiconductor lasers. For this reason a detuned pumping with rack-sized Nd:YLF lasers at 1047 nm wavelength is usually preferred, but the pump requirements at such a wavelength are further increased at 600 mW levels. A bidirectional pumping scheme with a Nd:YLF laser was adopted, as shown in Fig. 1.

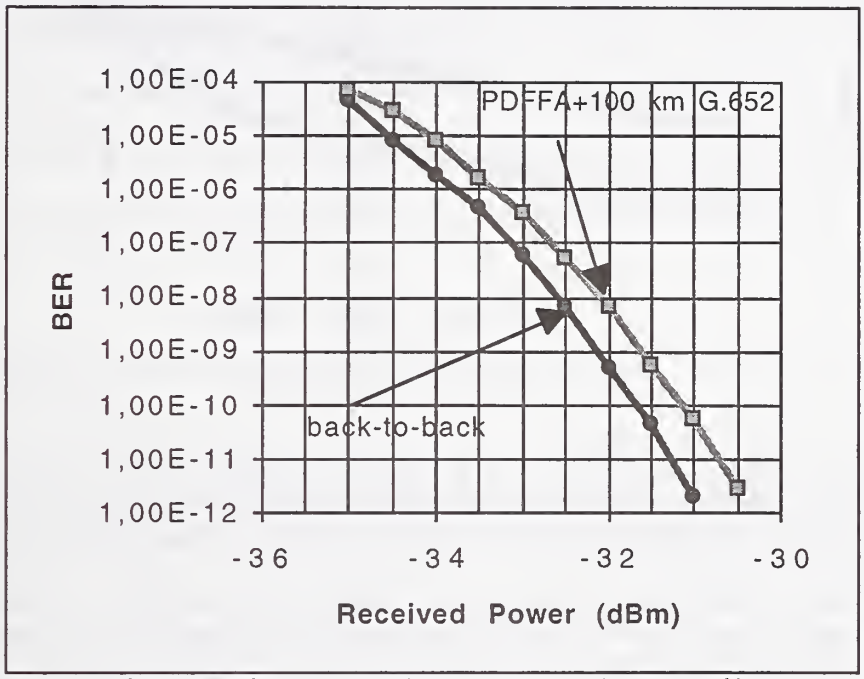

Fig. 4 - BER performance of the PDFFA booster over 100 km G.652 fiber transmission.

Best results obtained so far (λ=1300 nm) are insertion loss 11.4 dB, net gain 27.6 dB (-30 dBm signal input) and saturation power 14 dBm (-6 dBm input). The noise figure is around 7 dB, 2 dB of which are due to input coupling losses: these could be greatly reduced using an ISF more similar to the fluoride fiber (the presently used ISF has NA=0.32). Figs. 2 and 3 show gain and noise versus input power for the SWORD 2.2g PDFFA amplifier, at different signal wavelengths. Using two pump sources, the device reaches an output power of nearly 20 dBm.

3. Characterisation of the PDFFA The system characterization of the PDFFA has been made in a digital transmission experiment. A standard DFB laser emitting at 1311 nm was directly modulated at 2.5 Gbit/s with a 2^{31}-1 PRBS. This source injected a -2.5 dBm signal into the PDFFA, corresponding to a 13 dBm signal output power. A 100 km span of G.652 fiber was used for the transmission experiment, with the SWORD 2.2g amplifier boosting the source signal. Light was detected using a p-i-n FET receiver with a -32.5 dBm sensitivity at a 10^{-9} BER in back-to-back configuration, see Fig. 4. When using the booster followed by a variable optical attenuator simulating the transmission span, no penalty is observed with respect to the direct source-receiver coupling. Fig. 4 shows that in the actual experiment, the BER penalty is limited to 0.5 dB with respect to back-to-back configuration. This result confirms the viability of using such PDFFAs for the upgrade of already installed G.652 optical links. The capability of reducing coupling losses at the input of the PDFFA below the present 2 dB value, also shows that this result can still be improved.

When transmitting high power signals over long distances, it is possible that nonlinear effects could produce transmission impairments. That is the reason why work is in progress to compare non linearities in the second and third window. Because of its lowest threshold, stimulated Brillouin scattering was investigated first. A threshold of 8-9 mW was

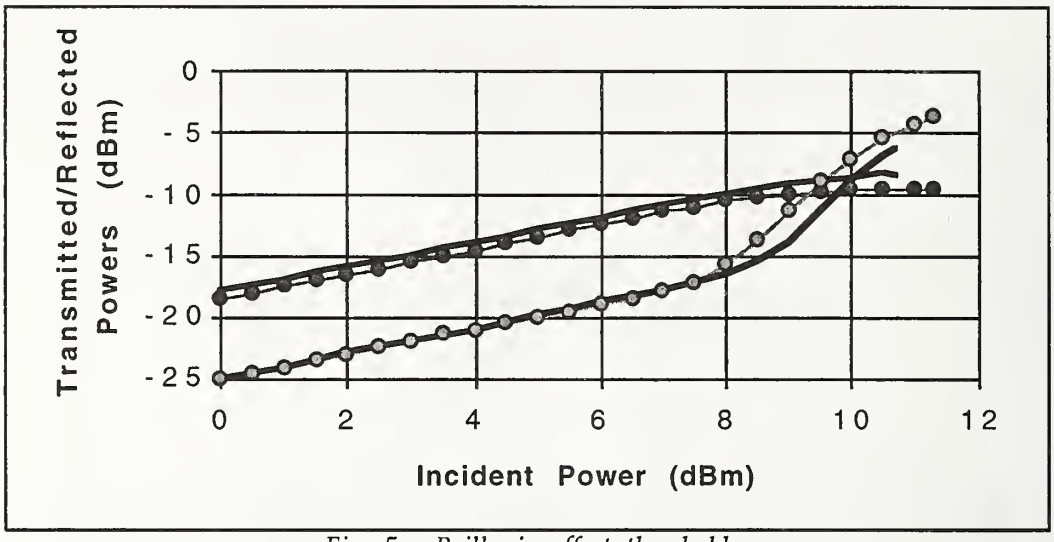

Fig. 5 - Brillouin effect threshold.

found for both an external cavity tunable semiconductor laser and the DFB laser previously used for the transmission experiment. These figures are quite similar to those reported at 1550 nm. Further measurements are in progress concerning the efficiency of four-wave-mixing in the second window, the results of which will also be presented at the symposium.

4. Conclusions Until few years ago, only SOAs were available for 1300 nm telecom applications. Their advantages were known and employed in logical and in signal elaboration applications, and for optical loss compensation in integrated optic circuits. On the other hand, their strong nonlinearities affected applications in line amplification and multichannel systems. Now, second window OFAs seem to have reached a certain maturity and a first generation of such devices is already available on the market. The development of sufficiently intense semiconductor lasers for peak absorption LD pumping of PDFFAs would be a key topic for the realization of a second generation of such amplifiers, able to upgrade presently installed G.652 optical links and to promote a balanced evolution of the optical network.

Acknowledgement We thank Dr. M. Artiglia and Dr. P. Di Vita for useful discussions during the preparation of this work.

References

[1] S. Tsuji et al., "High-gain polarization-independent semiconductor optical amplifier with a large optical cavity and angled buried facets", *Opt. Ampl. & Their Appl.*, 1990, PDP-5.

[2] L.F. Tiemeijer et al., "Progress in 1.3 µm Polarization Insensitive Multiple Quantum Well Laser Amplifiers", *Opt. Ampl. & Their Appl.*, Breckenridge, (CO, USA), 1994, WD1.

[3] Y. Miyajima, T. Sugawa, Y. Fukasaku, "38.2 dB amplification at 1.31 µm and possibility of 0.98 µm pumping in Pr^{3+}-doped fluoride fiber", *Electron. Lett.* Vol. 27, p. 1706 (1991).

[4] T.J. Whitley et al., "High output power from an efficient Praseodymium-doped fluoride fiber amplifier", *IEEE Photon. Technol. Lett.* Vol. 4, p. 401 (1993).

[5] M. Potenza, B. Sordo, T. Tambosso, "Second Window Optical Amplifiers: Comparison of Different Pumping Wavelengths and fibers", *Opt. Fiber Technol.* Vol. 1, pagg. 322-326 (1995).

All-Fiber Superfluorescent Light Source at 1.06 μm

V. Reichel, A. Ertmer, M. Rothhardt, H.-R. Müller, H. Bartelt

Institut für Physikalische Hochtechnologie e.V. Jena

Helmholtzweg 4, 07743 Jena, Germany

Introduction

For different applications in the large field of measurement technique it would be very useful to have powerful and broadband light sources because the available white light sources often don't have enough power to solve the measurement problem. In some wavelength regions (0.85 μm, 1.3 μm) such sources already exist. Mostly these are semiconductor laser diodes which work below their laser threshold or superluminescence diodes. In the 1.55μm region a very simple solution was found some years ago. Using an Er-doped fiber amplifier without any input signal (noise source) it is very easy to create a broadband and powerful light source for this wavelength. The same is possible for the Nd:YAG-region of 1.06 μm by using Nd-doped fibers as was experimentally shown by Liu et al. [1].

In context with the development of silica based, Nd-doped double-clad fibers for the application in high-power fiber lasers [2] we have investigated the spectral behaviour of the emission in the wavelength region around 1.06 μm in the nonresonant and the partly resonant case, respectively.

As an result we present a light source based on a specially designed rare-earth doped fiber with a spectral bandwidth of more than 5 nm and a peak power of more than 1 mW in the nonresonant single-pass gain regime.

Setup

The principal approach for the investigation of the superfluorescence light source can be seen in figure 1.
For pumping the Nd-doped fiber we used a Peltier-cooled (TEC) laser diode with FC-connector at 810 nm emission wavelength and a maximum output power at the end of a multimode fiber pigtail (length: 2.5 m; diameter cladding/core: 140 /125 μm) of 800 mW from SIEMENS AG (Typ 487406).
The Nd-doped double-clad silica fiber under test was manufactured in our laboratory. The first cladding surrounding the Nd-doped monomode core is a pure silica core with a diameter of 130 μm and a numerical aperture (NA) of 0.38. The second cladding is a silicon rubber with a low refractive index. The Nd-concentration amounts to 1300 ppm and the fluorescence lifetime 430 μs.
The pump light is coupled into the active fiber by a fiber-fiber coupling with the help of a 3-axes fiber launch system.
The spectral behaviour was measured by a PC-controlled optical spectrum analyser (OSA) in dependence on the fiberlength, the reflectivity at the fiber endfaces and the pump power.

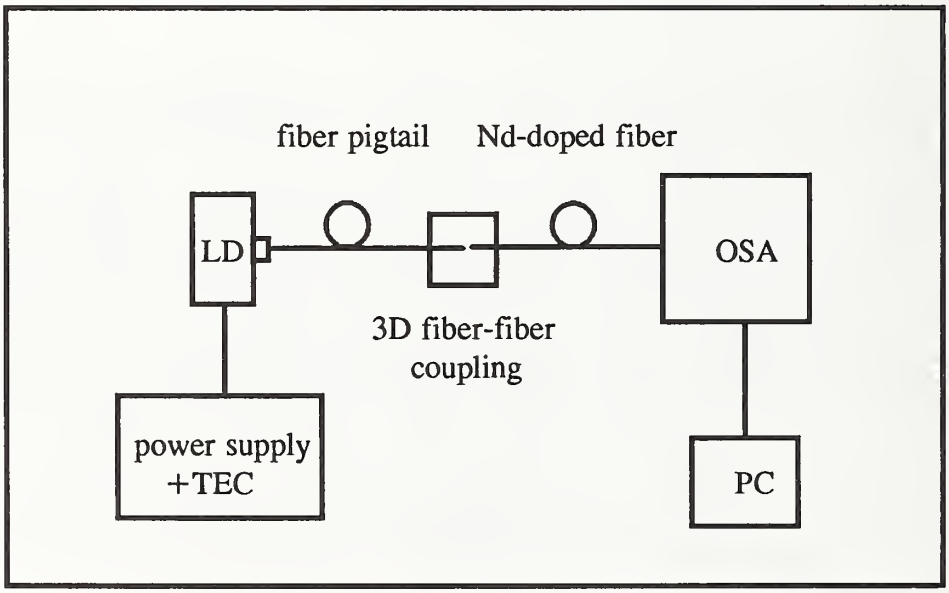

Figure 1: Setup scheme of the superfluorescence light source

Results

First of all we measured the superfluorescence spectra (ASE) in forward and backward direction in the single-pass gain modus depending on the pump power and compared these results with our numerical simulations using the relaxation method [3].
Figure 2 shows a typical spectrum of the superfluorescence light source. In this case the peak power is around 2 mW and the spectral bandwidth (FWHM) is 6 nm. The spectral resolution of the spectrum analyzer is 0.5 nm.

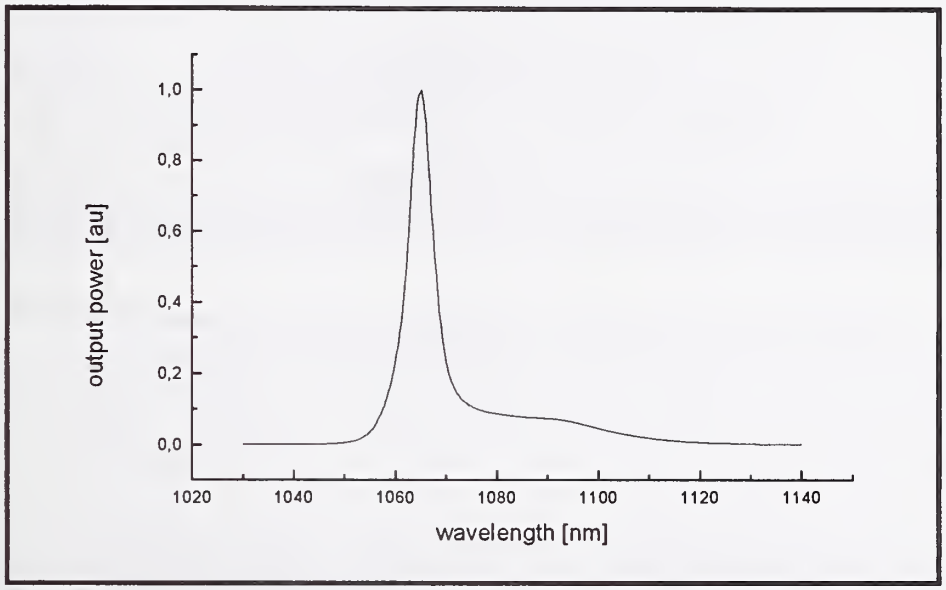

Figure 2: *Spectral behaviour of a superfluorescence light source at 1.06 μm; fiber length : 70 m*

In addition, we measured the dependence of the output power and the spectral bandwidth on the fiber length. We investigated different lengths between 10 and 70 m.
In figure 3 we demonstrate the dependence of the spectral bandwidth on the pump power in the nonresonant case. It can be easily seen that the bandwidth drops down with increasing pump power. When the laser threshold is reached the source begins to lase and the broadband continuous spectrum changes to a typical mode spectrum of a laser. Hence, the spectral bandwidth decreases to the bandwidth of the single modes.
Following these measurements in the single-path gain regime the reflectivity at the outcoupling end of the fiber was increased step by step. At first we cut the fiber endfaces without any angles (reflectivity 4%) and then we used dichroic mirrors with a high reflectivity for the pump light and a partially reflecting (24-76%) for the signal wavelength. This way we approached a double-pass gain device.
The output power increased step by step to several 10 mW, whereas the spectral bandwidth decreases slowly. Detailed results will be demonstrated at the conference.
In a first application we used the superfluorescence light source for the online control and characterisation during the manufacturing of fiber Bragg gratings at 1.06 μm.

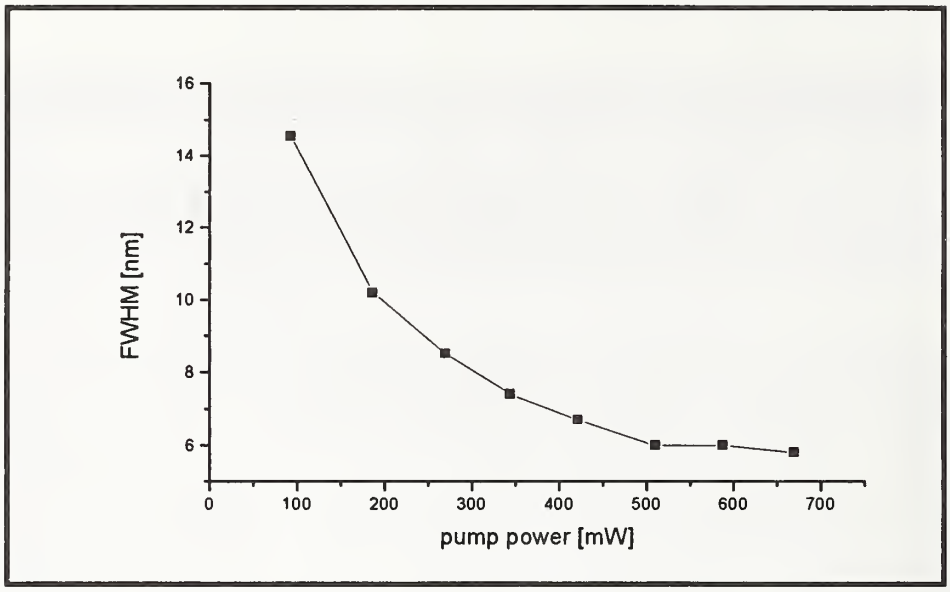

Figure 3: Dependence of the spectral bandwidth on the pump power

Conclusion

In conclusion we developed a powerful and broadband superfluorescence light source in the very interesting wavelength region of 1.06 μm using a Nd-doped double-clad silica fiber.
We presented experimental results on the behaviour of the light source, characterizing the linewidth and output power with variations in pump power, fiber length and reflectivity at one fiber end.
In principle, this technique can be used for the telecommunication wavelengths too by substituting the rare earth element Neodymium by Praseodymium and Erbium, respectively.
We have shown that this light source is a useful instrument for the online control during the manufacturing of fiber Bragg gratings.
Some further applications for this kind of light source exist in the field of measurement technique and especially in the field of fiber sensors (e.g. gyroscopes).

References

[1] K. Liu et al.: " 10 mW superfluorescent single-mode fibre source at 1060 nm", Electron. Lett. 23 (1987), pp. 1320-21

[2] H. Zellmer et al.: " High power cw neodymium-doped fiber laser operating at 9.2W with high beam quality", Optics Lett., 20 (1995), pp. 578-80

[3] V. Reichel et al.: " Spectral Behaviour of Nd-doped Double-Clad Fibers", will be presented at CLEO/EUROPE 1996, Hamburg

Results of COST 241 EDFA Round-Robin on Gain and Noise Figure

F.W. Willems
Lucent Technologies
Network Systems Nederland BV
P.O. Box 18, 1270 AA HUIZEN, The Netherlands

M. Artiglia, CSELT, Italy
C. Larsen, Lycom, Denmark
C. Soccolich, Lucent Technologies, USA
B. Heens, FPM, Belgium

Abstract: We present gain and noise figure measurement results from an EDFA round-robin using the OSA methods. This round-robin was performed in the framework of COST 241.

1. Introduction

COST 241, "Characterization of Advanced Fibers for the new Photonic Networks", working group 3, study group 2,"Fibre Amplifier Engineering", is currently performing an EDFA round-robin among the participants of this group. After some initial evaluation of the inticacies of such a round-robin [1], we started to use an AMOCO 17 dBm optical amplifier for the round-robin. This device, besides being extremely sturdy, shows a rather peculiar wavelength characteristic and is therefore very well suited to evaluate the various measurement methods for gain and noise figure, as they are currently evaluated. In the present round-robin, we have restricted ourselves to the "optical" measurement methods.

2. Measurement methods

Along with the Round-Robin module, copies are supplied of the IEC documents that describe the measurement methods for gain and noise figure. In particular: IEC SC 86C/WG3 documents 1290-1-1 (Gain by OSA) [2] and 1290-3-2, (Noise by OSA) [3] are of relevance for this round-robin. Next we will shortly describe these measurement methods.

Gain by OSA: the optical source can be either a *fixed wavelength* optical source (DFB, DBR, External Cavity Laser or a LED with optical filter) or a *wavelength tunable* optical source. In the calibration step, the optical powers entering the Device Under Test (DUT) are calibrated against an optical power meter. Read-outs from the Optical Spectrum Analyzer (OSA) are aligned with these data. The OSA can now be used for calibrated optical power measurements. The gain is defined as output power minus input power, with corrections for the Amplified Spontaneous Emission (ASE).

Noise Figure by OSA: The noise figure, NF, basically, is an "electrical" parameter, since it is by definition the input Signal-to-Noise Ratio (SNR), divided by the output SNR, assuming a shot noise limited signal source. However, theoretically, it can be shown that, at least in the

small signal regime, the NF can also be determined by optical means, by measuring the ASE-level in a certain optical bandwidth B, and by measuring the gain G. The signal-spontaneous beatnoise contribution to the NF can then be calculated by NF=ASE/(hνGB).

To determine the ASE level, currently three methods exist:

- *interpolation:* the ASE curve around the signal wavelength is measured and a curve fit is applied to the data; the value of the fit at the signal's wavelength is taken as the ASE value for the NF calculation. The disadvantage of this method is that the measured curve is a superposition of the ASE and the amplified Source Spontaneous Emission (ASSE), therefore one has to correct for the ASSE.
- *polarization nulling:* the polarized signal component is filtered from the total optical signal from the DUT, leaving the ASE perpendicular to the signal and its ASSE to be measured by the OSA. The disadvantage of this method is that it measures not the ASE component giving rise to s-sp beatnoise. Polarization Hole Burning effects are not taken into account by this method.
- *pulse recovery:* the input optical signal is temporarily shut down. The total ASE is measured at a certain defined point in time and the ASE in saturation is calculated using assumed ASE recovery.

Five participants, A-E, were included till now in the round-robin. All used the Polarization Nulling Technique. One lab, E, also used the interpolation and the pulse recovery technique.

3. Measurement results

The figures below show the gain and noise figure at 1550 and 1535 nm respectively, as measured by the particpant in the round-robin. First let us compare the *gain data* as measured with the polarization nulling technique. The spread at 1535 nm is around 3 dB and at 1550 nm around 2 dB. However note the inconsistancy in the data for the two wavelengths from participant E. Also, a large difference exist between the data from different methods as used by participant E. The interpolation method gives an overestimate and the pulse method gives an underestimate, however this tendency is again largest at 1535 nm.

The spread in the *noise figure data* is, as expected, even larger than the spread in the gain data. However, the spread is now also a function of input power. It is interesting to note that the spread is nearly equal for the two wavelengths. One would have expected that the noise figure measurement at 1550 nm would give less room for error, since the ASE spectrum is flatter in this wavelength region. Large differences occur especially at the high signal input powers, since the results are in this case heavily dependent on the quality of the signal extinction. The large difference between the 1535 noise figure data below -25 dBm input power of participant D and the rest of the data can be attributed to the fact that also D's gain data is high compared to the rest of the field, possibly because of a flaw in the ASE subtraction procedure. Note the deviation of the interpolation and polarization nulling data from participant E from the rest of the data, including E's pulse data, which fits quite well with the rest of the field.

Since the noise figure by optical method is determined by the quotient of ASE level and gain, a systematic error in the optical power measurement is hidden in the noise figure data, if this is the only error source. This is shown nicely in the noise figure data for 1550 nm, where the noise figures as determined by A-D cluster very well, while the gain data show a large spread.

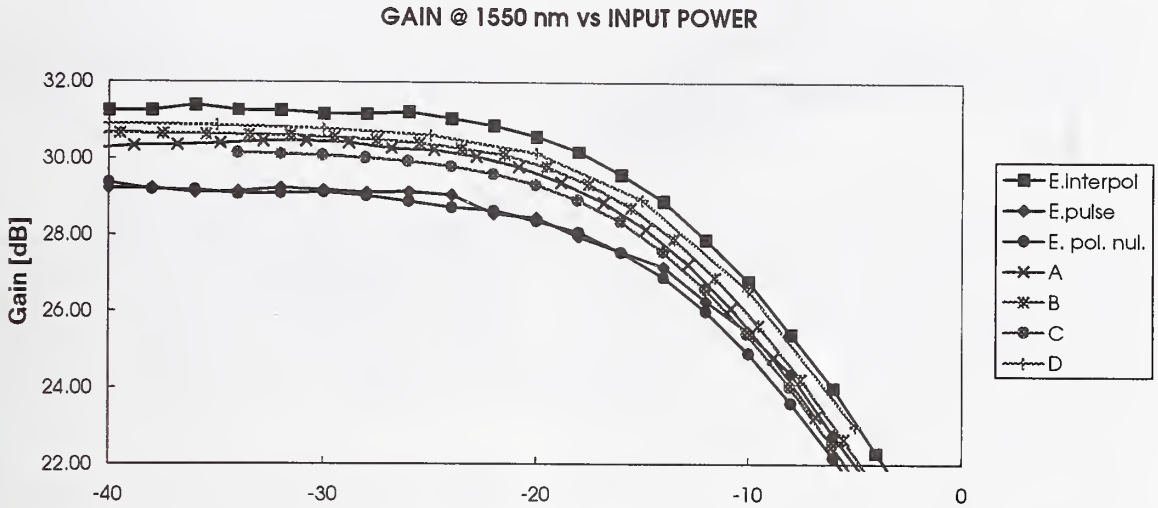

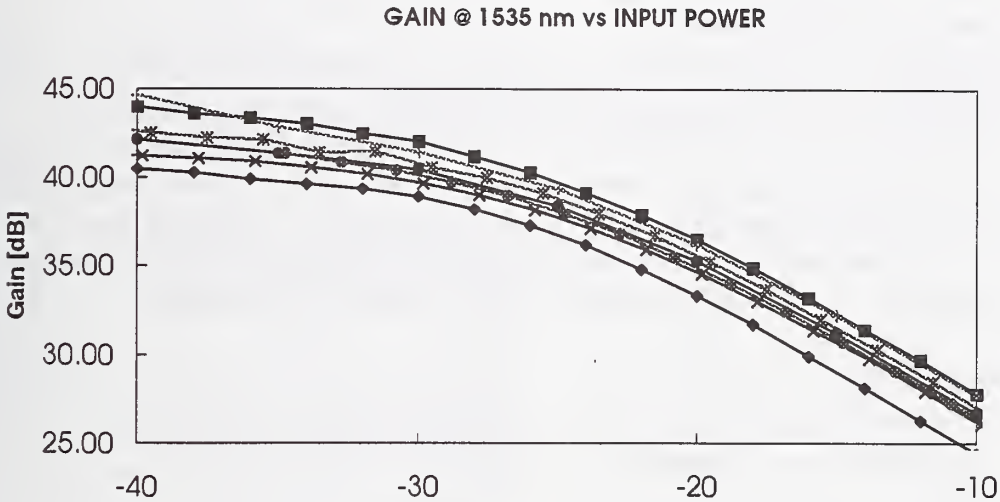

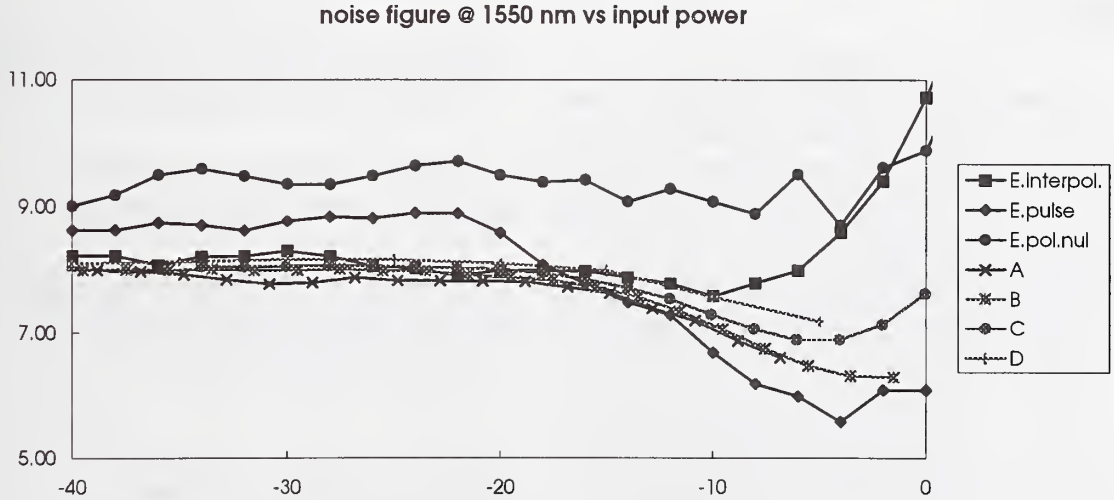

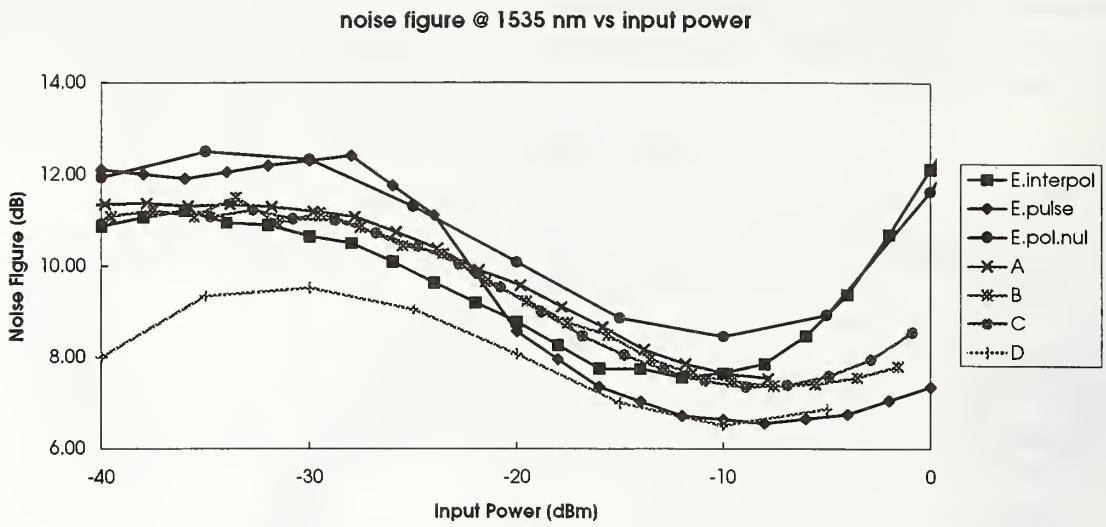

4. Discussion and conclusions

Five participant used the polarization nulling method to measure gain and noise figure of an optical fiber amplifier, in a first international round-robin organised in the COST 241 framework. The spread in the measurement data is more than a few dBs. Possible causes for this are, hopefully, disregarding (part of the) calibration instructions as mentioned in the IEC documents or not following exactly the measurement procedures as lined out in these documents. Careful evaluation of the data and the way they were gathered seems therefore needed in this phase of the round-robin, and will be performed in the near future.

Acknowledgements

Dr. Vobian, Deutsche Telekom -FTZ, Darmstadt, is greatfully acknowledged for the provision of the AMOCO optical amplifier.

References

1. F.W. Willems, "*The intricacies of an EDFA round-robin: First observations from COST-241 and RACE "COMFORT"*, in proceedings of the Symposium on Optical Fiber Measurements, Boulder, September 1994.
2. IEC SC 86C Publication 1290-1-1, Basic specification for Optical fibre amplifiers test methods, "Test methods for gain parameters, Optical Spectrum analyzer method". Latest version Feb. 1996.
3. IEC SC 86C Publication 1290-3-2, Basic specification for Optical amplifiers test-methods, "Test methods for noise figure parameters, Optical Spectrum analyzer method. Latest version, Feb .1996.

A GENERAL METHOD FOR MEASURING THE ELECTRIC-FIELD-DEPENDENT ABSORPTION COEFFICIENT IN QUANTUM CONFINED STRUCTURES

J.F. Siliquini, M.G. Xu and J.M. Dell

Department of Electrical and Electronic Engineering, The University of Western Australia, Nedlands, WA, 6907, Australia

ABSTRACT

A simple method of measuring the electric-field-dependent absorption coefficient in quantum confined structures is presented. This is achieved by measuring the photocurrent, transmitted power and quantum efficiency of the device and using a simple analytical expression to extract the absorption coefficient.

INTRODUCTION

Electroabsorption in semiconductor multiple quantum wells (MQWs)[1], superlattices (SLs) [2] and hetero n-i-p-i[3] structures is critical to the operation of many electro-optical. Accurate measurement of the absorption coefficient as a function of both wavelength and applied electric field is essential for correct design of these devices.

The most direct method of measuring absorption coefficient is by simultaneous measurement of the reflectance and transmittance[4]. While this method is simple in concept and has been applied to MQW devices[5], it is difficult in practice with significant error possible.

Because of these difficulties the most common technique for obtaining the absorption coefficient uses the measured photocurrent alone (e.g. [6,7]). This technique ignores interference effects within the test structure which can result in large errors in the derived absorption coefficient. This technique is adequate in long AR coated devices such as waveguide modulators, but requires complete device fabrication and careful optical alignment if results are to be accurate.

Other methods to extract absorption coefficient are based on measurement of photocurrent and transmittance[8,9]. This technique has been applied to MQW waveguide devices in which the incident light is parallel to the MQW layers where interference effects can be ignored, but again requires careful alignment. The direct application of this technique to transverse structures results in significant errors.

In this work we propose a modified method to determine the absorption coefficient by using measured photocurrent and transmitted power in the transverse direction as inputs into a simple closed form equation. This technique takes into account resonance effects in the test structure and requires no knowledge of the total thickness of the device after fabrication (the absorbing layer thickness is still required). An accurate method of determining the internal quantum efficiency is also proposed. The error analysis presented shows this method to be as accurate as the measured reflectance/transmittance method while requiring a significantly less demanding experimental setup.

ABSORPTANCE/TRANSMISSION MODEL

A typical three layer structure used for electroabsorption measurements is shown in Fig.1.

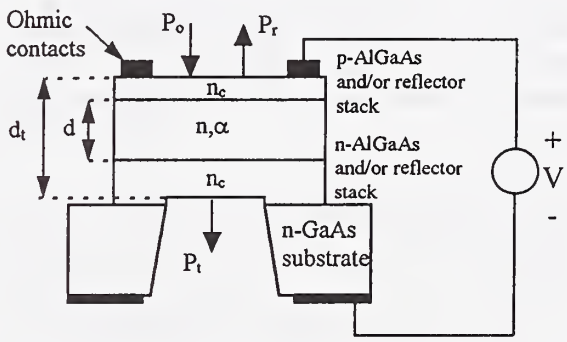

Figure 1. Schematic diagram of the MQW device used in the device model.

The middle layer is the absorbing MQW layer with absorption coefficient α, and thickness d. The top and bottom layers are transparent wide-bandgap cladding layers used to form a p-i-n diode which is reversed biased to vary the electric field in the nominally undoped middle absorbing layer. In some structures these may be $\lambda/4$ reflector stacks. To model this device an approximation is made which assumes that the device is an absorbing layer of thickness d inside a Fabry-Perot cavity of arbitary finesse and free spectral range. Since the refractive index difference between the absorbing and cladding layers is usually small, the error introduced in using this assumption (which is verified in the error

analysis below) is also small. Thus, the 3-layered structure (two reflector spacers plus absorbing region) can be treated as a single layer with average refractive index, $\bar{n}$ and total thickness, d_t. Under these conditions, the normal incidence reflectance, R, transmittance, T, and absorptance, A, can be written as:

$$R = \frac{\left(\sqrt{R_1} - \sqrt{R_2}e^{-\alpha d}\right)^2 + 4\sqrt{R_1R_2}e^{-\alpha d}\sin^2 kd_t}{\left(1 - \sqrt{R_1R_2}e^{-\alpha d}\right)^2 + 4\sqrt{R_1R_2}e^{-\alpha d}\sin^2 kd_t} \quad (1)$$

$$T = \frac{(1-R_1)(1-R_2)e^{-\alpha d}}{\left(1 - \sqrt{R_1R_2}e^{-\alpha d}\right)^2 + 4\sqrt{R_1R_2}e^{-\alpha d}\sin^2 kd_t} \quad (2)$$

$$A = \frac{(1-R_1)\left[1 - R_2e^{-2\alpha d} - (1-R_2)e^{-\alpha d}\right]}{\left(1 - \sqrt{R_1R_2}e^{-\alpha d}\right)^2 + 4\sqrt{R_1R_2}e^{-\alpha d}\sin^2 kd_t} \quad (3)$$

where $k = 2\pi\bar{n}/\lambda$, d is the absorbing layer thickness and R_1 and R_2 are the reflectances at the top and bottom of the structure, respectively. The photocurrent of the device of Fig. 1 is given by

$$I_{ph} = \eta(V)\frac{\lambda e}{hc}P_oA \quad (4)$$

where $\eta(V)$ is the quantum efficiency (which is a function of the applied bias), λ is the signal wavelength and P_o is the incident power. The ratio of transmitted power, $P_t = P_oT$, to the photocurrent given in Eq. (4) is then

$$\frac{I_{ph}}{P_t} = \frac{\eta(V)\lambda e}{hc}\left[\frac{1 - R_2e^{-2\alpha d}}{(1-R_2)e^{-\alpha d}} - 1\right] \quad (5)$$

Solving Eq. (5) for α gives

$$\alpha = -\frac{1}{d}\ln\left[\frac{-(B+1)(1-R_2) + \sqrt{(B+1)^2(1-R_2)^2 + 4R_2}}{2R_2}\right] \quad (6)$$

where $B = hcI_{ph} / P_t\lambda\eta(V)$. Equation (6) relates the absorption coefficient to the measured photocurrent and transmitted power. Although the calculation of α is dependent on the absorbing layer thickness, it is independent of the total layer thickness which may not be accurately known. Another important feature of this method is the fact that it is not necessary to simultaneously measure the photocurrent and transmitted power as is the case in the reflectance/transmittance method of Gerber[5]. In the current model, the quantities I_{ph} and P_t can be measured independently. Where there is a difference in the incident power used for measuring I_{ph} and P_t, then the ratio of these incident powers need to be included in Eq. (5).

The fundamental assumptions made in arriving at Eq. (6) are

a) The refractive index is constant in the material,
b) The quantum efficiency, $\eta(V)$, is accurately known,
c) The reflectivity, R_2, can be determined and,
d) The thickness of the absorbing layer is known.

The first assumption has two consequences: firstly, that the reflectivity does not change with wavelength, and secondly, the only reflections of consequence are those at the air-semiconductor interfaces. The effect of this first assumption on the accuracy of the technique are a result of changes in Fabry-Perot interference effects. An analysis of Eq. (6) shows that α is relatively insensitive to small uncertainties in R_2. An assumption similar to (d) is needed in all techniques only measuring two parameters. Of the four assumptions, the accurate knowledge of $\eta(V)$ is the most difficult to determine with several workers (erroneously) assuming this quantity to be unity[6,7]. Determination of $\eta(V)$ is therefore very important. In the absence of significant variation in absorptance, A, the photocurrent is directly proportional to $\eta(V)$. To a first order, the quantum efficiency can be assumed to be wavelength independent. By choosing an incident wavelength such that the absorption coefficient is known to remain high (but not necessarily constant) over the entire bias voltage range of interest, then the value of the absorptance A will remain approximately constant. In this case, the variation of measured photocurrent with bias voltage at constant incident power and wavelength, is a direct measure of the quantum efficiency of the MQW photodiode.

EXPERIMENTAL EXAMPLE

To illustrate the use of this method, the field dependent absorption characteristics of a MQW structure were investigated. The MQW sample used was grown by metal organic chemical vapor deposition on a Si-doped n^+ GaAs (100) substrate to the following layer specification: 0.5 μm of n^+ GaAs (buffer), 1.0 μm of n^+ $Al_{0.5}Ga_{0.5}As$ (etch stop), 50nm of n $Al_{0.8}Ga_{0.2}As$, a MQW region consisting of 50 layers of GaAs 7.5nm thick and 49 layers of $Al_{0.8}Ga_{0.2}As$ 4.5nm thick, 50nm of p $Al_{0.8}Ga_{0.2}As$, 50nm of p $Al_{0.3}Ga_{0.7}As$ and a cap of 20nm p^+ GaAs for contacting. Standard processing technology was used to fabricate mesa diodes with geometry of that shown in Fig. 1.

Light from a tungsten lamp was passed through a SPEX-270M monochromator, mechanically chopped and coupled to the sample through a multimode

optical fibre (NA=0.1). The spectral dependence of the power incident on the sample was determined by removing the sample and measuring the photocurrent of a calibrated Newport Ge photodiode detector in conjunction with a transimpedence pre-amplifier and lock-in amplifier. To ensure that the power incident on the calibrated detector was the same as that incident on the test sample, the optical fibre was placed in very close proximity (~ 0.5μm) to the device under test. The transmitted light was detected using the same calibrated photodiode detector as was used to measure the incident power. The photocurrent was also measured by a transimpedence pre-amplifier and lock-in amplifier combination. The value of reflectivity R_2 was taken as that for normal incident light at the air/semiconductor interface.

The quantum efficiency was determined using the technique described above. In this case a signal wavelength of 760nm was used where α (and therefore A) is expected to be high and approximately constant with applied electric field. This was verified after data analysis. It should be noted that this value of λ is still longer than λ_{direct} for $Al_{0.8}Ga_{0.2}As$. Figure 2 shows the measured photocurrent, as well as, the derived quantum efficiency from Eq. (3). As is evident from Fig. 2, the quantum efficiency approaches unity as the bias field is increased due to carrier sweepout dominating over recombination. The bias required to saturate the quantum efficiency to unity is approximately 6V. This is considerably higher than the fields seen by other workers [10] (by a factor of approximately 3) in similar MQW structures using $Al_{0.3}Ga_{0.7}As$ as barriers. We attribute this effect to the increased barrier height of the $Al_{0.8}Ga_{0.2}As$ barriers used in our case.

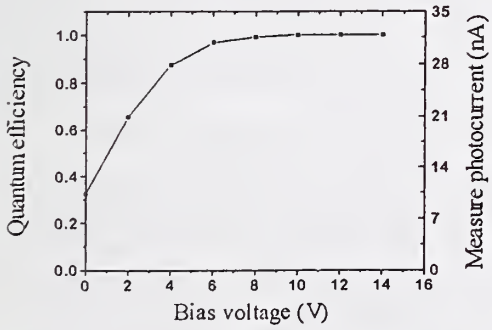

Figure 2 Experimental photocurrent Versus bias at λ=760nm. At this wavelength the absorptance is large and constant with bias. The scale on the right indicates the derived quantum efficiency as per Eq. (3)

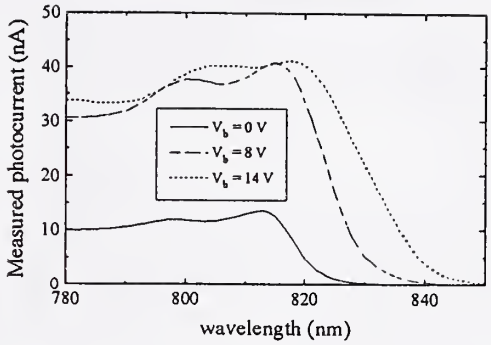

Figure 3 Measured photocurrent at three values of bias voltage.

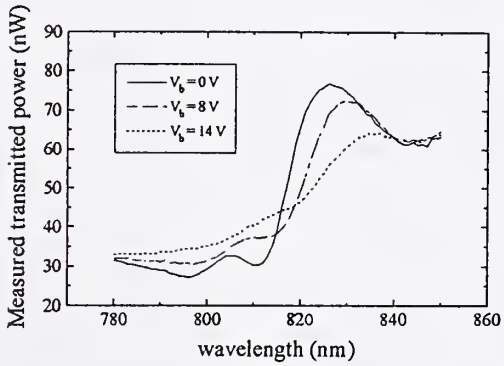

Figure 4 Measured transmitted power at three values of bias voltage.

This highlights the errors that are possible in assuming unity quantum efficiency in extraction of α when using measured photocurrent, particularly at low applied bias. The measured photocurrent and transmitted power as a function of wavelength and applied bias, are shown in Figs. 3 and 4, respectively. From these results the electric field dependent absorption coefficient of the MQW device can be determined. The results of using this technique are illustrated in Fig. 5 and represents first measurement of absorption coefficient in x=0.8 composition $GaAs/Al_xGa_{1-x}As$ MWQ structures. Compared with lower $GaAs/Al_xGa_{1-x}As$ MQWs (e.g. x=0.3) we observe a broadening and a reduction in oscillator strength of the heavy-hole exciton peak. This may be due to the fluctuations in the quantum well widths, background doping and possibly tunneling into the lower X minima in the $Al_{0.8}Ga_{0.2}As$, which can rapidly ionize the exciton and cause lifetime broadening[7].

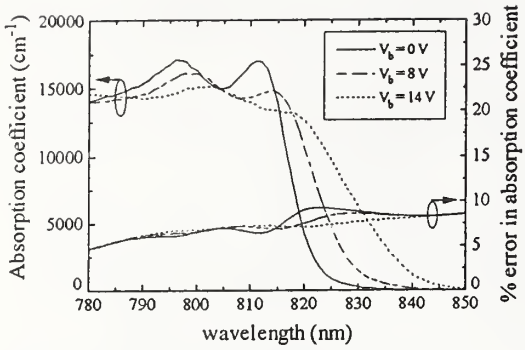

Figure 5 Derived absorption coefficient using the measured data of Figs. (2)-(4) and using the developed model of Eq. (6). Also shown is the total error in the measured value of absorption coefficient.

DISCUSSION AND CONCLUSIONS

Other than errors in experimental measurements, the principle error in determination of α is the assumption relating to the assumed 3 layer model of the device. To examine this error an exact model that takes into account reflections of all boundaries is used to derive the values for the transmitted power and photocurrent. The structure considered in the exact model is identical to the MQW device measured above. The wavelength dependent absorption coefficient is assumed to be that shown in Fig. 5. For the purposes of determining the extent of errors at different values of absorption coefficient, it is further assumed that the MQW layer has the same refractive index dispersion as GaAs (which is readily available[11,12]). The calculated values of the transmitted power and photocurrent from the exact model are then used as inputs into the single layer model (i.e. Eq. (6)) and the estimated absorption coefficient is calculated. This estimated value is then compared with the initial assumed absorption spectrum.

The error incurred in using the approximate model together with measurement error (approximately 4%) are shown in Fig. 5. This figure shows that the maximum error in using the model occurs when any one of the device layers (i.e. either cladding or MQW layer) thickness corresponds to an odd multiple of quarter wavelength thick. At resonant wavelengths the number of reflections of light at the inner boundaries are maximum and thus the error in using the single layer model is maximum. Since Fabry-Perot interference effects are more pronounced when absorption is small, the errors induced by the single layer model are largest in this region.

In conclusion, a simple technique and model has been derived which relates the measured photocurrent and transmitted power in MQW structures to the electric-field-dependent absorption coefficient. Although the model takes into account the Fabry-Perot resonances in the device, it does not require knowledge of the total device thickness nor does it require the simultaneous measurement of the photocurrent and transmitted power. This allows an extremely simple experimental setup to be used for measurement of absorption coefficient. A simple method of determining the electric-field-dependent quantum efficiency using photocurrent measurements has also been presented. Experimental results show that the absorption coefficient can be determined using the developed model. An initial error analysis indicates that total errors of less than 9% can be expected when using the model where internal reflections are neglected compared to when internal reflections are not ignored. The maximum error in using the model occurs at low values of absorption coefficient.

ACKNOWLEDGMENT : The authors wish to acknowledge the Cooperative Research Centre for Broadband Telecommunications and Networking for financial support of this project.

REFERENCES

[1] R.H. Yan, R.J. Simes, and L.A. Coldren, *IEEE J. Quantum Electron.*, **25**, 2272, 1989

[2] K.K. Law, R.H. Yan, L.A. Coldren, and J.L. Merz, *Appl. Phys. Lett.*, **57**, 1345, 1990

[3] J. Maserjian, P.O. Andersson, B.R. Hancock, J.M. Iannellis, S.T. Eng, F.J. Grunthaner, K.K. Law, P.O. Holtz, R.J. Simes, L.A. Coldren, A.C. Gossard, and J.L. Merz, *Appl. Phys. Lett.*, **28**, 4801, 1989

[4] Heavens, O. S., *"Optical properties of thin solid films"*, Dover Publications, New York, 1991.

[5] D.S. Gerber and G.N. Maracas, *IEEE J. Quantum Electron.*, **29**, 2589, 1993

[6] P.J. Stevens, M. Whitehead, G. Parry, and K. Woodbridge, *IEEE J. Quantum Electron.*, **24**, 2007, 1988

[7] B. Pezeshki, S.M. Lord, T.B. Boykin, and J.S. Harris, Jr, *Appl. Phys. Lett.*, **60**, 2779, 1992

[8] T.H. Wood, *Appl. Phys. Lett.*, **48**, 1413, 1986

[9] M.K. Chin, *IEEE Photonic Tech. Lett.*, **4**, 866, 1992

[10] A.M. Fox, D.A.B. Miller, G. Livescu, J.E. Cunningham and W.Y. Jan, *IEEE J. Quantum Electron.*, **27**, 2281, 1991

[11] D.D. Sell, H.C. Casey, and K.W. Wecht, *J. Appl. Phys.*, **45**, 2650, 1974

[12] D.E. Aspnes, S.M. Kelso, R.A. Logan, and R. Bhat, *J. Appl. Phys.*, **60**, 754, 1986

MEASURING THE RELIABILITY OF FIBER OPTIC COMPONENTS

L.A. Reith
Bellcore

1. Introduction

The estimation of reliability for fiber optic components is still in its infancy. Although many failure modes have been identified, and progress is being made in the determination of underlying failure mechanisms, only a few studies have attempted to estimate component lifetimes or failure rates.[1-3] This is in part due to the immaturity of the technology. Many causes of failure have been identified with quality control or processing issues, such as poor connector polishing quality or adhesive failure in components due to improper adhesive cure. Now that many of these failure mechanisms have been recognized and ways to avoid them identified, we are in a better position to look into long-term wear-out failures. The onset of component degradation may not be obvious, however. Unlike active optical or electronic devices which often show gradual performance degradation, the optical performance of passive fiber components may not degrade at all; sudden, catastrophic failure is often the first indication that the reliability of the component is in doubt (e.g., crack-growth in fiber-based components). Due to the critical nature of information and data travelling over today's fiber networks, prevention and/or prediction of failures is a major concern. Both laboratory and field testing are needed to provide information leading to failure prevention and to increase our confidence in the reliability of our networks.

After the component design, materials, and assembly processes have been chosen to optimize performance and reliability, laboratory testing is the first phase of product evaluation. Most of the laboratory tests used for fiber optic components are derived from standard tests developed for the electronics industry. While these tests are often directly applicable to fiber optic components, there are cases where these tests are not adequate. For example, many tests developed for adhesives do not test its compatibility with fiber or its ability to maintain dimensional stability to the sub-micron tolerances required in many fiber-optic applications. Much work has been accomplished and is continuing in this area in standards bodies such as the Telecommunications Industries Association (TIA) and the International Electrotechnical Commission (IEC), which develop standard fiber optic test procedures (FOTPs in the TIA) specifically for optical fibers, components, and devices.

Regardless of how extensive and rigorous laboratory testing is, however, unanticipated field failures are hard to prevent. It is difficult to simulate actual installation procedures in the laboratory, or to predict how different elements of the network will interact to cause failures. For example, a number of fiber breaks in mechanical splices due to torsional stresses were identified in one set of field failures. It was discovered that the breaks were occurring due to large stresses generated when thick (900 μm) buffer-coated fibers were looped to mount the splices into splice trays. Due to the identification and study of this problem, a new, torsional loading test was devised to better simulate actual field conditions.[4]

In addition to installation practices, no laboratory test can replicate the combined effects of heat, humidity bending and/or tensile stress, stress cycling, dust and dirt, condensation, and contaminants that components actually experience in the field. To this end, Bellcore has established environmental test facilities (ETFs) in three climate extremes (hot and humid (Louisiana), bitter cold with wide temperature extremes (Maine), and hot and dry (Arizona)). These have been established for long-term testing of components in extreme service environments. A number of passive fiber optic components, mounted in pedestals, boxes and aerial closures, are currently being optically monitored at these sites, and components are periodically returned to Bellcore for additional measurements to ascertain degradation. In addition to optical data, temperature and humidity data are being collected.[5, 6]

This paper will provide examples of some current findings in both laboratory and field testing to illustrate our approach to the determination of fiber optic component reliability. We will discuss examples including optical connectors, splices, and branching components.

2. Connectors

Reports of connector field failures have been rare. However, most connectors in use thus far are deployed in protected office environments and not exposed to high humidities and large temperature swings. Laboratory testing has shown that many connector failures are due to quality control problems related to the polishing of the connector endface. Figure 1(a) illustrates an ideal connector endface geometry where the connector endface is radiussed with the optical fiber flush to the spherical surface. This geometry is intended to ensure that the fiber cores will always make good physical contact. Figure 1(b) illustrates a more typical endface geometry, where the spherical radius is not centered on the optical axis (apex offset), and the fiber may be protruding or recessed with respect to the spherical surface. The result of these effects is that a gap will exist between the fiber cores. When two connector plugs are mated, the springloading forces will cause some ferrule endface deformation and small gaps can be closed. However, if the endface geometry parameters fall too far outside a given range, gaps will exist that can result in high reflectance and large reflectance variation with temperature.

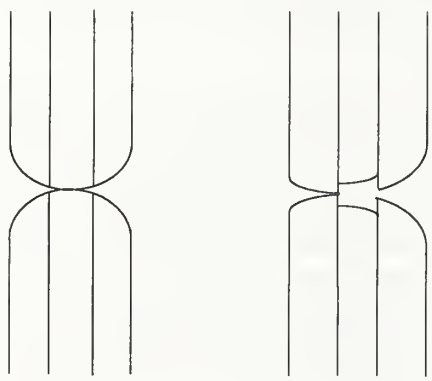

(a) (b)

Figure 1. (a) Ideal connector endface geometry and (b) typical endface geometry.

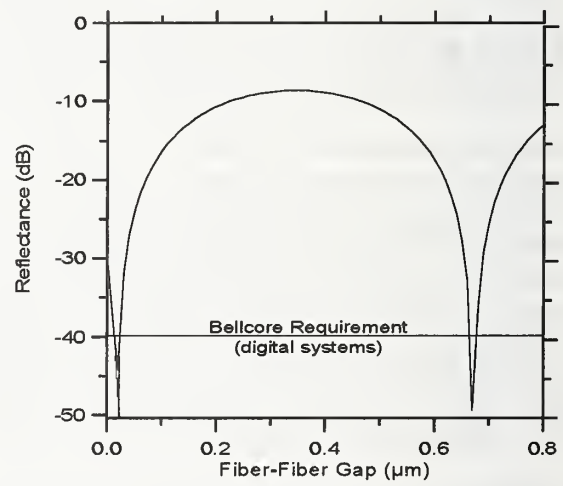

Figure 2. Reflectance as a function of gap size for a typical connector.

Figure 2 shows calculated reflectance for a connector as a function of gap size at 1310 nm. Even for connectors with physical contact the reflectance is finite, due to the formation of a high-index subsurface damaged layer during the polishing process.[7] As a gap opens up, the reflectance typically improves, going through a minimum for very small gaps before beginning to increase.

Assuming that connectors initially meet endface geometry requirements, one major reliability concern is the ability of the adhesive to maintain the fiber position relative to the ferrule within submicron tolerances after aging in the field. Although several connectors installed at our field sites showed evidence of initial quality control problems, only one connector has shown degradation in the optical performance over time. This connector was recently removed from our field test facility in Louisiana after being on test 3 years. The connector had marginal physical contact from the outset, but the condition gradually worsened over time. Figure 3 shows the optical reflectance performance for several days shortly after its initial installation, and over the same temperature range in the laboratory during post-mortem analyses (at the end of the 3-year period the reflectance was beyond the dynamic range of the onsite OTDR).

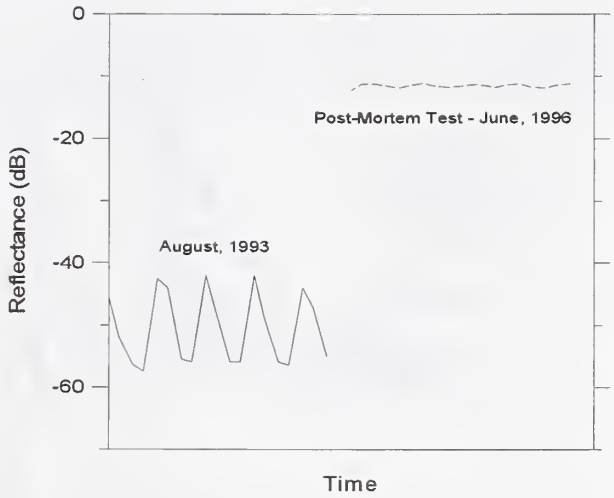

Figure 3. Reflectance of an optical connector (a) after initial installation and (b) after 3 years in the field.

The type of behavior illustrated in Figure 3 is representative of what we have often seen in our laboratory testing. By correlating the results of laboratory experiments with predicted gap sizes from boundary element analyses, it has been possible to determine requirements for the connector endface geometry parameters which will ensure physical contact.[8,9] We have designed test fixtures in which radiussed, blank zirconia "indentors" are mated against connectors to simulate worst-case connector loading conditions. In this way, connector endfaces can be loaded under controlled conditions in different aging environments. We can measure changes in the position of the fiber relative to the ferrule and measure degradation before it shows up as an optical performance failure. We have established baseline performance data for a number of different adhesives under load and find that mechanical performance is strongly correlated to the adhesive glass transition temperature, which should be at least 20 °C above the operating temperature of the connector for optimum performance.[10] We now complete endface characterizations for all connectors newly installed at the ETFs, including measurements of ferrule radius of curvature, fiber protrusion/recess, and apex offset, using both interferometric and contacting-stylus type measurement equipment. In future, we anticipate that comparisons of laboratory and field analyses will help us relate actual field lifetimes to accelerated laboratory testing.

3. Splices

Splices are the only type of fiber optic component deployed in the field in large numbers, and most are fusion splices. Although mechanical splices are not as popular, they are still deployed in large numbers compared with connectors or branching components.

Fusion splices have a very good reliability track record. Although handling operations to assemble the splice (stripping the coating, cleaning, and cleaving) greatly weaken the fiber, the application of a typical heat-shrink protector sleeve normally brings the splice back to a strength comparable to the pristine fiber, as illustrated by the tensile test strength distribution data plotted in Figure 6.[11] Aging of splices in the laboratory has shown that the integrity of the heat-shrink protector can degrade, causing the splice strength to weaken. To date no failures have occurred at our ETFs, and, similarly to connectors, most reported field failures have occurred due to improper assembly practices or use of inappropriate sleeve designs.[12] New types of fusion protector sleeves of clip-on designs have recently come on the market, however. These are typically not as strong as heat-shrink protectors, and their ultimate reliability remains to be seen.

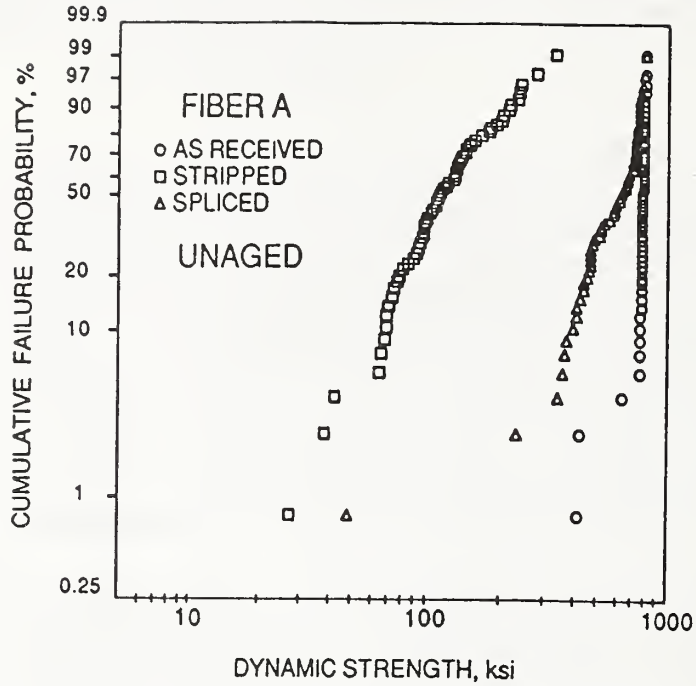

Figure 6. Fusion splice strength before (diamonds) and after (squares) application of the protector sleeve compared with the original fiber strength (circles).

There have been occasional reports of field failures of mechanical splices. Most have been associated with design flaws or improper assembly practices. For example, the series of torsional fiber breaks mentioned in the introduction occurred when splices that did not provide strain relief were used in conjunction with 900 μm buffer-coated fiber, and the fibers were twisted as they were looped into the splice storage trays. Either a change in the way splices are mounted in the storage tray, to avoid the application of torsional stresses, or a change in splice design, to provide strain relief, will prevent this type of failure.

Although mechanical splices come in a variety of designs, they typically are not designed to ensure good physical contact of the fiber endfaces. Therefore, most use index-matching gels in the central alignment mechanism to reduce loss and reflectance, and to help protect the fibers from the outside environment. Although typical matching gels are hydrophobic, the presence of pollutants, particularly detergent or ammonia, can aid water in migrating along the glass/gel interface or diffusing into the gel.[13] If mechanical splices are immersed, they can fail when water migrates around the ends of the fibers, resulting in refractive index discontinuities. There is also evidence from laboratory testing that moisture can penetrate the splice in high humidity environments and cause failures.[12] However, no performance degradation has occurred at any of our ETFs. At present, splices in Louisiana on test for more than 3 years have had no failures.

4. Branching Devices

Like connectors, branching devices are not yet deployed in the field in large numbers. Field failures have occurred, however, and these often have been due to fiber breakage.[13] Laboratory failures have been reported arising primarily from materials incompatibility, often adhesives failures and mismatches in the coefficients of thermal expansion in the packaging materials. Loss of adhesion, or bending stresses on the fibers (sometimes resulting in fiber breakage) were typical. In one report, estimated FIT rates for 2x2 splitters were 10 to 100 times higher than the targeted FIT rates of 50.[1]

We have identified only one failure of a branching component due to fiber breakage at our ETFs, and that we believe was due to handling damage and not in-service degradation. However, we have seen some cases in Louisiana where there have been anomalous loss variations. Figure 7 shows one example. This 3-dB coupler had increased loss during the summer months.

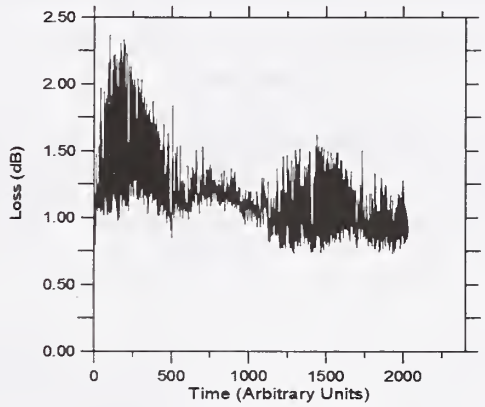

Figure 7. Loss for a 3-dB coupler on test in Louisiana from April, 1994 through February, 1996.

The branching components are test are typicaly installed back-to-back; that is the output leads are fused in-line with each other as illustrated in Figure 8. Although the components are spaced far enough apart to measure loss and reflectance for each component individually, the OTDR measures performance across multiple legs of the component. If we assume the coupling ratio to be equally split, the actual insertion loss can be calculated to be $L = L_{meas} + (3/2) \log_2 N$, where L_{meas} is the apparent loss measured by the OTDR and N is the number of fiber branches (2 for a 3-dB coupler).[14] If the coupling ratio, excess loss, or loss of an individual leg varies, the apparent loss will vary, but it is impossible to determine the source of the loss variation without more in-depth diagnostic analyses more easily performed in the laboratory. At present, we are performing such laboratory post-mortems on branching components recently removed from the Louisian ETF.

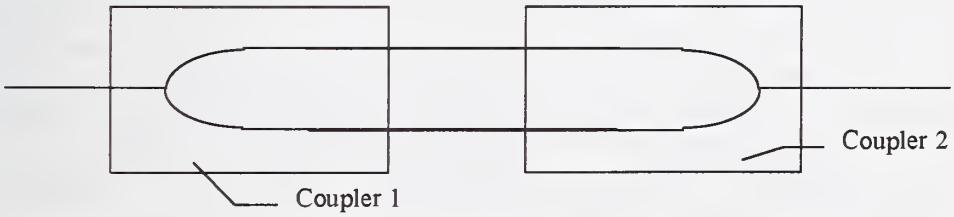

Figure 8. Configuration for ETF OTDR measurements.

5. Conclusions

Little data for in-service field reliability exists. To date, most field failures and many laboratory failures occur at the time of installation and can be attributed to quality control problems in either the component or its installation. However, many of these problems have now been identified and we are beginning longer-term studies to look for true wear-out mechanisms. This requires both laboratory and field testing.

At Bellcore we have developed several new laboratory tests, particularly for adhesives used in optical components, that we feel are more pertinent for fiber optic component reliability than the conventional tests used for electronics applications. In addition, we have established test facilities in three extreme climate conditions to gain data on actual field conditions and field failures to begin to correlate laboratory test data to in-service performance. Although much work remains, we have laid the necessary groundwork to begin to resolve long-term reliability issues.

Acknowledgements

The author would like to thank E.M. Vogel, O.S. Gebizlioglu, I.M. Plitz, S. Etemad, R.A. Frantz, and H.H. Yuce for useful discussions, use of their data, and their collaborations in developing the content of this paper.

References

1. "Results of Accelerated Lifetests on Passive Optical Splitters", M. Gadonna, T. Draycott, and S. Gundersen, *Proc. 13th Annual Conf. on Eur. Fibre Optic Comm. and Networks*, p. 65, 1995.

2. "Reliability Evaluation for PON Power Splitters", M. Gadonna, M. Redstall, and S. Gundersen, *SPIE Proc. on FO Materials and Comp.*, Vol. 2290, pg. 170, 1994.

3. "Reliability of Passive Fibre Optic Branching Devices", N. Fabricius, *IEE Colloquim on FO Cable Systems*, No. 1994/023, 1994.

4. "Torsional Criteria Development for Optical Fiber Splices", S.M. Leopold, G. Kiss, A. Pellegrino, and N. Gehlot, *Proc. 7th Annual National Fiber OpticEngineers Conference (NFOEC)*, pg. 260, 1991.

5. "Establishment of an Environmental Test Facility for Fiber-Optic Components at Morgan City-Amelia, LA", P. Briggs, C. Burpee, L. Slavin, J.P. Varachi, and H.H. Yuce, *Proc. 10th Annual NFOEC*, pg. 111, 1994.

6. "Construction of a Cold-Weather Environmental Test Facility for Optical Fiber, Cable, and Components", R.A. Frantz, L.A. Reith, G. Karl, C. Weeks, D. Leavitt, and D. Barker, *Proc. 11th Annual NFOEC*, pg. 734, 1995.

7. "Evaluation Method and Performance of Advanced Low-Reflection Optical Connectors", K. Kanayama, Y. Ando, R. Nagase, and S. Iwano, *Proc. 41st International Wire and Cable Symposium (IWCS)*, pg. 785, 1992.

8. "Highly Stable Physical-Contact Optical Fiber Connectors with Spherical Convex Ends", T. Shintaku, E. Sugita, and R. Nagase, *J. Lightwave Tech.*, Vol. 11, pg. 241, 1993.

9. "Effect of Ferrule-Endface Geometry on Connector Intermateability", L.A. Reith, P.B. Grimado, and J.Brickel, *Proc. 11th Annual NFOEC*, pg. 635, 1995.

10. "Reliability of Epoxy Adhesives in Ceramic-Ferrule Optical Connectors", L.A. Reith, R.A. Frantz, P.B. Grimado, I.M. Plitz, O.S. Gebizlioglu, and D.A. Dolinoy, *Proc. 43rd IWCS*, pg. 790, 1994.

11. "Mechanical Reliability of Fiber Optic Splices", L.A. Reith, H.H. Yuce, and P.B. Grimado, *Proc. of the Inter. Symp. Fiber Optic Networks and Video Comm.*, Berlin, FRG, April 5-8, pp. 316, 1993.

12. "Analysis of Optical Interconnection Failures by Analytical Techniques", H.H. Yuce, J.P. Varachi, Jr., and T. Wei, *Proc. 9th Annual NFOEC*, pg. 251, 1993.

13. "Stability of Mechanical Splices: Void Formation and Groundwater Immersion", G.D. Kiss, E. Hershkowitz, I.M. Plitz, L.A. Reith, and E.M. Vogel, *Proc. 10th Annual NFOEC*, pg. 13, 1994.

12 "Effects of High-Humidity Temperature Cycling on Mechanical Splice Performance", L.A. Reith, R.A. Frantz, and D.A. Dolinoy, *SPIE Proc. 2290*, pg. 139, 1994.

13. "Passive Optical Branching Components: Increasing their Reliability", M.P. Dugan, *SPIE Proc. 1973*, pg. 13, 1993.

14. "OTDR Measurements Through Optical Splitters", F.P. Kapron and J.D. Berardinelli, *Tech. Dig., Symp. Optical Fiber Measurements*, pg. 7, 1992.

Opto-Mechanical Method for Measurement of Ferrule Concentricity and Roundness Error

Paul Townley-Smith and Costas Saravanos

Siecor Corp., 9275 Denton Highway, Keller, TX

Abstract: A novel method for determining ferrule concentricity and roundness error of the outside diameter is presented, based on a Fast-Fourier Transform (FFT) of microhole position at different angular orientations of the ferrule. The resulting concentricity value is independent of the roundness error.

I. Introduction

Connector insertion loss is one of the most important parameters in fiber-optic transmission system design. Because concentricity error in the ferrule is a major contributor to insertion loss, accurate measurement and control of this parameter is very important to the connector manufacturing industry. Currently, all measurements of concentricity error are influenced by the roundness error of the outside diameter of the ferrule, which reduces the precision and accuracy. At the same time ferrule roundness error is an important parameter that characterizes the quality of the ferrule. A separation between ferrule concentricity and roundness error will improve the control of connector insertion loss and identify ferrules with poor roundness error. A standard opto-mechanical method for ferrule concentricity measurement[1,2] positions a ferrule in a v-groove as shown in Figure 1. The position of the center of the microhole is measured, then the part is rotated through 180° and the position of the microhole is measured again. The difference between the two microhole positions is calculated as concentricity. This measurement is accurate and precise when the roundness error of the outside diameter is small compared to the concentricity. As the roundness error increases the concentricity measurement accuracy reduces because the roundness error contributes to the movement of the ferrule microhole as it is rotated. Other standard methods[3] improve the measurements precision by monitoring the position of the center of the microhole at several different angular orientations of the ferrule. However the accuracy would still suffer because of the contribution of roundness error. This paper proposes that an appropriate application of a FFT to the microhole position data can be used to separate pure concentricity and roundness error achieving improved precision and accuracy in the measurement of concentricity while obtaining an accurate roundness error measurement.

II. Theory

For a perfectly round ferrule rotating in a v-groove as shown in figure 2, the center of the microhole will trace out a path given by

$$x = x_0 + \left(\frac{c}{2}\right)\sin\theta \tag{1}$$

$$y = y_0 + \left(\frac{c}{2}\right)\cos\theta \tag{2}$$

where x_0 and y_0 are the coordinates of the center of the outside diameter of the ferrule, c is the concentricity of the ferrule, θ is the current rotation angle of the ferrule. For a ferrule that has an outside diameter that is out of round, we can define the radius $r(\theta)$ as

$$r(\theta) = r_0 + \delta(\theta) \tag{3}$$

where r_0 is the mean radius of the ferrule and $\delta(\theta)$ is the roundness error. As long as $|\delta(\theta)| << r_0$ any roundness error will manifest itself as an offset perpendicular to the surface of the v-groove. For a 90° v-groove, the x and y offsets due to roundness error will be orthogonal to each other, and will also be related by a $\pi/2$ phase factor. Thus in the presence of roundness error, the center of the microhole will trace out a path given by

$$x(\theta) = x_0 + \left(\frac{c}{2}\right)\sin\theta + \delta(\theta) \tag{4}$$

$$y(\theta) = y_0 + \left(\frac{c}{2}\right)\cos\theta + \delta\left(\theta + \frac{\pi}{2}\right) \tag{5}$$

as the ferrule is rotated in the v-groove. N consecutive discrete values of x and y coordinates of the center of the microhole are taken equally spaced in θ and covering one complete revolution of the part. The FFT of the x or y data will have a magnitude of $c/2$ at the one cycle per revolution frequency component, which is interpreted as concentricity. The Inverse FFT (IFFT) of the transformed data with the concentricity and mean offset components removed, will yield the roundness error traces. From these traces, the peak-to-valley error, lobe frequencies or other useful roundness error measures can be obtained. The concentricity and roundness error estimates based on x and y data can be averaged together to improve measurement precision.

III. Experimental

All measurements were made with an apparatus as shown in Figure 1. The ferrule is backlit with a high power white light source, and rotated in the v-groove. A video camera is attached to a high power microscope. The video images are processed in the computer to calculate the center of the microhole.

To examine the accuracy of the roundness error measurement, several ferrules were measured using the proposed method and using a stylus type mechanical roundness error measurement system. The comparison of the measurements is shown in Figure 3, and demonstrates the high correlation between these two instruments. Figure 4 compares the raw data trace, the FFT roundness error and

the stylus-type roundness error traces for one part. As seen in the figure, the raw trace does not directly reveal the concentricity and roundness error of the part. However, an accurate roundness error measurement is obtained using the FFT method.

Figure 5 is a demonstration of the 2-point methods accuracy problems. A few ferrules with varying roundness error to concentricity ratio were measured. The ferrules were measured several times using the 2-point method and once using the FFT method. The average of all measurements using the 2-point method were recorded and the difference from FFT-based concentricity was calculated. As shown in the figure, the two methods converge for low roundness error/concentricity ratios as expected, but diverge rapidly at ratios higher than 0.5.

IV. Conclusions

A new method for measuring ceramic ferrule roundness error and concentricity has been presented. This method can separate the concentricity and roundness error of ferrules using an FFT algorithm. In that way, the measurement accuracy, repeatability and correlation to connector insertion loss is improved significantly.

V. References

1. IEC Publication 1300-3-25 "Concentricity of Ferrules", International Electrotechnical Commission, 3, rue de Varembe, Geneva, Switzerland
2. Pasturczyk, Z.; Wong, B.; Saravanos, C., "Fiber Optic Geometry Test Station", *Proceedings of the IWCS*, pp. 623-626, 1989
3. TIA/EIA-455-135, "Connector Ferrule Inside and Outside Diameter Circular Runout," Telecommunications Industry Association-Electronic Industries Association, 2500 Wilson Blvd., Suite 300, Arlington VA 22201.

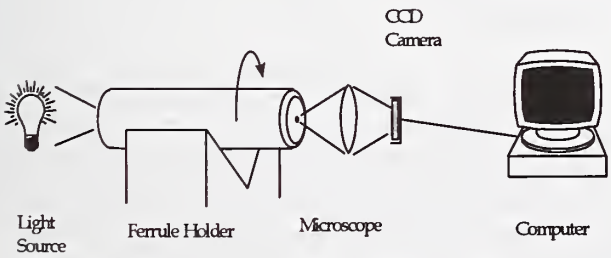

Figure 1. Ferrule Measurement Apparatus.

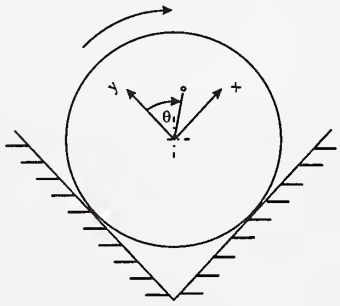

Figure 2. Ferrule in V-groove

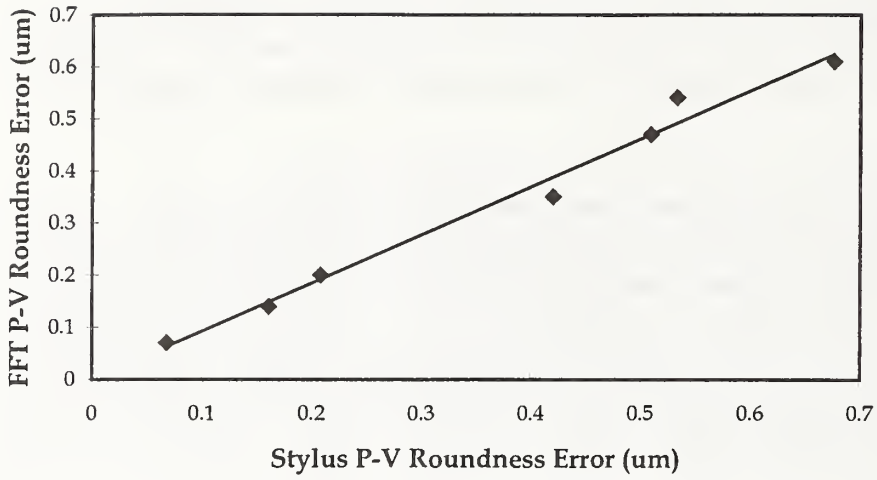

Figure 3. FFT roundness error vs stylus type roundness error

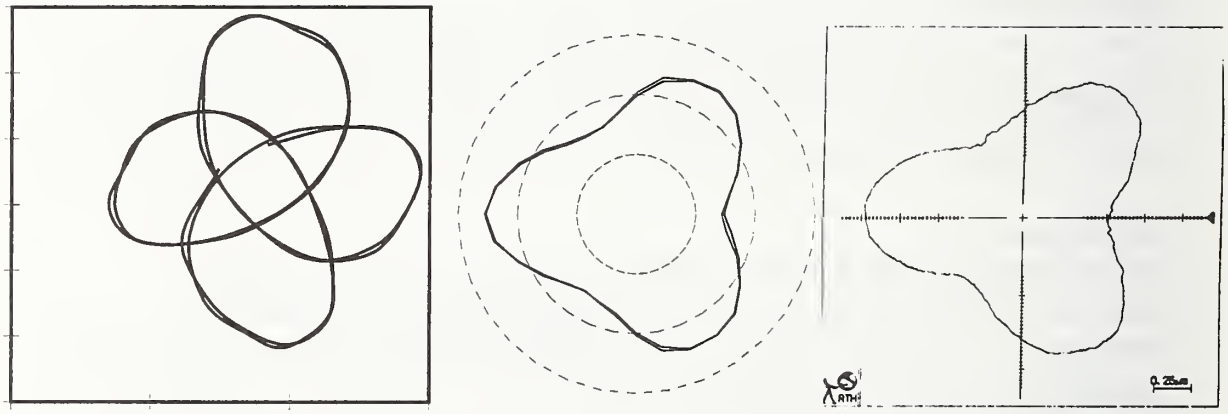

(a) (b) (c)

Figure 4. (a) Raw data trace, (b) FFT roundness error, (c) Mechanical Stylus roundness error

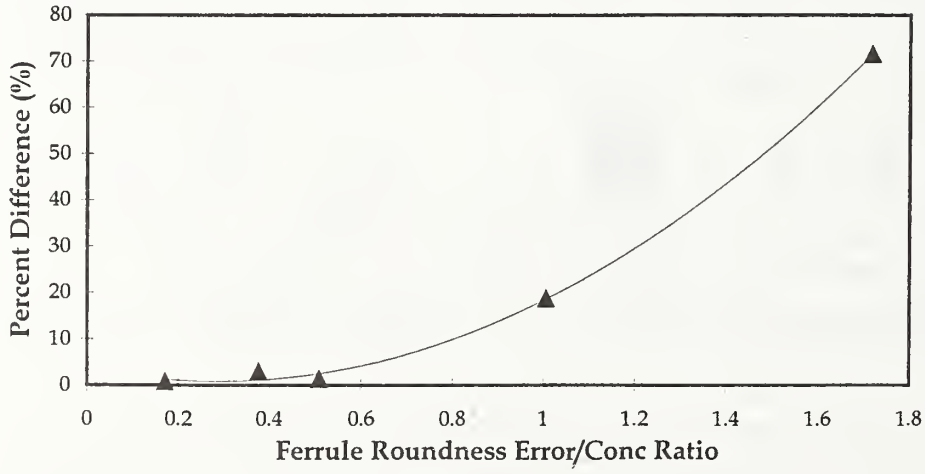

Figure 5. Difference between two point and FFT Concentricity

Errors due to connectors in optical fiber power meters

Igor Vayshenker, Xiaoyu Li, Darryl A. Keenan, and Thomas R. Scott
National Institute of Standards and Technology, 325 Broadway, Boulder, CO 80303

Abstract

We discuss results of a major potential error source in the use of optical fiber power meters: outputs can vary dramatically when using various types of connectors or even connectors of the same type but from different vendors. We investigate the magnitude of this connector-induced variation by calibrating several types of optical fiber power meters at three telecommunications wavelengths of 850, 1310, and 1550 nm. In these measurements we vary the connector type and connector vendor, and observe the resulting offsets in calibration results. Observed variations of as much as 10% were found, due, presumably, to the different reflection properties of the detectors, windows, and connectors involved. A test meter user, therefore, can expect an error as large as 10% if the optical fiber power meter is used with a different connector (or vendor) than that used for calibration.

1. Introduction

When optical fiber power is measured, radiation is transmitted to an optical fiber power meter through a fiber attached to a detector by a fiber connector and adapter. The proximity of a fiber connector to a detector and its associated window provide an opportunity for reflections to introduce errors in the power readings.[1,2] Even though the measurements using connectors are generally repeatable, the connectors can skew the measurements results. To investigate this issue we conducted a study involving the calibration of optical fiber power meters using various types of connectors. We selected six common connector types: FC/PC, FC/APC, ST, biconic, SC, and SMA from four vendors chosen randomly (the vendors are identified by letters A through D). Calibrations were performed on four types of power meters (the meters are identified by numbers 1 through 4) at three telecommunications wavelengths: 850, 1310, and 1550 nm.

2. Measurement system

The system depicted in Figure 1 was used to perform the calibrations. As a reference we used a commercially available, electrically calibrated pyroelectric radiometer (ECPR).[3] The detector is approximately 8 mm in diameter and has very low reflectance over the wavelength range. The pyroelectric sensor is made of lithium tantalate and is covered with a gold-black coating.

The calibration system contains three laser sources and a positioning stage for comparing the outputs of the ECPR and the test meter. All the optical fibers in the system are single-mode. Each laser source plate contains a laser diode whose output is transmitted through a fiber to a fiber splitter from which about 1% of the energy travels through a fiber to a monitor. Power changes (for example, due to diode laser instability) are taken into account by the monitor readings. The fiber jumper cables are stationary during the calibrations. Power is coupled directly into the pyroelectric detector or the test meter. The incident power was about 100 μW.

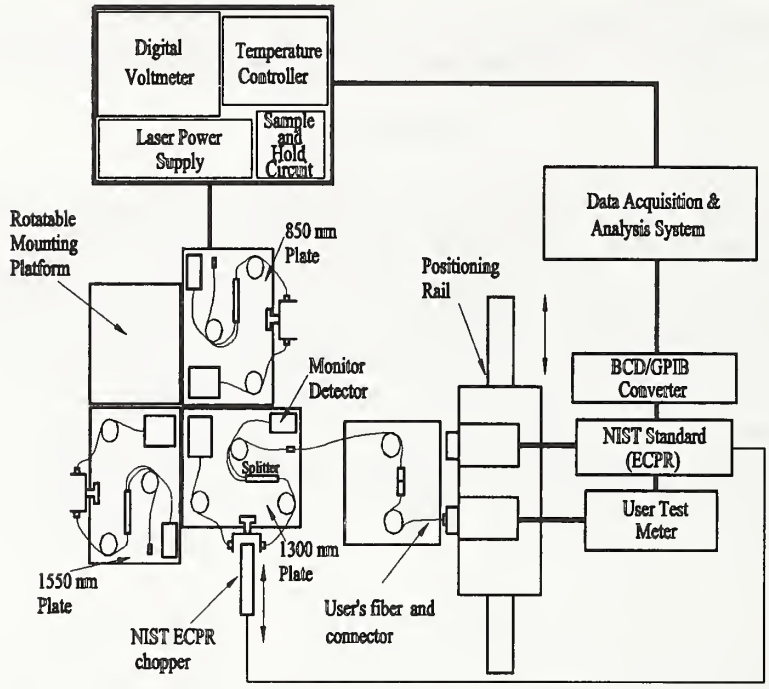

Figure 1. The measurement system.

Table I. Connector study variables.

Connector Types: FC/PC, FC/APC, ST, biconic, SC, and SMA
Connector Vendors: A-D
Wavelength: 853, 1307, and 1549 nm
Meter/Detector Type: Meter 1 (Si & Ge remote sensors; angled), Meter 2 (InGaAs fiber-pigtailed sensor), Meter 3 (Ge sensor with window; not angled), and Meter 4 (windowless Ge sensor; not angled).

3. Results

The measurement variables are given in Table I; the results are reported in the form of Figures 1-8. Due to the format of this paper, we included only a few of the measurement results. We performed 5 data runs for each measurement; the data show that the repeatability of measurements performed with a specific connector is reliable. The connector's offset is consistent. Figures 1-4 depict the results for four power meters and six connectors referenced to an FC/PC connector for vendor C. The largest differences occurred for the germanium power meter with a window (the sensor was not angled). Placing a sensor at a small angle will decrease the reflection between the sensor, the sensor window, and the connector. The observed differences were more than 10%. Figures 5-8 depict the results for four power meters and four connector vendors

referenced to ST connector for vendor A. Again, the largest differences (8%) were observed for the germanium power meter with a window. Vendor B's connectors caused a greater offset than that caused by connectors of all other vendors.

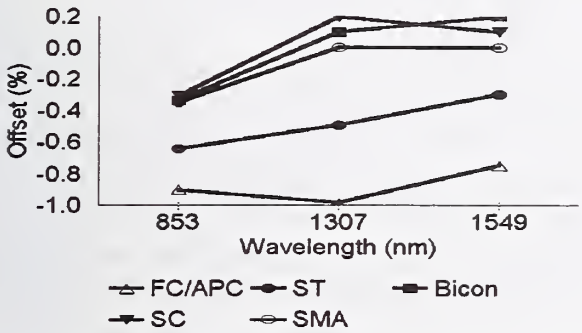

Figure 2. Si & Ge power meter (angled); referenced to FC/PC for vendor C.

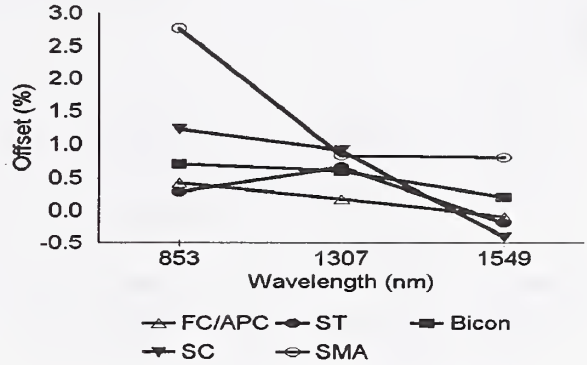

Figure 3. InGaAs power meter (fiber-pigtailed); referenced to FC/PC for vendor C.

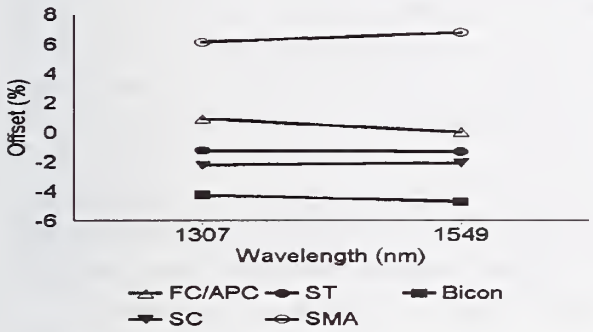

Figure 4. Ge power meter with window (not angled); referenced to FC/PC for vendor C.

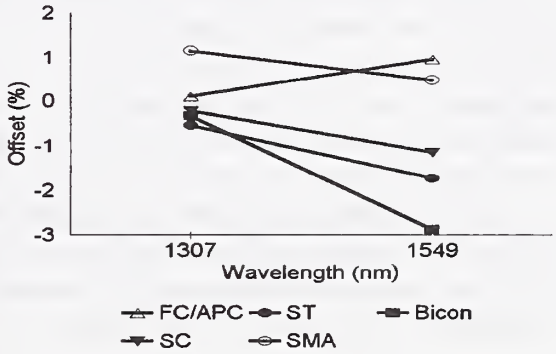

Figure 5. Ge power meter without window (not angled); referenced to FC/PC for vendor C.

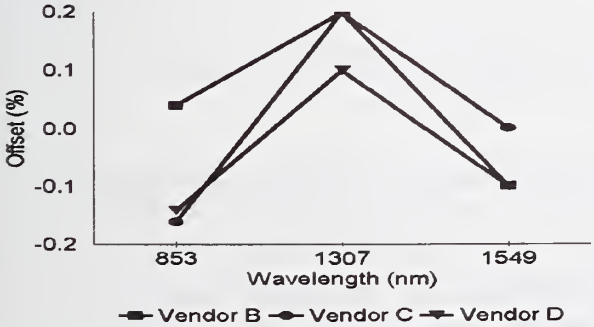

Figure 6. Si & Ge power meter (angled); referenced to ST for vendor A.

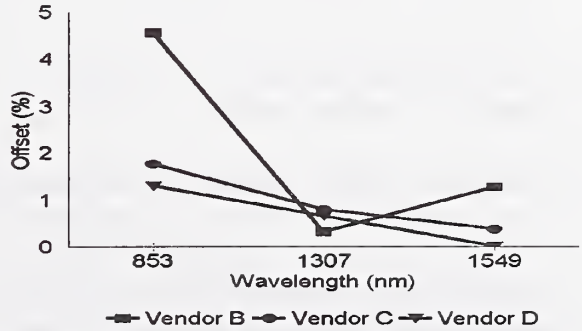

Figure 7. InGaAs power meter (fiber-pigtailed); referenced to ST for vendor A.

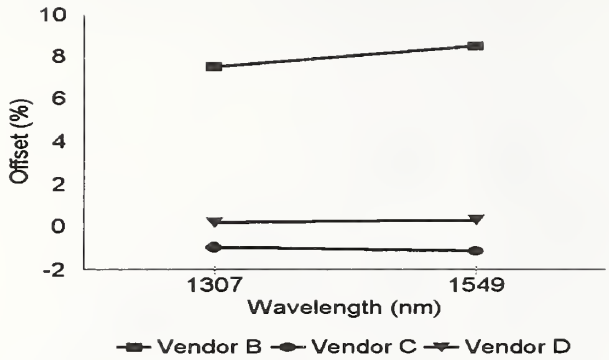

Figure 8. Ge power meter with window (not angled); referenced to ST for vendor A.

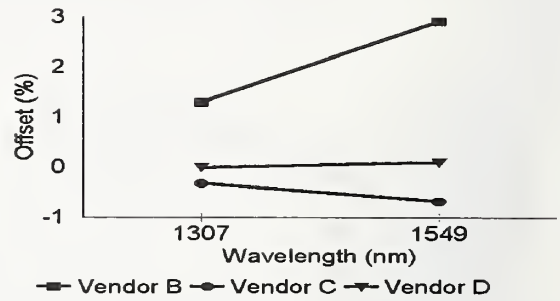

Figure 9. Ge power meter without window (not angled); referenced to ST for vendor A.

4. Conclusions

We found significant measurement offsets resulting from the use of various connectors and a variability within a single connector type obtained from different vendors. Thus, errors could likely occur when changing types of connectors or connector vendors on fibers connected to optical fiber power meters. For accurate measurements during the calibration of the instrument, we suggest that the meter owner should be aware of the connector's effects. A transfer standard, whose output is insensitive to the connector types, is a useful tool when determining effects due to various connectors. The connector adapter used with the connector is an integral part of the measurement.

The magnitude of the errors is wavelength-dependent. The offset is small if a connector does not have a reflecting surface or a power meter sensor is angled. A connector with a reflecting surface will cause the meter to read incorrectly, usually higher. It is very important to calibrate an optical fiber power meter with the same type of a connector used in the actual measurement.

Acknowledgments

This work is supported by the Calibration Coordination Group (CCG) of the Department of Defense; the lead agency for this project is the U.S. Army, Huntsville, Alabama.

References

1. R.L. Gallawa and Xiaoyu Li, "Calibration of optical fiber power meters: the effect of connectors," Applied Optics, Vol. 26, No. 7, pp. 1170-1174, April 1, 1987.

2. Xiaoyu Li and R.L. Gallawa, "Calibrated optical fiber power meters: errors due to variations in connectors," Fiber and Integrated Optics, Vol. 7, pp. 241-248, March 3, 1988.

3. R.J. Phelan, Jr. and A.R. Cook, "Electrically Calibrated Pyroelectric Optical-Radiation Detector," Applied Optics, Vol. 12, p. 2494, October 1973.

MU-type PANDA Fiber Connector

R. Nagase and S. Mitachi
NTT Opto-electronics Laboratories
Tokai, Naka-gun, Ibaraki 319-11, Japan

Introduction

Polarization-maintaining fibers (PMFs) e. g., PANDA fiber[1], are widely used in the field of optical sensing systems[2] and advanced telecommunication systems[3]. We require high performance and compact PMF connectors to improve these practical systems. However, there is no PMF connector smaller than the SC connector[4] because of the design difficulty involved in precisely matching the principal axes of connected PMFs.

In this paper we propose a keying accuracy requirement for PMF connectors which will allow the realization of PMF connection with high extinction ratio propagation. And also we describe the design principle and performance of a compact, newly developed MU-type PANDA fiber connector.

Definitions and measurement of the keying accuracy and the extinction ratio

Figure 1 shows an experimental configuration for measuring the direction of the principal axis (PA) of a PMF and its extinction ratio. Linearly polarized light with a constant power in any direction can be produced by using a setup consisting of a polarizer (P_1), a quarter wave plate (Q) and a polarizer (P_2). The patch cord under test is measured in the following way. First, an analyzer (A) and a polarizer (P_2) are adjusted so that the transmitted light power has a minimum value of P_{min} (dBm). The PAs of connectors C_1 and C_2 are parallel to the principal axes of P_2 and A, respectively. Then analyzer A is adjusted so that the transmitted power has a maximum value of P_{max} (dBm). We define the extinction ratio (ER) of the output signal as P_{max} - P_{min} in dB units. The value of ER changes along the fiber because of the modal birefringence.

Keying accuracy requirement

The minimum extinction ratio Er_{min} for a PA misalignment angle θ between connected PMFs is given by[5]

$$Er_{\min} = 10\log(\tan^2\theta). \tag{1}$$

To achieve a minimum ER of 20 dB, the allowable misalignment angle is estimated to be 6° from eq. (1), i. e., the keying accuracy should be ±3° (Fig. 3). If two PMF patch cords are connected, the minimum total extinction ratio Ert_{min} will be

$$Ert_{\min} = -20\log(10^{-Er_1/20} + 10^{-Er_2/20} + \tan\theta) \tag{2}$$

where Er_1 and Er_2 are the individual ER values of two patch cords. A typical patch cord with a several-meter-long PMF and two connectors has an ER of 25 ~ 35 dB.

Figure 4 shows the measured ER of randomly concatenated PMF connectors whose keying accuracies were better than ±3°. We confirmed that all measured ER values were higher than the calculated Ert_{min} from eq. (2), and a keying accuracy of ±3° is sufficient to achieve an ER of 20 dB.

MU-type PANDA fiber connector design

(1) Keying accuracy: PANDA fiber has a clear geometric axis (GA) parallel to the stress applying parts (SAPs) as shown in Fig. 2. It is known that the angle between the PA and the GA is less than 1°[6]. It is much easier to observe the GAs by microscope than to measure the PA directions. Therefore, we have established a keying accuracy of ±2° for GAs.

(2) Keying direction: A PANDA fiber has an elliptic cross section whose major axis is parallel to the y-axis (as shown in Fig. 2) because of the SAPs shrink as the fiber is drawn. Therefore, after it has been glued to the ferrule, the fiber core has a tendency to shift in the x-axis direction. Figure 5 shows the measured fiber core eccentricity directions. The key direction (0°) was set in the x-axis direction. The distribution will usually be uniform, however, in this case about 90% of the core direction distribution was localized in the ±60° region. It is desirable to achieve a low connection loss[7], therefore, the keying direction should be set in the x-axis direction as shown in Fig. 2.

(3) Ferrule structure: A ferrule floating mechanism is essential for realizing stable connection. In particular, the floating distance cannot be reduced if the MU connector is used as a backplane connector[8]. Therefore, we have designed a new MU-type ferrule with a specially designed coupling device as shown in Fig. 6. The ferrule can float from the plug housing by the same distance as a normal MU plug, but it cannot rotate around the ferrule axis. The flange can be pressed into the ferrule in any direction after the fiber has been glued to the ferrule.

(4) Plug housing: The rectangular shaped design and the push-pull latching mechanism used for MU connectors are suitable for PMF connectors because no torque is applied to the ferrule during the coupling operation.

Characteristics of MU-type PANDA fiber connector

We assembled 2 m-long MU-SC patch cords with 10 μm MFD PANDA fibers and measured them at an 1310 nm LD light source. Figure 7 shows an MU plug attached to a PANDA fiber.

We confirmed that the keying accuracy for the GA of a PANDA fiber can be adjusted to within ±2° of plug key using microscope observations of the SAPs and flange pressing technique as shown in Fig. 8 (a). The average ER was 27.3 dB for random concatenations of 2 patch cords as shown in Fig. 8 (b). Figure 8 (c) shows the connection repeatability. The ER fluctuations were less than 8 dB for 500 mate-demate cycles. The average connection loss was 0.11 dB for random concatenations as shown in Fig. 8 (d). The return loss of a connection point was typically 50 dB. These values are similar to those of normal MU connectors for SM fibers.

Conclusion

We investigated the extinction ratio degradation of PMF connections and determined a keying accuracy of ±2° for geometric axes and the desirable keying direction for PANDA fiber connectors. We have also developed a compact MU-type PANDA fiber connector which can be used for both fiber cable coupling and as a backplane connector. It features a high extinction ratio for random connections (typically over 20 dB), good connection repeatability, and a low connection loss (typically 0.11 dB).

References

[1] T. Hosaka, et al., *Electron. Lett.*, Vol. 21, no. 20, pp. 920-921, 1985.
[2] R. Ulrich, et al., *Opt. Lett.*, Vol. 4, pp. 152-154, 1979.
[3] T. Kataoka, et al., *Electron. Lett.*, Vol. 27, no. 11, pp. 943-944, 1991.
[4] R. Nagase, et al., in *Proc. IEICE General Conf.*, Japan, paper C-280, 1991 (in Japanese).

[5] I. Yokohama, et al., *IEEE J. Lightwave Technol.*, Vol. LT-5, no. 7, pp. 910-915, 1987.
[6] Y. Kikuchi,et al., in *Proc. IOOC '89*, paper 19B3-12, 1989.
[7] Y. Ando, et al., *IEICE Trans.*, Vol. E77-C, No. 12, pp. 1970-1982, 1994.
[8] S. Iwano, et al., *IEEE J. Lightwave Tech.*, vol. 10, no. 10, pp. 1356-1362, 1992.

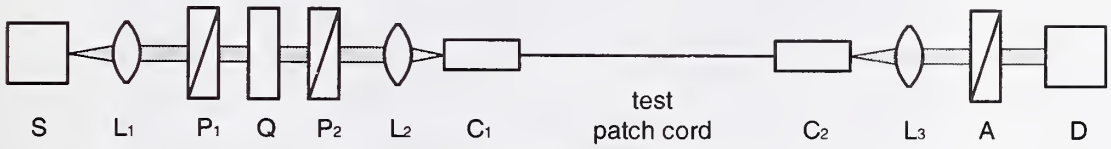

Fig. 1. The experimental configuration for the direction of PA and the ER measurement

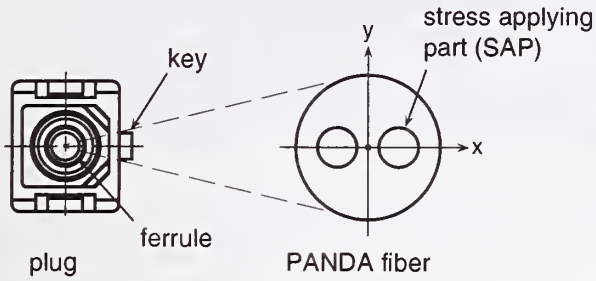

Fig. 2. PANDA fiber and its connector plug geometry

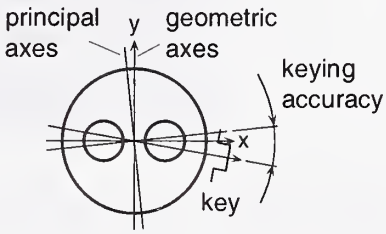

Fig. 3. Definition of keying accuracy

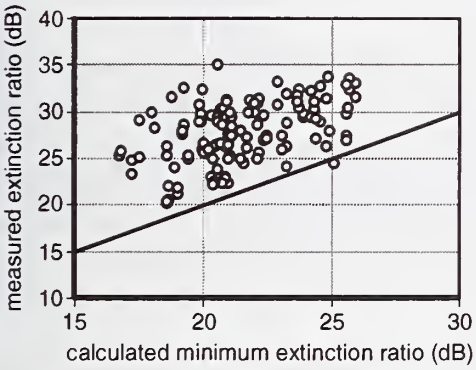

Fig. 4. Experimental results for randomly concatenated PMF connectors

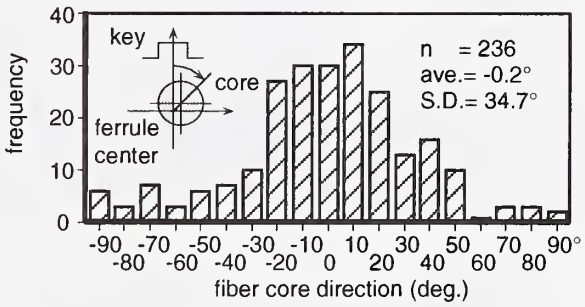

Fig. 5. Distribution of the fiber core eccentricity directions

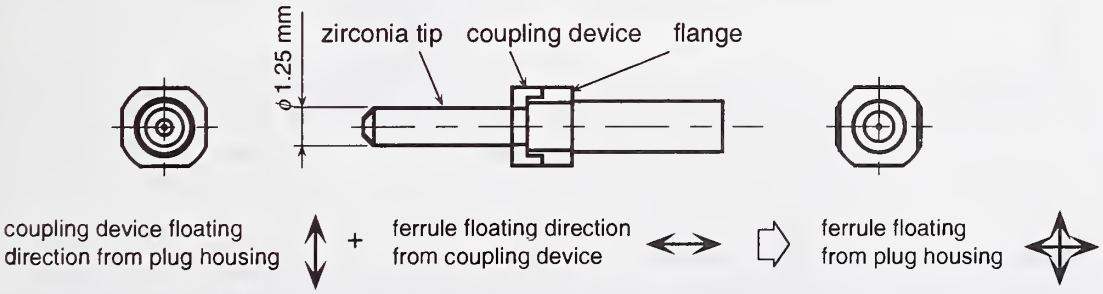

Fig. 6. Structure of the ferrule for an MU-type PANDA fiber connector

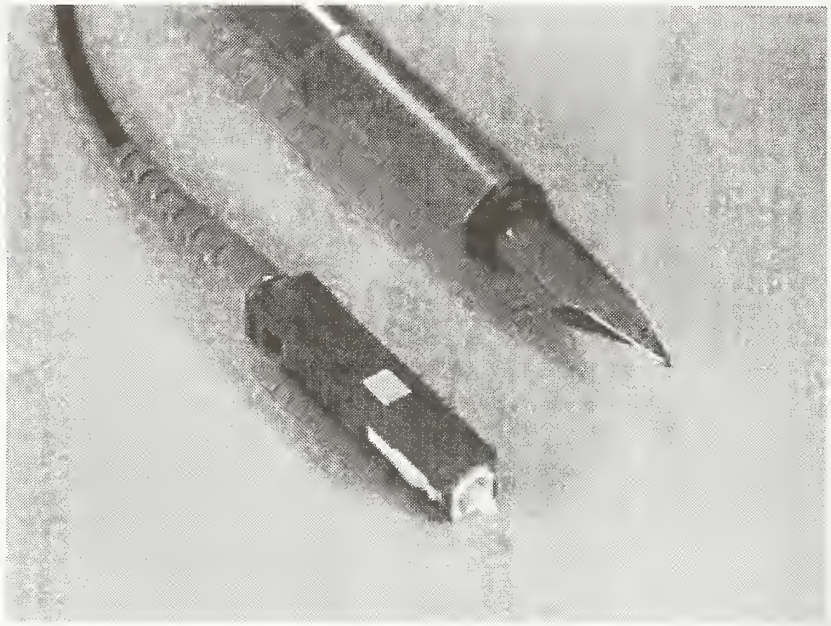

Fig. 7. MU-type PANDA fiber connector plug

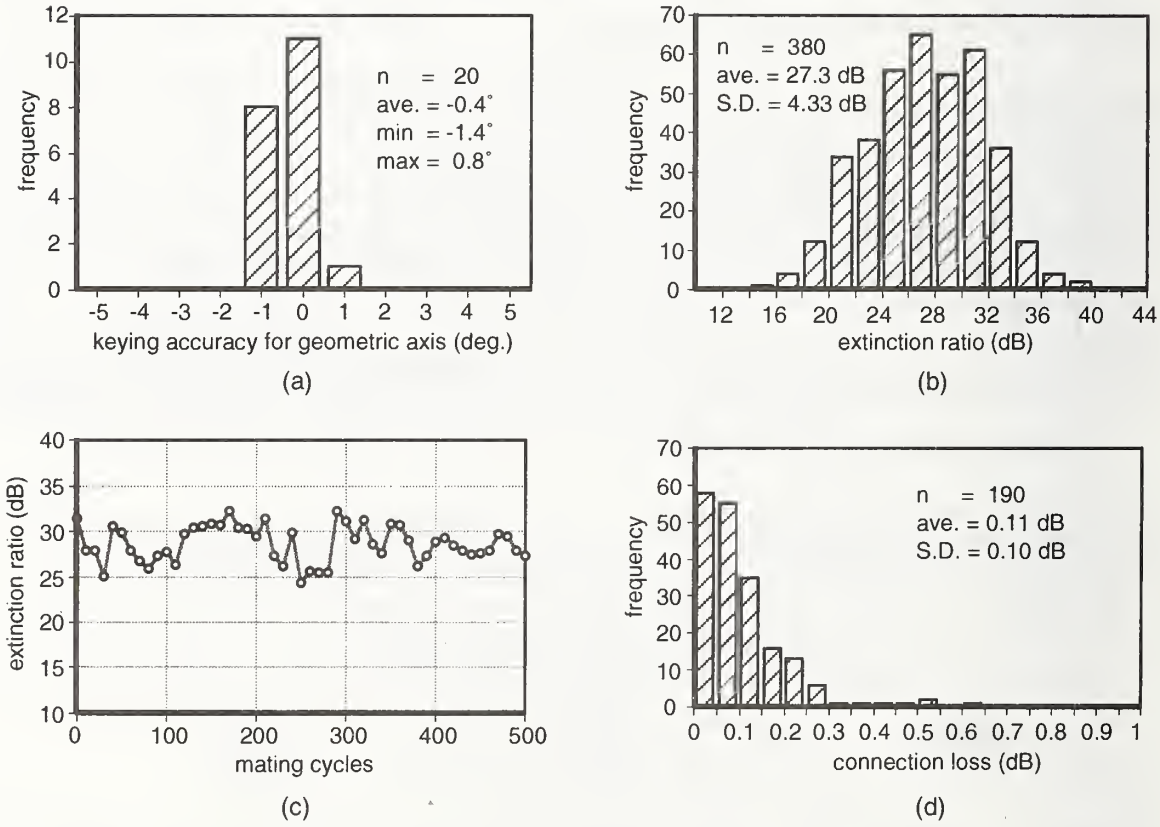

Fig. 8. Characteristics of MU-type PANDA fiber connectors; (a) keying accuracy of the PANDA fiber geometric axes, (b) measured extinction ratio of randomly concatenated connector pairs, (c) connection repeatability, and (d) connection loss of randomly concatenated connector pairs.

High Performance Single -Mode wavelength independent all-fiber build-out attenuator

Shin-Lo Chia

AMP Passive Products Division

2525 E. Bayshore Rd. Palo Alto, CA 94303

Tel : 415-493-8008 FAX: 415-493-8924

e-mail: AMPMS.kap00110@AMPUSEM1.amp.com

Abstract

A very high performance, cost-effective, miniature, wavelength independent all-fiber Single Mode attenuator is demonstrated. The device maintains consistent attenuation in both jumper-to-jumper, and direct-to-detector applications.

Summary

In this paper a novel, all-fiber attenuator that uses a high attenuation core single-mode fiber is proposed and demonstrated. The basic process is as follows: (1) A length of standard single-mode fiber is fusion spliced to the attenuation fiber. (2) The attenuation fiber is cleaved at a precisely controlled length which will yield the required attenuation. (3) Another fiber is fused to the other end of the attenuation fiber [See Figure 1 (a)]. (4) The finished attenuator is assembled into the ferrules and PC polished [See Figure 1 (b)]. (5) The ferrule assembly is packaged as a build-out attenuator [See Figure 1 (c)].

The net attenuation provided by the proposed design depends on the following factors:

1. Absorption by the dopant material in the core.
2. Overlap integral between the mode field and the physical attenuation core.
3. Mode field mismatch at each fusion junction.
4. Modal interference and noise generated by the four optical interfaces in the attenuator system.

In order to determine the specific characteristics required of the core dopant, a beam propagation model was constructed. In the model simulation, from 0.0 to 5.0 mm is the standard S.M. fiber. From 5.0 to 15.0 mm distance, the absorption coefficient of the core is assumed to be wavelength independent, and is adjusted to produce an attenuation of 1 dB/mm with a 6 μm diameter core. Then from 15.0 to 20.0 mm the standard S.M. fiber is replicated. As expected, the model exhibits a pronounced wavelength dependence effect, showing a decreasing loss vs. wavelength. (Refer to Fig. 2) This arises from the fact that the longer wavelengths with larger mode field diameters will

decrease the overlap integral (attenuation) between the mode field and the attenuation core. In order to achieve true wavelength independence in the finished device, this effect must be compensated for by the wavelength response characteristics of the proposed attenuating fiber.

Figure 3 shows the total contribution effect of the wavelength dependency for the attenuation fiber BOA. The center line shows the normalized measurment BOA spectral response. A attenuation value increase with the increase of wavelength . This response is balanced between the dopant absorption and the mode propagation loss dependence. A third modal noise ripple effect could add to the balanced response and make the final BOA spectral with the ripple on. However, the carefully design the attenuation fiber with better matching characteristics and well control the fusion quality between the attenuation fiber and standard fiber could dramatically decrease the modal noise effect.

The key component in this attenuator is a specialized attenuation fiber which has been manufactured to meet these specific criteria. The attenuation fiber is manufactured by using a Ge-Al co-doped silicate core and introducing transition metals [4] or rare earth elements to the core. A difficulty arises when increasing the dopant concentration in order to achieve high attenuation per unit length as required when fabricating a very short length attenuator. High dopant concentration may increase the NA value dramatically and also reduce the modal noise effect; but increase backreflection and cut-off wavelength as well. Current research centers on the determination of the optimal characteristics required of the attenuation fiber. When these parameters are finalized, and fiber is produced to these specifications, manufacturing will become a simple matter of controlling the quality of the fusion splice, and the accuracy of the length of the attenuation fiber. These process readily lend themselves to cost-effective mass production.

An additional undesirable side effect of the mismatch in NA between the two fiber types is a discrepancy in effective attenuation between an application where the attenuator is used in line between two single-mode cables and when the output of the attenuator is coupled directly into a detector. In the latter case, any light which has scattered into the cladding can represent a significant portion of the output signal and reduce the originally designed attenuation level especially in high attenuation level (15 dB and above). A significant reduction of these cladding modes can be effected by chemically etching away some of the cladding of the attenuation fiber.

After the first optimized attenuation fiber was obtained and tested, an entire range of attenuators was successfully fabricated and tested. The current precision fusion and cleaving process can be controlled by ± 50 μm, allowing accurate production of attenuators with values as low as 0.75 dB or as much as 25 dB simply by controlling the length of the attenuating fiber included in the device. Figure 4 shows a typical wavelength scan for such an attenuator. It can be seen that all meet attenuator tolerance requirements within the 1260 to 1360 nm and 1430 to 1580 nm passbands as specified in Bellcore TA-TSY-000910.

When fusing the standard fiber to the attenuation fiber, the fusion joint has no more than -65 dB backreflection. Therefore, the backreflection of the build-out attenuator as shown in Figure 1 is not limited by the attenuator element itself but by the polishing quality of the ferrule ends.

Currently, a new Ultra-PC polishing process better than 55 dB in return loss and with less than 50 nm fiber undercut [6] has been successfully demonstrated and implemented in this BOA product.

Conclusions

A very ragged and high performance all fiber attenuator that revolutionize installation and operation simplicity has been obtained. The manufacturing is just a simple matter of controlling the quality of the fusion splice, and the accuracy of the length of the attenuation fiber. These processes readily lend themselves to cost-effective mass production. Also, the new attenuator meets all Bellcore requirements for attenuator tolerance, backreflection, polarization stability, humidity resistance, etc.

References

1. J.C. Goodwin and P.J. Vella, " Modal noise in short fiber section " ,J. Lightwave Tech., Vol. 9, pp. 954-958, 1991.
2. S. Heckma, " Modal noise in single mode operated slightly above cut-off ", Electron letter. Vol. 17, pp. 499-500, 1981
3. R. A. Throckorton, D. Harris, " Modal interference in field installable single-mode fiber-optic connector" NFOEC' 94, Vol.3, pp. 399-406, San Diego, 1994
4. P. C. Schultz, " Optical absorption of the transition elements in vitreous silica ", J. of the American ceramic society, Vol. 57, No 7, pp.309-313, 1974
5. "Generic Requirements for Fiber Optic Attenuators", TR-TSY-000910 Issue 2, Sep. 1992.
6. "Generic Requirements for Single-Mode Optical Fiber Connector", GR-326-CORE Issue 1, Dec. 1994.

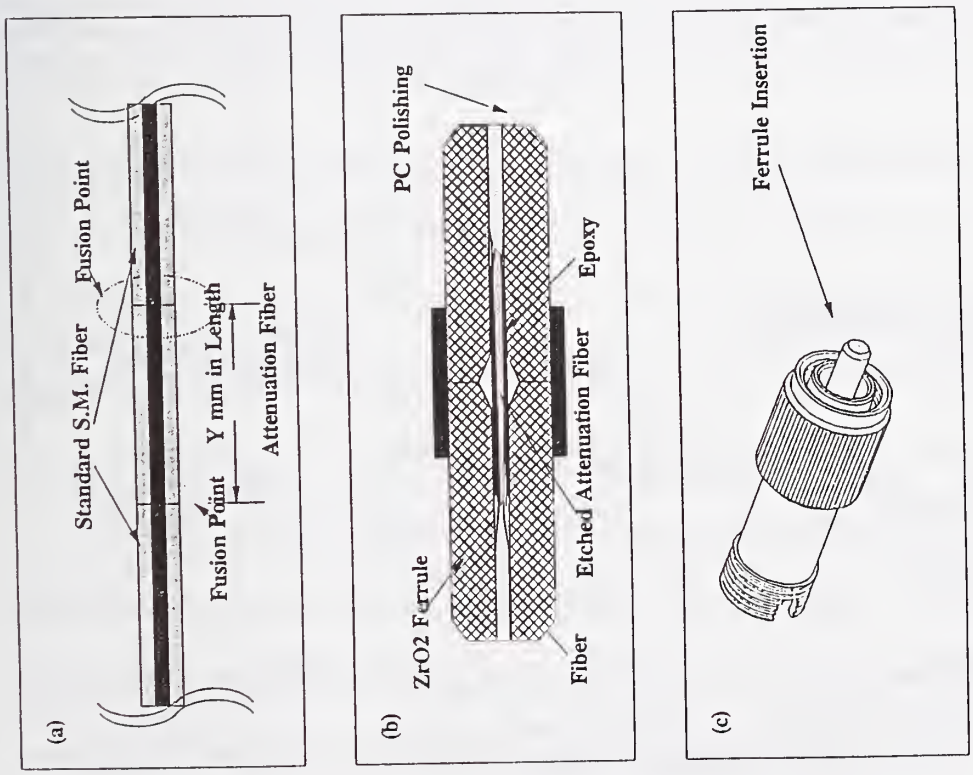

Figure 1. All fiber build-out attenuator: (a) fiber cleaving and fusion; finished attenuator is assembled into the ferrules and PC polished ; ferrule assembly is packaged as a build-out attenuator.

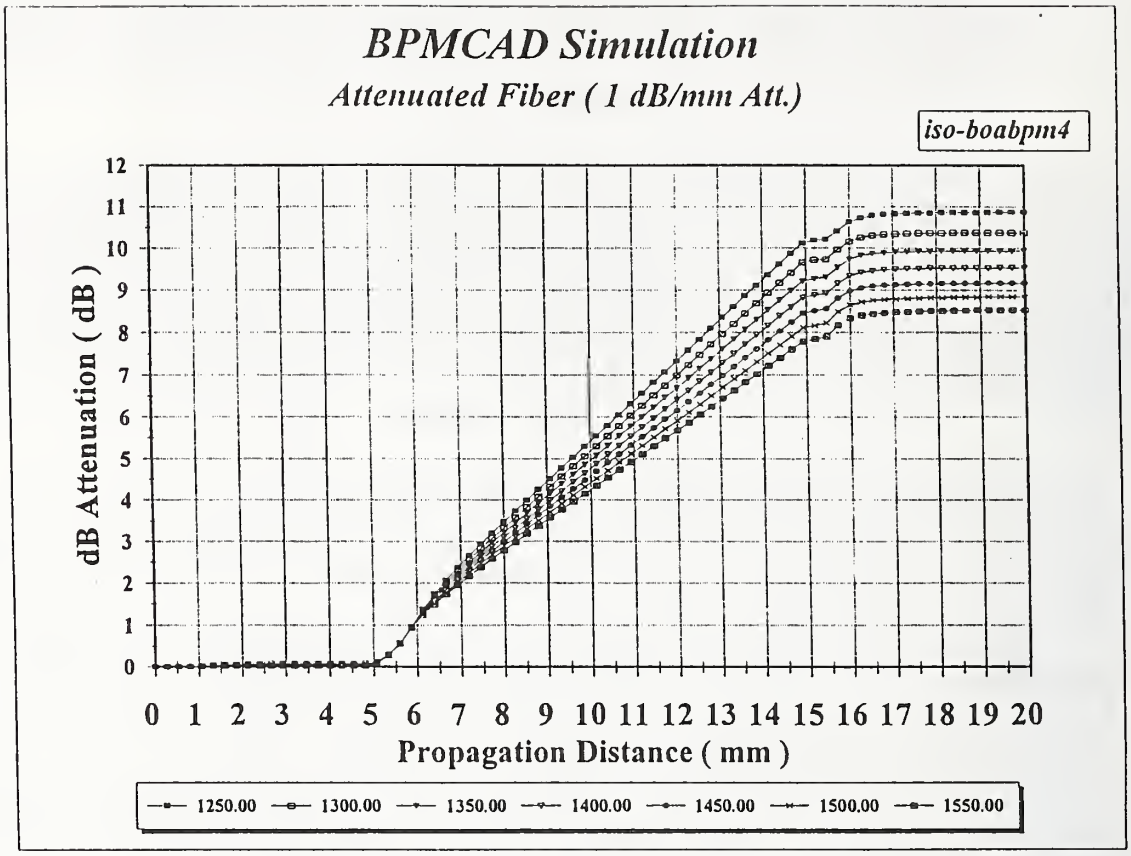

Figure 2. Graph shows the calculated results of the BPM model simulation. From 0.0 to 5.0 mm is the standard S.M. fiber. From 5.0 to 15.0 mm distance, the absorption coefficient of the core is assumed to be wavelength independent, and is adjusted to produce an attenuation of 1 dB/mm a 6 μm diameter core. Then from 15.0 to 20.0 mm the standard S.M. fiber is replicated.

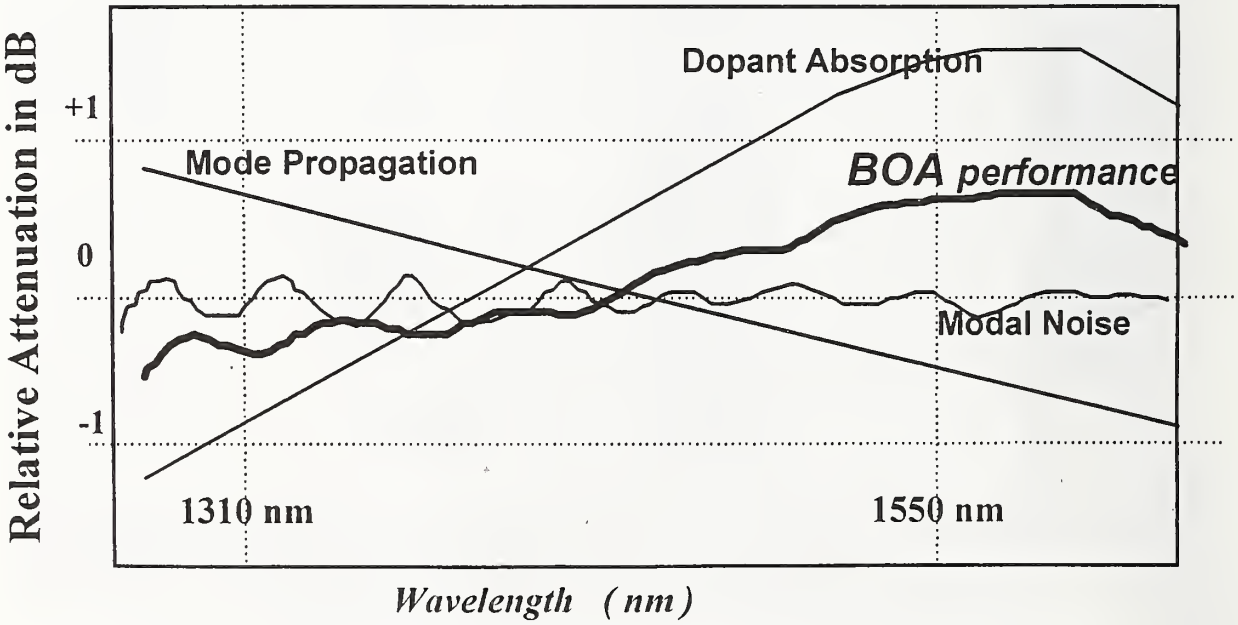

Figure 3. Total wavelength dependency effects for the attenuation fiber BOA

Nonlinear coefficient of optical fibers at 1550 nm

Valéria L. da Silva, Y. Liu, A.J. Antos, G.E. Berkey and M.A. Newhouse

Corning Incorporated, Science and Technology Division,
Sullivan Park, NY 14831

A major revolution in lightwave transmission system is ocurring with the advent of erbium-doped fiber amplifiers. They have allowed transmission over transoceanic distances without the need of electronic repeaters and enabled high speed, multiwavelength terrestrial transmission systems. On the other hand, the use of optical amplifiers has increased the optical signal power to a point where nonlinear effects start to become important and impose serious limitations to system performance. The magnitude of the major nonlinear effects, self-phase modulation (SPM) and four-wave mixing (FWM), depend on the nonlinear coefficient n_2/A_{eff} (nonlinear refractive index/effective area). Therefore it is important to measure the n_2/A_{eff} for telecommunication fibers. In this paper we will review measurements of the nonlinear coefficient by different laboratories and present results obtained at our laboratory on different types of fibers of interest in transmission systems at 1550 nm.

The value of n_2/A_{eff} is usually obtained by measuring the magnitude of nonlinear effects such as self-phase modulation, cross-phase modulation or four-wave mixing. By an independent measurement of the A_{eff}, n_2 can be obtained. Almost all measurements of n_2 for non-polarization-preserving dispersion-shifted fibers resulted in a value of 2.3 ± 0.1 x

10^{-20} m^2/W at 1.5 μm [1-6]. The exceptions were cross-phase modulation measurements in which the pump source is slowly modulated. In these cases, higher n_2 values were obtained, 2.7 - 2.9 x 10^{-20} m^2/W [7,8]. The higher n_2 is attributed to the electrostriction contribution, which becomes significant for pulsewidths of ~1 ns or longer [9].

Current lightwave systems use other fibers besides dispersion-shifted fibers. Since n_2 depends on the amount of GeO_2 and the mode-field profile, it is important to measure n_2 in the different fibers. We measured the n_2/A_{eff} coefficient, using the self-phase modulation technique [2,11], for three different fibers: dispersion-shifted fiber (DSF), large effective area fiber (LEAF) [10] and dispersion compensating fiber (DSF). The characteristics of the measured fibers are summarized in Table 1.

Fiber Type	Length (km)	λ_{meas} (nm)	α @ 1550 nm (dB/km)	λ_0 (nm)	Dispersion (ps/km/nm)	MFD (μm)	A_{eff} (μm^2)
DSF	5.0	1545	0.21	1547	-0.16	8.32	51
DCF1	1.0	1550	0.50		-88.7	5.98	29
DCF2	1.0	1550	0.85		-125.6	5.67	28
LEAF	2.9	1535	0.21	1538	-0.37	9.79	88

Table 1. Characteristics of the measured optical fibers. The effective areas were measured by the far-field pattern method.

The major effect of SPM is to broaden the spectra of input pulses at high input powers. The amount of broadening depends on the fiber length, peak input power and fiber dispersion. In our measurements, we used relatively long pulses (~40 ps) and short fiber lengths in order to avoid any dispersion effects. Under these conditions, the spectral broadening factor for a Gaussian pulse is given by [11]:

$$\frac{(\Delta\omega)_{out}}{(\Delta\omega)_{in}} = \left[1 + \frac{4}{3\sqrt{3}}\left(\frac{2\pi}{\lambda}\frac{n_2}{A_{eff}}PL_{eff}\right)^2\right]^{1/2} \tag{1}$$

where $\Delta\omega$ is the RMS spectral width, λ is the wavelength, P is the peak input power and L_{eff} is the effective length.

We measured the output spectrum as a function of the peak input power utilizing the experimental setup depicted in Fig. 1. The pulse source consisted of a mode-locked tunable external cavity laser producing 40 ps pulses at 5.0 GHz repetition rate followed by an erbium-doped fiber power amplifier with saturated output power of 20 dBm. In order to increase the peak power od the pulses, an electro-optic modulator with a duty cycle of ~10% was introduced prior to the optical fiber amplifier. The resulting pulses had a peak power in excess of 2.5 Watts allowing the use of short fiber lengths (1-5 km) and reducing the effect of fiber dispersion.

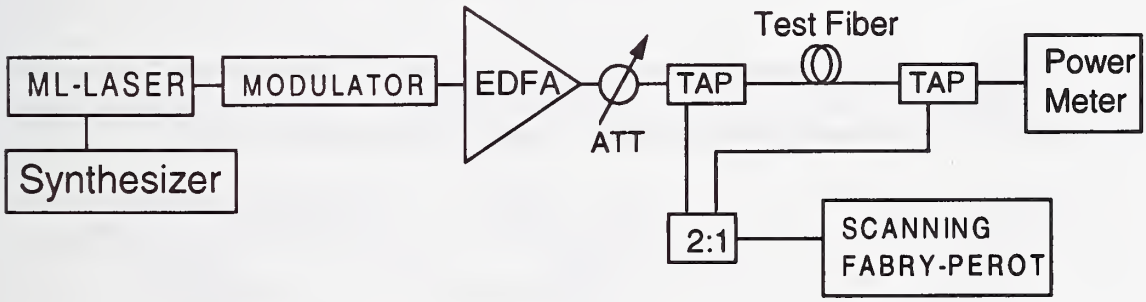

Figure 1. Experimental setup.

The spectral broadening factor $(\Delta\omega)_{out}/(\Delta\omega)_{in}$ as a function of the peak input power is shown in Fig. 2 for the measured optical fibers; the ratio between the DSF value and the other fibers is shown in Table 2. As expected, the spectral broadening is less severe in

LEAF than in DSF. Our results show that n_2/A_{eff} of LEAF is ~1.7 times smaller than DSF wich is in very good agreement with the ratio between measured effective areas.

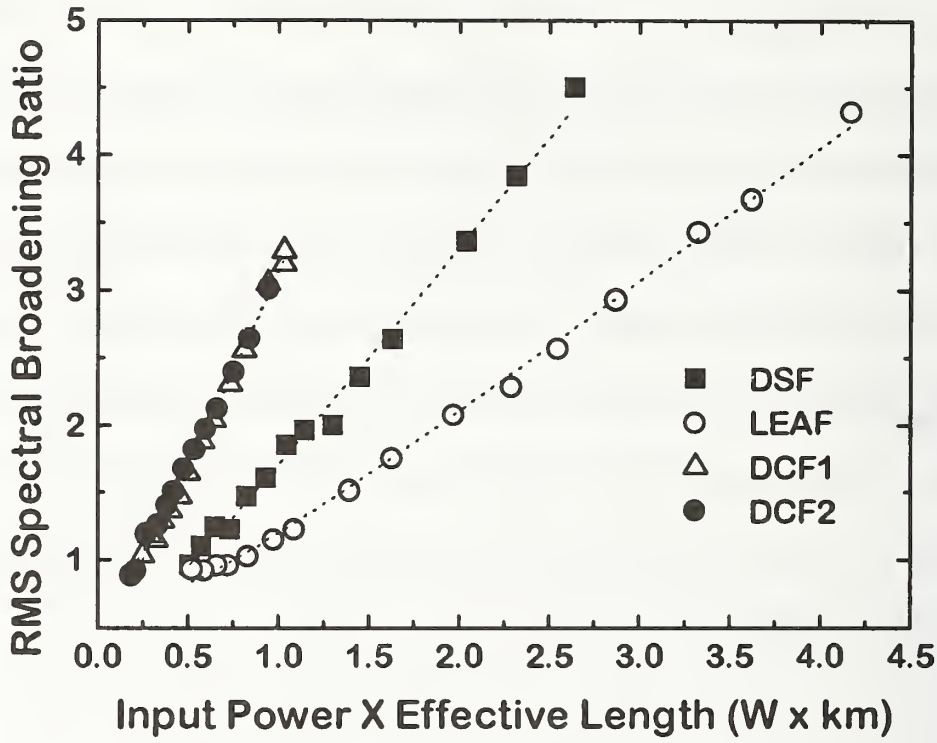

Figure 2. Ratio of output and input RMS spectral widths as a function of peak input power times the effective length for a dispersion-shifted fiber (DSF), large effective area dispersion-shifted fiber (LEAF) and dispersion compensating fibers (DCF). Dashed lines are a fitting to Eq. 1.

Fiber Type	$A_{eff}/(A_{eff})^{DSF}$	$(n_2/A_{eff})^{DSF}/(n_2/A_{eff})$
DCF1	0.56	0.53
DCF2	0.54	0.53
LEAF	1.72	1.70

Table 2. Measured values of A_{eff} and n_2/A_{eff} normalized to DSF values.

The n_2/A_{eff} of DCFs is expected to be higher than in DSFs because of the smaller A_{eff} and higher GeO_2 content. It was measured to be ~3.0 times higher than in DSF in Ref. [7] and between 2.4 - 3.5 times higher in Ref. [6]. Our measurements of two different

DCFs, however, show an increase of only 1.9 times in the n_2/A_{eff}, which agrees very well with the decrease of ~1.8 in the A_{eff} . This indicates that, unlike the DCFs used in Ref. [6] and [7], our DCFs have an n_2 comparable to DSFs.

REFERENCES:

[1] L. Pringent and J.P. Hamaide, IEEE Photon. Technol. Lett., vol. 5, pp. 1092 (1993).

[2] R.H. Stolen, K.S. Kim, S.E. Evangelides, G.T. Harvey, W.A. Reed, OFC'95, Paper FD-1, San Diego, CA.

[3] Y. Namihira, A. Miyata and N. Tanahashi, Electron. Lett. vol. 30, pp. 1171 (1994).

[4] M. Artiglia, E. Ciaramella and B. Sordo, Electron. Lett. vol. 31, p. 1012 (1995).

[5] S. Chernikov and J.R. Taylor, OFC'96, paper ThS5.

[6] A. Boskovic et al., CLEO'96, paper CMA7.

[7] T. Kato, Y. Suetsugu, M. Takagi, E. Sasaoka, and M. Nishimura, Opt. Lett. vol.20, pp. 988 (1995).

[8] A. Fellegara et al., OFC'95, paper ThS4.

[9] E.L. Buckland and R.W. Boyd, OFC'96, paper ThF2.

[10] Y. Liu, V.L. da Silva, A.J. Antos, V.A. Bhagavatula, D.Q. Chowdhury, and M.A. Newhouse, IOOC'95, Paper PD-19, Hong Kong.

[11] G.P. Agrawal, "Nonlinear fiber optics", Academic Press, 1989.

Polarization independent nonlinear refractive index measurement in optical fiber

Andrea Melloni and Mario Martinelli
Politecnico di Milano, Dip. Elettronica e Informazione
Andrea Del Core and Andrea Fellegara
ITALTEL, BUTR, Castelletto di Settimo Milanese

Abstract

Two techniques for the polarization independent measurement of the nonlinear refractive index n_2 of optical fibers for telecommunications are presented. They allow accurate measurements of n_2 and the evaluation of the nonlinear response of any optical fiber employed in transmission optical systems.

Introduction

Optical fiber nonlinearities can represent a serious drawback in optically amplified transmission systems. The availability of a simple and accurate method for the measurement of the nonlinear refractive index n_2 (or n_2/A_{eff}) is a really important issue, especially since when optical fiber providers offer a large varieties of special fibers with particular nonlinear characteristics, such as doped fiber or fibers with very large or very small effective area. The value of n_2 can be recovered by various methods: Self-Phase Modulation (SPM) [1], Cross-Phase Modulation (XPM) [2, 3] and Modulation Instability (MI) [4]. Methods based on SPM determine the distortion of a very short optical pulse after the propagation in the fiber and those based on XPM measure the phase shift induced on a weak probe beam by an intense optical beam (the pump). Unfortunately all these methods are polarization dependent and the recovered value of n_2 contains an uncertainty due to the State of Polarization (SOP) evolution of the optical propagating beams. As a result, it is rather difficult to evaluate accurately n_2, especially in telecommunication fibers where the polarization is not preserved.

In this contribution two simple and effective XPM based techniques that are intrinsically insensitive to the relationship between the probe and pump SOP's are presented. The proposed techniques allow to evaluate the Kerr coefficient, and hence to recover n_2, in common fiber for telecommunications with an high insensitivity to polarization perturbations. The first one is based on the use of an Ortho Conjugated Mirror [5], is very simple, accurate and is useful for low frequencies measurements. The second one uses two orthogonally polarized uncoherent pumps and can investigate the nonlinear frequency behaviour of the fiber. Both techniques, moreover, allow to determine the impact of the Kerr nonlinearity in a general section of a digital transmission optical line.

The insensibility to polarization

In a XPM based technique, an intense pump optical field induce, propagating in the optical fiber, a non linear phase shift on the CW probe. By measuring the peak value $\Delta\Phi$ of the induced phase shift, n_2 is recovered by the relation:

$$\Delta\Phi = 2\frac{2\pi n_2}{\lambda A_{eff}} P_p L_{eff} b \tag{1}$$

where P_p is the pump peak power, L_{eff} the effective length of the fiber, A_{eff} the effective core area, λ the probe wavelength and the probe SPM contribution has been neglected. b is the polarization parameter and assume an unpredictable value between one third and one, depending on the relative SOP between probe and pump.

Let's now suppose to have two equal intensity square modulated incorrelated pumps, P_1 and P_2, propagating in the Fiber Under Test (FUT) and keeping orthogonal SOP's *in each fiber section.* The proof that follows apply also in the case of two orthogonal probes and a single pump [6]. The two pumps induce a phase shift $\Delta\Phi_1$ and $\Delta\Phi_2$ on the probe, with polarization parameters b_1 and b_2. The values of b_1 and b_2 are unknown, as well as the evolution of the polarization states along the fiber, but their sum is constant and equal to 4/3 whatever it is the input pump and probe SOP and the birefringence of the fibers. The detected phase shift, $\Delta\Phi_1 + \Delta\Phi_2$, is therefore polarization independent as well as the recovered n_2.

This can be shown by considering the Poincarè sphere shown in Fig. 1, where fields SOP's in a generic section of the fiber are shown. b_1 is the weighted sum of the projection of the pump SOP $|\text{Pump}_1\rangle$ over the probe SOP $|\text{Probe}\rangle$ and its orthogonal SOP $|\text{OppositeProbe}\rangle$. The same apply to the second pump. b_1 and b_2 are given by

$$b_1 = 1\ \cos^2(\frac{\alpha}{2}) + \frac{1}{3}\sin^2(\frac{\alpha}{2}) \qquad \text{and} \qquad b_2 = 1\ \cos^2(\frac{\beta}{2}) + \frac{1}{3}\sin^2(\frac{\beta}{2}), \tag{2}$$

and because $\alpha + \beta = \pi$, $b_1 + b_2 = 4/3$.

In the following section two techniques that realize this condition are presented, together with some experimental results.

Experimental setups and results

The first scheme that permits a polarization independent measurement of n_2 is shown in Fig. 2. The scheme is based on the Ortho Conjugated Mirror (OCM), a device that time reverses the propagation from the point of view of the polarization state [5]. The FUT is inserted in one arm of the Michelson interferometer, fed by the probe source. The square wave intensity modulated pump beam, powered by an optical amplifier, propagate only in the FUT. The Kerr action occurs therefore twice: first in the counterpropagating modality and then, after the reflection on the OCM, also in the copropagating modality. The OCM, force the SOP of the copropagating probe to be orthogonal to the conterpropagating one *in each section* of the fiber and hence the phase shift peak value is polarization independent [7, 8]. The proof is equivalent to that developed in the previous section [6]. The upper frequency limit of the pump signal modulation is $v/4L$, v being the group velocity and L

the fiber length, in order to have also a couterpropagating contribution in the form given by eq. (1).

If a normal mirror is used instead of an OCM, |Probe⟩ is not anywhere orthogonal to |OppositeProbe⟩ and the term $(b_1 + b_2)$ remains undetermined. Fig. 3 reports values of n_2/A_{eff} recovered by measuring the induced phase shift (1) for 10 random input pump SOP of a DS fiber at 100KHz. The achieved accuracy is better than 1%. As a comparison, results obtained with a normal mirror are also reported, showing a dispersion of about 10%.

The second technique proposed can be used to investigate also the nonlinear frequency response of a fiber. As in the previous technique, the phase shift induced by the pump on the probe optical beam is measured by an interferometric technique. The insensitiveness to the polarization is achieved by using as a pump two incoherent and orthogonally polarized optical beams P_1 and P_2. The optical circuit is shown in Fig. 4. The pump signal is splitted by a coupler and then recombined by a polarizing beam combiner (PBC). One of the two beams is delayed by some coherence time. The delay line is then adjusted to obtain a square wave modulated optical pump. The two polarization controllers ($PC_{1,2}$) permit to match the right polarization of the PBC and maximize the pump power. The pump signal is therefore composed by two incoherent optical beam with the same intensity and orthogonally polarized.

Both pumps copropagate with the probe in the FUT costituting one arm of a Mach-Zehnder interferometer, inducing a non linear phase shift that modify the probe coherent function [9]. Hence, the intensity (proportional to the phase shift) detected by a balanced interferometer is the sum of only the two contributions given by the two orthogonal pumps while the cross contribute is negligible. The detected intensity is polarization independent because the two pumps keep orthogonal SOP in any section of the fiber. The contribution of the polarization mode dispersion is negligible because of the small length of the FUT.

At low frequencies (up to 100KHz) both techniques give the same value of n_2, within the measurements errors. Measurements show a polarization dependence lower than 1% also for the second technique. Several sections of SMR and DS fibers have been measured with the pump powered by an ITALTEL AF18-D optical amplifier. FUT length between 200 and 600 meters have been considered. At 1550 nm the low frequency recovered value of n_2/A_{eff} is $2.8 \cdot 10^{-10} W^{-1}$ for SMR fibers and between 4.8 and $6.8 \cdot 10^{-10} W^{-1}$ for DS fibers, depending on fibers.

References

[1] K. S. Kim, R. H. Stolen, W. A. Red and K. W. Quoi, Optics Letter 19, Feb. 1994

[2] A. Wada, T. O. Tsun and R. Yamauchi, Proc. ECOC'93, paper MoB1.2, Berlin 1993

[3] M. Monerie and Y. Durteste, Electronic Lett. 23, p. 961-963 (1987)

[4] M. Artiglia, B. Ciaramella, B. Sordo, Electronic Lett. 31, p. 1012-1013 (1995).

[5] M. Martinelli, Journal of Modern Optics, 1992, vol. 39, p. 451-455

[6] L. Amato, A. Fellegara, P. Sacchetto, P. Boffi, A. Melloni and M. Martinelli, Optics Letter 21, April 1996

[7] P. Boffi, A. Fellegara and M. Martinelli, Optics Communications, 1996

[8] A. Fellegara, L. Amato, P. Sacchetto, P. Boffi, A. Melloni e M. Martinelli, Proc. OFC '96, paper ThS4, 288 (1996).

[9] J. T. Manassah, Optics Letter 16, November 1991

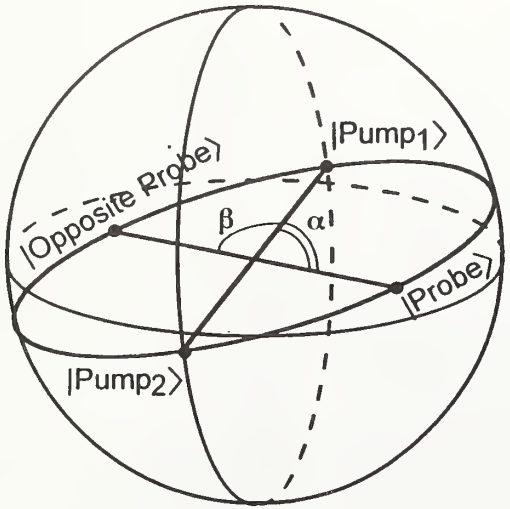

Fig. 1 - Representation on the poincarè sphere of the fields SOP's in a generic section of the fiber

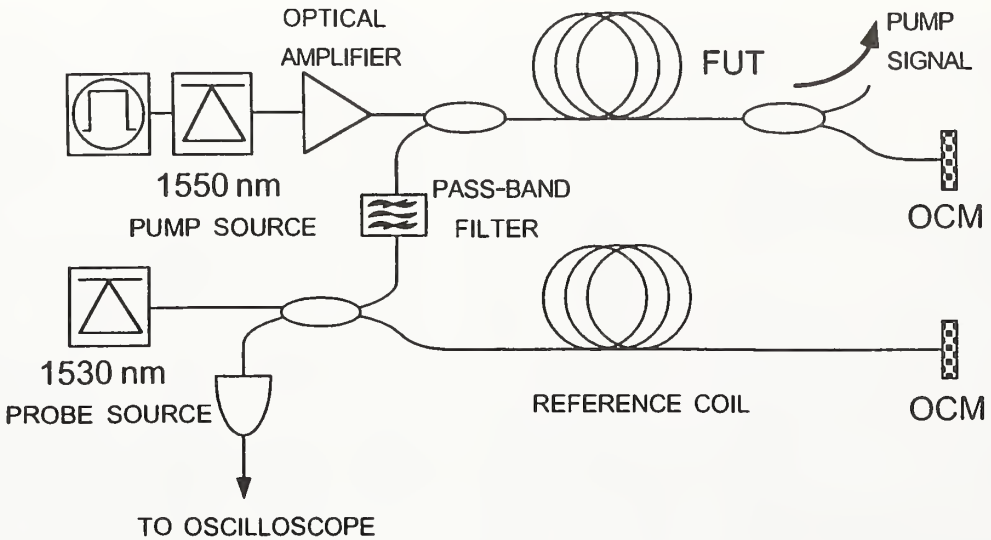

Fig. 2 - Experimental setup of the technique that uses an Ortho Conjugated Mirror

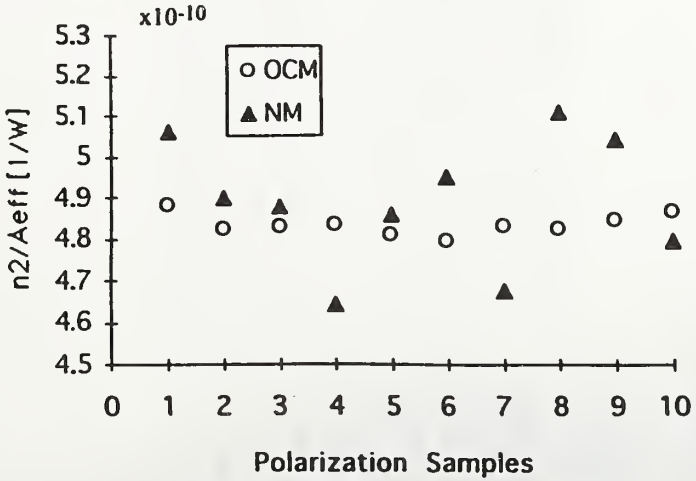

Fig. 3 - n_2/A_{eff} dispersion measured with a normal mirror and an OCM for 10 random input pump SOP

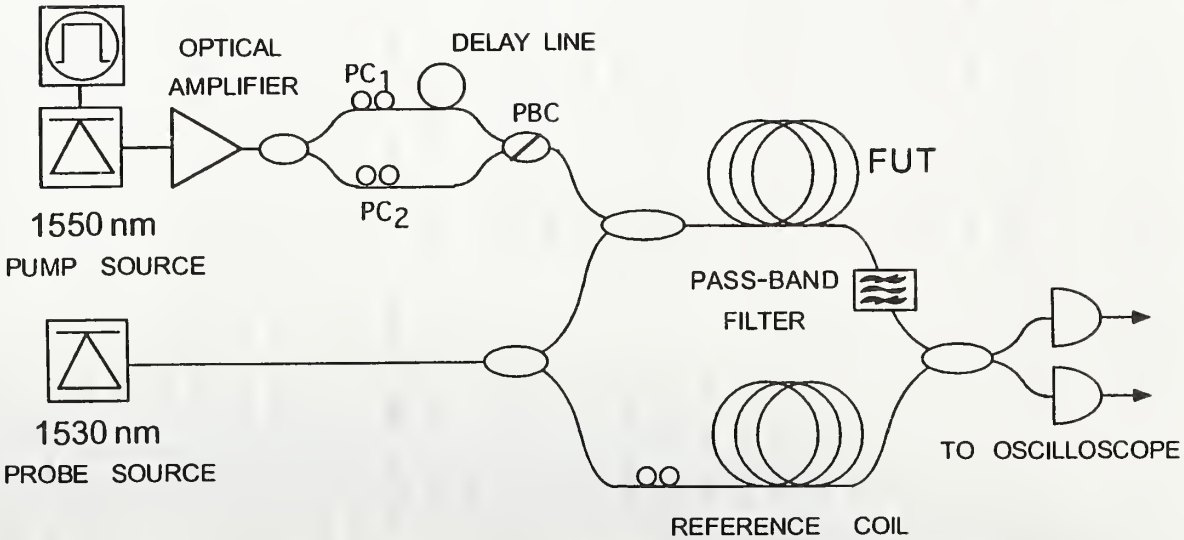

Fig. 4 - Experimental setup of the technique that uses two uncoherent orthogonal pumps

Interferometric Determination of the Nonlinear Refractive Index n_2 of Optical Fibers

F.Wittl*, J.Vobian**, G.Herchenröder** and W. Dultz**
* Techn. Univ. Darmstadt, Institut für Angewandte Physik
** Deutsche Telekom, Technologiezentrum Darmstadt

Abstract

The nonlinear refraction indices n_2 of several optical fibers were measured with a Sagnac interferometer at a wavelength of 1053 nm (NdYLF-laser). The n_2-values of the different fibers were determined to be between 2.0 and 3.3 times 10^{-20} m^2/W respectively.

Introduction

For high pulse power applications of optical fibers (e.g. soliton transmission) the knowledge of the nonlinear refractive index is of essential importance. Therefore, the participants of a European COST-Action (COST 241, Characterization of Advanced Fibers for the New Photonic Network) decided to compare several measurement techniques in order to get the most reliable n_2-values. What we present here, is our contribution to that COST-Action.

For a pulse with the power $P(t)$ propagating in a medium, the refractive index (n) with nonlinear correction is commonly described by [e.g. Sto72, Agr89]

$$n = n_0 + n_2 \cdot \frac{P(t)}{A_{eff}} \qquad (1)$$

A_{eff} is the effective core area of the fundamental fiber mode with the field distribution $E(r,\varphi)$ and is determined by [e.g. Agr89]

$$A_{eff} = \frac{\left[\iint E^2(r,\varphi) r dr d\varphi\right]^2}{\iint E^4(r,\varphi) r dr d\varphi} \qquad (2)$$

The nonlinear prolongation of the optical path length for a pulse with a central wavelength λ and a peak pulse power P can be represented by an induced phase shift [e.g. Mei95a]

$$\Phi_{nl} = \frac{2\pi}{\lambda} \cdot L_{eff} \cdot n_2 \cdot \frac{1}{A_{eff}} \cdot m \cdot P \qquad (3)$$

Here, instead of the fiber length L an effective length L_{eff} has to be used, due to absorption losses with the absorption coefficient α. This effective length is defined as:

$$L_{eff} = \frac{1 - \exp(-\alpha \cdot L)}{\alpha} \qquad (4)$$

The factor m in (3) is a polarisation parameter. For linearly polarised light $m = 1$ by definition of the nonlinear refractive index. For other kinds of polarisation states there are still some discussions about the value of m. If sufficiently long fibers are used (some hundred meters), polarisation can be regarded as completely "scrambled" and therefore a value of $m = 8/9$ is now commonly accepted [Eva92],[Cher96].

Measurement technique and experimental setup

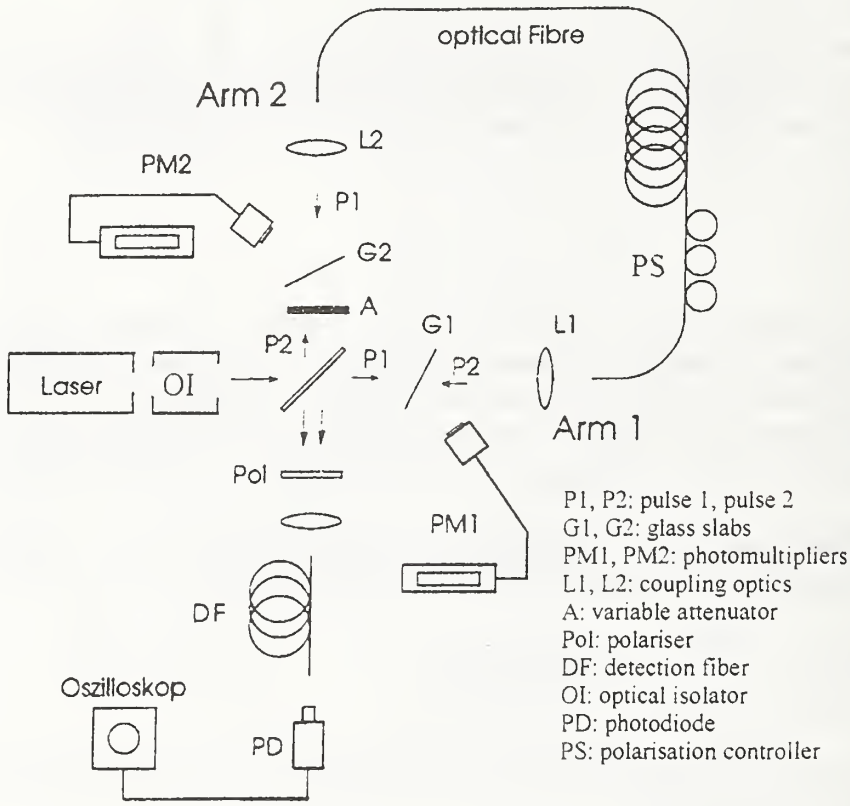

Fig.1) Experimental setup

Our measurement technique uses the principle of the Sagnac interferometer (Fig.1). A similar setup used by Artiglia et al. and which was also part of the COST 241 project has been recently published [Art96]. A laser pulse is split into two equal parts by a 50/50-beam splitter. The two pulses created in this way are counterpropagating through the fiber to be measured. One of the pulses can be attenuated variably before entering the fiber and therefore induces a smaller nonlinear refractive index than the non diminished one, which passes also the attenuator, but after being transmitted through the fiber. Due to (3) the induced phase difference of the two pulses with peak pulse powers P_1 and P_2 is determined by

$$\Delta\Phi_{nl} = \frac{2\pi}{\lambda} \cdot L_{eff} \cdot n_2 \cdot \frac{1}{A_{eff}} \cdot m \cdot |P_1 - P_2| \qquad (5)$$

The parts of the pulses passing the beam splitter in the right direction afterwards, are coupled into a "detection" fiber and due to (5) result in an interference signal detected with a photodiode and an oscilloscope at the end of this fiber. From the measurement of the power differences $|P_1 - P_2|$, necessary to obtain suceeding maxima and minima of the signal, which means phase differences of $\Delta\Phi_{nl} = l \cdot \pi$ (l = 1,2,3...), the effective nonlinearity n_2/A_{eff} can be calculated. After measuring the effective core area A_{eff} with both refracted near field technique and transversal offset method [Vob89], the nonlinear refractive index n_2 can be determined.

An Nd:YLF laser was used as light source. We had average powers of 5W-18W, a repetition rate of 76 Mhz at a wavelength of 1053 nm. The FWHM pulse width of this laser could be reduced down to 30 ps, but for the sake of better visibility of the interference patterns we only used FWHM widths of 50 ps - 150 ps. To avoid pulse disturbing feedback effects from the interferometer to the laser, an optical isolator has to be used.

Results:

Fig. 2 shows some typical measured interference patterns and in Table 1 the determined values of nonlinear refractive index as well as the effective core areas of some measured fibers are listed. Table 2 shows n_2-values of three of our fibers measured by other participants of COST-Action at nearly the same wavelength.

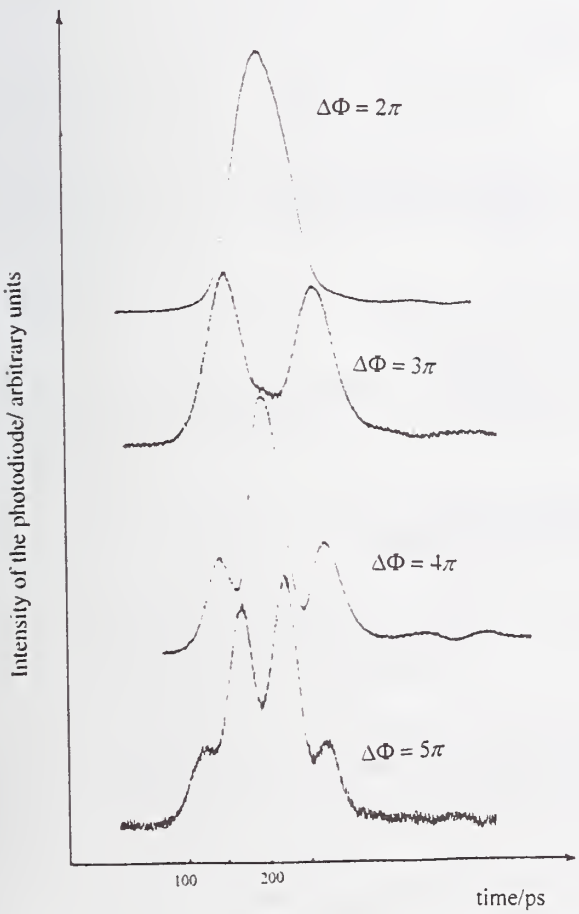

Fig.2) Maxima and minima of interference of a standard single mode fiber due to nonlinear phase shift

$n_2 / 10^{-20} \frac{m^2}{W}$	A_{eff} / μm^2	fiber type
2.1	19.5	Siemens Raman Fiber
2.5	62.3	Siemens Standard SMF
3.1	21.1	DC-fiber A, Jydsk Telekom
3.3	18.5	DC-fiber B, Jydsk Telekom
3.0	72.4	dep. cladding, Philips

Table 1: Experimental results obtained for n_2 values of some fibres

$n_2 / 10^{-20} \frac{m^2}{W}$	$@\lambda / nm$	Fiber type, references
3.0-3.1	1064	DC-fiber A, Jydsk Telekom [CO96], [Mei95]
3.0	1064	DC-fiber B, Jydsk Telekom, [CO96]
2.4	1064	Siemens Standard SMF, [Mei95]

Table 2: Experimental n_2-values obtained for the same fibers by other participants of COST-241 at nearly the same wavelength as our measurements

The experimental results are in good agreement with each other. Also the most drastic deviation (DC-fiber B, Jydsk Telekom) is between our estimated experimentl error of about 10-15%, which is mostly due to the well known difficulties of determining absolute values of intensities. Another source of error is that we supposed to have completely scrambled polarisation, but it is not quite clear whether or not in our measurments (fiber lengths $L \approx 200$ m) this can be regarded as true (m=8/9 or m=1). Further measurements are planned in order to clarify this question.

References:

[Agr89]: Govind P. Agraval: Nonlinear Fiber Optics, Academic Press Inc., San Diego

[Art96]: M. Artiglia, R. Caponi, F. Cisternino, C. Naddeo, D. Roccato Opt. Fib. Techn. 2, 75-79 (1996)

[Cher96] : S.V. Chernikov, OFC96, Techn. Digest, ThS5, 289

[Eva92]: S.G. Evangelides, L.F. Mollenauer, J.P. Gordon, N.S. Bergano: J. Lightwave Technol., Vol.10 (1992), S.28

[Mei95]: J.Meier: Dissertation, in: Fortschr. Ber. VDI-Reihe 8, Nr. 443, VDI-Verlag, Düsseldorf 1995

[Mei95a]: J.Meier: 3rd Optical Fiber Measurment Conference (OFMC95) Lüttich (Belgien) 1995, Proceedings

[Sto78]: R.H.Stolen, C.Lin: Phys. Rev. A, At. Mol. Opt. Phys., Vol. 17(1978), S.1448

[C096]: COST-241 report, S. B. Andreasen, Feb.96

[Vob89]: J. Vobian, G. Herchenröder, EFOC89, Techn. Digest

Inverse method for systematic investigations of linear and nonlinear properties of dispersion-shifted and dispersion-compensating fibers

R. Boness (TU Dresden), S. Unger, J. Kirchhof (IPHT Jena), F. Wittl, J. Vobian (FTZ Darmstadt), K.-F. Klein (FH Giessen-Friedberg), Germany

Abstract

The inverse method allows a defined profile to be calculated making use of prescribed dispersion curves, cutoff wavelength and field radii.

For example, we calculated and verified disperion-compensating fibers (DC fibers) with high compensation ratios (CR) up to 30 with the disadvantage of relatively high attenuation values [1]. In this paper we will present DC fibers with medium CR values and low attenuation values. An interesting new field are dispersion shifted-fibers (DS fibers) with high effective area minimizing nonlinear effects due to low n_2 values.

Theoretical considerations

The effective area A_{eff} is an important parameter in long-haul fiber transmission systems, above all, in the case of DS fibers. It should be large to minimize nonlinear effects. On the other hand, small A_{eff} values of the DC fibers may be advantageous for investigations of nonlinear effects in fibers. In any case, the dopant concentration should be not too high in order to reduce the attenuation of the fibers under test.

We will present an iterative inversion method to optimize the refractive-index profile and radius parameters with respect to prescribed dispersion and the Petermann-II field radius values in the vicinity of 1550 nm. We assume that $A_{eff} = \pi w_f^2$ is a good approximation of the effective area of the fiber [2]. In principle, we can investigate any reasonable refractive-index profile, of course within the frame work of technological limits.

In order to determine the corresponding parameters of these special fibers, we have to solve a so-called inverse problem, which can be done for some prescribed dispersion values at different wavelengths only using multi-dimensional optimization methods [1]. We have to minimize a generalized standard deviation given by

$$F(x) = \sum_{i=1}^{n} b_i (D(\lambda_i, x) - D_i)^2 + b_{n+1}(\lambda_c(x) - \lambda_{c0})^2 + b_{n+2}(w_f(x, \lambda_0) - w_{f0})^2 \qquad (1)$$

with respect to the unknown vector x.

x := vector of relative refraction indices Δ_i $(1 \le i \le m)$ and the fibre radius, thus dim(x) = m+1, in general, $m \le 4$.

$2\Delta_i := \dfrac{n_i^2 - n_c^2}{n_c^2}$ with n_c- refractive index of the outer cladding region in general, 1.4573

D_i := prescribed discrete dispersion values at λ_i within 1530 to 1600 nm ($1 \le i \le n$ with $n \ge \dim(x)$).

λ_{c0}:= prescribed cutoff of the LP_{11}-mode, w_{f0} prescribed PETERMANN-II -radius at λ_0=1550nm,

b_i := some suitable positive weight factors.

In order to minimize the functional Eq.(1), we make use of the Levenberg-Marquardt algorithm [3] (damped Gauss-Newton method). Our programme is based on a very stable and accurate method for dispersion calculations without any numerical differentiation [1] on the basis of the scalar wave equation.

In formula (1) we assume w_{f0} =5.64 μm (corresponding to A_{eff}≈100 μm^2) and obtain the profile, dispersion and field-radii curves presented in in Fig. 1a,b,c. For comparison in standard dispersion-shifted fibers w_f ≈4.3 μm (A_{eff} ≤ 60 μm^2), for special DS fibers A_{eff} values up to 90 μm^2 were reported [4]. Figures 1a to 1c document that triple clad fibers (TC fibers) are an optimal solution of the problem, relatively low dopant concentrations are sufficient, the fiber radii are relatively large which avoids technological problems.

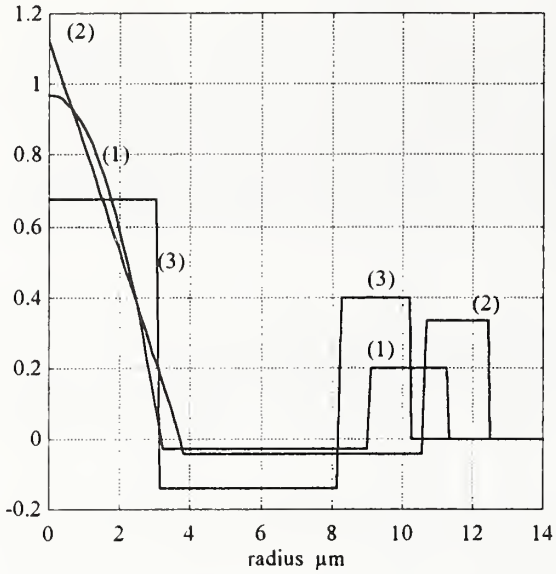

Fig 1.a.: Calculated TC-profiles 2Δ(r) with parabolic (1),linear (2) and constant (3) core refractive index functions

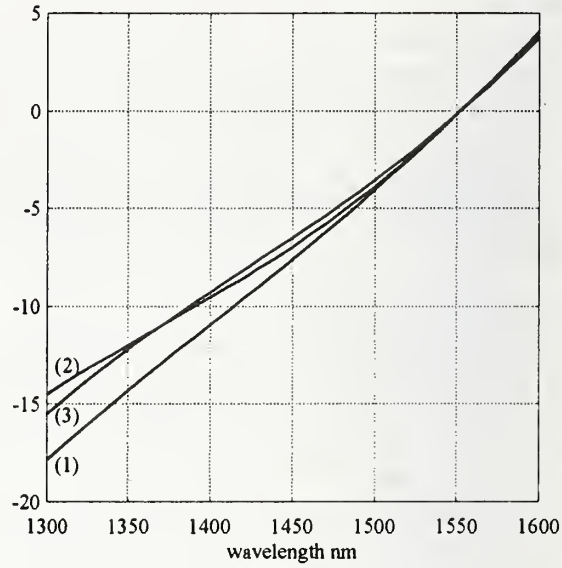

Fig. 1.b: Chromatic dispersion curves for the different profiles (1), (2), (3)

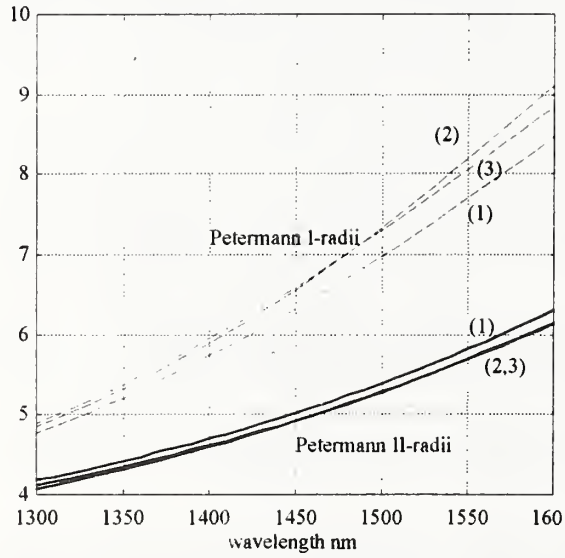

Fig 1.c: Field radii curves for the profiles (1), (2) and (3).

The slope of the dispersion curves at 1550 nm corresponds to that of standard DS fibers. It is possible to prescribe other slope values at 1550 nm. The slope may also be zero. The dispersion and Petermann II field radii curves for the different profiles in the vicinity of 1550 nm do not differ very much. w_{f0} is approximately 5.6 μm, which corresponds to an effective area of about 100 μm^2 . Our second goal was the development of DC fibres with a medium compensation ratio (CR=10) and low attenuation values.
In this case we only can prescribe the dispersion values in the vicinity of 1550 nm but not the Petermann II field radii. Our inverse method presents the profil curves in Fig. 2a.

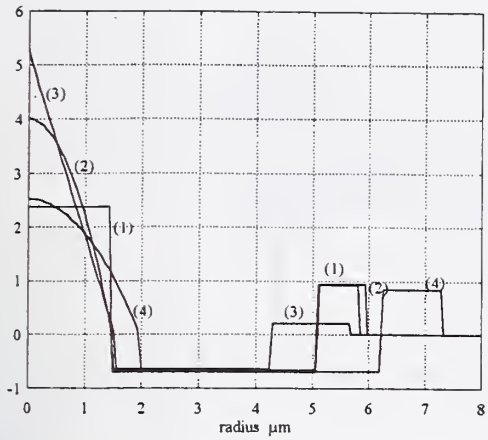

Fig 2.a.: Calculated TC profiles 2Δ(r) with constant (1), parabolic (2,4) and linear (3) core segments

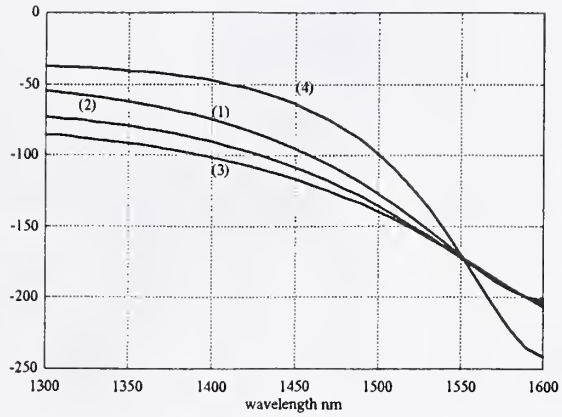

Fig. 2.b: Chromatic dispersion curves for the different profiles (1) to (4)

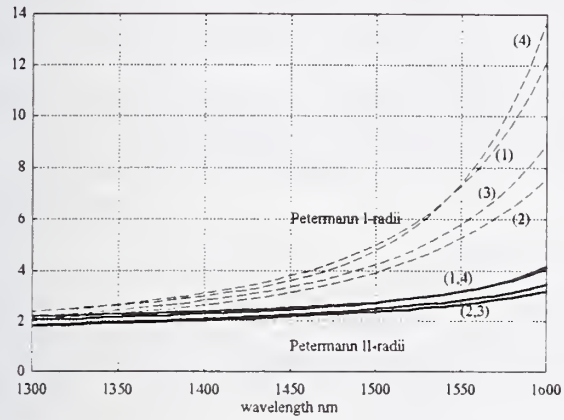

Fig 2.c: Field radii curves for the profiles (1) to (4).

All the profiles (1) to (4) yield CR=10, but only the profiles (1) to (3) result in a second-order dispersion compensation. Fig. 2a shows that the stepwise constant profile results in the lowest 2Δ value. The parabolic profile (4) also results in a low dopant concentration, but we do not obtain a compensation of the slope.
Fig. 2.c shows that the Petermann II field radii are smaller than those of Fig. 1.c. As a consequence, large n_2 values have to be taken into account.

Measuring procedures and practical results

First experiments were undertaken to fabricate and to analyze the features of DC and DS fibers which were fabricated by MCVD. A general problem of the fiber preparation is the realization of a high refractive index in the core together with small fiber-core values, especially in the case of DC fibers. The germanium content of the core is determined rather by diffusion than by the chemistry of incorporation during the deposition because of the strong increase of the diffusion coefficient of germanium with the concentration [1].
Fig. 3.a,b show the TC profiles of the DS and DC fibers measured at the preforms together with the corresponding ESI curves.
The mode-field diameter w_f and consequently the effective area was determined by making use of the transverse offset-method. From the obtained autocorrelation MFD w_f was calculated using the formula of Calzavara, Coppa, Di Vita [5].
The chromatic dispersion measurements were performed with the aid of a raman fiber laser with a mode-locked Nd:YLF laser used as a pump source and a Mach-Zehnder interferometer for measurements on short fiber pieces [1].
The measurement of the nonlinear Kerr coefficient n_2 was performed making use of the Sagnac interferometer principle [6]. Thereby a pulse of a mode-locked Nd:YLF laser is split into two parts which are passing through the fiber in opposite directions and have different power values. For detection the two pulse parts are superimposed again. From the interference pattern the nonlinear phase shift and consequently the nonlinear refractive index n_2 can be calculated.

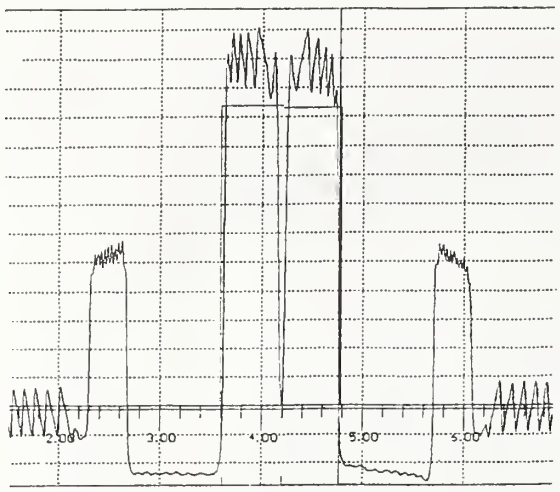

Fig. 3a TC profile of the DS fiber

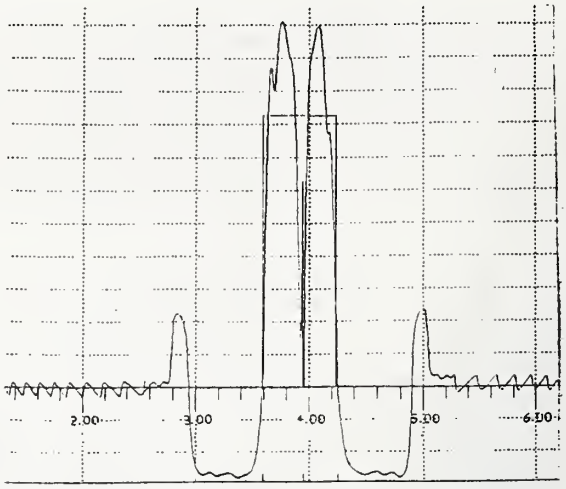

Fig. 3b TC profile of the DC fiber

The measured effective area of the DS fiber yields 74 μm^2. Values up to 100 μm^2 can be verified. . The measured effective area of the DC fiber is 23.8 μm^2, in good agreement with the theoretical value (Fig. 2.c).

The Kerr coefficient of the DS fiber was determined at $\approx 2.5*10^{-20}$ m^2W^{-1}. n_2 of the DC fiber was not measurable due to the stimulated Raman scattering effect.In any case, the wavelength was 1550 nm.

Figs. 4 and 5 present the measured dispersion curves of the DS fiber and the DC fiber, respectively.

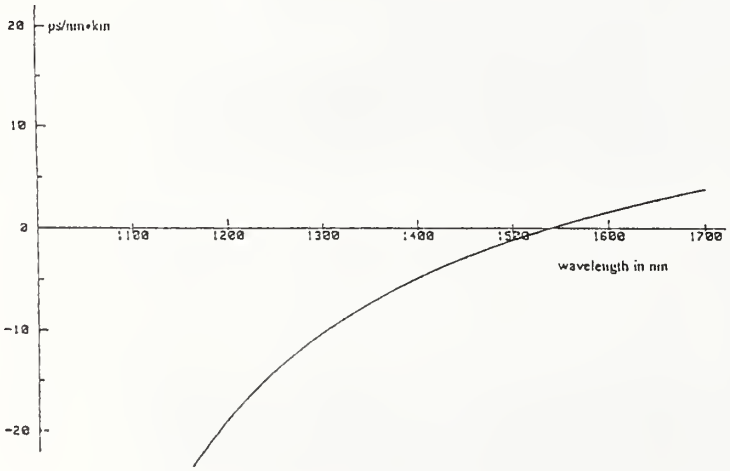

Fig. 4 Dispersion curve of the DS fiber

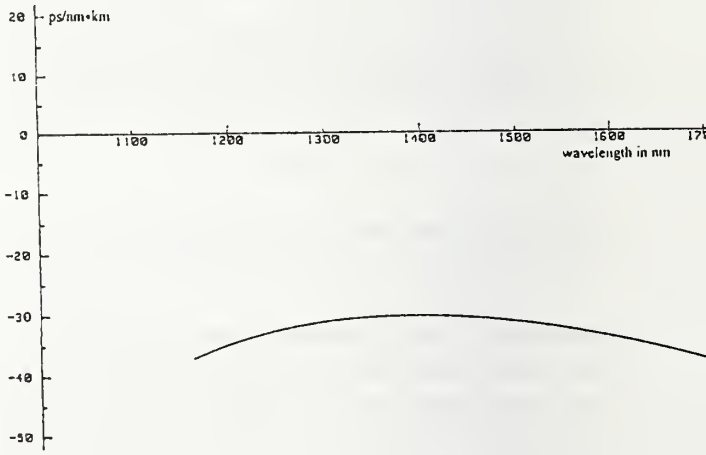

Fig. 5 Dispersion curve of the DC fiber

References

[1] R. Boneß, W. Nowak, J. Vobian, S. Unger, J. Kirchhof: Tailoring of dispersion-compensation fibres with high compensation ratios up to 30. Pure Appl. Opt. 5 (1995), p. 333

[2] P. Nouchi, P. Sansonetti, J. von Wirth, B. Perrin, Alcatel Alsthom Recherche (Marcoussis, F.): Large Effective Area Dispersion Shifted Fibre for Long Haul and High Bit-Rate Transmission. EFOC&N (Brighton), June 1995, pp. 101-103

[3] J. M.Ortega, C.Rheinboldt.: Iterative Solution of nonlinear Equations in several Variables. New York, Academic Press 1970

[4] Y. Liu, A. Joe Antos, M. A. Newhouse: Large effective area dispersion-shifted fibers with dual-ring index profiles. OFC '96 Technical Digest, Section WK 15, pp.165-166

[5] J. Vobian, G. Herchenröder, E. Unterseher: Comparison of mode-field diameters of normal and advanced SM- fibers measured with the transverse offset-method with calculations based on refractive index measurements. EFOC/LAN 89 (Amsterdam), June 1989, pp. 232

[6] F. Wittl, J. Vobian, G. Herchenröder, W. Dultz, T. Tschudi: Interferometrische Bestimmung des nichtlinearen Brechungsindex n_2 optischer Fasern. 97. Jahrestagung der DGaO, Mai 1996, Neuchatel/Schweiz

Effective Area Measurement Comparison Between Direct Far Field Scan and Variable Aperture Method in the Far Field

Michael J. Hackert and M. Ajaaz Zainul
Corning, Inc.
Corning, New York 14831

Summary

A key parameter in determining the impact of non-linearities such as self phase modulation (SPM) and four wave mixing (FWM) in high speed, optically amplified systems is the effective area (A_{eff}) of the fiber. This paper describes modeling and experimental results for measuring A_{eff} using direct far field scanning and the variable aperture method in the far field (VAMFF). The modeling and experimental results confirm that both measurement methods give equivalent results. However, far field data (by either method) must be collected to at least 0.4 numerical aperture (NA), but preferably 0.5 NA or larger to minimize the error resulting from truncation of the data collection. The impact of this truncation is evaluated in this work.

Introduction

As the state-of-the-art in fiber optic systems has pushed to faster speeds and longer lengths, the impact of non-linear effects such as self phase modulation (SPM) and four wave mixing (FWM) has increased in importance. Fortunately, these effects can be effectively modeled using the non-linear coefficient n_2/A_{eff} (non-linear refractive index / effective area).[1] Variation in the effect of non-linearities from fiber to fiber is controlled by effective area (A_{eff}). Thus, A_{eff} is a key parameter to be monitored.

A_{eff} can be measured by two techniques[2] - direct measurement of the far field pattern and the variable aperture method in the far field (VAMFF). These are the same techniques used for measuring mode field diameter (MFD). In this paper, a comparison is made between the two methods for measuring A_{eff}. The comparison has two parts. First, the problem is approached analytically using modeling. The percent disagreement between the two methods is predicted. The second part summarizes the experimental results. Also, the impact of the maximum NA of the VAMFF system is evaluated. Similar comparisons for MFD were also made to confirm the analysis methods and experimental set ups.

Modeling Results

The simulations started with direct far field scan data. Power as a function of angle was gathered as described in EIA/TIA-455-164A[2]. An example of 3 types of fiber profiles were included in the analysis - standard single-mode fiber (Corning's SMF 28™), standard dispersion shifted (DS) single-mode fiber (Corning's SMF/DS™), and large effective area dispersion shifted fiber. Readings were obtained up to a maximum available numerical aperture (NA) of 0.3338 for this particular far field scanner.

A_{eff} and MFD were then found using the direct far field scan formulas (1), (2) and (3) given below:

$$MFD = 2w_0 = \frac{\sqrt{2}\lambda}{\pi}\left[\frac{\int_0^\infty P_m(\theta)\sin\theta\cos\theta d\theta}{\int_0^\infty P_m(\theta)\sin^3\theta\cos\theta d\theta}\right]^{\frac{1}{2}} \quad (1)$$

$$A_{eff} = 2\pi \frac{\left[\int_0^\infty E(r)^2 r\,dr\right]^2}{\int_0^\infty E(r)^4 r\,dr} \tag{2}$$

where

$$E(r) = E_0 \int_0^\infty [P_m(\theta)]^{1/2} J_0(r\beta \sin\theta) \sin 2\theta\, d\theta \tag{3}$$

P_m is the far field power distribution,
θ is the subtended half angle in the far field ,
r is the radial distance from the fiber's core ,
$\beta = 2\pi/\lambda$,
J_0 is the zeroeth order Bessel function of the first kind, and
E (r) is the near field's electric field.

The next step was to select a definite set of values for the apertures on an aperture wheel for a VAMFF system. The corresponding powers for the variable aperture technique were then simulated using the same power versus angle data. MFD was then determined from the simulated VAMFF data using formulas (5) and (6) utilizing a trapezoidal fit.

MFD for the VAMFF is given by:

$$MFD = 2w_0 = \frac{\sqrt{2}\lambda}{\pi}\left[\int_0^\pi a(\theta)\sin 2\theta d\theta\right]^{-1/2} \tag{5}$$

where

$$a(\theta) = 1 - \left(\frac{P(\theta)}{P_{max}}\right) \tag{6}$$

$P(\theta)$ is the power transmitted through each aperture,
P_{max} is the power transmitted through the largest aperture, and
θ is the subtended half angle of each aperture from the fiber end.

Use of formulas (7) and (8) below together with formula (2) above allowed A_{eff} to be determined from the modeled VAMFF data.

$$P_{FF} = \frac{1}{\rho}\frac{d(P_{VAMFF})}{d\rho} \tag{7}$$

$$E(r) = E_0 \int_0^\infty [P_{FF}]^{1/2} J_0(r\bar{\rho}) d\rho^2 \tag{8}$$

where

P_{VAMFF} is the power through each aperture on the VAMFF,
$\rho = (2\pi/\lambda)\sin(\theta)$,
P_{FF} is the equivalent average direct far field power,
J_0 is the zeroeth order Bessel function of the first kind, and
r is the radial distance from the fiber's core.

The aperture wheel in Table 1 with a maximum numerical aperture of 0.3329 was selected for the VAMFF system. Table 2 summarizes the subsequent results of the modeling. The results indicate there is good correlation between the two systems for measuring A_{eff} and MFD. The largest disagreement was on DS and Large A_{eff} DS fibers. This is likely attributable to the limitation set by using a maximum numerical aperture of 0.3329. If the maximum numerical aperture is increased, the predicted differences between the direct far field measurement and VAMFF on DS fibers should reduce quite markedly.

Test Results

In order to empirically confirm the conclusions from the modeling work, a direct far field scanner was set up according to FOTP 164[2]. It was designed to have a maximum scan of greater than 0.6 NA and a dynamic range of greater than 55 dB. Tests confirmed that its angular accuracy was better than ±0.0005 radian over its full scan angle and that its detector was linear to approximately 5% over its dynamic range.

The experiment consisted of measuring a sample of 9 fibers including standard single-mode fiber, standard dispersion shifted (DS) single-mode fiber, and large effective area dispersion shifted fiber. The fibers were chosen to span a wide range of A_{eff} values. The samples were measured on both the direct far field scanner and the VAMFF measurement system at both 1310 and 1550 nm. The maximum angle for the far field scans was 0.4 NA for the standard single-mode fiber and 0.6 for the other fibers. The fibers were measured 3 times each and the data used to calculate both MFD and A_{eff}. The MFD values agreed within approximately 0.05 μm (< 1%) confirming the accuracy of the two measurement systems. The average A_{eff} values are given in Table 3. The average bias for the 9 samples is also given (-0.28 and -1.81 μm^2 at 1310 and 1550 nm, respectively). These results are consistent with the results from the modeling and show that both measurement methods have equivalent ability to measure A_{eff}.

The last evaluation performed was to determine the impact of restricting the NA used in the calculation. The impact is shown in Figures 1 and 2 for A_{eff} and MFD, respectively. The relative difference in each parameter compared to the value at 0.6 NA is plotted versus the maximum NA of the calculation. It is evident from the analysis that the impact is relatively negligible as long as the NA is greater than 0.4. Of course, an NA of 0.5 or 0.6 is more desirable.

Conclusions

A_{eff} is a critical parameter in determining the non-linear performance of high speed, amplified fiber optic systems. Both mathematical modeling and empirical test data have shown that both the direct far field scan data and the variable aperture method in the far field (VAMFF) methods of measuring A_{eff} give equivalent results as long as the data included in the analysis includes sufficient angular extent. A minimum of 0.4 NA is required, but 0.5 NA or greater is desirable.

References

1. "Comparison of Non-linear Coefficient of Optical Fibers at 1550 nm," Valeria L. da Silva, et. al., ThA4, OFC 1996.

2. EIA/TIA-455-164A "Single-mode Fiber, Measurement of Mode Field Diameter by Far Field Scanning," EIA/TIA-455-167A Mode Field Diameter Method in the Far Field," draft TIA/EIA-455-132 "Measurement of the Effective Area of Single-mode Fiber."

0.0139	0.0218	0.0264	0.0350	0.0433
0.0494	0.0641	0.0785	0.0930	0.1069
0.1211	0.1364	0.1521	0.1619	0.1770
0.1921	0.2266	0.2552	0.2928	0.3329

Table 1 - The values of the numerical apertures used on the aperture wheel on the VAMFF system that produced the modeling results in Table 2.

	A_{eff} (μm^2)			MFD (μm)		
	Direct Far Field	VAMFF	Percent Difference	Direct Far Field	VAMFF	Percent Difference
Dispersion Shifted Fiber	44.00	45.02	2.32	7.693	7.859	2.17
Large A_{eff} DS	82.64	84.29	2	10.07	10.25	1.8
Standard SMF	74.45	74.65	0.27	10.064	10.229	1.6

Table 2 - 1550 nm modeling results using the VAMFF system aperture wheel in Table 1.

A_{eff}	AVERAGE VAMFF		AVERAGE Direct FF		Delta (μm^2)		Delta (Percent)	
FIBER ID	1310 nm	1550 nm	1310 nm	1550 nm	1310 nm	1550 nm	1310 nm	1550 nm
DS #1	28.83	43.12	28.82	43.53	0.01	-0.40	0.0%	-0.9%
DS #2	32.27	51.16	32.29	51.31	-0.02	-0.16	-0.1%	-0.3%
Large A_{eff} DS 1	47.30	84.14	47.27	85.37	0.04	-1.24	0.1%	-1.4%
Large A_{eff} DS 2	34.39	59.46	34.56	61.68	-0.17	-2.22	-0.5%	-3.6%
Large A_{eff} DS 3	44.70	68.91	37.97	72.24	6.72	-3.33	17.7%	-4.6%
Std SMF #1	63.52	78.87	65.55	81.54	-2.03	-2.67	-3.1%	-3.3%
Std SMF #2	64.65	81.11	66.96	83.25	-2.31	-2.14	-3.4%	-2.6%
Std SMF #3	66.34	83.26	68.93	85.22	-2.59	-1.97	-3.8%	-2.3%
Std SMF #4	66.52	83.59	68.68	85.76	-2.16	-2.17	-3.1%	-2.5%
				Average Delta	-0.28	-1.81	0.4%	-2.4%

Table 3 - A_{eff} comparison between Direct Far Field (FF) and VAMFF.

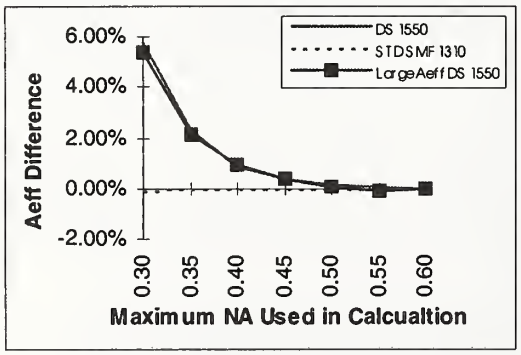

Fig. 1 Maximum NA's impact on A_{eff} bias between direct far field and VAMFF

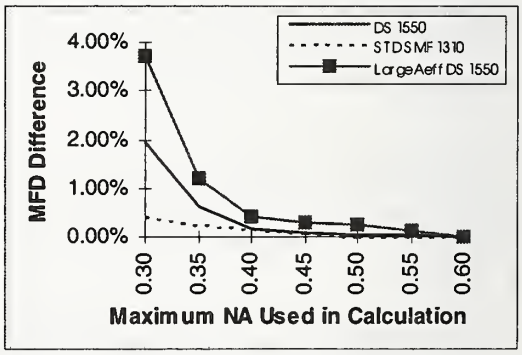

Fig. 2 Maximum NA's impact on MFD bias between direct far field and VAMFF

Characterizing Components for High Speed Data Interconnects

David Smith
Honeywell, Micro Switch
Richardson, Texas , USA
dsmith@micro.honeywell.com

Introduction

The rapidly growing use of optical fiber in high speed LANs and data interconnects has placed new demands on technologies required to support them. Although fiber was employed in 10 Mb/s Ethernet links, it was not used near the limits of its performance capabilities. Even in 100MB/s FDDI, where the sources were typically 1300nm LEDs, the fiber was not really the component that limited link performance.

At data rates around 0.5 GB/s, 1300 nm LEDs still provide acceptable performance, although the combination of slow edge speeds, low coupled power and large spectral width placed these components close to the limits of their performance. At data rates beyond ATM 622 MB/s ,there is no feasible alternative to using a semiconductor laser and in fact, many of the standards permit lower cost 850 nm lasers and LEDs to be used at data rates lower than 1 GB/s (e.g. Fiber Channel 531 MB/s, 265 MB/s and ATM 155 MB/s). However, even lasers do not solve all problems, and at rates above 1 GB/s, the modal bandwidth of multimode fiber begins to limit the transmission distances even at 1300nm.

For cost reasons, AlGaAs CD lasers have generally been employed at speeds up to 1 GB/s, but a new type of laser, the Vertical Cavity Surface Emitting Laser (VCSEL) is showing great promise as the source of the future because it has the potential of meeting all the system requirements and simultaneously being low cost, high speed, low coherence and can be manufactured as an array for parallel optical buses. It is anticipated that VCSELs may eventually replace other types of sources. Although there is much published in the literature concerning VCSELs, little has been published about the characteristics and performance of these devices in typical data communication links, where their first use as commercial sources is already emerging. This paper will address some of the issues surrounding the characterization of optical sources, in particular VCSELs, for high speed data communications.

Characterization of VCSEL sources.

VCSEL Structure

The VCSEL structure described in this paper is a high reliability, multimode, gain guided device with proton bombarded carrier confinement implants as described in [1,2]. The device, intended for commercial LAN use, has an implant inner diameter of 20 microns and an aperture of 15 microns. This provides the best balance between modulation rate, threshold current , series resistance and spectral width. However, apertures up to 30 microns are also employed. All these devices are designed to be single longitudinal mode but multi-transverse mode. The simultaneous lasing in multiple transverse modes ensures low source coherence, greatly minimizing interference effects like modal noise compared with CD lasers. [3]

Modal Noise.

Modal noise [4] occurs when a coherent source generates time-varying, modal interference patterns (speckle) in a multimode fiber and these speckles encounter a mode selective loss such as an offset lossy connector joint. The ensuing degradation of the optical signal-to-noise ratio can generate error floors if the source has adequate coherence, and the loss is large enough. Since these amplitude fluctuations can have a large spectral component at very low frequencies (drift) in a real data link, the statistics are effectively non-stationary, making their effect difficult to predict. Consequently a test methodology, based on [5] is under development in TIA/EIA FO-6.5 [6] to enable the accurate measurement of the modal noise penalty created by mode selective loss. The suitability of the source is assessed by measuring its BER performance in a test path containing 3 separate 1 dB mode selective loss (MSL) points placed close to the laser and followed by 200m of multimode fiber. This BER is compared to the BER in a reference path with no MSL, but otherwise identical. The statistics are made stationary over the duration of the measurement by employing a "fiber shaker" which agitates the fiber and thoroughly

explores the speckle states. The amount of sensitivity penalty tolerated is specified by the data link standard, but typically 0.5 dB is used for 62.5 /125 micron fiber. Due to their low coherence, VCSELs show significantly lower penalties than CD lasers for an equivalent amount of MSL (Fig. 1). This raises the possibility that unlike CD lasers, VCSELs will not require any testing for modal noise since they are have adequately low coherence by design and the link specifications limit total connector loss to 3 dB. Although, to the author's knowledge, there is not a single instance of a short wavelength link employing CD lasers ever having failed due to modal noise in the field, this will help alleviate the impression that modal noise is a problem for laser links.

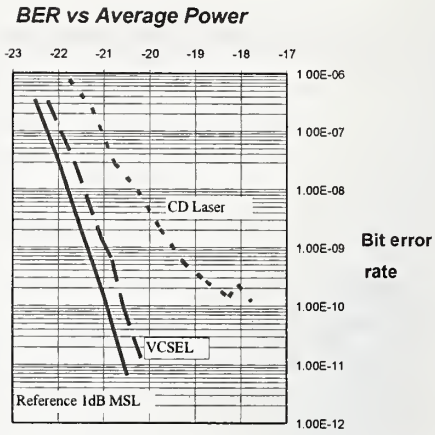

Fig 1. Modal Noise Comparison of 850 nm VCSEL and 820 nm CD laser with 6dB MSL.

Modulation Characteristics

The modulation characteristics of lasers are critical for their use in data communication links. These characteristics include such parameters as rise time, fall time, jitter, small signal bandwidth, duty cycle distortion and turn-on delay. The exact values of these parameters are precisely defined in the appropriate standards for any given protocol but in practice the suitability of the laser is determined by superimposing its 'eye' pattern on a mask defined in [7]. If VCSELs are required to support data rates beyond 1 GB/s it is essential that their modulation properties are well understood. and characterized.

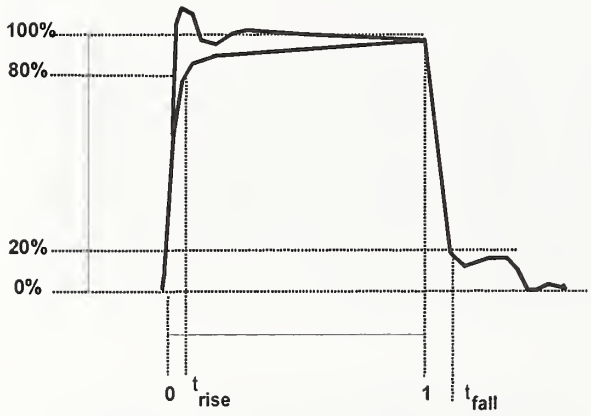

Fig 2. Schematic of 1 nsec VCSEL pulse showing characteristic features.

Fig 2 shows the schematic of a 'typical' optical pulse from a VCSEL. Most VCSELs have a 0-80% rise time and 100%-20% fall time that is extremely fast. Properly designed gain guided , multimode VCSELs, routinely have rise times <60 psec and fall times < 100 psec when measured from the 20 - 80% points (Fig 3). These fast edge speeds are consistent with the Fourier Transform of the small signal modulation bandwidths observed (Fig 4) when the VCSEL is biased above threshold and close to its peak operating current (5 - 10 mA). Fig 5 shows that these VCSELs can support data rates at least up to 3 GB/s sec which should be adequate for data link communications for many years in the future.

As can be seen in fig 2, however , the final 20% of the pulse amplitude can exhibit anomalous tailing effects . The duration of these effects is usually independent of the fast edge speed but may extend to 1.5 nsec. Different devices adjacent on the wafer can show different behavior. At one extreme some devices exhibit an overshoot followed by a slow decay, at the other extreme, a slow rise. In general the behavior can be anywhere between these extremes and can vary with bias conditions on any one laser.

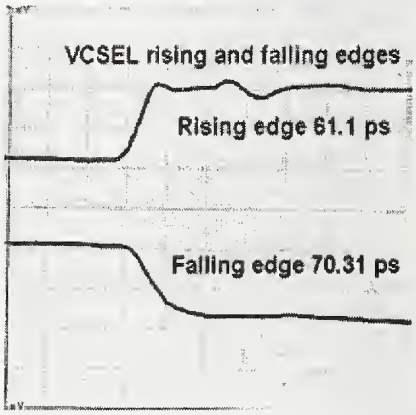

Fig 3. VCSEL rise/fall times

A. Valle et al. [8] have shown that when a lateral diffusion term is added to the rate equations, spatial hole burning and carrier diffusion create a mechanism for strong competition between modes in particular if the modes are strongly overlapped, often leading to dominance of a single mode. They also point out that if the modes are sufficiently spatially independent, the may lase independently although they are competing for the same total gain. On turn-off, spatial hole burning can also induce a carrier gradient which causes carriers to fall into the region which

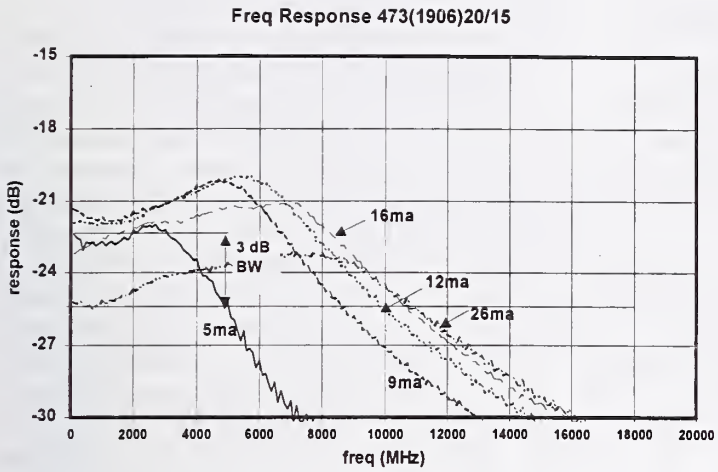

Fig 4. Small Signal Frequency Response

has already been turned off, and cause it to rise briefly above threshold again. This would explain the off-state bounce that we observe.

This theory does not explain all the effects on the rising edge however. Rising edge speed is affected by differential turn on delay of different modes, and diffusion effects caused by lateral inhomogeneities as the carrier density reaches equilibrium. A feature unique to multi-transverse mode lasers where there is some spatial independence between modes, is that there appear to be regions of the laser which may remain sub-threshold when other regions are already lasing, even though the entire region is being pumped. This means that the non-lasing regions will have long carrier recombination lifetimes since they are dominated by spontaneous recombination.

Evidence for this has been observed by examining the emissions from VCSELs in the plane of the junction. Test structures were made by surrounding the VCSEL with a secondary VCSEL structure and using it as a photodetector. Fig 6 is a plot of the detected photocurrent vs. laser bias current from this structure. This shows that the spontaneous emission does not entirely clamp at threshold as expected from simple laser theory. In fact it continues to rise, although there is a clear discontinuity in the curve as each mode reaches its own unique threshold, suggesting that at least locally, the spontaneous emission is pinned as expected from conventional laser theory. However, even at 10 ma the spontaneous emission has not fully saturated.

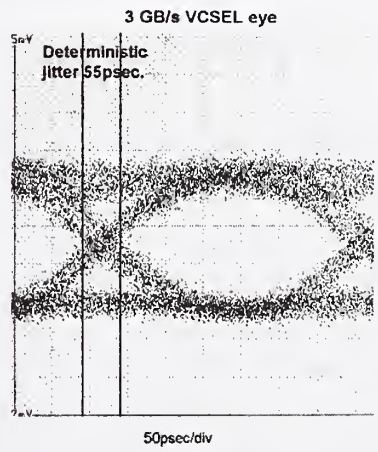

Fig 5. 3 GB/s "Eye"

These sub-threshold regions act like parasitic capacitance hanging on the lasing regions. Since this effect implies that the quasi-Fermi levels are not uniformly clamped across the active region, this can only be true if there is enough lateral resistance to permit a difference in potential difference across the device. The combination of the capacitance and resistance may well result in a slow turn-on due to the RC time constants alone, but also the carrier inhomogeneity induced by this mechanism will cause carriers to diffuse from the non-lasing regions into the lasing regions presumably limited by the carrier lifetime which is of the order of the 1.5 nsec tail that we observe. Given the complexity of the VCSEL mode pattern, this is an extremely difficult effect to model precisely.

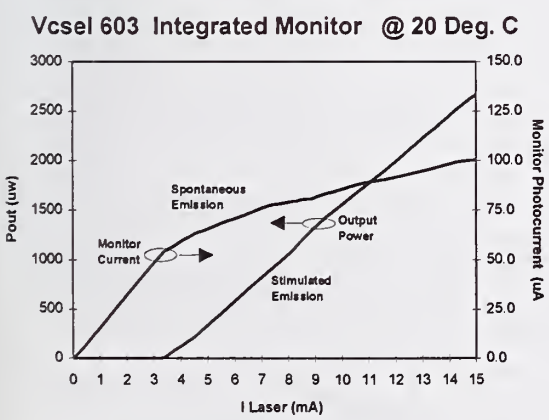

Fig 6. Spontaneous Emission

None of these mechanisms appear to explain why some lasers show a significant overshoot on the rising edge even after the relaxation resonance has been filtered. However, the inclusion of modal "shadowing" (i.e. light not being emitted due to lasing under the metal contact) in the rate equations shows that such an effect is possible. Lam [9] has shown in a study

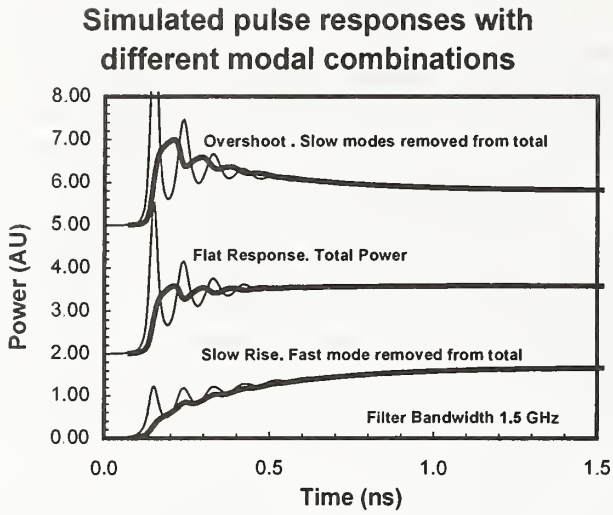

Fig 7. Effect of selective modal transmission

of pulse characteristics in quantum-well edge emitting lasers that even if the *total* photon output reaches equilibrium rapidly, the *individual* modes of a multimode laser may take many times longer to reach equilibrium. Some modes initially overshoot beyond their equilibrium, others undershoot and climb to equilibrium slowly. Clearly, these two behaviors must compensate each other when the modes are added to give the total power. However, if some of the modal power is occluded, then the compensation will not be perfect and the result may be a photon output which either overshoots or exhibits a slow rise depending on which modes are blocked. Fig 7 shows the result of a simplified rate equation simulation which limits the number of lasing modes to three. The three curve families show the total power, an instance where the slower modes were shadowed producing overshoot, and an example where the faster mode was shadowed, producing a slow rise. In each case the plot contains both the unfiltered waveform and a version which has been filtered with typical system filtering that one would expect in a gigabit system application. This example is intended to be illustrative only and exaggerates the effects. Fig 8 shows some actual results with a VCSEL which showed these effects clearly and which started lasing in a ring near the contact pad where shadowing is likely to occur. The different traces represent different bias currents and the traces are scaled and overlaid to ease comparison of the effects. In this case the fastest pulse corresponded to the highest drive current. The impedance of the VCSEL was 20 Ohms and an external series resistor of 30 Ohms was added to obtain impedance matching. The VCSEL impedance only varied by 5% throughout the measurement. A more detailed analysis of this mechanism is to be presented in a future paper.

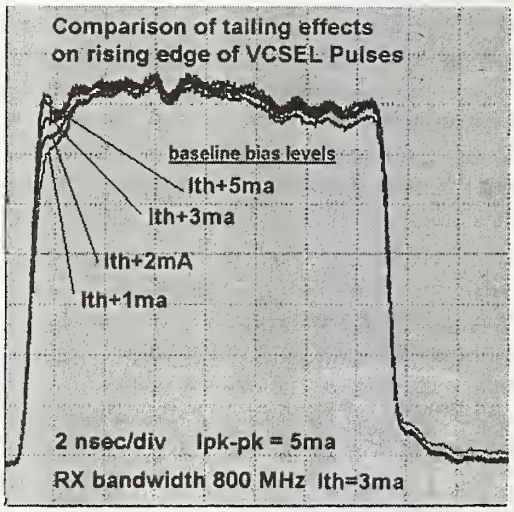

Fig 8. Rising edge distortion effects

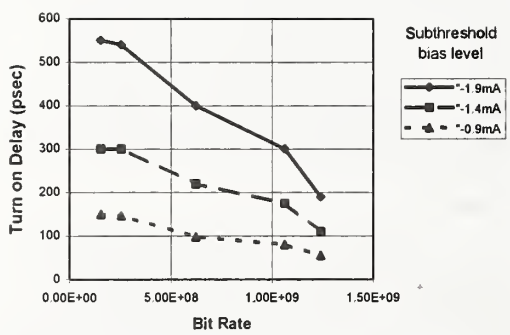

Fig. 9 Turn-on delay vs bit rate for various bias levels

The importance of understanding this mechanism lies in the fact that although they are fast, multimode VCSELs should exhibit some slow tailing due to their transverse structure. It is important that characterization of rise time is not fooled by these shadowing effects and the laser is designed to eliminate this effect.

Systematic jitter.

The main source of jitter in any laser, other than parasitics, is turn on delay. Fig 9 shows the measured rising edge turn-on delay vs. bit rate for a VCSEL using a 5 mA pk-pk modulation current pulse under different bias conditions. The definition of turn-on delay in this case was the delay of the rising edge measured to the pulse midpoint (where zero delay was defined as the delay observed for a

pulse biased far above threshold) for a 101010... data stream at the system clock rate. As expected, turn on delay is reduced as one increases the bias level closer to threshold.[10] The turn-on delay reduces as bit rate increases for constant bias conditions. However, this result is an artifact of the measurement technique where the data is an NRZ 101010... stream. The pulse must be adequately long to allow the carrier density to reach its equilibrium "off" state, when the laser is turned off. For short intervals between pulses the carrier density may not reach equilibrium and pattern dependent effects may be present. When a laser is being characterized for turn on delay jitter, it is essential that either pseudo random data is used or pulses of adequate length are used if a PRBS is not available to avoid this effect. This is particularly true if the VCSEL is being modulated from zero-bias [11], or when trying to assess the effects of jitter on the BER when running the VCSEL with no feedback control [12]

Fig 10. Normalized Threshold Current vs Temperature

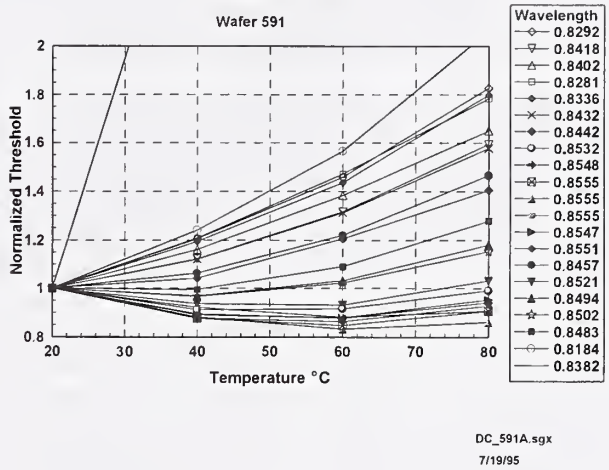

Threshold temperature sensitivity and open loop bias control.

Like all lasers, VCSELs have threshold currents which vary with temperature. However, because the VCSEL is a single longitudinal mode laser whose lasing wavelength can be placed anywhere on the gain peak, the reduction in gain with temperature can be offset by the change in the peak wavelength of the gain peak with temperature. This allows the designer to select a wavelength at which the threshold shows very little change with temperature. Fig 10 shows the normalized change in threshold with temperature for many devices scattered over a wafer. It can be seen that a significant range of devices exhibit a very low sensitivity of threshold to temperature over what would be described as a typical operating temperature range in a LAN application. This allows selected VCSELs to be operated in an open loop configuration with no feedback or monitoring circuitry. The device can be biased at the lowest threshold in the desired temperature range, and the amount of drift that can be tolerated would depend on what level of turn-on delay can be tolerated by the system. [12] Fig 9 shows that for systems around 1 Gb/s , where the peak to peak systematic jitter limit is around 180 psec, this approach is feasible if the VCSEL bias is kept within 0.9 mA below threshold. For lower bit rates this range extends further. This method could be particularly useful where a very simple architecture is required, for example driving a VCSEL directly from a logic gate, where eye safety levels are of minor importance, and where there is no space to include monitor detectors to control the bias point for example in high density, low cost back plane applications. Devices which do not meet these requirements, particularly at high data rates can be used with a monitor diode to establish a control loop.

Fig 11. Effects of incomplete fiber coupling on VCSEL modulation.

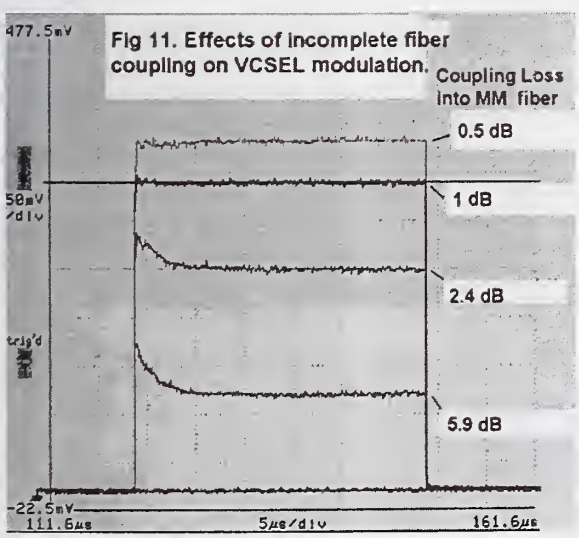

Coupling the source to a fiber.

An equally important part of using a laser source is the ability to couple it to an optical fiber. VCSELs

are useful devices in this respect. In fact multimode VCSELs, which commonly range from 15 micron diameter to 25 micron diameter active apertures are particularly easy to couple to optical fibers. They do not require high magnification lenses , they have circular beam geometry, and have relatively low NA around 0.1 - 0.15. This would allow a fiber to be coupled directly to a VCSEL, but since all commercial transceivers are connectorized , a lens will generally be employed for reliability purposes to translate the effective source point to a place where there is no risk of damaging the VCSEL with the fiber.

The optimal coupling configuration of a VCSEL or any laser to a multimode fiber is to launch a spot centered on the fiber core, with a diameter less than half the fiber core diameter. This will achieve a number of goals. It will eliminate modal noise resulting from connector loss .[13] It will eliminate most connector loss in a link. [13] It will enhance the bandwidth of multimode fiber by reducing differential mode delay with most FDDI compliant fiber. It will permit use of either 62.5/125 micron and 50/125 micron graded index MM fiber with no coupling loss. It will prevent variations in the VCSEL numerical aperture from affecting coupled power. Fig 11 shows what happens to the pulse when a VCSEL overfills a fiber at launch (up to 6 dB coupling loss). If the fiber is overfilled, the coupled power varies with time due to an increase in the NA of the VCSEL beam as a result of thermal lensing and mode focusing. [14,15] The effect occurs primarily at the thermal time constant of the chip, and has a much smaller effect for more reasonable coupling losses. Fig 11 shows that it is negligible at 1 dB coupling loss. This type of distortion would cause problems in high speed systems only if one attempted to set up the AC power levels by measuring the DC L-I characteristics of a device. This is not a trivial issue however, since for manufacturing purposes, it is desirable to avoid AC testing. Clearly it is best to avoid this problem at source and ensure that there is no mode selective coupling loss at the connector.

Conclusion.

VCSELs are an ideal source for future high speed LAN applications due to their high speed, good reliability, low coherence, and the ability to use them in array configurations and other high density applications with no monitor circuit and no feedback control. However, being multi-transverse mode devices , they have attributes that require careful management and characterization to ensure satisfactory performance. This is a relatively new, but fast growing technology and one would expect to see these characteristics designed out of the devices in a manner similar the design improvements of edge emitting lasers.

References

1. R.A.Morgan et al., IEEE Photonics Technology Letters, Vol 7, No 5, May 1995, p441.
2. J.K.Guenter et al, Proceedings of the SPIE, Vol. 2683.
3. Hahn, K.M., et al. Electronic Letters, Vol. 29, No.16, Aug 5, 1993 pp. 1482-1483.
4. R.E.Epworth, Technical Digest, Fourth European Conference on Optical Communication, Genoa (1978), pp 492-501.
5. R.J.S Bates et al., Optical and Quantum Electronics, vol 27, pp. 203-224,1995.
6. Draft Worging Group Document describing the measurement technique is available. Contact the author by e-mail for a copy.
7. "Optical Interfaces for Equipments and systems relating to the synchronous Digital Hierarchy." ITU-T Recommendation G.957 1993.
8. A. Valle, J. Sarma, K.A.Shore, IEEE Journal of Quantum Electronics, QE-31, No 8, Aug. 1995, pp 1423-1431.
9. Y.Lam, J.P.Loehr, J.Singh, IEEE Journal of Quantum Electronics, QE-28, No. 5, May 1992.
10. Chinone et al., IEEE J.Quantum Electronics, QE-10, 81 (1974).
11. D.M. Currer, K.Y.Lau, IEEE Photon. Techol. Lett., Vol. 7, pp. 4-6, 1995.
12. K.Obermann et al., IEEE Photon. Techol. Lett., Vol. 8, No.1 pp. 31-33, 1995.
13. T.H.Wood, L.A.Ewell, IEEE J. Lightwave Tech. Vol LT-4, No. 4, April 1986.
14. Zhiao,Y., McInerny, J.G., Morgan, R.A., Optical Engineering, Vol. 33, No. 12, Dec 1994
15. Zhang, J-P., Petermann, K., IEE Proc Optoelectron., Vol. 142, No.1, Feb 1995

Modal Optical Coupling Efficiency Measurements and Modeling for Fiber Interconnections

J. Sutherland, G. George and J.P. Krusius
Cornell University, School of Electrical Engineering, Ithaca NY 14853

Abstract - Measurements and modeling of modal optical coupling efficiency have been performed on fiber-to-fiber interconnection links. Modeling results have been validated with measurements of single-mode to multimode fiber coupling for axial separations and lateral misalignment. The model agrees with power-normalized coupling efficiency measurements under these conditions to within 15% for large axial separations. The modeling approach is suitable for fiber-to-fiber, laser diode-to-fiber, fiber-to-rectangular waveguide interconnections.

1. Introduction

Typical optical links employ multiple fiber-to-fiber interconnections. Minimization of coupling losses at each interconnection leads to improved bit error rate (BER) performance and reduced power dissipation at sources and detectors. Multimode fiber-to-fiber coupling has been modelled using ray tracing techniques [1-3], but these methods are unable to account for variations in launching fiber mode power amplitude and phase distribution, and they cannot predict the modal energy distribution in the receiving fiber. We have developed a mode-based optical coupling model which predicts coupling efficiencies for multimode fiber-to-fiber interconnections with axial separations and lateral misalignments [4,5]. The approach requires prior knowledge of the modal power distribution in the launching fiber. Since the modal power distribution is general difficult to measure in multimode fibers, this paper presents coupling efficiency measurements and modeling for a configuration where the source modal power distribution is known: single-mode to multimode fiber coupling. The model is also applicable to emerging low-cost laser diode-to-fiber couplers where alignment tolerances are relaxed by coupling into large diameter multimode fibers [6,7], and fiber-to-rectangular waveguide couplers.

2. Coupling Efficiency Measurements

Coupling efficiency measurements were performed using the experimental setup shown in Fig. 1. Light was launched into a 2230 m long single-mode optical fiber from an HP1552SM 1322 nm laser source. The single-mode fiber had a nominal core diameter of 8.3 μm and a step-index profile with $\Delta n = 0.36\%$. These fiber parameters ensure population of only the lowest order mode, with cladding and unguided modes stripped due to the fiber's length [8]. Light was coupled from the single-mode fiber into a 50 μm core diameter multimode fiber with 125 μm cladding diameter and a step-index profile with $\Delta n = 3\%$. The multimode fiber was 50 m long to help strip out cladding and unguided modes. The far end of the multimode fiber was attached to an HP 81532A optical detector, which provides power measurements accurate to ±4%.

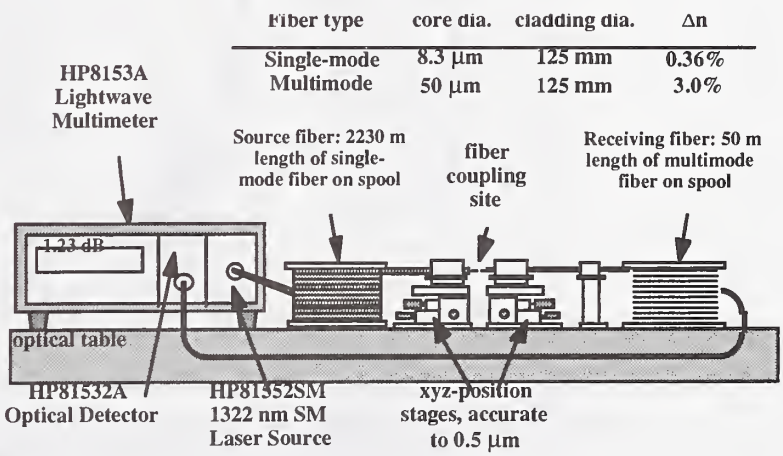

Fig. 1. Experimental setup used to measure optical coupling efficiency for 1322 nm light coupled from a single-mode fiber into a multimode fiber.

Axial and lateral misalignment of the two fibers was controlled using two Newport 561 XYZ-micropositioners. Each micropositioner has been characterized for repeatable positioning accurate to 0.5 μm. Fiber end faces were prepared using a Fujikura CT-04 high precision fiber cleaver. No end face polishing was performed, but all fiber ends were optically inspected for surface defects prior to measurement. Averaged measurement results for axial separations and lateral misalignments are shown in Figs. 2 and 3, respectively. Both figures illustrate the effects of reflections at short axial misalignments.

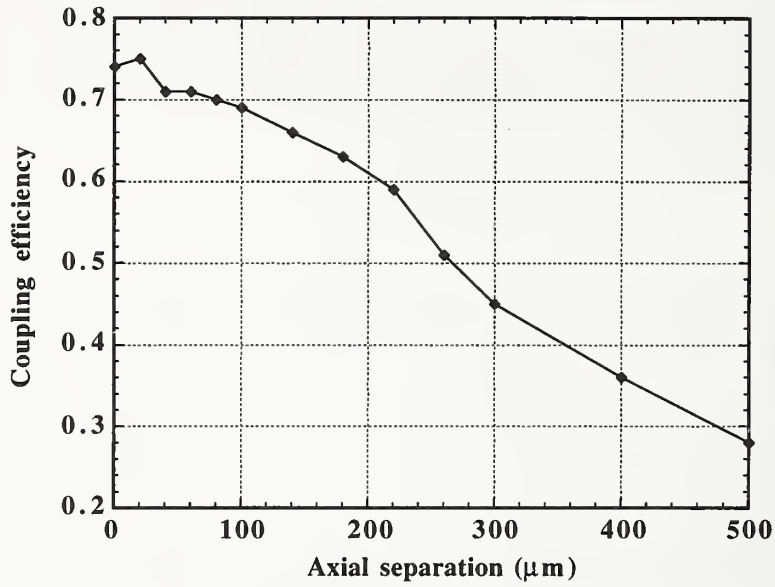

Fig. 2. Measured single-mode to multimode fiber coupling efficiency for axial separations.

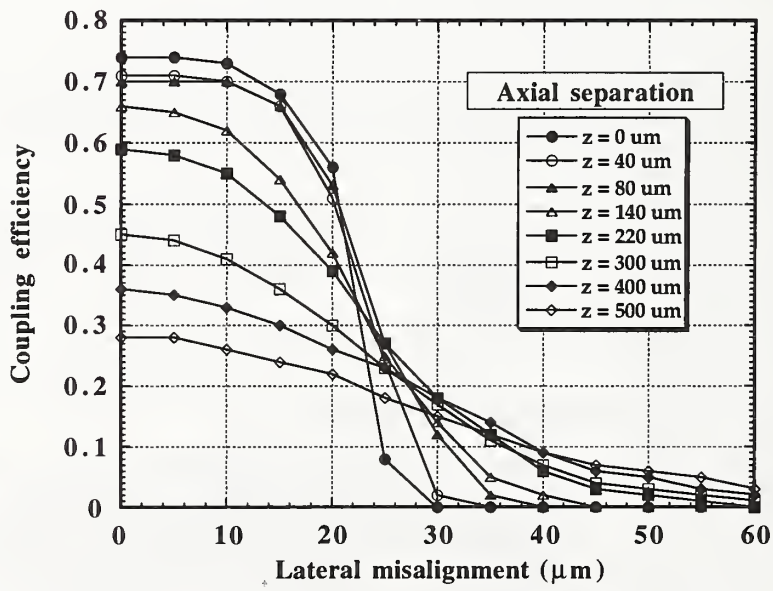

Fig. 3. Measured single-mode to multimode fiber coupling efficiency for lateral misalignment at various axial separations.

2. Optical Coupling Modeling

The single-mode to multimode fiber coupling configuration shown in Fig. 1 was simulated using our modal coupling model. The simulation program computed source fiber mode, diffracted the mode onto the receiving fiber face, and computed the numerical inner product of source modes onto the receiving fiber modes. Derivations related to source and receiving fiber mode structures, efficient diffraction of source modes, and overlap integral computation have been presented previously [4,5]. The coupling model includes consideration of reflections at the source and receiving fiber faces. Computation of coupling efficiency for each axial separation and lateral misalignment case required approximately two minutes of CPU time on an HP-700 series workstation.

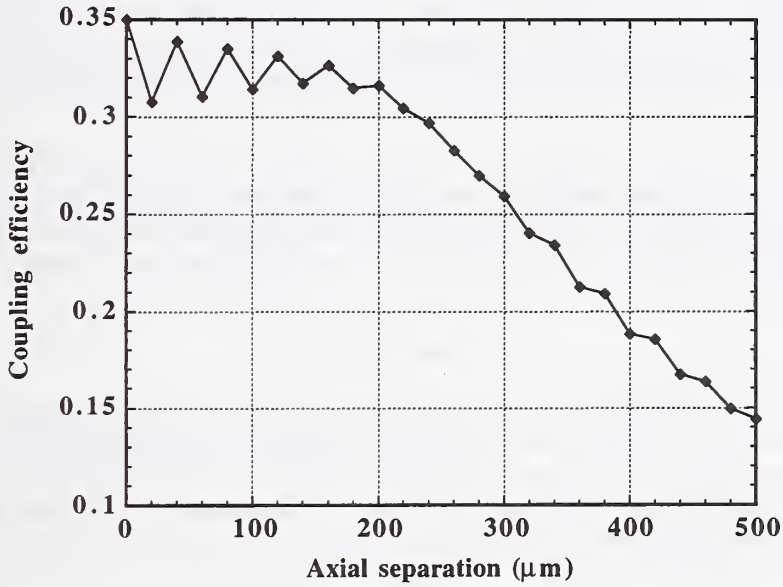

Fig. 4. Simulated single-mode to multimode fiber coupling efficiency for axial separations.

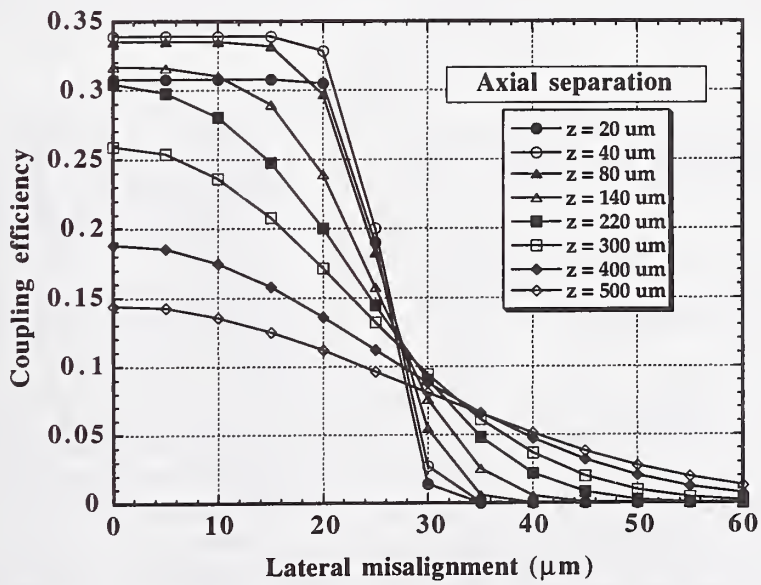

Fig. 5. Simulated single-mode to multimode fiber coupling efficiency for lateral misalignment at various axial separations.

Figs 4 and 5 show comparisons of measurement and simulation for axial separations and lateral misalignments, respectively. Reflection effects are evident in Fig. 4 for small axial separations. The limited number of data points leads to an aliasing effect that can be corrected with additional data points. Comparison of measurement and simulated coupling efficiency plots for axial separations and lateral misalignment shows agreement in general shape and trends, but simulations consistently predict maximum coupling efficiencies which are approximately 3dB less than measured coupling efficiencies. If the measurement and simulation coupling efficiency plots are normalized so that maximum coupled powers are equalized, the axial separation and lateral misalignment curves generally agree to within 15%. For small axial separations, this agreement falls to within 50% for some lateral misalignment cases. This deviation may be associated with additional source mode coupling into receiving fiber modes as the remaining unguided portion of the source mode field distribution diffracts within unguided fiber modes. This effect would also explain the absolute difference in coupled power found between measurement and simulation. Even with these deviations, the single-mode to multimode coupling case demonstrates a prediction of fiber coupling efficiency based solely on physical fiber parameters and the coupled light wavelength.

This modeling approach may be extended to fibers of arbitrary refractive-index profiles which satisfy the weakly-guided approximation, and rectangular waveguides. Phase coherence effects can be modeled for short fibers, and lenses and other elements with well-defined ABCD matrices can be modeled. Finally, this method is computationally efficient, especially when considering the large number of modes involved in the coupling process.

4. Conclusion

We have developed a modal coupling approach for modeling optical coupling between misaligned optical fibers. Simulated coupling efficiencies for axial separations and lateral misalignments and give good agreement with measurement results, although second-order effects limit accuracy at short distances. The model predicted power-normalized coupling efficiencies for axial separations and lateral misalignments to within 15% for large axial separations. The approach is also applicable to laser diode-to-multimode fiber coupling and fiber-to-waveguide coupling.

Acknowledgments

This work was supported by ARPA Optoelectronics Technology Center (contract #MDA972-95-1-0002) and Cornell Industry Electronic Packaging Alliance.

References

[1] S. C. Mettler, "A general characterization of splice loss for multimode optical fibers," Bell System Technical Journal, vol. 58, no. 10, pp. 2163-2182, Oct. 1979.

[2] P. Di Vita, and U. Rossi, "Realistic evaluation of coupling loss between different optical fibers," Journal of Optical Communications, vol. 1, no. 1, pp. 26-32, Jan. 1980.

[3] Y. Daido, E. Miyauchi, and T. Iwama, "Measuring fiber connection loss using steady-state power distribution: a method," Applied Optics, vol. 20, no. 3, pp. 451-456, Mar. 1981.

[4] J. Sutherland, G. George, and J. P. Krusius, "Optical coupling and alignment tolerances in optoelectronic array interface assemblies," *Proc. of the 45th Elec. Comp. & Tech. Conf.*, pp 577-583, 1995.

[5] J. Sutherland, G. George, S. Van der Groen and J. P. Krusius, "Alignment tolerance measurements and optical coupling modeling for optoelectronic array interface assemblies," *Proc. of the 46th Elec. Comp. & Tech. Conf.*, pp 480-486, 1996.

[6] M. S. Cohen, G. W. Johnson et al, "Low-cost fabrication of optical subassemblies," *Proc. of the 46th Elec. Comp. & Tech. Conf.*, pp 1093-1100, 1996.

[7] J. M. Trewhella, M. M. Oprysko et al, "Unibody plastic injection-molded optical sub-assembly for large core fiber," *Proc. of the 46th Elec. Comp. & Tech. Conf.*, pp 1116-1121, 1996.

[8] G. Keiser, *Optical Fiber Communication*, McGraw-Hill, New York, NY, pp. 123-124, 1983.

Dispersion-compensating fibers with high birefringence

J. Vobian, G. Herchenröder (FTZ Darmstadt), K. Mörl (IPHT Jena)

Abstract

For different applications, dispersion-compensating fibers (DC fibers) with high birefringence may be very useful and advantageous, for instance, in fiber lasers in ring laser, but also in Fabry-Perot configurations Polarization-Maintaining Dispersion-Compensating (PM-DC) fibers can used for the compensation for chromatic dispersion and stabilizing of the output pulses by defined polarisation controlling. Also for several sensor applications PM-DC-fibers can be installed with great benefit.

In this paper, we present two PM-DC fibers with very high dispersion values in the third optical window and, additionally, with very high birefringence values due to the elliptical cores (shape-induced or geometrical birefringence).

Tailoring of the PM-DC-fibers

We have presented an iterative, inverse method for calculating the refractive-index profile and radius parameters of fibers with respect to prescribed dispersion and mode-field diameter values (Petermann II) in the vicinity of 1550nm making use of the Levenberg-Marquardt algorithm on the basis of the scalar Helmholtz equation and the singular Sturm-Liouville eigenvalue solution [1], [2].

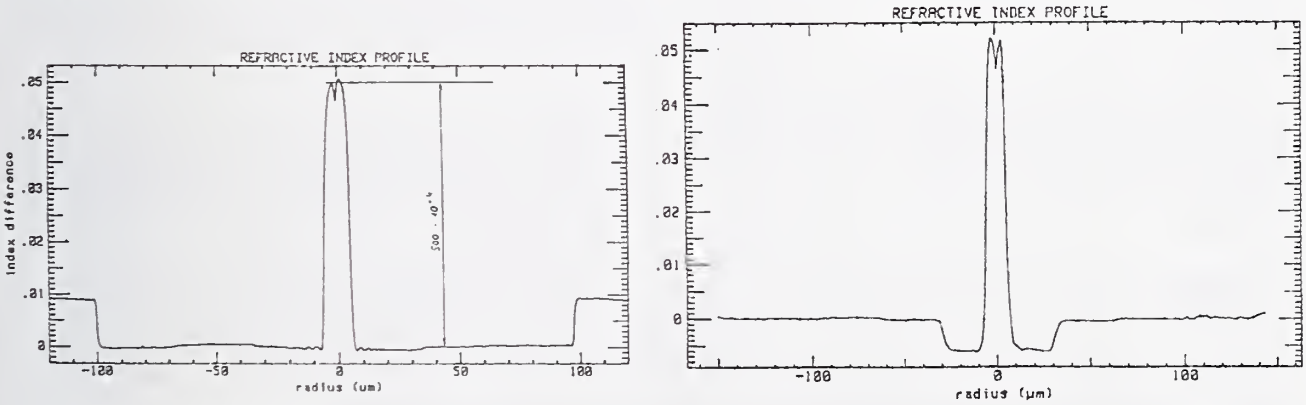

Fig. 1 n(r)-profiles of the step-index fiber and the W-fiber

The high birefringence was obtained by elliptical cores of the fibers taking advantage of shape-induced or geometrical birefringence instead of stress-induced birefringence of commercial Polarization-Maintaining (PM) fibers.The PM-DC fibers (79M and 82M) were fabricated by MCVD at the Institute of High Technology, Jena, Germany [1], [2]. *Fig.1* shows the two fiber profiles. As a consequence of the small core diameter, it is not possible to measure a quantitatively correct n(r)-profile using the convential Refracted Near Field (RNF) technique. The core level n(r)≈0 cannot be resolved and is, therefore, too low. For the n(r) measurements, a part of the preform was drawn to a fiber with a cladding diameter of 300µm. *Fig. 2* shows the fiber geometry of the W-fiber 82M.

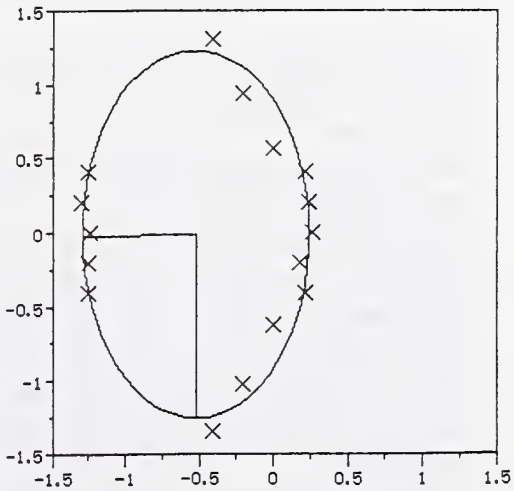

Fig. 2 Core geometry of the W-fiber (elliptic fit)

Measurements of the chromatic dispersion D(λ)

The measurements were performed making use of the Raman-fiber laser (RFL) and a Mach-Zehnder interferometer (MZI) [3]. As a consequence of the necessary fit-function representation, an extrapolation beyond the measuring range is forbidden. For this reason and for the improvement of the accuracy in the third optical window and the reduction of the influence of the fit function, it is important to establish a high upper limit of the wavelength range and to have as many measuring points as possible. In the case of the RFL this upper limit is 1740nm, the maximum number of measuring points amounts to 30. Other advantages of this set-up are a good reproducibility and a high accuracy, the standard deviation of the measured group delay data is comparable with that of interferometric methods. No spectral gap exists as in the case of semiconductor- or LED-set-ups. D(λ) measurements of DC fibers with high negative dispersion values are easily possible.

Measurements on short fiber pieces can be performed with the aid of a Mach-Zehnder interferometer (MZI) with an incoherent radiation source [3]. The upper limit of the measuring range is high (1700nm), a large number of measuring points can be obtained (up to 30) which guarantees a high accuracy, again no λ-gap exists. Dispersion measurements on DC fibers with

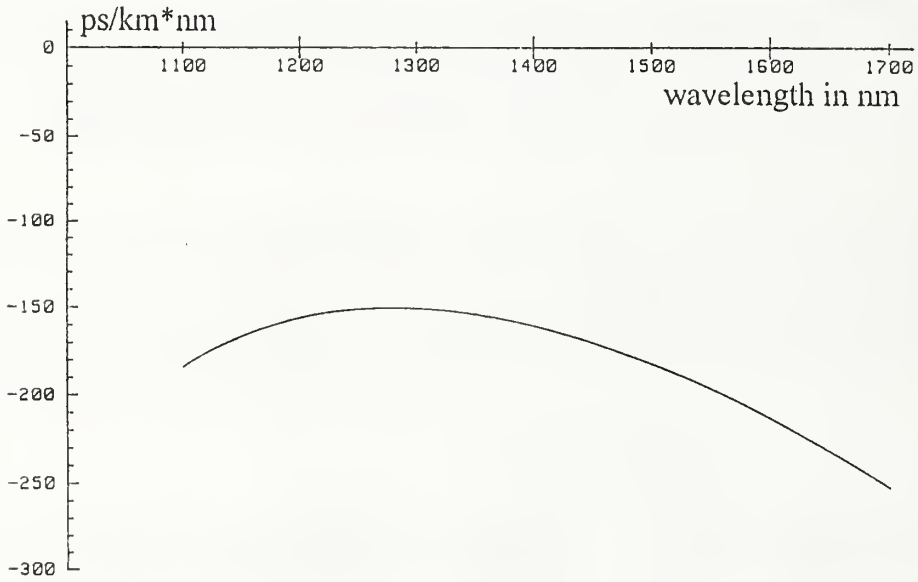

Fig. 3 Chromatic dispersion of the W-fiber, Raman-fiber laser measurement

very high negative dispersion values are possible, but not trivial. Because of the large difference of the group delay in both arms of the interferometer, normally, no interference patterns can be observed. Two ways out are possible: shortening of the fiber under test (in general, ≤2cm length difference between reference and test fibers) and/or lengthening of the optical path in the air gap in the reference arm by an optically dense medium (Schott SF59 glass cylinder with n≈2).

In *Table 1* the dispersion measurements are compiled. The differences between RFL- and MZI-results can be commented by fiber inhomogeneities, the measurements were performed on long fibers and short fiber pieces, respectively. But, in general, the agreement is satisfying. *Fig. 3* shows the dispersion curve of the W-fiber measured with the RFL. Important are the very high negative dispersion values in the third optical window and the negative slope of the curve [2].

As mentioned above, both fibers have also a high birefringence. As a consequence, the RFL-laser pulse launched into the fiber is split into two pulses (*Fig. 4*), λ=1550nm, fiber length L is 615m.

PM-DC fiber	Measuring set-up	D(1300nm) in ps/km*nm	D(1540nm) in ps/km*nm	D(1550nm) in ps/km*nm	Elliptic fit large/small axis
W-fiber 82M	Raman-fiber laser	-150.7	-194.7	-197.8	2.48/1.54μm
	Mach-Zehnder interferometer	-148.3	-192.2	-195.3	
Step-index fiber 79M	Raman-fiber laser	-160.5	-105.0	-102.2	2.24/1.26μm
	Mach-Zehnder interferometer	-154.8	-101.2	-98.8	

Table 1 Chromatic dispersion measuring results for two PM-DC fibers 79M and 82M

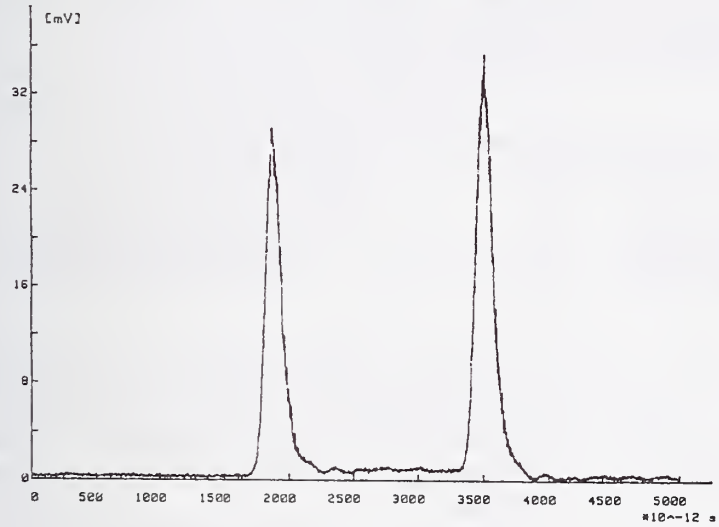

Fig. 4 Double-pulse presentation, step-index fiber, λ=1550nm, fiberlength L=615m

The distance of the two pulses (1619ps) is a measure of the polarization-mode dispersion (PMD) which is 2.63ps/m in this case.

PMD measurements with a Michelson interferometer

The PMD measurements with the Michelson interferometer are performed in the time domain [4] with an incoherent LED light source ($\Delta\lambda \approx 60$nm) [5].

The relations between the group birefringence B_G, group beatlength l_G and the PMD ($\Delta\tau_{GP}$) are:

$$\Delta\tau_{GP} = \frac{\Delta t_{GP}}{L} = \frac{B_G}{c}, \qquad (1)$$

$$l_G = \frac{\lambda}{B_G}, \qquad (2)$$

In *Table 2* the measuring results are compiled, the PMD-, B_G- and l_G-values for 4 wavelengths. For comparison the results of measurements with the Michelson interferometer on commercial PM (High Birefringence) fibers are added (PANDA-, YORK bow-tie- and HiBi-AT&T-fibers). These latter measurements are in very good agreement with results obtained by earlier measurements making use of the MZI and the Wavelength-Scanning Method [6]. It is obvious that the birefringence and PMD values of the W- and step-index fibers are remarkably higher and the group beatlength clearly lower than those of the commercial PM fibers with their stress-induced birefringence which depends only weakly on the wavelength. On the other hand the B_G- or PMD-dependence of the W- and step-index fibers is evident. For the 79M fiber, PMD and B_G decrease with increasing wavelength, in the case of fiber 82M both parameters increase with λ. These results demonstrate the complicated wavelength dependence of the birefringent fibers.

Wavelength in nm		1276	1321	1516	1546
Parameter	Fiber				
PMD in ps/m	W-fiber 82M	5.64	5.91	8.68	8.89
	Step-index fiber 79M	3.34	3.28	2.67	2.56
	PANDA fiber	1. 44		1.47	-
	YORK bow-tie fiber	2. 18		2.22	-
	AT&T-PM fiber	0. 77		0.78	-
Group birefringence B_G*10^{-4}	W-fiber 82M	16.92	17.73	26.04	26.67
	Step-index fiber 79M	10.02	9.84	8.01	7.68
	PANDA fiber	4. 32		4.40	-
	YORK bow-tie fiber	6. 54		6.66	-
	AT&T-PM fiber	2. 30		2.35	-
Group beatlength in mm	W-fiber 82M	0.75	0.75	0.58	0.58
	Step-index fiber 79M	1.27	1.34	1.89	2.01
	PANDA fiber	3. 01		3.42	-
	YORK bow-tie fiber	1. 97		2.25	-
	AT&T-PM fiber	5. 58		6.46	-

Table 2 PMD, group birefringence and group beatlength of the two PM-DC fibers and three commercial PM fibers for comparison

It is interesting to state the perfect agreement of the PMD value obtained with the double-pulse approach with the corresponding value in *Table 2.*

References

[1] R. Boness, J. Vobian, S. Unger, J. Kirchhof: Tailoring of Dispersion-Compensation Fibers with High Compensation Ratios up to 30. Technical Digest Symposium on Optical Fiber Measurements, Boulder 1994, p. 181-184

[2] R. Boness, W. Nowak, J. Vobian, S. Unger, J. Kirchhof: Tailoring of dispersion-compensation fibres with high compensation ratios up to 30. Pure Appl. Opt. 5 (1995), p. 333-344

[3] J. Vobian: Chromatic and Polarization Dispersion Measurements of Single-Mode Fibers with a Mach-Zehnder Interferometer between 1200 and 1700nm. J. Opt. Commun. 11 (1990) 1, p. 29-36

[4] N. Gisin, J.-P. Von der Weid, J.-P. Pellaux: Polarization Mode Dispersion of Short and Long Single-Mode Fibers. J. Lightw. Technol. Vol. 9, No.7 (1991), p. 821-827

[5] V. Reichel, J. Vobian, N. Gisin: Polarization mode dispersion measurements on long buried cables. Proc. EFOC&N 93, The Hague 1993, p. 56-61

[6] Ch. Chojetzki, H. Schmitzer, J. Vobian, W. Dultz: Four interferometric methods for the determination of the birefringence and polarization dispersion of polarization maintaining optical fibers. Technical Digest Symposium on Optical Fiber Measurements, Boulder 1992, p. 155-158. NIST Special Publication 839

Accurate wavelength calibration for optical spectrum analysers

D A Humphreys

National Physical Laboratory, Teddington, Middlesex, TW11 0LW, UK

Introduction

An Optical Spectrum Analyser (OSA) is a versatile instrument for measuring optical power as a function of wavelength (and polarization in some instruments). Because of their widespread industrial use, the diversity of applications and the mechanical nature of the design there is considerable interest in OSA calibration. To meet this industrial need, we are developing calibration techniques for these instruments and participating in the International Electrotechnical Commission (IEC) working group to standardise procedures for OSA calibration. The key parameters of interest are:

- Centre wavelength accuracy
- Linearity of wavelength scale
- Instrument response
- Resolution bandwidth
- Power response
- Power linearity (with power and wavelength)
- Pulse performance
- Polarization sensitivity

The wavelength accuracy and linearity of the wavelength scale are important parameters for users, particularly so for the development of wavelength division multiplex systems where the separation of the optical sources may be 1 nm or less. Typically the accuracy of the OSA will be limited by mechanical constraints. These may be corrected at the design stage using software algorithms and a calibration procedure. The wavelength scale of an OSA can be calibrated using a variety of fixed wavelength sources.

Spot wavelength calibration

There has been considerable interest in realising suitable reference standard lines at the 1.5 μm optical fibre band[1,2]. These include gas lasers and atomic opto-galvanic transitions and molecular absorption features[3]. The width of these lines is typically 500 MHz - 1 GHz so a single frequency tuneable laser locked system will have an overall accuracy of the order of tens of MHz.

At NPL, we use an opto-galvanic transition in Krypton[4] at 1547.825 nm (DFB laser) and a CO absorption at 1560.5 nm (external-cavity laser)[5]. The accuracy of these systems significantly exceeds the requirements for OSA calibration.

Emission lines from discharge lamps give a series of line spectra and provide a lower cost alternative calibration method. The intensity of these lines is low, typically 1-20 pW depending on the line and optical fibre type, but is sufficient to provide a calibration. A list of higher intensity lines[6,7] for noble gases is shown in table 1. Lines falling in the optical fibre communications wavelength range have been highlighted and lines used in this work are printed in bold type.

Wavelength scale linearity

Two approaches have been considered for the measurement of wavelength scale linearity: A tuneable laser used in conjunction with a wavemeter or calibrated (or self-calibrating) Fabry-Perot Etalon (FP) transmission artifact. The advantage of the calibration artifact is that the response can be modelled and results calculated for a wider range of wavelengths. The tuneable laser/wavemeter is useful for applications where the OSA is used over a restricted wavelength range. The calibration can be performed prior to use to give the highest

level of accuracy.

Table 1. Selected emission lines for noble gasses							
Atom	Wavelength	Atom	Wavelength	Atom	Wavelength	Atom	Wavelength
Kr	810.659	Ne	1029.824	Ne	1198.819	Xe	1414.631
Kr	811.513	Ar	1047.292	Ne	1206.964	Xe	1424.485
Kr	819.231	Ne	1056.53	Ne	1246.28	Kr	1443.074
Kr	826.551	Ne	1080.103	Xe	1262.684	Xe	1473.683
Kr	830.039	He	1083.322	Ne	1269.267	Kr	1473.846
Kr	851.121	He	1083.331	Ne	1291.555	Kr	1476.671
Kr	877.916	Ne	1084.745	**Kr**	**1318.102**	Ne	1523.488
Kr	893.114	Ne	1114.607	Ne	1322.286	**Kr**	**1524.378**
Ar	912.547	Ne	1115.081	Ar	1331.685	**Kr**	**1533.915**
Ar	922.703	Ne	1139.355	Ar	1337.077	Kr	1537.624
Ar	935.679	Ne	1141.226	Ar	1350.788	Xe	1542.261
Ar	966.043	Ne	1152.59	Kr	1362.614	Xe	1605.767
Ne	966.807	Ne	1152.818	**Kr**	**1363.795**	Xe	1673.272
Kr	975.443	Ne	1153.95	Xe	1366.079	**Kr**	**1678.971**
Ar	978.719	Ne	1161.726	Kr	1366.213	Kr	1685.809
Xe	980.239	Ne	1177.001	Ar	1372.233	Kr	1690.137
Xe	992.591	Ne	1179.227	Kr	1374.261	Kr	1694.043
Kr	1022.426	**Kr**	**1182.261**	Kr	1404.95	Xe	1733.05

Resolution bandwidth

The resolution bandwidth, $\Delta\lambda(\lambda)$, is an important parameter for optical noise-figure measurements. Because an OSA is a grating instrument, the resolution is limited by the size of the input and output apertures. As these have a finite width, the light incident on the grating will not be completely parallel. If the input aperture contribution is ignored, then the resolution of the instrument is proportional to the width of the aperture in front of the photodetector. At normal incidence the instrument bandwidth will be given by equation 1:

$$\Delta\lambda = 2\delta\theta\sqrt{\frac{d^2}{m^2} - \lambda^2} \qquad (1)$$

where $\Delta\lambda$, is the full width at half maximum of the instrument function and $\delta\theta$ is the acceptance angle of the output aperture and m is the grating order.

In practice the response will be approximately rectangular for wide resolutions and triangular/gaussian for the minimum resolutions. As expected, multi-mode and single-mode fibres have different instrument

responses.

The minimum resolution bandwidth of a commercial OSA is typically 0.1 nm which corresponds to a frequency of 12.5 GHz at 1550 nm.

Measurements

An OSA was calibrated over the range 1180 nm - 1680 nm using six lines from a high-intensity Kr discharge lamp. The linearity over the intervening points was measured using a calibration artefact and two LED sources. The measured results (figure 1) were normalised (figure 2) for source intensity variation and system sensitivity using equation 2:

$$R_{norm} = \frac{P_{artefact} - P_{noise}}{P_{reference} - P_{noise}} \qquad (2)$$

where R_{norm} is the normalised artefact response and the optical powers are in Watts..

The emission lines were used to provide calibration for both the OSA and the artefact. The calculations were performed in three stages:

1. Estimate the FP spacing from measurements around each of the Kr emission lines.

2. Calculate the true value of the spacing from measurements at the Kr emission lines.

3. Determine the wavelength scale linearity.

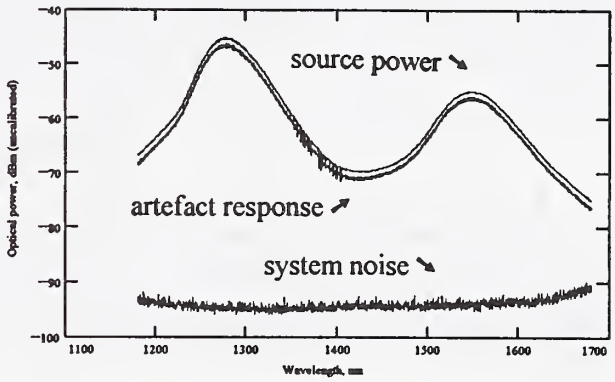

Figure 1 Source-power, artefact response and system noise results

The calculated linearity with wavelength (figure 3) give the correction factor for air and vacuum wavelengths.

The variation of the resolution bandwidth was also investigated as a function of wavelength. A rectangular fit was used for the 1 nm banwidth and a trianglular fit was used for the 0.1 nm bandwidth. The results (figure 4) indicate that at 0.1 nm the wavelength dependent effects are well balanced but at 1 nm the grating angle effect is dominant.

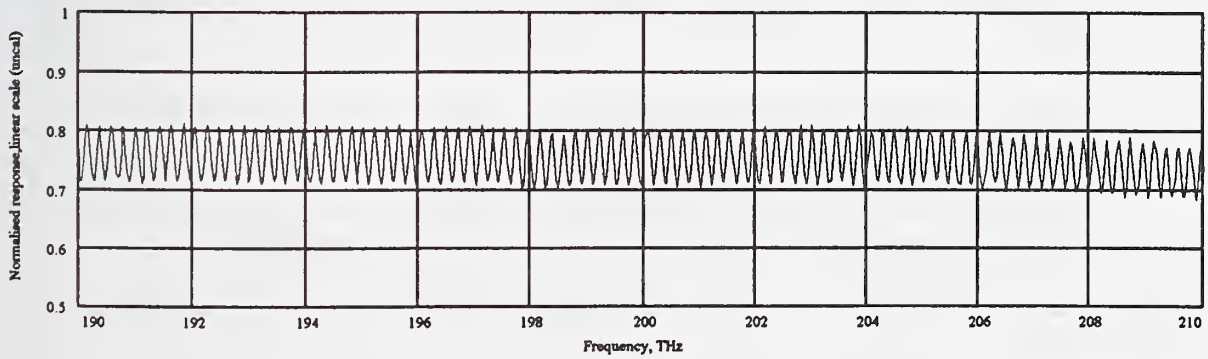

Figure 2 Normalised artefact response over limited range

Summary

The work at NPL to provide traceable calibration for OSA wavelength scales has been outlined. Calibration results over the range 1180 - 1680 nm for a commercial OSA have been presented.

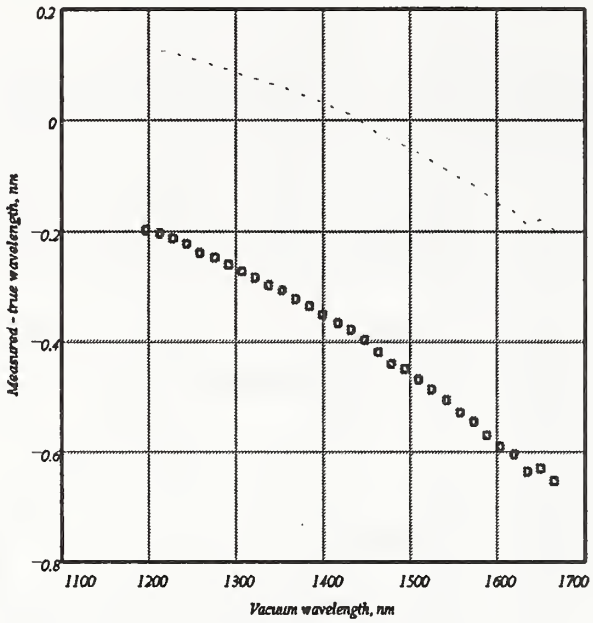

Figure 3 Wavelength correction factor air (line), vacuum (points)

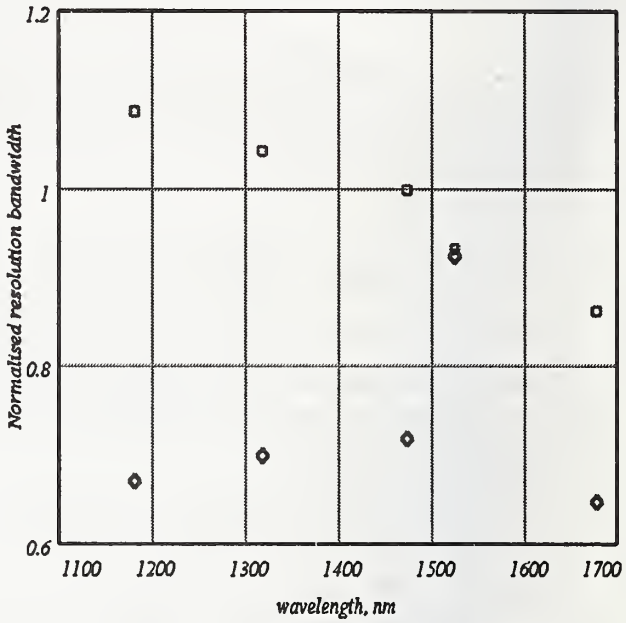

Figure 4 Wavelength dependence of the resolution bandwidth

References

1. D J E Knight et al.: 'Frequency standards for the optical-fiber communication bands: a review of user requirements and of physical possibilities for meeting them in practice', OSA 1993 Annual Meeting, 3-8 October 1993, Toronto Canada. Paper MB1 (invited), pp. 2-3.

2. A I Lucero et al: 'Survey of atomic transitions for absolute frequency locking of lasers for lightwave systems', IEEE Photonics Technology Letters, Vol. 3 (5), pp. 484-486, May 1991.

3. F Bertinetto et al: Frequency stabilization of DFB laser diodes to Hydrogen, Iodide at 1.5364 μm', OFC 1993.

4. D J E Knight et al: 'Frequency measurements on HI and Kr line at 1.548 μm', 10th European Frequency and Time Forum, 5-7 March 1996, Brighton, UK

5. D J E Knight et al: 'Absolute frequency measurement of the 3-0 R(21) transition of CO at 1.5605 μm for optical communication standards', Proc. EFTF 95, Besançon, March 1995.

6. CRC Handbook of Chemistry and Physics, 70th edition, R C Weast and D R Lide (ed), CRC Press, 1989.

7. Eldén: J. Opt. Soc. Am., 1953, **43**, 339

Nonlinearity of optical fiber power meters

Igor Vayshenker, Shao Yang*, Xiaoyu Li, Thomas R. Scott

National Institute of Standards and Technology, 325 Broadway, Boulder, CO 80303
*Ohmeda Medical Systems, Inc., Louisville, CO 80027

Abstract

We have developed a system for measuring the nonlinearity of optical fiber power meters over a dynamic range of more than 60 dB at three telecommunications wavelengths. This system uses optical fiber components and is designed to accommodate common optical powers; it is based on the triplet superposition method. This system provides accurate determination of optical power meter nonlinearity through the use of correction factors.

1. Introduction

The basic assumption for accurate optical power measurement is that the meter output reading is directly proportional to the optical input power. This proportionality property is called linearity, and the departure from this direct proportionality is defined as nonlinearity. Optical power meter nonlinearity is defined as the relative difference between the responsivity at an arbitrary power and the responsivity at the calibration power:[1]

$$\Delta_{NL}(P;P_c) = \frac{R(P) - R(P_c)}{R(P_c)}, \tag{1}$$

where R(P)=V/P is the responsivity of the meter at optical power P, the subscript c indicates the calibration point, and V is the meter output. A function that describes the relationship between the incident optical power P and the optical meter output is called the response function. The inverse of the response function is called the conversion function and is depicted in Figure 1.

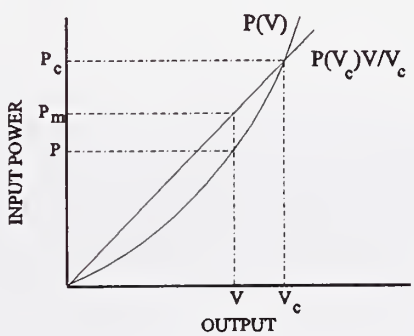

Figure 1. The conversion function.

It is often more convenient to use the conversion function rather than the response function. We can define the nonlinearity in terms of the output V as

$$\Delta_{NL}(V;V_c) = \frac{P(V_c)V}{P(V)V_c} - 1. \tag{2}$$

When the nonlinearity is small, a polynomial can represent the conversion function sufficiently well.

While the calibration gives the true input power from the power meter reading (output) at the calibration point, the measurement of nonlinearity and range discontinuity, together with calibration, provides this input-output relationship at any power within the entire dynamic range of the power meter.

It is, therefore, convenient to express the measured nonlinearity in terms of the conversion function P=P(V), which relates the input power P to the output V, and referenced to the calibration output V_c.

1.1. Correction Factor for Nonlinearity and Range Discontinuity

The true input power P is obtained from the power meter reading V by

$$P = \frac{V}{F_c \cdot CF}, \tag{3}$$

where $F_c = V_c/P_c$ is the calibration factor,

$$\begin{aligned} CF &= \frac{a_1[c]}{a_1[m]} \times \frac{1+\sum_{k=2}^{n} b_k[c]V_c^{k-1}}{1+\sum_{k=2}^{n} b_k[m]V^{k-1}} \\ &= \frac{a_1[c]}{a_1[m]}[1+\Delta_{NL}(V;0)-\Delta_{NL}(V_c;0)], \end{aligned} \tag{4}$$

a correction factor due to nonlinearity and range discontinuity, m is a number that corresponds to a specific range of an optical power meter, a_k and b_k are coefficients, and c corresponds to the calibration point. Consequently, each range of a power meter has its own correction factor. The degree of polynomial, n is usually equal to 3 or 4 depending on the size of the data standard deviation.

2. Measurement system and results

We have based the operation of our system on the triplet superposition method [2,3,4] which relies on the principle that, for a linear meter, the sum of meter outputs corresponding to inputs from two individual beams should equal the output when the two beams are combined and incident on the meter at the same time. The measurement system is depicted in Figure 2. We use a high-power, single-mode, fiber-pigtailed diode laser whose output power is stabilized; the laser is temperature-controlled. An external optical attenuator with a dynamic range of 60 dB is used to provide variable optical power. The optical power from the attenuator is divided into two approximately equal parts by introducing a 3 dB fiber splitter; one of the splitter arms has an additional length of fiber to avoid interference. A computer-controlled shutter is inserted into a collimated-beam section in each arm. Both signals are recombined in a 3 dB fiber coupler. We use single-mode fiber components throughout the system. We call a platform with fiber components and two shutters a switching matrix. The measurements were performed by taking sets of three power readings from the test meter: (1) shutter 1 is open and shutter 2 is closed, (2) shutter 1 is closed and shutter 2 is open, and (3) both shutters are open. This sequence is then repeated at different powers.

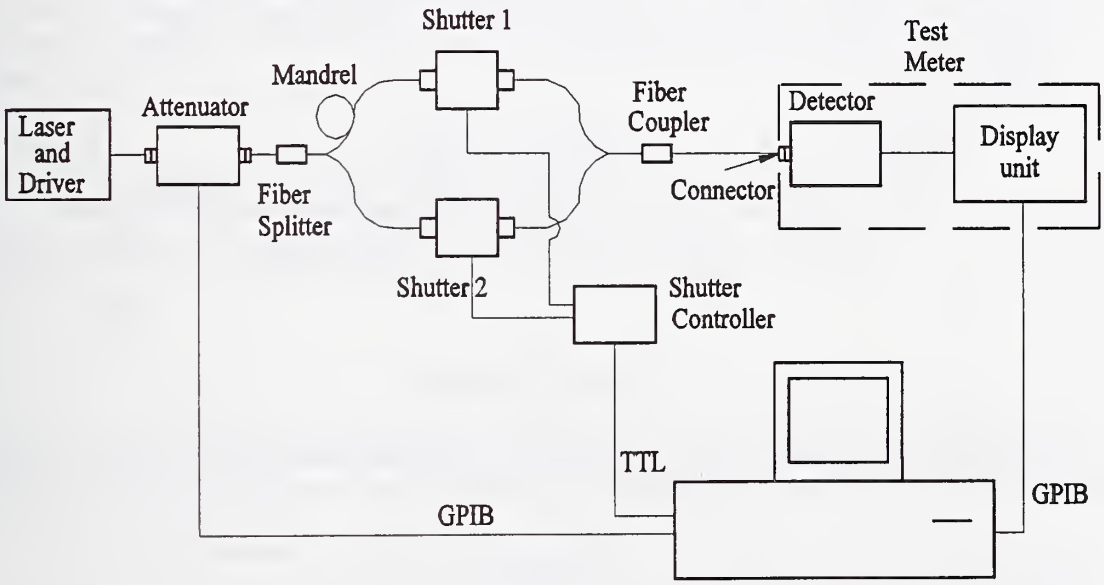

Figure 2. Measurement system.

We constructed two switching matrices: one for 850 nm, and the other for both 1300 nm and 1550 nm. Both switching matrices shared one attenuator. To measure the range discontinuity (offsets between range or scale settings), readings are taken at the lower power end of each range and compared to the readings on the higher power region of the next lower range (if any) at a constant power. The calculated correction factors result from the meter nonlinearity within each range, combined with the range discontinuity.

Figures 3 and 4 depict correction factors obtained on a typical optical power meter at 850 nm and 1300 nm, respectively. Each data group represents a separate power range of the meter. The same optical power meter was significantly nonlinear at 850 nm (Figure 3) and very linear at 1300

nm (Figure 4) .

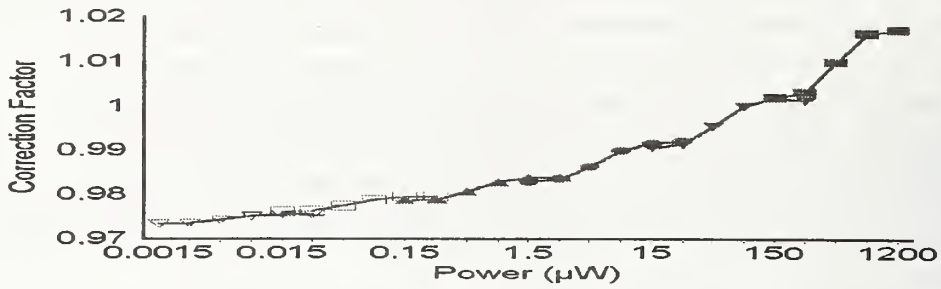

Figure 3. Correction factor vs. power at 850 nm.

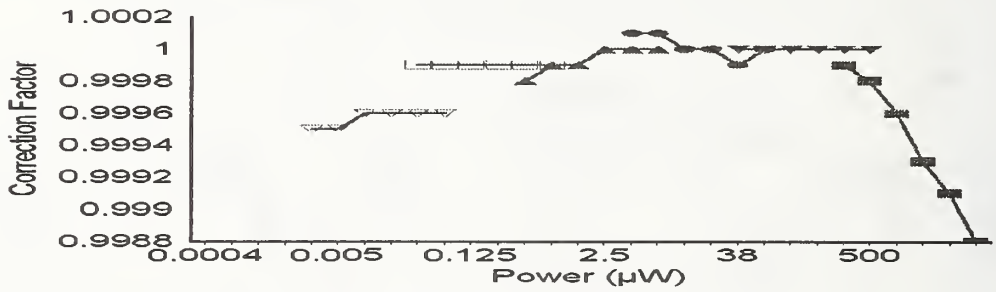

Figure 4. Correction factor vs. power at 1300 nm.

Acknowledgments

This work is supported by the Navy's Metrology R&D Calibration Standards Program under the management of Joe Dressel (NAVSEA 04312).

References

1. "Calibration of Fiber-Optic Power Meters," Draft International Standard, IEC TC 86, June 25,1992.

2. S. Yang, I. Vayshenker, X. Li, and T.R. Scott, "Optical detector nonlinearity: a comparison of five methods," Digest, Conf. Precision Electromagnetic Measurements, pp. 455-456, June-July 1994.

3. S. Yang, I. Vayshenker, X. Li, M. Zander and T.R. Scott, "Optical detector nonlinearity: Simulation," Natl. Inst. Stand. Technol. Technical Note 1376, May 19, 1995.

4. I. Vayshenker, S. Yang, X. Li, and T.R. Scott, "Automated measurement of nonlinearity of optical fiber power meters," Proc. SPIE, Vol. 2550, pp. 12-19, San Diego, CA, July 11-12, 1995.

Methods of Suppressing Stimulated Brillouin Scattering in Optical Fibers by Manipulation of the Fiber Properties

Clifford Headley, J. B. Clayton, and W. A. Reed

I INTRODUCTION

Stimulated Brillouin scattering (SBS) is a nonlinear optical process. Its occurance in optical fibers is characterised by an energy transfer from an input (pump) wave to a backward-traveling frequency-downshifted (Stokes) wave.[1,2] This occurs because the pump light generates an acoustic wave through the process of electrostriction. The acoustic wave causes a periodic modulation of the fibers refractive index creating a Bragg grating from which photons can be scattered. Because both energy and momentum must be conserved, counterpropagating photons are preferentially amplified. The frequency of the photons that are preferentially amplified is slightly less than that of the pump wave, due to the Doppler shift associated with the grating moving at the acoustic velocity. If a wave with the appropriate frequency shift is propagating counter to the pump wave it will be amplified. However, even in the absence of an input signal, SBS generates a Stokes wave from spontaneously scattered photons.

Both active and passive methods have been employed to suppress SBS. Active methods involve broadening the spectral width of the input pulse,[2] while passive methods involve modulating the fiber characteristics.[3-20] It is the passive techniques which are discussed here. Section II defines several terms and parameters necessary to understand the approaches described. Section III reviews the suppression techniques, and Section IV provides an experimental example. Finally, Section V summarizes.

II BACKGROUND

Stimulated Brillouin scattering is characterized by several parameters. These include the Brillouin frequency shift, ν_B, given as [1,2]

$$\nu_B = \frac{2n\nu_A}{\lambda_p}, \tag{1}$$

where n is the refractive index for light at the pump wavelength, ν_A is the velocity of the acoustic wave in the optical fiber, and λ_p is the wavelength of the pump light. ν_B represents the frequency difference between the pump and Stokes wave. The Brillouin frequency shift is typically on the order of 10 GHz at a wavelength of 1.55 μm in silica.

The growth in the energy of the Stokes wave at frequency ν is characterized by the Brillouin-gain coefficient $g_B(\nu)$. Assuming that the acoustic waves decay at a exponential rate characterized by the time coefficient T_B, and that the pump laser is operating in the continuous wave (cw) or quasi-cw (pulse width $T_0 >> T_B$) regime the Brillouin gain spectrum has a Lorentzian profile [1], with a peak value at $\nu = \nu_B$. The Brillouin gain spectrum is also characterized by its full width at half maximum, $\Delta\nu_B$, which is related to the lifetime of the acoustic waves by the expression $\Delta\nu_B = (\pi T_B)^{-1}$. $\Delta\nu_B$ is typically tens of MHz, and this relatively narrow spectral linewidth aids suppression techniques. If the assumption of the cw or quasi-cw operating regime is removed (pulse width $T_0 < T_B$) studies show that the SBS gain is significantly reduced, so that other nonlinear effects become important.[3]

In order to compare the effect of SBS between different fibers a figure of merit is necessary. Such a measure can be somewhat arbitrarily chosen. However, a convenient and often used condition is a threshold input power, P_{th}, defined as the input power necessary for the Stokes light at the input end of the fiber to equal the transmitted pump light. Assuming a Lorentzian gain profile this criterion is given by, [1]

$$\frac{g_B(\nu_B)\, P_{th} L_{eff}}{A_{eff}} \cong 21k\,, \tag{2}$$

where A_{eff} is the effective core area of the fiber, and L_{eff} is the effective interaction length of the fiber and is given by [1], $L_{eff} = \alpha^{-1}[1\text{-}\exp(-\alpha L)]$ where α is the loss coefficient of the fiber and L the actual fiber length. The factor k in Eq. (4) has a value between 1-2 depending on how well the pump and Stokes wave maintain their polarization states along the fiber. A value of k = 1.5 occurs when the polarization is completely scrambled.[21] For input pump powers greater than P_{th} the effects of SBS are considered significant.

P_{th} is a good figure of merit because it allows the calculation of the maximum power one can put into a fiber before SBS becomes significant. However, it has several disadvantages. The first shortcoming is that P_{th} increases with loss giving the impression one has a better fiber. To overcome this difficulty, a criterion which may be used is to specify an output power, $P_{out} = P_{th}(L) - \alpha L$, which is the amount of power that would be transmitted through a fiber of length L when P_{th} is the input power. The second drawback is that P_{th} is length dependent, and therefore does not readily allow the comparison of fibers of different lengths. To overcome this difficulty an increase in power P_{inc} may be specified. P_{inc} represents the increase in pump power into a fiber prepared using an SBS suppression technique compared to the same length of fiber prepared without applying SBS suppression. The increase in SBS threshold is then valid for arbitrary lengths of the fiber.

A final note about comparing the effects of SBS from one fiber to a next. $g_B(\nu_B)$ is dependent on the spectral width of the pump source, a fact that is used in active SBS suppression techniques. Hence the difference in pump spectral width must be accounted for when comparing fibers tested with different pump sources.

III SUPPRESSION TECHNIQUES

With the definitions given above an understanding of the passive methods used to suppress SBS can be obtained. These techniques rely on varying either the waveguide or material properties of the fiber so that the Brillouin frequency changes before the Stokes light at a given frequency reaches threshold.[4-19]. Because of the narrow linewidth of the Brillouin-gain curve, a small change in ν_B means that a new Stokes frequency is being amplified, thereby reducing pump depletion. Equation (1) shows ν_B can be changed by varying n or v_A.

The fiber properties can be modulated both during (fabrication processes) or after (external modulation) fabrication. As a general principal, fabrication processes have the advantage that the SBS suppression is an inherent property of the fiber and no additional effort is needed during fiber installation. However, the downside of fabrication processes compared to external modulation is that they tend to have a more drastic effect on other fiber properties such as loss or dispersion. External modulation techniques can be more easily applied to fibers such as dispersion compensating fibers (DCF) which are sitting in a hut and more accessible and also have less freedom in the design parameters. In what follows several techniques will be discussed. These methods include varying the fiber core area,[4-6], fiber-dopant concentration,[7-11] strain along the fiber,[12-16], inserting optical isolators along the fiber,[16] and temperature of the fiber[18-20],

III. 1 Fabrication Processes

During the fabrication process there are several properties of the fiber which can be modulated. These include the fiber core radius, fiber dopant concentration and residual strain induced on the fiber by the drawing process.

III.1.a Core Radius

Varying the fiber core radius along the fiber leads to a reduction in SBS. This results because a given fiber supports certain acoustic modes, [22-25] which travel at acoustic velocities determined by fiber

parameters such as core area. Changing v_A leads to a varying v_B and hence a reduction in SBS. It has been shown that v_B varies inversely with the core diameter.[4-6] In an experiment performed by Shiraki *et. al.* at a pump wavelength of 1.55 μm, a 14 km length of fiber whose mode field diameter changed from 8.11 μm to 6.93 μm showed a change in Brillouin frequency shift, δv_B, of 49 MHz.[4] This resulted in an increase in P_{th} of about 3.6 dB compared to similar fibers with constant radii. It should be noted that the appearance of multiple peaks in the SBS spectrum is due to more than one acoustic mode contributing to the SBS process.

From a practical standpoint, one problem in the fabrication of this fiber is that changing the core radius of the fiber affects other fiber properties such as dispersion and loss. The dispersion of an ordinary step index fiber increases with increasing core area.[5] In addition, the fiber diameter used in systems is a standardized value, and achieving a low-loss splice between two fibers of dissimilar areas is very difficult.

III.1.b Dopant Concentration

By changing the dopant concentration along the length of an optical fiber SBS effects can be reduced.[7-11] Both v_A and n are affected by the dopant concentration, but the majority of the shift in v_B arises form variation in v_A. This is because the material density, ρ, of the fiber is related to the amount of dopants present, and the velocity of sound in turn depends on ρ.[7] As already indicated a varying acoustic velocity modulates v_B and leads to the suppression of SBS.

In an experiment performed by Tateda *et. al.* [9] and by Shiraki *et. al.* [10,11] with fluorine as a dopant the refractive indices of the core and the inner cladding were monotonically lowered while keeping the relative index difference between the core and cladding the same. While the exact variation will depend on fiber type, in [10] a 7 dB increase in P_{th} was observed for a 350 MHz shift in v_B. By taking the derivative of Eq. (1) with respect to dopant concentration, and using the values of 356 MHz and 0.2 % for the changes in Brillouin frequency and fiber refractive index respectively, this calculation shows that it must be the change in acoustic velocity that leads to a change in v_B. By fabricating fibers with various dopant concentrations,[11] v_B was shown empirically to vary as $v_B = 11.045 - 0.277(F) + 0.045(GeO_2)$ [GHz].

One of the major drawbacks of this technique is that like changing the core radius, changing the dopant concentration affects other fiber properties. When F is added to a silica fiber the refractive index of the fiber decreases whereas GeO_2 increases n. As the index of the fiber is increased along the fiber length the fiber loss also increases. The opposite relationship between n and the dispersion holds true.[8]

III.1.c Strain

By varying the strain induced on a fiber during the draw process, the Young's modulus (defined as the ratio of stress to strain) of the fiber is modulated. The acoustic velocity of the fiber depends on the Young's modulus, therefore, changing the strain along the fiber raises the Brillouin threshold. A periodic residual strain can be applied to the fiber by varying the draw tension on the fiber during fabrication.[12,25]

In an experiment performed by Wada *et. al.* the drawing tension was varied rectangulary with an amplitude of 16 g every 2.5 km for a 23 km length of fiber.[12] A predicted 75 MHz change in v_B led to a 3 dB increase in the Brillouin threshold power. In this experiment, a fluorine-doped cladding\silica core fiber was used because the higher viscosity of the core caused it to solidify first during the drawing process, so that most of the residual strain due to draw tension will be in the core.

The reverse situation is true for the case of germanium-doped core\silica clad fibers, and the effect of strain in this type of fiber is reduced. This is the major drawback of this technique. [12] A second consideration is that there is a possible reduction in the lifetime of the fiber associated with introducing a higher strain in the fiber.

III. 2 External Modulation

Three external modulation techniques will be discussed here, varying the fiber strain, inserting isolators along the fiber, and introducing a temperature variation along the fiber.

III.2.a Strain

The effect of strain on reducing the SBS threshold was described in Section III.1.c, the difference here is that the strain is induced on the fiber after fabrication.[13-16] The relationship between the residual strain change, $\delta\varepsilon$, and the frequency shift, $\delta\nu_B(\varepsilon)$, normalized to the unstrained frequency shift, $\nu_B(0)$, was calculated and verified for a variety of cladding/ core dopant values for both fluorine and germanium doped fibers by Kurashima *et. al.*.[16] A linear variation was measured, and while the exact value of this parameter depends on which dopant is used and how much of it, the variation with these parameters was fairly small[13-16].

In one very clever experiment by Yoshizawa et. al. [14,15] twelve strands of optical fibers were wrapped around a coated wire. Four such bundles of twelve optical fibers were themselves then wrapped around a larger coated wire. The effect of this double wrapping was to vary the strain along the fiber sinusoidally, which in turn varied the velocity of sound in the fiber leading to a 7 dB increase in the SBS threshold. Moreover the fiber loss was measured and found to be equal to that before the wrapping.

The major drawback to this particular method of SBS suppression is that the lifetime of the cable is reduced. In the experiment described above, carbon coated fiber was used because of the increased strain. In addition implementing the strain variation can be difficult.

III.2.b Isolators

One of the most simple and obvious ways of reducing SBS is to introduce a directionally dependent loss into the fiber so that any backscattered light is reduced whilst the input light is passed. This can be done by the insertion of optical isolators along the fiber.[17] Under ideal conditions where there is no isolator insertion the increase in the SBS threshold should be N + 1 where N is the number of isolators. In an experiment performed by Takustina *et. al.* an isolator was inserted into a fiber, it was shown that the transmitted power level for SBS was raised by 1.2 dB. This deviation from the predicted 3 dB ideal value is due to insertion losses and less than total isolation.

This technique suffers from the problems of very minimal improvement, significant increase in the fiber loss, increased cost associated with buying isolators, and splicing into the fiber. However, this result made a very significant point, and that is that the ideal placement of the isolator is towards the beginning of the fiber span, a principle which is useful for all SBS suppression techniques

III.2.c Temperature

The Brillouin frequency shift experienced by a fiber is temperature dependent. If a length dependent temperature change is applied across the fiber length then the effect of SBS can be reduced.[18-20] Mathematically, the temperature variation of ν_B can be found by taking the derivative with respect to temperature, T, of Eq. (1). Both ν_A and n have a temperature dependence, but the dominant contribution to this frequency shift comes from the change in refractive index, with the change in acoustic velocity accounting for only about 7 % of the total contribution.[19] The linear variation of ν_B with temperature was found by Kurashima *et. al.* to be 1.33 MHz/°C for a silica core\flourine-doped cladding fiber, and for germanium-doped core/silica cladding fiber 1.17 MHz/°C, both measured with a 1.32 μm wavelength.[18] Exact values for a fiber will depend on the dopant concentration. For both fibers the core cladding index difference was 0.3%. Interestingly enough it is found that the Brillouin gain bandwidth also decreased linearly as temperature increased.[18]

In another experiment conducted by Imai *et. al.* half of a fiber spool was heated and hence a temperature gradient was introduced along the fiber.[20] As the temperature gradient along the fiber was increased the SBS threshold was raised by 3.5 dB corresponding to a 35 °C temperature difference across the fiber.

There are two drawbacks to this procedure. The first is that this is more difficult to implement for fibers that are distributed along a span. This technique more readily lends itself to fibers that that remain on a spool such as dispersion compensating fiber. It maybe especially useful for fiber spools in devices which can be packaged to take advantage of the heat generated by other devices, as some form of power supply is necessary in order to supply heat to or cool the fiber

IV EXPERIMENTAL RESULTS

Figure 1 shows a typical experimental setup for measuring the increase in Brillouin threshold in a fiber sample. The output of the pump laser passes through a variable attenuator, which controls the power entering the test fiber. From the attenuator the light goes through port 1 of a tap which nominally sends 99 % of the light into the test fiber through port 2, while 1 % of the light is measured at port 3 as a monitor of the input signal. One percent of any light that is backscattered in the fiber enters the tap through port 2, is detected on the 4th arm of the tap, and this signal is used as a measure of the Stokes light. The loss across each port and the exact percentage of light transmitted at ports 3 and 4 are

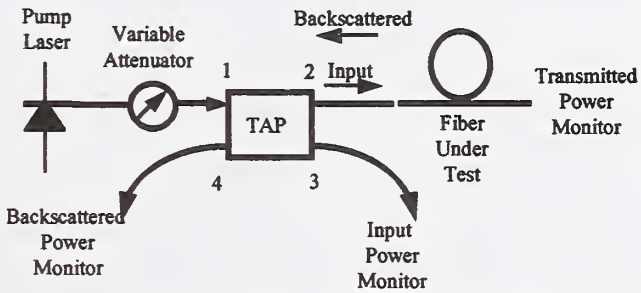

Fig. 1 Stimulated Brillouin scattering measurement setup.

measured by inserting known power values into ports 1 and 2 respectively and measuring the power across the other arms. The Brillouin frequency shift is measured using a HP71400C Lighhtwave System Analyzer.

For illustrative purposes the use of temperature to increase the Brillouin threshold is studied. Twelve kilometers of dispersion compensating fiber was wound onto three separate spools, with the first and last sections each 3 km long. This allows portions of the fiber to be independently cooled in LN_2, and the corresponding SBS threshold for that situation to be measured. When the input and output ends of the fiber were cooled there was a 3dB increase in the P_{th}. The reason for this is seen in Fig. 2, which is a plot of the normalized spectrum of the beat signal between the pump and Stokes signal, (a) when the

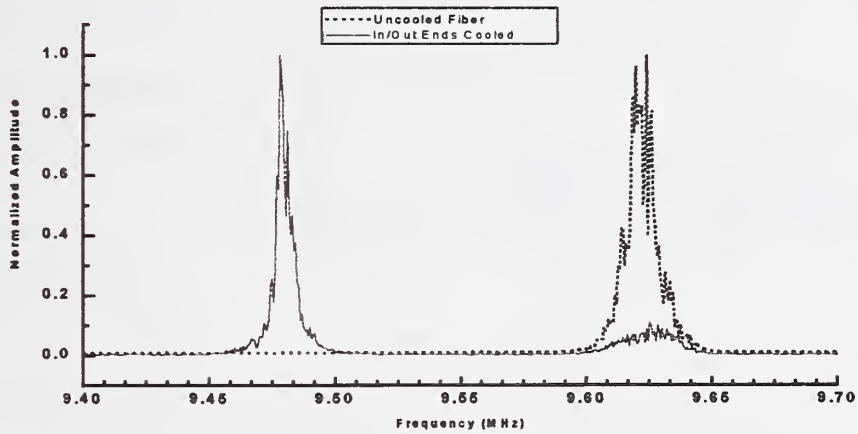

Figure 2. Plot of Brillouin frequency shift for (a) uncooled fiber (dotted) and (b) input and output ends cooled (solid).

fiber is uncooled and (b) when the input and output ends of the fiber are cooled These results show that cooling the fiber has the effect of shifting a portion of the Stokes energy by 150 MHz. This result corresponds to a temperature coefficient of Brillouin frequency shift $d\nu_B/dT$ of 0.75 MHz/°C, a figure

lower than that given in Section III.2.c due to the larger amount of Ge doping in dispersion compensating fiber.[18] The shift in frequency of the Stokes energy leads to the reduction in SBS threshold.

V. CONCLUSIONS

Several techniques for reducing SBS both during and after fiber fabrication were reviewed. These techniques included modulating the fiber properties such as core radius, dopant concentration, fiber strain both during and after production, temperature along the length of the fiber, and inserting isolators. The advantages and disadvantages of each particular technique were given. For heuristic purposes, an experiment to measure the increase in Brillouin threshold due to temperature changes was presented.

REFERENCES

1. G. P. Agrawal, *Nonlinear Fiber Optics*, 2nd ed. (Academic, San Diego, 1995).
2. D. Cotter, J. Opt. Commun., **4**, 10-19 (1983).
3. A. R. Chraplyvy, IEEE J. Lightwave Technol., **8**, 1548-1557 (1990).
4. K. Shiraki, M. Ohashi and M. Tateda, Electron. Lett., **31**, 668-669 (1995).
5. K. Shiraki, M. Ohashi and M. Tateda, Proc. 21st Conf. on Opt. Comm. 325-328 (1995).
6. M. Ohashi, N. Shibata and K. Shiraki, Electron. Lett., **28**, 900-902 (1995).
7. R. W. Tkach, A. R. Chraplyvy and R. M. Derosier, Electron. Lett., **22**, 1011-1013 (1986).
8. M. Ohashi and M. Tateda, J. Lightwave Technol., **11**, 1941-1945 (1993).
9. M. Tateda, M. Ohashi and K. Shiraki, OFC/IOOC 1993 Technical Digest paperThJ4.
10. K. Shiraki, M. Ohashi, and M. Tateda, J. Lightwave Technol., **14**, 549-554 (1996).
11. K. Shiraki, M. Ohashi, and M. Tateda, J. Lightwave Technol., **14**, 50-57 (1996).
12. A. Wada, T. Nozawa, D. Tanaka, T. Sakai, and R. Yamauchi, Proc. European Conf. on Opt. Commun. 1991 MoB1, (1991).
13. T. Horiguchi, T. Kurashima and M. Tateda, IEEE Photon. Techn. Lett., **1**, 107-108 (1989).
14. N. Yoshizawa, T. Horiguchi and T. Kurashima, Electron. Lett., **27**, 1100-1101 (1991).
15. N. Yoshizawa and T. Imai, J. Lightwave Technol., **11**, 1518-1522 (1993).
16. T. Kurashima, T. Horiguchi, and M. Tateda, 7th International Conf. on Integrated Optics and Optical Fiber Communication, **4**, 21C4-2 70-71 (Kobe Japan 1989)
17. Y. Takushima and T. Okoshi, Electron. Lett., **28**, 1155-1157 (1992).
18. T. Kurashima, T. Horiguchi and M. Tateda, IEEE Photon. Techn. Lett., **2**, 718-720) (1990).
19. D. Culverhouse, F. Farahi, C. N. Pannell, and D. A. Jackson, Electron. Lett. **25**, 913-915 (1989).
20. Y. Imai and N. Shimada, IEEE Photon. Techn. Lett., **5**, 1335-1337 (1993).
21. C. K. Jen. A, Safaai-Jazi and G. Farnell, IEEE Trans. Ultrasonics, ferroelectrics and frequency control, **33**, 634-643 (1986).
22. N. Shibata, K. Okamoto and Y. Azuma, J. Opt. Soc. Am. B, **6**, 1167-1174 (1989).
23. W. Henry, Int. J. Optoelec., **7**, 453-478 (1992).
24. M. Ohashi, N. Shibata and K. Shiraki, Electron. Lett., **28**, 900-902 (1992).
25. U. Paek and C. Kurkjian, J. Am. Ceramic Soc. **58**, 330-335 (1975).

Local Analysis of Stimulated Brillouin Interaction in Installed Fiber Optics Cables

Marc Niklès, Luc Thévenaz, Pascal Salina*, Philippe A. Robert

Swiss Federal Institute of Technology, Metrology Laboratory, CH-1015 Lausanne, Switzerland

* Swiss Telecom PTT, Ostermundigenstr. 93, CH-3029 Bern, Switzerland

Brillouin gain spectrum measurement along an optical fiber has recently gained a lot of interests owing to its potentiality for strain monitoring in installed telecom cables [1,2]. The purpose of this paper is to show that this potentiality is being now effective, since field measurements of installed fiber optics cables *currently in operation* are demonstrated. A portable instrument has been developed, based on an original experimental configuration developed in our Institute [3] that is shortly described below.

The Brillouin Gain Spectrum (BGS) in silical optical fibers is downshifted with respect to the pump light frequency by the Brillouin frequency shift ν_B which takes values from 11.5 to 13 GHz depending on the refractive index profile at a pump wavelength near 1300 nm [4]. The value of ν_B turns out to be very strain sensitive, shifting ν_B by about 600 MHz per percent of elongation [5]. This measurement requires two light waves propagating in opposite directions throughout the fiber, since Stimulated Brillouin Scattering (SBS) amplification is possible only in the backward direction. One light wave pumps the medium and the other acts as a probe signal, experiencing amplification when it lies within the Brillouin gain spectral range.

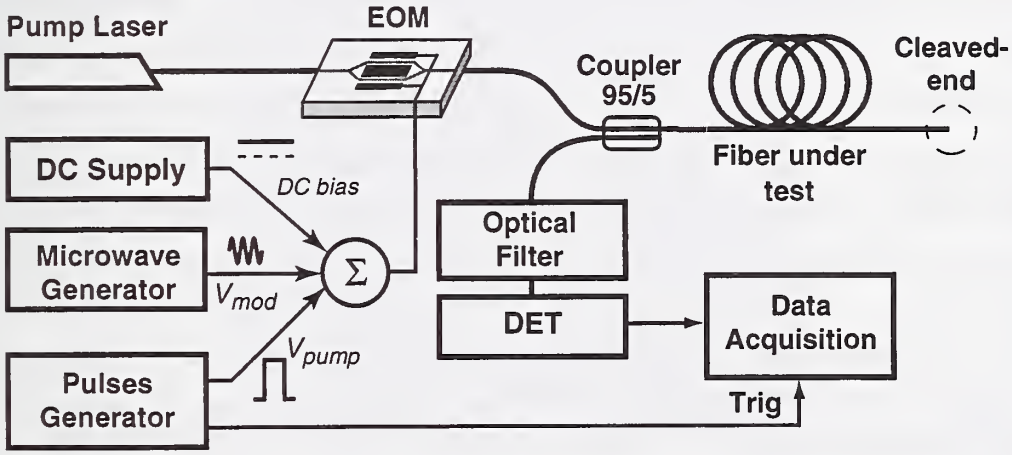

Fig.1: Experimental setup used for distributed temperature measurement.

Distributed measurements can be performed using a modified OTDR technique. The experimental configuration shown in Fig.1 is based on the pump and probe technique and presents the following advantages for field measurements: *1) a single fiber end is accessed, 2) a single laser source is used, 3) few optical elements are required.*

An ultra-wideband integrated $LiNbO_3$ intensity electrooptic modulator (EOM) is the key element of the setup, since it is used for: 1) pulsing the CW laser light from a 150mW Nd:YAG laser to form the pump signal, 2) the generation and frequency tuning of the probe signal. The frequency shift of the laser light is achieved by simply applying a CW microwave signal on the EOM electrodes. This creates sidebands in the laser spectrum, so that the first lower sideband lies in the BGS generated by the pump, when the modulation frequency f_m is close to the Brillouin frequency shift ν_B. The DC bias voltage on the EOM basically just determines the amount of transmitted amplitude of the fundamental frequency. It is set, so that the carrier is totally suppressed and the remaining probe signal is uniquely made of the modulation sidebands. The CW probe and the pump pulses are both launched into the fiber under test at the same fiber end. The pump pulse provides gain to the probe signal during its forward propagation through the SBS process while the probe signal is amplified on the way back. Only a few percent of reflection is necessary at the fiber far end, so that Fresnel reflection is actually sufficient. Since the first upper sideband is not relevant for the measurement and even has a negative effect on the contrast, it must be suppressed using an optical filter. The probe intensity is monitored as a function of time and the delay between the launch of the pump pulse and the detection of the probe signal gives the positional information.

This technique makes the scan of the probe optical frequency very simple and convenient by just varying the microwave signal frequency. Since this technique uses a single laser and a modulator for the generation of the pump and probe signals, it insures a perfect stability of their frequency difference. Measurements of the distribution of the Brillouin frequency shift along a sensing fiber can therefore be performed with an excellent resolution using this technique. The measured standard deviation in the determination of the Brillouin shift frequency is 300 kHz. The best spatial resolution obtained so far is 15 m for a standard fiber, given by the minimum pump pulse width leaving a sufficient gain.

Local analysis of stimulated Brillouin interaction (LASBI) measurements were carried out on a 6.8 km-fiber optics cable link between the Swiss Telecom exchange stations of Versoix and Anières across the lake of Geneva, Switzerland. A part of the cable is designed for underwater applications and contains 2 tubes with 10 single mode optical fibers. Each fiber link is actually made of 5 segments of fibers spliced together. The topographical arrangement is schematically shown in Fig.2a, the successive splices being indicated by S1 through S4. Starting from the exchange station of Versoix, the conduit route can be described as follow: the first section of cable (560m) is a standard unarmoured telecom fiber optics cable, then 60m of the same cable (S1-S2) is used to join the underwater cable (armoured reinforced cable). The first 460m of the underwater cable goes through the lake of Geneva shore line and approximately 3700m are laid on the lake bed. On the other waterside, 360m of conduit brings the cable to a manhole where it is spliced (S3) to a 550m standard telecom cable. Finally 590m of another cable joins from S4 to the exchange station of Anières.

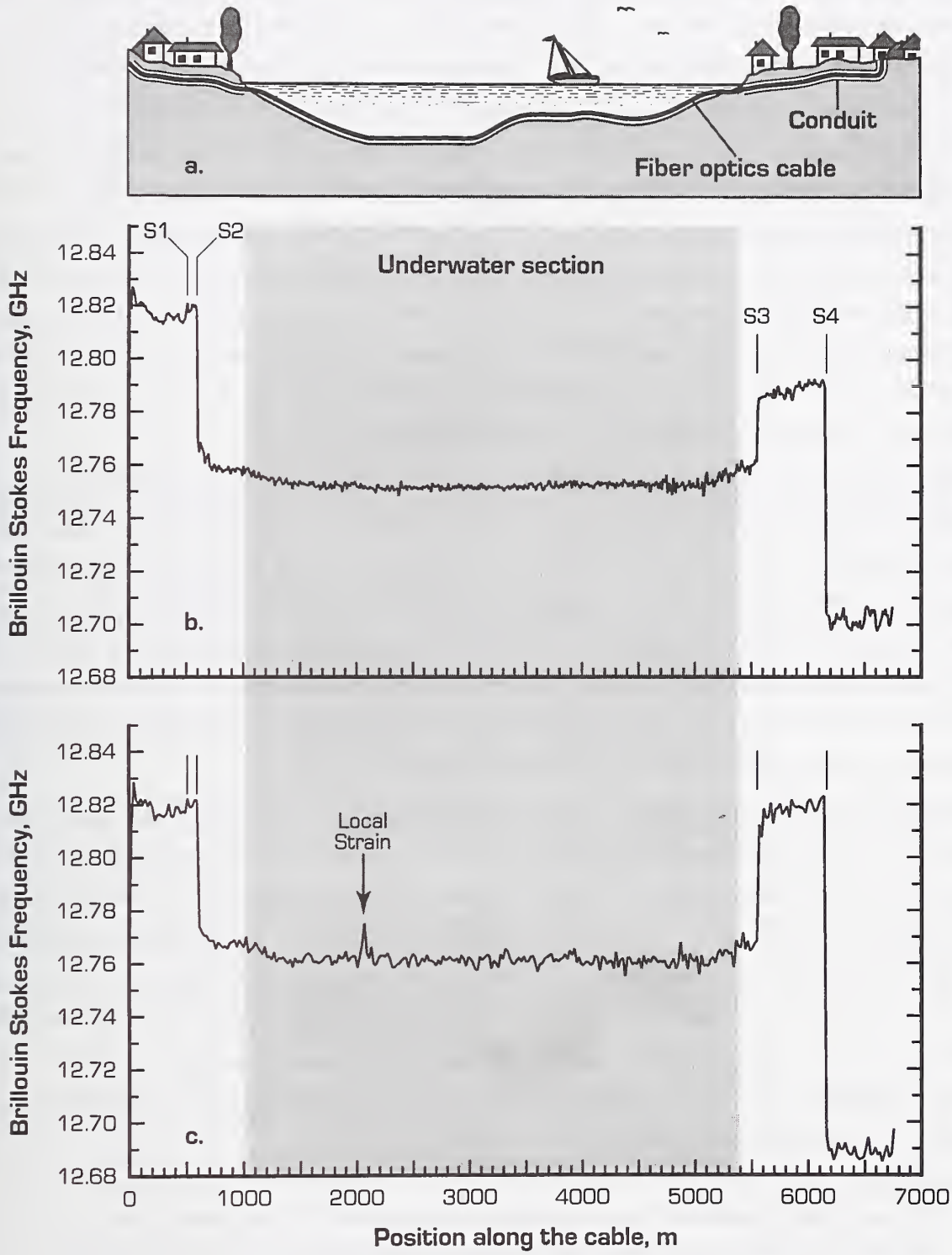

Fig.2 *Measurement of the Brillouin frequency shift on a underwater fiber optics cable. Topographical representation of the cable route (a). Local Brillouin frequency shift measured with a 20m spatial resolution for 2 different fibers of the cable (b and c).*

Several optical fibers of the cable have been tested. Fig. 2b and 2c shows the Brillouin frequency shift ν_B along two fibers measured with a 20m spatial resolution. The different sections of the cable are clearly identified by their different ν_B. The ν_B value can differ from fiber to fiber depending on the fiber parameter [3].

On the terrestrial route, the cable is installed in a conduit. The temperature being relatively constant in the conduit, the changes in the Brillouin frequency shift are attributed to local strain. On the contrary the underwater portion is just laid on the lake bed and is consequently subjected to temperature variations. As a matter of fact the temperature gradient of the water is clearly observed on the two plots of Fig.2. The temperature is measured to be actually 5°C colder (frequency shift of 6.45 MHz smaller) at the deepest point (61m depth, positions 2000m to 3000m in the cable) than the water temperature nearby the shores (positions 1090m and 5300m). At 2600m away from the shore (position 3690m) the depth of the lake goes up to 31m and an 1°C increase is detected.

Concerning the strain experienced by the fibers, the first and last sections of the cable are installed through a winding route and undergo many strong curvatures. Nevertheless the variations of the measured Brillouin frequency shift (Fig.2b) is 12.9MHz and 11.6MHz for the first and last section respectively, corresponding to $2.15*10^{-4}$ and $1.9*10^{-4}$ equivalent strain. The section between S3 and S4 presents a slight slope that corresponds to a $1.1*10^{-4}$ strain. In Fig.2c the peak at position 2100m in the underwater section is attributed to a local strain. Even though the magnitude of the perturbation is not perfectly resolved because of the spatial resolution of the system (20m), the problem is easily detected. However the local strain is probably higher than the measured $2.7*10^{-4}$.

A portable instrument for local Brillouin gain spectrum analysis has been built and was used for on site measurements. Using the LASBI system, a fiber optics link can be guarantied to be strain free, which is the key information for its long-term reliability. Tests have been conducted on currently operating telecom cables and show that local strain can be introduced in the fiber by the installation procedure. The different fiber sections of fiber optics cables can also be easily identified, which is an interesting feature for diagnostic purposes. The results from this technique are steadily improving along with system optimization, in particular for spatial resolution. Other measurements were carried out on different installations such as aerial cables. These measurements show very minor fluctuations of the Brillouin shift, so that fibers are granted to be strain free.

References

1. T.Horiguchi, T.Kurashima, M.Tateda, *IEEE Photonics Technol. Lett.*, **2**, (1990), p.352.
2. M.Tateda, T.Horiguchi, T.Kurashima, K.Ishihara, *J. Lightwave Technol.*, 8, (1990), p.1269.
3. L. Thévenaz, M. Niklès, P. Robert, in *Symposium on Optical Fiber Measurement, Boulder CO, NIST Special Publication 864 (US Gov. Printing Office, Washington, D.C.)*, p.211 (1994),
4. M.Niklès, L.Thévenaz, P. Robert, *Optics Lett.*, 21, (1996), p.758.
5. M. Niklès, C. Gabioud, L. Thévenaz, P. Robert, in *3rd Optical Fibre Measurements Conference* , OFMC'95 (Liège), paper VII.2. (1995).

Non-invasive mapping of dispersion in optical fibers

R. M. Jopson
Crawford Hill Lab
Bell Labs, Lucent Technologies
Holmdel, NJ 07733 USA

M. Eiselt
Heinrich Hertz Institut
Berlin, Germany

Fiber chromatic dispersion has played an important role in the design of optical fiber systems for more than a decade. Until the advent of the eminently practical erbium-doped fiber amplifier, the systems were more or less linear; hence, it was only the integrated dispersion over a fiber span that influenced system performance. As we have become more sophisticated in our use of optical fiber, and ever more greedy in extracting performance from lightwave systems, fiber nonlinearity has become important either as a tool or as an impairment. As a consequence, it has become important to know the distribution of the chromatic dispersion along a fiber span rather than just the average dispersion. Dispersion management, in which a dispersion "map" is chosen so as to minimize the effects of fiber nonlinearities, is becoming an important tool.

Traditional fiber dispersion measurement determines only the average dispersion of a fiber span. However, in dispersion-shifted fiber (DSF), dispersion is known to vary as a function of location in the fiber. In one (destructive) measurement[1] using a 10-km length of DSF cut into four 2.5-km segments, it was found that the average dispersion zero wavelength for the segments varied by at least 1 nm - a significant deviation for some applications. Deployment of erbium-doped fiber amplifiers (EDFA's)in lightwave systems has led to "dispersion management" as a tool for system designers to further enhance system performance and to suppress optical nonlinearities.

An early method[2] for mapping the distribution of dispersion in a fiber span is based on Rayleigh backscattering. This technique relies on the dependence of the dispersion zero on the fiber core size. If the doping of the preform does not change over its length then changes in the dispersion zero can be inferred from changes in the core size. Changes in core size can be estimated using optical time-domain reflectometry (OTDR) to determine the capture ration for Rayleigh backscattered light. By summing OTDR measurements taken in opposite directions, the effects of fiber loss can be removed and changes in the capture ratio can be observed and used to determine variation in the fiber dispersion zero.

Recently, a non-destructive dispersion measurement method was described[3] that determined the local dispersion zero from modulation-instability-induced gain at wavelengths longer than the dispersion zero. A strong pump pulse of wavelength λ_p and a weak signal pulse of wavelength λ_s are injected simultaneously into a test fiber with $\lambda_p - \lambda_s$ being 5 to 10 nm. The backscattered signal light is observed through OTDR. When the

pump wavelength is near the dispersion zero, but in the anomalous dispersion region, the modulation instability will provide gain for the probe pulse, gain that can be observed in the OTDR trace. Thus reduction in the slope of the OTDR at a particular distance into the fiber indicates that the pump is experiencing anomalous dispersion at that point in the fiber. To map fiber dispersion, the pump and probe wavelengths are swept, maintaining a constant separation, $\lambda_p - \lambda_s$, and the resultant OTDR traces are recorded. The dispersion zero of a particular point in the fiber is at the short-wavelength side of those pump wavelengths for which modulation-instability gain is observed. This technique has demonstrated a wavelength resolution of 0.2 nm and a distance resolution of about a kilometer.

Another technique[4] uses partially-degenerate four-photon mixing[5,6] to determine the dispersion zero. This technique will be the topic of the remainder of this summary. The mixing generates an idler wave from pump and signal waves of angular frequencies ω_p and ω_s propagating in the fiber. The power of the idler wave with frequency $\omega_i = 2\omega_p - \omega_s$, will be maximized when the process is phase matched, that is, when $\Delta\beta = 2\beta(\omega_p) - \beta(\omega_s) - \beta(\omega_i) = 0$, where $\beta(\omega)$ is the propagation constant. To first approximation, phase matching occurs when ω_p is set to the dispersion zero of the fiber[5]. We measured the zero-dispersion wavelength by tuning ω_p and looking for a maximum in the idler power. Distance resolution was obtained by using signal and pump pulses with widely-separated wavelengths. As illustrated in Figure 1, the differing group velocities of the pump and signal pulses cause the pump pulse to overtake the signal pulse (assuming the pump wavelength is near the dispersion zero of the fiber). With sufficient group-velocity dispersion and short enough pulses, the region of overlap of the pulses occurs over some useful distance which will be the distance resolution of the technique. The timing of the pulses at ω_s and ω_p can then be adjusted so that this overlap occurs at some desired point within the fiber.

The apparatus used is shown in Figure 2. A master oscillator - power amplifier chip operating at a single frequency of 1486.45 nm provided the signal. It was modulated by a $LiNbO_3$ Mach-Zehnder modulator to generate a 100-MHz train of pulses having a FWHM of 100 ps. Pump pulses with a FWHM of 60 ps were generated by an actively modelocked EDFA ring laser which could be tuned over the gain bandwidth of the EDFA with a combination of a 4-nm FWHM thin-film tunable filter and a 0.1-nm FWHM tunable fiber Fabry-Perot filter. The two pulses were combined with a 1480/1550 wavelength-division multiplexer and coupled into the test fiber. Relative pulse delay was adjusted by a variable electrical delay line. The dispersion between the signal and the pump was 140 ps/km. With appropriate delay, the pulses overlapped for about 1 km in the fiber. At the input to the test fiber, the peak signal power was 0 dBm while the pump had a peak power of +17 dBm. The generated idler near 1610 nm was observed on an optical spectrum analyzer. A travelling-wave Bragg grating band-reject filter attenuated the ~1546-nm signal entering the optical spectrum analyzer to reduce scattering-induced background within the instrument. The amount of ~1610-nm light generated varied by more than 10 dB with changes in pump and signal polarizations. This variation was reduced to less than 0.2 dB by modulating the polarization of the signal with a great-circle polarization scrambler. The spectral features obtained using the scrambler closely mimicked those obtained by

optimizing the polarizations at each wavelength.

While the technique requires that ω_p be scanned near the dispersion zero of the fiber, almost any signal wavelength will work. The pulse overlap range in the fiber decreases as the minus two power of ω_s - ω_p, so a large separation will provide good position resolution. However, improved resolution comes at the expense of decreased mixing efficiency. Also, separations beyond the 60-nm used in our measurements put the mixing-product in a spectral region of decreasing detector sensitivity and increasing fiber loss. We chose 1485-nm as a convenient compromise for the signal wavelength because of the availability of high-power sources. Positional resolution can also be improved by using short pulses, but wavelength resolution will suffer for signal pulse widths much shorter than 30 ps due to spectral broadening.

Maximal mixing efficiency actually occurs when ω_p is set slightly off the dispersion zero because of Kerr-effect shifts[5] and high-order curvature[7] in $\beta(\omega)$. For our power levels, the Kerr-effect shift was negligible. To determine the higher-order curvature shift precisely, one needs to know the fourth (and higher) order curvature of $\beta(\omega)$ at each desired location in the fiber. However, we found that the average curvature obtained from a conventional chromatic dispersion measurement was sufficient to determine the curvature shift to within ±0.1 nm at any location in the fiber. In the measurement described here, the dispersion zero was the phase-matching wavelength plus 1.2 nm.

To test the accuracy of the technique, we chose a 9.7 km length of DSF with an interesting dispersion-zero profile and nondestructively measured the dispersion zero from each end. We then cut the fiber into 500-m sections and measured the average dispersion of each section using conventional means. The results are shown in Figure 3, where the non-destructive data has been corrected for the $\beta(\omega)$-curvature shift described above by adding 1.2 nm to the measured phase-matching wavelengths. This correction was obtained from a dispersion measurement of the intact fiber. The good agreement between nondestructive measurements made from opposite ends shows that there are no large systematic errors that depend on the position of the overlap region. It can also be seen that the non-destructive measurements agree with the destructive measurements to within ±0.2 nm when the latter data is averaged over 1 km. Some of the observed discrepancy is caused by variation of the dispersion zero within the overlap region.

The spectrum produced by the technique can reveal more detailed information about variations in the dispersion zero than would be inferred from the 1-km location resolution. For example, a splice between fibers with different dispersion zeros appears as two peaks in the mixing spectrum. One of these peaks grows as the delay increases while the other peak shrinks. By observing the growth and diminution of these peaks, one can obtain a more accurate fiber dispersion-zero map than is obtained when this information is reduced to the one number shown in Figure 3. Figure 4 shows the noninvasively-measured map of the zero-dispersion wavelength of a concatenated fiber. Analysis of the spectral peaks in the region surrounding the fiber splice near 24 km, shows that the distance resolution (15% to 85% of asymptotic peak height) of the measurement shown here is 1.4 km.

The growing awareness of a need for non-destructively mapping chromatic dispersion in fibers has spawned a number of techniques for measuring zero-dispersion wavelengths or in some cases, the measuring fiber dispersion at some desired wavelength. Current non-invasive techniques for dispersion-zero measurements have a distance resolution of 0.1 to 1 km and a wavelength resolution of several tenths of nanometer. Advances are being made rapidly, and it is likely that before this talk is given, we will see new techniques and resolution improvements to existing techniques.

[1] K.Inoue, "Four-wave mixing in an optical fiber in the zero-dispersion wavelength region", *J. Lightwave Technol.,* **10,** pp. 1553-1561, (1992).

[2] M. Ohashi and M. Tateda, "Novel Technique for measuring longitudinal chromatic dispersion distribution in singlemode fibres", *Electron. Lett.,* **29,** 426-428, (1993).

[3] S. Nishi and M. Saruwatari, "Technique for measuring the distributed zero-dispersion wavelength of optical fibres using pulse amplification caused by modulation instability", *Electron. Lett.,* **31,** pp. 225-226, (1995).

[4] A. M. Vengsarkar, and U. Koren, "Non-destructive dispersion -zero measurements along an optical fibre", *Electron. Lett.,* **31,** pp. 2115-2117, (1995).

[5] R. H. Stolen and J. E. Bjorkholm, "Parametric amplification and frequency conversion in optical fibers", *IEEE J. Quantum. Electron.,* **QE-18**, pp. 1062-1072, (1982).

[6] N. Shibata, R. P. Braun, and R. G. Waarts, "Phase-mismatch dependence of efficiency of wave generation through four-wave mixing in a single-mode optical fiber," *IEEE J. Quantum. Electron.,* **QE-23**, pp. 1205-1210, (1987); see also R. W. Tkach, A. R. Chraplyvy, F. Forghieri, A. H. Gnauck, and R. M. Derosier, "Four-Photon Mixing and High-Speed WDM Systems", *J. Lightwave Technol.,* **13**, pp. 841-849, (1995).

[7] C. Lin, W. A. Reed, A. D. Pearson and H-T. Shang, "Phase matching in the minimum-chromatic-dispersion region of single-mode fibers for stimulated four-photon mixing," *Opt. Lett.,* **6**, pp. 493-495, (1981).

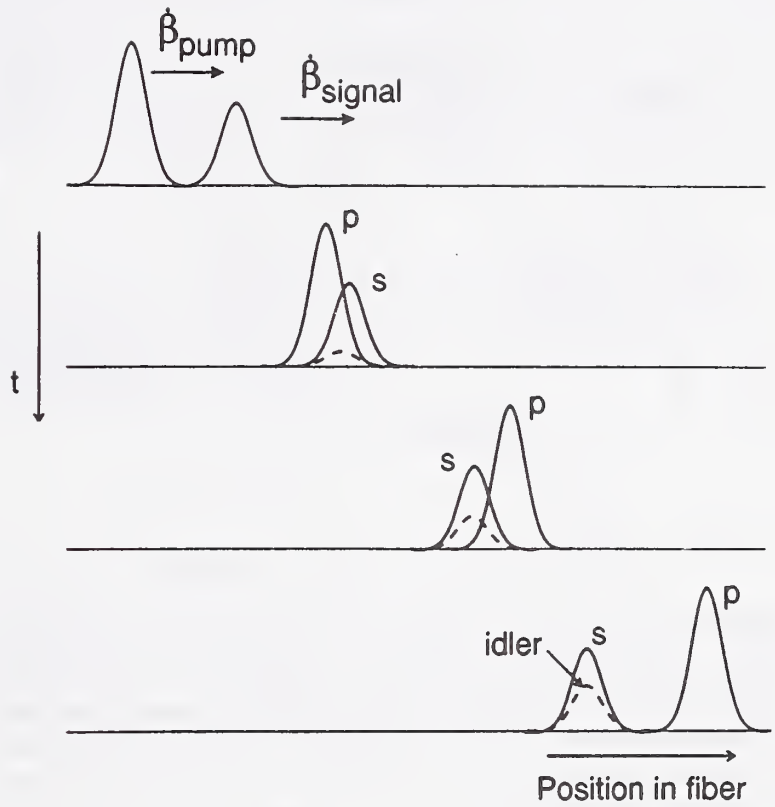

Figure 1: Schematic of the principle used in the four-wave mixing method for mapping fiber dispersion zeros. The relative positions of the pump pulse, labeled "p", and the signal pulse, labeled "s" are shown for successive times, t, as the pump overtakes the signal. During the overlap, an idler pulse is generated which will travel at a group velocity close to that of the signal pulse.

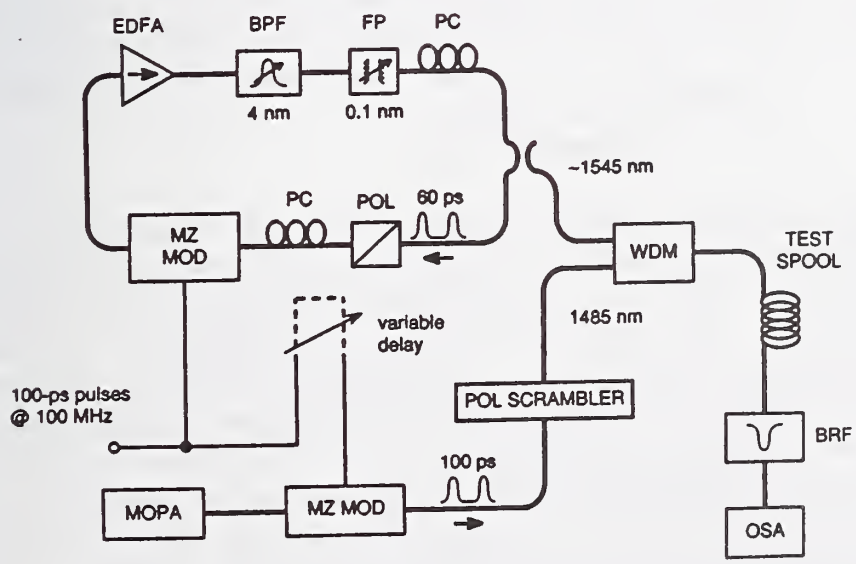

Figure 2: Apparatus. BPF, tunable band-pass filter; BRF, band-reject filter; EDFA, erbium-doped fiber amplifier; FP, tunable Fabry-Perot filter; MOPA, master oscillator power amplifier; MZ-MOD, Mach-Zehnder modulator; OSA, optical spectrum analyser; PC, polarization controller; POL, linear polarizer; POL SCRAMBLER, polarization scrambler; WDM, wavelength-division coupler; XCAV, external-cavity laser.

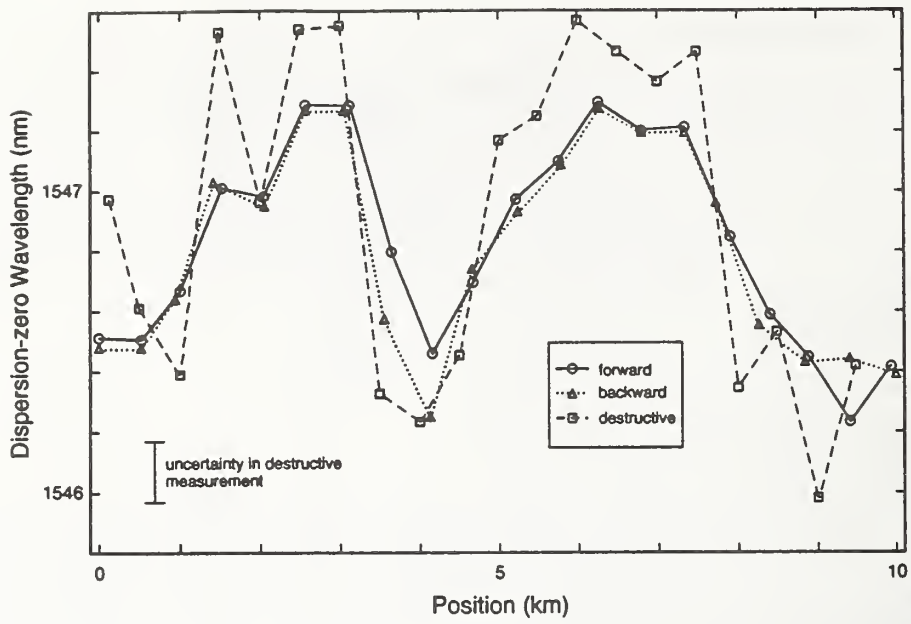

Figure 3: Measured dispersion zero as a function of position in a 9.7-km spool of fiber. The circles and triangles show the results of noninvasive measurement from either end of the fiber. The position resolution was about 1 km. The squares show the zeros in the dispersion curves measured by cutting the fiber into 500-m segments. The error bar shows the ±0.1-nm uncertainty of the destructive technique.

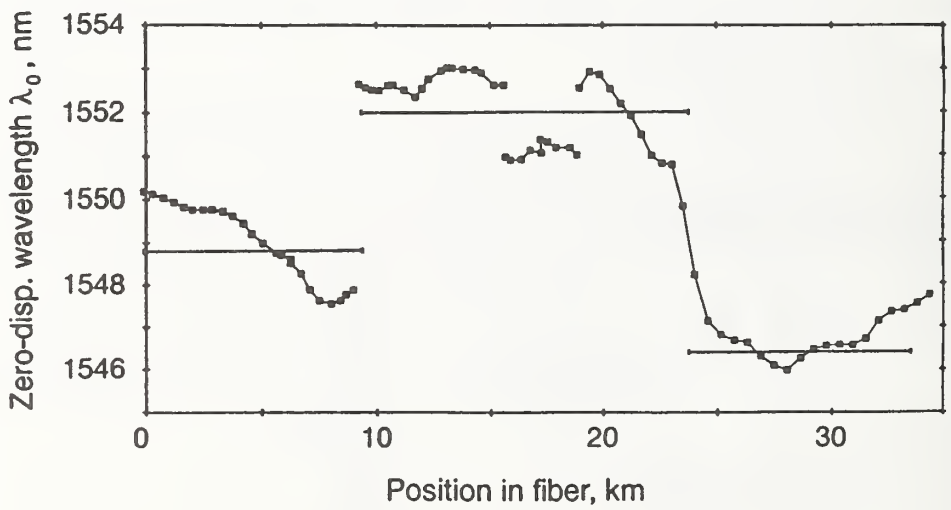

Figure 4: Dispersion-zero wavelength map of a 33.6-km fiber consisting of 3 concatenated pieces. Horizontal lines show the "average" dispersion zero of each piece as measured by conventional means.

Determination of Zero-Dispersion Wavelength in Optical Fiber Using Four-Wave Mixing

J. B. Schlager, S. E. Mechels, and D. L. Franzen
National Institute of Standards and Technology, 325 Broadway, Boulder CO 80303

Abstract

Wavelengths of measured maximum four-wave mixing efficiency in optical fiber are compared to zero-dispersion wavelengths measured with a highly accurate frequency-domain phase shift technique. The average absolute discrepancy between the two wavelengths determined on fifteen fibers is 0.19 nm; for an average pump-probe spacing of 5.9 nm, the average spectral width of the four-wave mixing efficiency curve is 0.45 nm.

I. Introduction

Four-wave mixing (FWM) is a parametric process that involves the interaction of four optical waves in a material.[1] The efficiency of this process depends on the nonlinear susceptibilities of the material, the light intensities, and phase matching between the light waves. In optical fiber optimal phase matching for FWM occurs at or near the zero-dispersion wavelength.[2] In this letter, we describe measurements of partially degenerate four-wave mixing efficiency near the zero-dispersion wavelength of several different fibers. In partially degenerate four-wave mixing the pump provides two of the four optical waves at the same optical frequency. The other two waves are the probe and the generated anti-Stokes light. With the probe light fixed at a given wavelength, we determine the pump wavelength which gives maximum anti-Stokes light intensity in the zero-dispersion wavelength region of the fiber. We compare this pump wavelength with accurate measurements of the zero-dispersion wavelength using the frequency-domain phase-shift technique.[3,4]

II. Experiment

The experimental configuration for obtaining FWM efficiency is shown in Fig. 1. Two tunable lasers provide the pump and probe lights. The pump laser is amplified with an erbium-doped fiber amplifier (EDFA) to a power of +10 dBm. The probe laser light at -3 dBm is mechanically chopped to allow narrow-band detection of the FWM signal with lock-in amplifier techniques. Light from each source passes through an optical bandpass filter to minimize the amplified spontaneous emission (ASE) light, which can overwhelm the FWM signal, and polarization controllers are used to bring the polarization states into coincidence. The pump and probe lights are combined in a fused-fiber coupler, traverse the test fiber, and continue on to the photoreceiver. An additional optical bandpass filter with sufficient bandwidth (2 nm, full width at half maximum) for the wavelength scan is used at the photoreceiver to further isolate the FWM signal. The detected signal is passed to a lock-in amplifier. A computer automatically tunes the pump laser and acquires the FWM efficiency data. Laser wavelengths are measured with an interferometric wavemeter having an accuracy of 1 ppm.

Figure 2 shows the frequency-domain phase shift (FDPS) system, which has been described elsewhere.[3,4] The output of a tunable laser is intensity modulated by an integrated-optic Mach-Zehnder modulator. The phase of the RF modulation is monitored by a vector voltmeter after detection, amplification and filtering. The test fiber is temperature controlled to ±0.15 °C. Laser wavelength is monitored by a wavemeter and matched to corresponding relative group delays with a temporal resolution of 0.15 ps. This system can determine zero-dispersion wavelength with a precision of better than 0.025 nm (three standard deviations).[5]

III. Results

A typical FWM spectrum is shown in Fig. 3. We acquired this spectrum with an optical spectrum analyzer placed just after a 10 km dispersion-shifted test fiber while the pump was tuned to the fiber's zero-dispersion wavelength. During FWM efficiency measurements, the probe light exiting the test fiber is attenuated relative to the FWM light by the additional optical bandpass filter. This ensures good FWM signal isolation at the lock-in amplifier. A FWM efficiency curve of a 10 km dispersion-shifted fiber is shown in Fig. 4. Here the mid-scan pump-probe wavelength separation was about 5 nm and the efficiency curve had a full width at half maximum (FWHM) width of 0.36 nm. The experimental data are plotted with a theoretical curve.[2] Although the match is good, we believe the discrepancy between the theory and experiment is primarily due to the variation of zero-dispersion wavelength along the length of the fiber. Some test fibers exhibited more complicated FWM efficiency curves, but a clear FWM efficiency peak was still discernible in these fibers. In addition, by increasing the pump-probe wavelength separation, we were able to achieve narrower efficiency curves. A mid-scan pump-probe wavelength separation of 11 nm (the maximum possible with the filters available) gave a FWM efficiency curve width of 0.11 nm FWHM with no appreciable shift in peak FWM efficiency wavelength. Theoretically, the maximum efficiency wavelength does not depend on pump-probe separation; however, in practice there are trade-offs. A small separation results in a spectrally broad efficiency curve while a large separation enhances the unwanted effects of polarization mode dispersion. The 6 nm mid-scan separation chosen for most of these measurements represents a good compromise given the optical bandpass filters available to us.

Comparisons between peak FWM efficiency wavelengths and zero-dispersion wavelengths measured by the FDPS system for fifteen commercially available dispersion-shifted fibers are presented in Table I.

In all fifteen fibers a single FWM efficiency peak clearly dominated, and the absolute discrepancy between this peak and λ_0 was on average less than 0.19 nm. The mid-scan pump-probe wavelength separation was about 4-5 nm for fibers A-D, 11 nm for fiber E, and 6 nm for fibers F-O. The dispersion slope $dD/d\lambda$ measured with the FDPS system ranged from 0.069 to 0.0735 ps/(nm^2·km) with an average of 0.0713 ps/(nm^2·km). The measured PMD at 1550 nm ranged from 0.03 to 0.11 ps/$\sqrt{\text{km}}$ for fibers A-E, and varied as much as 30 % for each fiber measured over time.

Most fiber specimens were examples of recently manufactured high-quality fibers. Cut-back measurements on four equal-length sections of one fiber showed a linear increase in zero-dispersion wavelength of 1.5 nm over a length of 10 km.

TABLE I
COMPARISON OF PEAK FWM EFFICIENCY AND ZERO-DISPERSION WAVELENGTH

Fiber (length)	λ_{probe} (nm)	$\lambda_{pump\ @\ peak\ FWM}$ (nm)	$\lambda_{o\ FDPS}$ (nm)	$\lambda_{FWM\ Spec.\ Width}$ (nm, FWHM)	$\lvert \lambda_{pmp\ @\ pk} - \lambda_0 \rvert$ (nm)
A (5 km)	1550.27	1544.69	1544.68	0.44	0.01
B (12 km)	1555.21	1551.36	1551.38	0.48	0.02
C (12 km)	1556.40	1552.54	1552.70	0.41	0.16
D (10 km)	1558.26	1553.37	1553.45	0.39	0.08
E (10 km)	1560.14	1549.20	1549.21	0.11	0.01
F (20 km)	1555.14	1548.94	1549.17	0.21	0.23
G (10 km)	1555.14	1548.96	1548.86	0.32	0.10
H (10 km)	1555.14	1549.14	1549.44	0.36	0.30
I (5 km)	1555.14	1549.12	1549.04	0.51	0.08
J (5 km)	1555.14	1549.57	1549.87	0.35	0.30
K (2.5 km)	1555.14	1549.12	1548.83	0.78	0.29
L (2.5 km)	1555.14	1549.14	1549.22	0.67	0.08
M (2.5 km)	1555.14	1549.33	1549.56	0.55	0.23
N (2.5 km)	1555.14	1549.44	1549.94	0.48	0.50
O (1.25 km)	1555.14	1549.37	1549.82	0.67	0.45

IV. REFERENCES

1. G. P. Agrawal, *Nonlinear Fiber Optics, 2nd Edition.* New York: Academic Press, 1995.
2. K. Inoue, "Four-wave mixing in an optical fiber in the zero-dispersion wavelength region," *J. Lightwave Technol.*, vol. 10, no. 11, pp. 1553-1561, 1992.
3. S. E. Mechels and D. L. Franzen, "Accurate measurements of zero-dispersion wavelength in single-mode fibers," *3rd Optical Fiber Measurement Conference Technical Program,* paper IV.2, 1995.
4. S. E. Mechels, J. B. Schlager, and D. L. Franzen, "Accurate zero-dispersion wavelength measurements in single-mode fibers: two frequency-domain methods," *LEOS 1995 Meeting Proceedings,* vol. 2, pp. 75-76, 1995.
5. S. E. Mechels, J. B. Schlager, and D. L. Franzen, "Accurate measurements of zero-dispersion wavelength in optical fibers," to be published in *J. Res. Nat'l. Inst. Stands. Technol.*

Contribution of NIST, not subject to copyright.

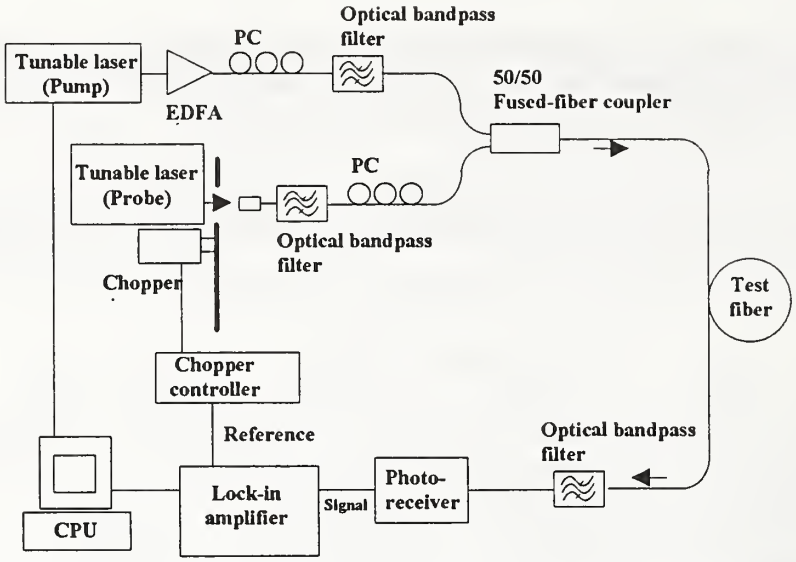

Figure 1. Experimental configuration for obtaining FWM efficiency: PC, polarization controller; CPU, personal computer.

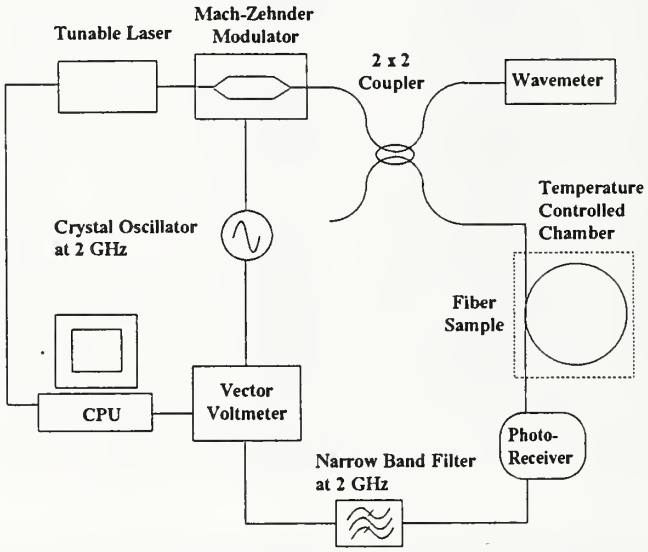

Figure 2. Frequency-domain phase shift system: CPU, personal computer.

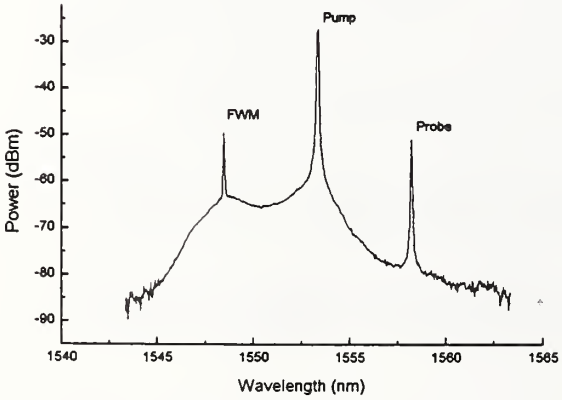

Figure 3. Partially degenerate FWM spectrum: FWM, four-wave mixing anti-Stokes peak.

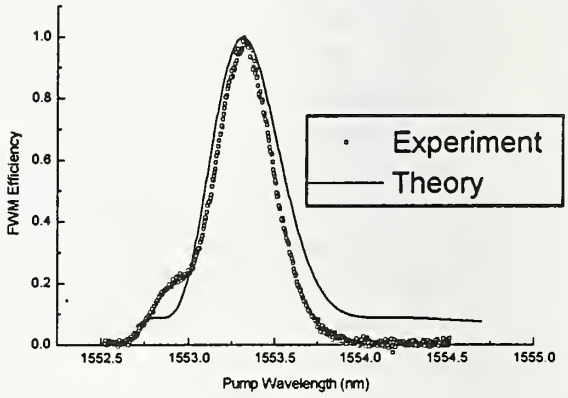

Figure 4. FWM efficiency versus wavelength in 10 km dispersion-shifted fiber. Mid-scan pump-probe separation is 7 nm.

Accuracy issues in comparisons of time- and frequency-domain polarization mode dispersion measurements

P.A. Williams
Optoelectronics Division - National Institute of Standards and Technology
325 Broadway, Boulder CO 80303, U.S.A.

If experimental comparisons are to be made between time- and frequency-domain measurements of polarization mode dispersion PMD, they must be done with a good understanding of the systematic and random uncertainties present. In this paper, I quantify sources of systematic uncertainties in time domain PMD measurements and demonstrate correction techniques on experimental data.

Until recently, theoretical and experimental work [1-10] claimed to support an equality between PMD measured in the time domain as the square root of the second moment σ of the autocorrelation function and PMD measured in the frequency domain as the RMS differential group delay (DGD), so that RMS DGD/σ = 1. However, the recent theory of Heffner [11] shows the issue to be more complicated, with RMS DGD/σ depending on the spectral shape of the time domain measurement source and only for large values of PMD-bandwidth product does the ratio demonstrate a constant value 0.866 which disagrees with previous theory by about 13%. Most of the referenced attempts to measure the RMS DGD/σ ratio lacked the precision to see a 13% effect. Furthermore, standard second moment evaluations of time-domain PMD have several sources of systematic uncertainties large enough to nullify comparison efforts. These systematic errors were avoided by one recent experimental work [12] which used a curve-fitting method to measure σ giving a value of RMS DGD/σ close to 0.9. However, curve-fitting is not always considered to be rigorous enough. So, I present corrections here which allow significant reductions of the systematic biases of the standard second moment calculation.

Measurements of PMD in highly polarization-mode-coupled optical fibers using an interferometric or equivalently wavelength scanning with Fourier transform (WSFT) technique produce an autocorrelation function illustrated by the one-sided example of Figure 1. This time domain response is a quasi-random amplitude (due to random phasing) under a Gaussian envelope. The PMD of the fiber can be measured by finding the square root of the second moment of this curve [13,14]

$$\sigma = \sqrt{\frac{\int I(t)\, t^2 dt}{\int I(t) dt}}. \qquad (1)$$

However, in calculating this quantity, systematic errors due to numerical integration, data clipping and central peak removal are encountered and must be corrected.

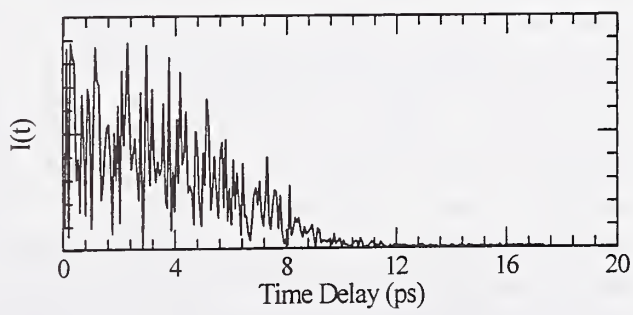

Figure 1 Typical Fourier-transformed wavelength scanning data.

A good approximation to Equation (1) is obtained using the trapezoidal integral approximation

$$\sigma = \sqrt{\frac{\sum_{k=a}^{b} I(t_k)t_k^2 - \frac{1}{2}I(t_a)t_a^2 - \frac{1}{2}I(t_b)t_b^2}{\sum_{k=a}^{b} I(t_k) - \frac{1}{2}I(t_a) - \frac{1}{2}I(t_b)}} \tag{2}$$

where t_a and t_b are the time coordinates of the first and last points used. A simpler rectangular approximation is sometimes used [13,14]. However, the numerical integration is usually carried out with the time coordinate sampled at the practical values t = 0, Δ, 2Δ,... for example, as opposed to the more appropriate t = Δ/2, 3Δ/2, 5Δ/2,... values (Δ is the sampling step size). It should be cautioned that for a single-sided data set as from WSFT, integrating from t_a=0 will underestimate σ by an amount dependent on the time domain sampling density η (number of data samples / σ). Under practical conditions, this can result in errors of several percent and the trapezoidal approximation represents a significant improvement (Figure 2).

Another systematic bias comes from limited range. The sampling range t_b can be limited by the wavelength resolution in WSFT measurements or the scan range of the interferometer. But, the first limit to be encountered is likely to be due to the signal to noise ratio of the system. Generally, the useable portion of the data is determined by some criteria such as the exclusion of data beyond the point t_b where the signal drops below 2 times the rms noise level [13,14]. However, clipping the data wing(s) in this way systematically biases the measured σ toward lower values. This can be seen from Equation (1) in that for a nominal gaussian, at large values of t, the positive integrand of the denominator I(t) approaches zero more quickly than the positive integrand of the numerator $I(t)t^2$. So, the result of excluding data at large values of t will be to bias σ toward smaller values. Figure 3 shows a computer simulated result of measurement error as a function of the data clipping point t_b/σ (solid curve) with σ being the true value of the square root of the second moment. The clipping error is substantial. Indeed, an RMS noise level of 6 or 7% would require clipping at $t_b/\sigma = 2$ giving an error on the order of 10% – large enough to bias measurements of RMS DGD/σ from 0.866 up to 1.0.

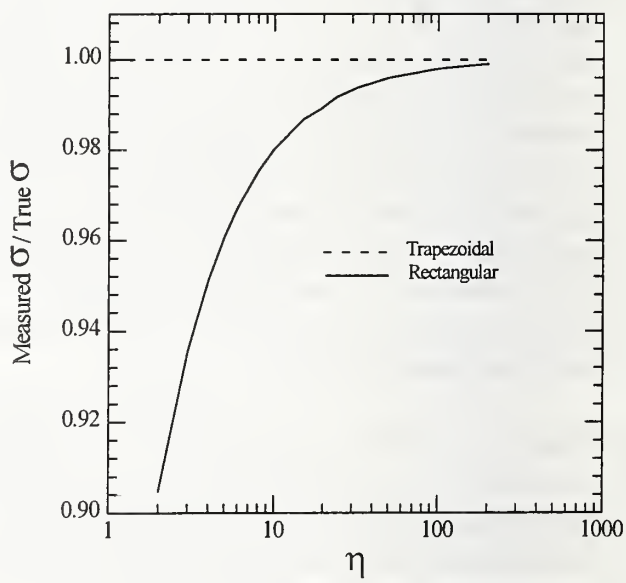

Figure 2 Measurement errors for trapezoidal (dashed) and rectangular (solid) integral approximations as a function of sampling density (the number of sampled points/σ) η.

To correct for this error, a simple look-up table is useful. The dashed curve of Figure 3 is the solid curve plotted as a function of t_b/σ_M where σ_M is the measured value of second moment. In practice, dividing σ_M by the value of the dashed correction curve at t_b/σ_M removes the clipping error. Of course, the correction has trouble for values of t_b/σ_M which are much less than 2 where the curve becomes very steep and small random errors in measuring σ_M are amplified by the correction factor. An example of the correction performance is shown in Figure 4 where σ is measured on simulated WSFT data (using the simulation of Reference 11) at various clipping levels and then compensated to give a corrected value. Clearly, the compensated σ performs well, within 2% of its unclipped value down to about the $t_b/\sigma_M = 2$ level.

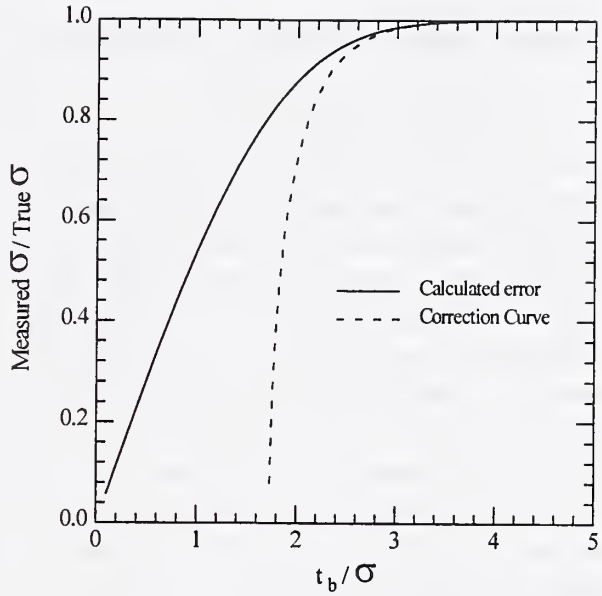

Figure 3 Data clipping error vs. sampled fraction of true second moment (solid) or measured second moment (dashed).

Another source of systematic error comes from removing the central peak from the time domain response. In autocorrelation interferometers, the interferogram has a large source autocorrelation peak around t =0 which contains no PMD information. A similar peak results from windowing in WSFT. In practice, σ is often calculated by simply adjusting t_a in Equation 2 to skip the data points under the central peak. However, the result is a systematic increase in measured σ. The reason can be seen in Equation 2, where eliminating low t values of I(t) reduces the value of the denominator more drastically than does eliminating low t values of $I(t)t^2$ from the numerator. The simplest technique to compensate this error is to substitute the values of I(t) where the central peak occurs with estimates of what I(t) would be without the central peak. As an example, this is illustrated for single-sided WSFT data (the procedure is identical for interferometric data). First, σ_M is measured using Equation (2) with t_a set to ignore values of I(t) which are dominated by the central peak.. Then σ_M is used to define new integration limits $t_a = \sigma_M/2$ and $t_b = \sigma_M$. Then $\sigma_{0.5\text{-}1}$ is measured using Equation (2) with these new limits and divided by 0.75 (the value of $\sigma_{0.5\text{-}1}$ for an ideal Gaussian of unit amplitude). The result of this division is an estimate at the amplitude A of the Gaussian

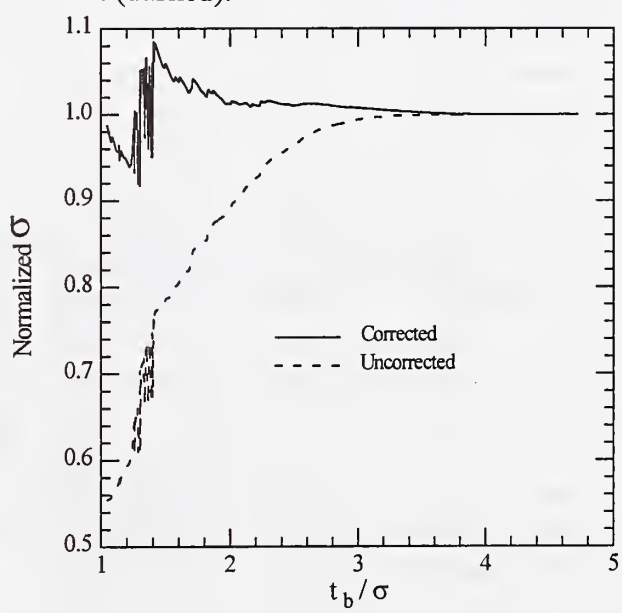

Figure 4 Normalized simulated measurements of uncorrected (solid) and corrected (dashed) second moment vs. sampled fraction of second moment.

function describing the time-domain response

$$I(t) = A\exp\left(\frac{-t^2}{2\sigma^2}\right). \qquad (3)$$

Then, σ_M and A are used along with Equation (3) to generate estimated values of $I(t < t_a)$. Finally, σ is recalculated using equation (2) with t_a=0. An example of the error and correction results is shown in figure 5 for computer simulated interferometric data.

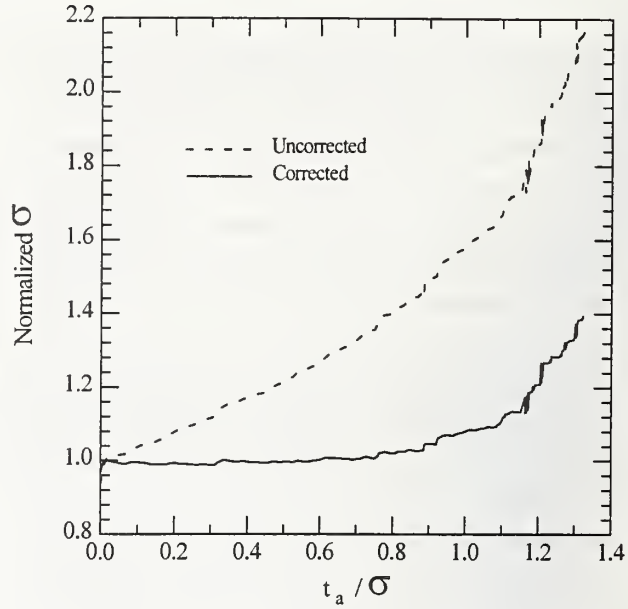

Figure 5 Normalized simulated measurements of uncorrected (solid) and corrected (dashed) second moment vs. starting measurement time/measured second moment.

It is worth mentioning that there is one systematic error in time domain measurements which is well known but often inappropriately corrected for. I refer to the source width subtraction technique

$$\sigma^2_{True} = \sigma^2_{Meas} - \sigma^2_{Source}. \qquad (4)$$

The idea is to subtract the square root of second moment of the Fourier transform of the optical source spectrum σ_{Source} from the measured square root of the second moment of the interferogram σ_{Meas} to yield the true square root of the second moment of the spectral response of the device under test σ_{True}. This technique comes from the fact that a function which is the product of two other functions has a variance of its Fourier transform which is equal to the sum of the variances of the Fourier transforms of the other two functions. However, application of Equation (4) to a WSFT or interferometric PMD measurement is inappropriate since σ_{Meas} is measured after the time domain response has undergone a non-linear enveloping technique. Specifically, this involves using the envelope of the photocurrent in the interferometric case or using the magnitude of the Fourier transform in the WSFT case. Both of these enveloping functions are non-linear modifications to the process which make Equation (4) non-applicable. So, while a finite source width still contributes a systematic bias to the measured second moment, there is not yet a rigorous method of correcting the error.

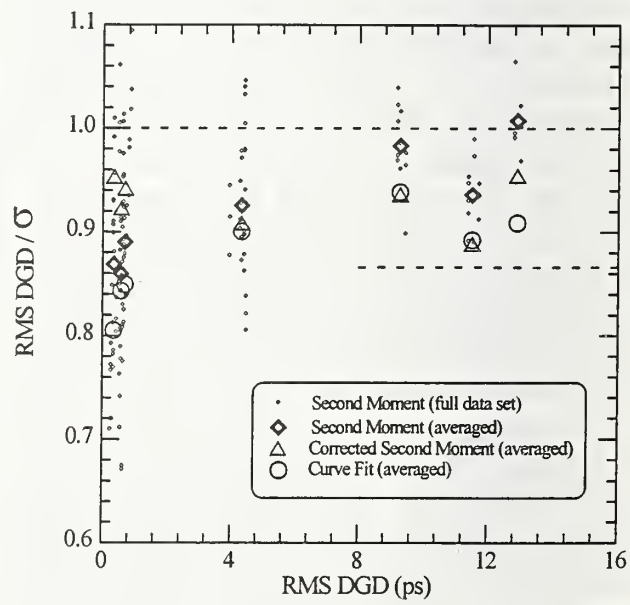

Figure 6 Ratio of frequency- and time-domain PMD measurements as a function of PMD.

In order to demonstrate the usefulness of the above corrections, the value of RMS DGD/σ is calculated using the data set from reference [12]. The data represents measurements of seven different fiber specimens using both Jones matrix eigenanalysis and WSFT techniques. σ is extracted from the WSFT data using Equation 2 with no correction factors. Then, the same σ is corrected using the above techniques. Finally, a third set of second moment values are obtained by performing a non-linear least squares fit of Equation 3 to the data sets. This curve-fit technique is not as susceptible to the systematic errors described above and acts as an estimate of the true value of σ. In Figure 6, the ratio of the frequency domain measurement of PMD (RMS DGD) and the associated time domain measurement σ are plotted as a function of the PMD of the fiber (RMS DGD). The upper dashed line indicates the previously predicted 1.0 ratio and the lower dashed line illustrates the asymptotic 0.866 value predicted by Heffner. The large data points represent the average of several statistically independent measurements. The small diamonds are the unaveraged uncorrected second moment measurements to illustrate the spread in data and the number of measurements. Clearly, the uncorrected second moment data yields values with a systematic bias of ~5% above the curve fit results. Application of the correction techniques to the data brings the second moment values into good agreement with the curve fit results as expected. Clearly, the corrected results indicate a ratio which is closer to 0.866 than to 1.0. However, a larger population of measurements is needed to make a quantitative judgement.

My thanks go to B.Heffner for providing some of the simulated data used in this work and for sharing with me some insight into the world of PMD.

[1] N.Gisin, Opt. Commun., **86**, 371-373 (1991).

[2] N.Gisin, and J.P.Pellaux, Optics Communications, **89**, 316-323 (1992).

[3] B.Perny, C.Zimmer, F.Prieto, and N.Gisin, Electron. Lett., **32**, 680-681 (1996).

[4] M.Artiglia, A.Chiantore, and A.Rossaro, Proc. Optical Fiber Measurements Conference '95, p. I.4 (1995).

[5] M.Artiglia, P.Morra, and C.Sartori, Proc. Optical Fiber Measurements Conference '95, p. II.6 (1995).

[6] N.Gisin, Proc. Symp. Optical Fiber Meas. '94, 149-154 (1994).

[7] N.Gisin, R.Passy, J.C.Bishoff, and B.Perny., IEEE Phot. Tech. Lett., **5**, 819-821 (1993).

[8] Y.Namihira and J.Maeda, Elec. Lett., **28**, 2265-2266 (1992).

[9] Y.Namihira and J. Maeda, Proc. Symp. Optical Fiber Meas. '92, 145-150 (1992)

[10] N.Gisin, R.Passy, B.Perny, A.Galtarossa, C.Someda, F.Bergamin, M.Schiano, and F.Matera, Electron. Lett., **27**, 2292-2293 (1991).

[11] B.L.Heffner, Opt. Lett., 113-115 (1996)

[12] P.A.Williams and P.R.Hernday, Proc. Opt. Fiber Meas. Conference '95, p. I.2 (1995).

[13] Fiber Optic Test Procedure (FOTP) 113, Telecommunications Industry Association.

[14] Fiber Optic Test Procedure (FOTP) 124, Telecommunications Industry Association.

How accurately can one measure a statistical quantity like Polarization Mode Dispersion?

N. Gisin[1], B. Gisin[1], J.P. Von der Weid[2] and R. Passy[2]
[1] *Group of Applied Physics University of Geneva, 1211 Geneva 4, Switzerland*
[2] *Center for Telecommunication Studies*
Pontifica Universita Catolica de Rio de Janeiro
Rio de Janeiro, Brasil

Different measurement techniques of PMD are presently available and under further investigations [1, 2, 3, 4]. All these techniques involve an averaging procedure. Indeed, this is necessary, since the Differential Group Delay (DGD) is a statistical quantity and PMD is defined either as the mean DGD or its RMS value. However, the statistical character of the DGD and the fact that any measurement involves only a finite sample set imply that there is an intrinsic limitation to the accuracy of PMD measurements. This limitation is independent of any measurement setup implementation, but is unavoidable, similarly to the well-known example of the measurement of the probability of coin tossing with only a finite number of trials. The main difficulty in evaluating this limitation in the case of PMD is that, contrary to the coin tossing example, the DGD at nearby wavelengths are not independent.

In order to present our result, let us introduce some notations. Let $\vec{\Omega}(\omega)$ denote the principal polarization state vector [6]. By convention, its norm equals the DGD: $\delta\tau(\omega) = \sqrt{\Omega_x^2(\omega) + \Omega_y^2(\omega) + \Omega_z^2(\omega)}$. In practice one is interested in statistical ensembles or in time ensembles. However, wavelength ensembles are much easier to produce. Furthermore, it is generally admitted that these different ensembles are statistically equivalent and there are good reasons [7] for doing so. Consequently, all major PMD measurement techniques are based on a wavelength ensemble [9, 10]. Note that large wavelength ranges correspond to long time fluctuations. Accordingly, we define the PMD Delay $\Delta\tau$ as the RMS value of the $\delta\tau(\omega)$:

$$\Delta\tau(\omega_1, \omega_2)^2 = \frac{1}{\omega_2 - \omega_1} \int_{\omega_1}^{\omega_2} \delta\tau(\omega)^2 d\omega \tag{1}$$

In practice the optical frequency range is limited by the laser tunability. Another limitation is due to the slight wavelength dependence of the modal birefringence and the polarization mode coupling length. However, in order to define a PMD value valid for arbitrary long time fluctuations, we shall assume in our model that the local modal birefringence and the mean polarization mode coupling length are wavelength independent. This amounts to assume that the modal field does not change over the considered wavelength range (i.e. all wavelengths see the same refractive index structure), hence the wavelength dependence of $\delta\tau(\omega)$ is only due to interferences between the different optical trajectories in the fiber [4]. With such an assumption, the theoretical mean PMD delay $\overline{\Delta\tau}$ can be defined as:

$$\overline{\Delta\tau} = \lim_{\omega_2 \to \infty} \Delta\tau(0, \omega_2) \tag{2}$$

Defining PMD this way has the great advantage that the probability space is well defined and the statistical ensemble of interest consists in all optical frequency intervals of length $\Delta\omega$. Henceforth

we study the variance of $\Delta\tau(\omega_1,\omega_2)^2$ when $\Delta\omega \equiv \omega_2 - \omega_1$ is finite (recall that the variance is defined as: $Var(X) = mean(X^2) - mean(X)^2$).

Let ω_j, j=1..N denote the optical frequencies at which the DGD $\delta\tau(\omega_j)$ are measured. Hence, this finite sample set corresponds to a measured value of PMD $\Delta\tau_{meas}$:

$$\Delta\tau^2_{meas} = \frac{1}{N}\sum_j \delta\tau(\omega_j)^2 = \frac{1}{N}\sum_j \left(\Omega_x(\omega_j)^2 + \Omega_y(\omega_j)^2 + \Omega_z(\omega_j)^2\right) \tag{3}$$

where each component of the principal state vector $\vec{\Omega}$ is a normal random variable [8] of zero mean and variance $\overline{\Delta\tau}^2/3$. Hence, $\Delta\tau^2_{meas}$ is the sum of three normal random variables of mean $\overline{\Delta\tau}^2/3$. Recall that for any normal random variable X, $Var(X^2)$=$2Var(X)^2$, and that the variance of the sum of independent random variables is simply the sum of the variances. Hence, if the $\Omega_k(\omega_j)$ would be independent, the variance of $\Delta\tau^2_{meas}$ would be equal to $\frac{2\overline{\Delta\tau}^4}{3N}$, but, clearly, they are not independent (think for instance that $\vec{\Omega}(\omega)$ is a continuous function of ω, values of $\delta\tau(\omega)$ at interpolating frequencies ω provide thus little additional information). The number of data that are effectively independent can however be estimated as follows. The functions $\Omega_k(\omega)$, k=x,y,z, have irregular oscillations, hence using the Nyquist theorem two points per cycle can be considered as independent. But the number N_e of extrema of $\Omega_k(\omega)$ is related to the PMD $\overline{\Delta\tau}$, similarly to the well known case of the extrema of the intensity passing through a fixed analyzer [3]. Hence, we arrive at our main result:

$$Var\left(\Delta\tau^2_{meas}\right) \approx \sqrt{\frac{3\pi}{8}}\frac{2k\pi}{3}\frac{\overline{\Delta\tau}^3}{\Delta\omega} \approx 2.3\frac{\overline{\Delta\tau}^3}{\Delta\omega} \tag{4}$$

Consequently, a measurement of the DGD over a wavelength range $\Delta\omega$ provides an approximate value $\Delta\tau_{meas}$ of the theoretical mean PMD delay $\overline{\Delta\tau}$:

$$\Delta\tau_{meas} \approx \overline{\Delta\tau}\left(1 \pm \frac{\alpha}{\sqrt{\overline{\Delta\tau}\Delta\omega}}\right) \tag{5}$$

where $\alpha = \frac{\sqrt{2.3}}{2} \approx 0.76$. A more elaborated derivation [12] of relation (5) and our numerical simulation confirm this relation, but with $\alpha \approx 0.9$.

For example, if $\Delta\omega = 100\frac{1}{ps}$ (corresponding in wavelengths to $\delta\lambda \approx 130$ nm around 1550 nm or to $\delta\lambda \approx 90$ nm around 1300 nm), then for a PMD of 1 ps, the measurement uncertainty due to the statistical nature of the DGD is of about 9%! For a PMD of 0.1 ps, the uncertainty is even as large as 28%.

It should be stressed that the above limitation (5) is not specific to one measurement scheme, but is intrinsic to all measurement techniques that average the DGD over a wavelength range. For example the figures 1 to 3 illustrate our result on simulations. **Figure 1** presents on 5000 numerical simulations the case of the Jones Matrix Eigenanalyses (JME) measurement method simulating a tunable laser over 90 nm around 1300 nm. The theoretical mean PMD value is obtained by computing the RMS DGD over 50.000 $\frac{1}{ps}$. Each point represents one run of the simulation software. The thick lines are the mean values and the mean plus and minus one standard deviation. The thinner lines are the theoretical curves with $\alpha = 0.9$. **Figures 2** and **3** are analogous, but for the extrema counting and interferometric measurement schemes, respectively. Figure 4 shows the ratio of simulated measurement results as obtained with the JME and interferometric methods.

In conclusion, a general formula (5) of the accuracy limitation to PMD measurement due to the statistical nature of the DGD has been derived. Present day commercial instruments are

already close to the predicted theoretical accuracy limitation.

Acknowledgment Financial support by the Swiss "Office Fédéral de l'Education et de la Science" within the European project COST 241 is gratefully acknowledged. Thanks are also due to Dr B. Perny for many helpful discussions.

References

[1] N. Gisin, J.P. Pellaux and J.P. Von Der Weid, J. Lightwave Tech. **9**, 821-827, 1991.

[2] B.L. Heffner, IEEE Photon. Tech. Lett. **4**, 1066-1069, 1992.

[3] C.D. Poole and D.L. Favin, J. Lightwave Tech. **12**, 917-929, 1994.

[4] N. Gisin and the COST 241 Group, Pure and Applied Optics **4**, 511-522, 1995.

[5] B. Perny, Ch. Zimmer, F. Prieto and N. Gisin, Electron. Lett. **32**, 680-681, 1996.

[6] C.D. Poole and R.E. Wagner, Electron. Lett. **22**, 1029-1030, 1986.

[7] N. Gisin, Opt. Communications **86**, 371-373, 1991.

[8] F. Curti, B. Daino, G. de Marchis and F. Matera, IEEE J. Lightwave Tech. **8**, 1162-1166, 1990.

[9] EIA/TIA, FOTP-113, FOTP-122 and FOTP-124, proposals on PMD measurement methods.

[10] ITU-T, SG15-WP4, Contributions on measurement methods of PMD.

[11] B.L. Heffner, Optics Lett. **21**, 113-115, 1996.

[12] N. Gisin et al., preprint, University of Geneva, 1996.

1 Figure Captions

1. Illustration of our main result (5) on 5000 numerical simulations for the case of the Jones Matrix Eigenanalyses (JME) measurement method simulating a tunable laser over 90 nm around 1300 nm. Each point represents one run of the software, simulating a concatenation of 200 polarization maintaining fibers of random orientation and birefringence. The theoretical mean PMD value $\overline{\Delta\tau}$ is obtained by computing the RMD DGD over 50.000 $\frac{1}{ps}$. $\Delta\tau_{JME}$ is computed according to published procedures [2]. The thick lines are the computed mean values and the mean plus and minus one standard deviation. The thinner lines are the theoretical curves (5) with $\alpha = 0.9$.

2. Same as figure 1, but for the extrema counting measurement method (using the polarization mode coupling $k = 0.82$ and the same value for $\alpha = 0.9$).

3. Same as figure 1, but for the interferometric measurement method (using the second moment of the interferogram with Heffner's [11] factor $\sqrt{\frac{3}{4}}$ and the same value for $\alpha = 0.9$).

4. Comparison of the JME and interferometric measurements over the same wavelength range. Note that the standard deviation of this ratio is identical to that of the previous graphs (the thin lines are the same on all graphs). This illustrates that the uncertainty is similar for all measurement methods.

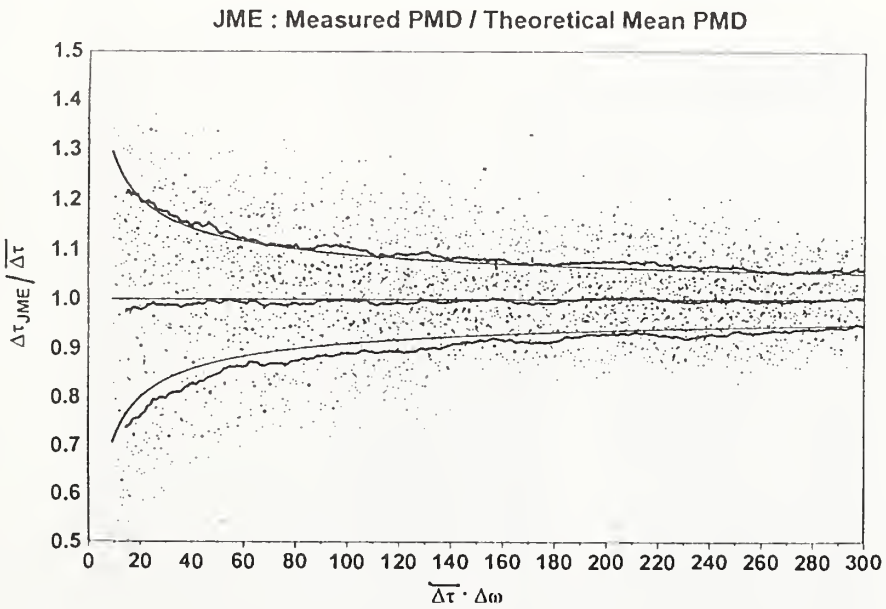
JME : Measured PMD / Theoretical Mean PMD
$\Delta\tau_{JME} / \overline{\Delta\tau}$
$\overline{\Delta\tau} \cdot \Delta\omega$

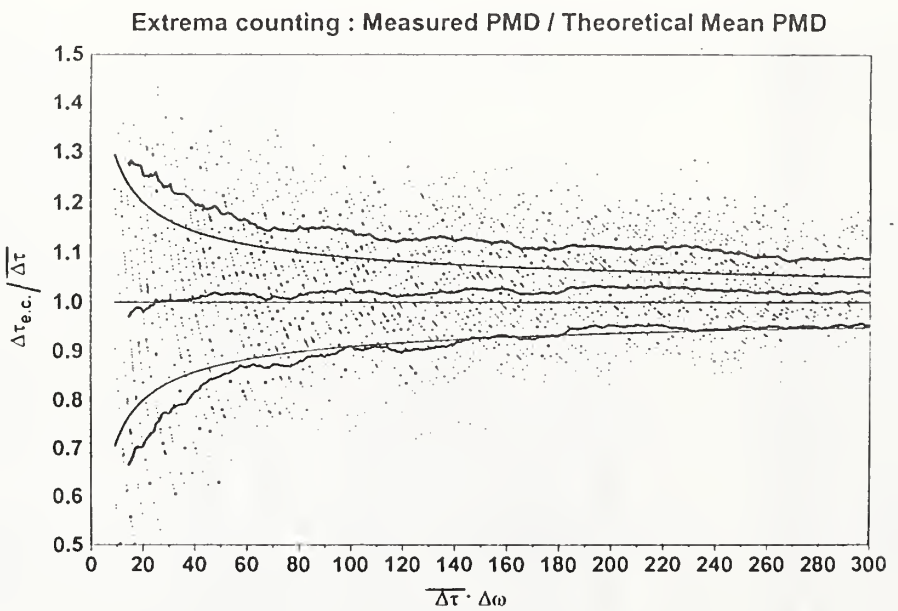
Extrema counting : Measured PMD / Theoretical Mean PMD
$\Delta\tau_{e.c.} / \overline{\Delta\tau}$
$\overline{\Delta\tau} \cdot \Delta\omega$

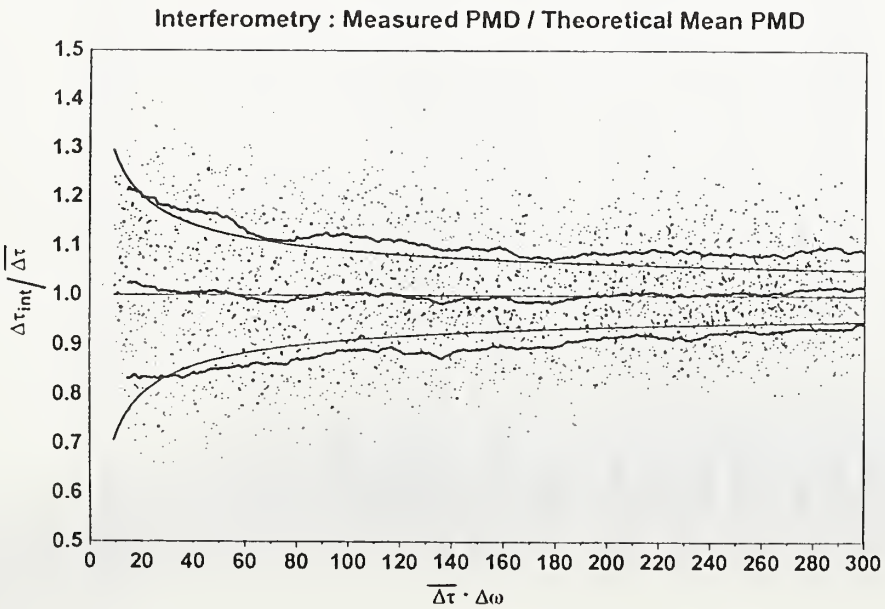
Interferometry : Measured PMD / Theoretical Mean PMD
$\Delta\tau_{int} / \overline{\Delta\tau}$
$\overline{\Delta\tau} \cdot \Delta\omega$

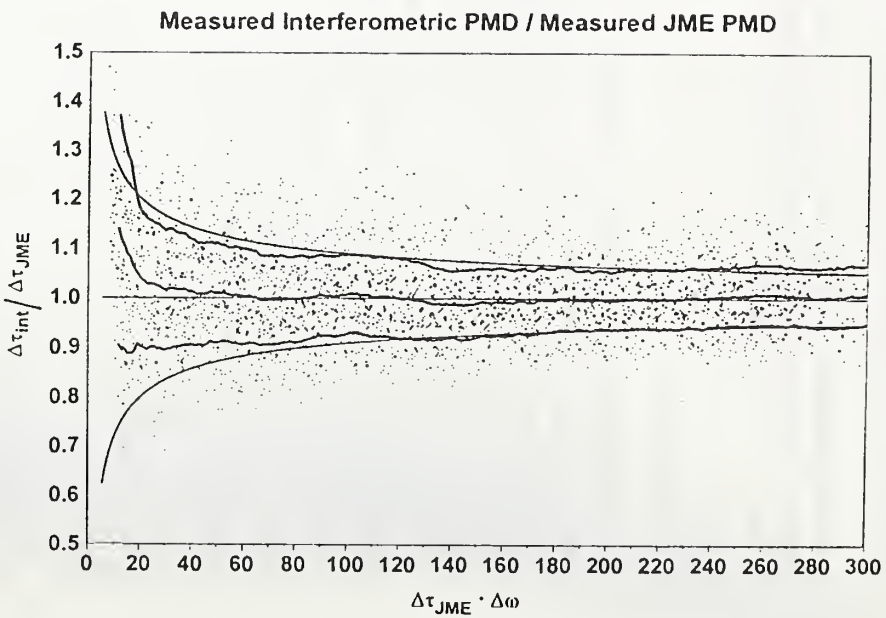
Measured Interferometric PMD / Measured JME PMD
$\Delta\tau_{int} / \Delta\tau_{JME}$
$\Delta\tau_{JME} \cdot \Delta\omega$

Compensation formula for noise threshold bias of interferometric PMD measurement

B. L. Heffner
Hewlett-Packard Laboratories, 3500 Deer Creek Road, Palo Alto, CA 94304

Interferometric measurement of the polarization-mode dispersion (PMD) of a highly mode-coupled fiber results in a roughly Gaussian envelope modulated by speckle noise. The width of the Gaussian envelope is often determined by calculation of the second moment of the interferometric response about the zero-delay point. The noise threshold required by this approach biases the result, leading to an apparent width smaller than the Gaussian width that would be measured in the absence of noise. The cause of the noise threshold bias is examined, and a formula is introduced that allows estimation of a noise-free Gaussian width based on real measurements with noise. An ensemble of experimental PMD measurements demonstrates that this formula removes the noise threshold bias.

The unprocessed output of an interferometric PMD measurement is the envelope $\mathcal{E}(t)$ of the a.c. photocurrent caused by interference fringes, as a function of the differential time delay t through an interferometer. When a highly mode-coupled fiber is measured, the resulting envelope $\mathcal{E}(t)$ consists of a roughly Gaussian envelope multiplied by a random amplitude analogous to optical speckle. Calculation of the PMD involves assessing the half-width σ of the Gaussian envelope $\mathcal{E}(t)$. The half-width is commonly assessed by calculating the second moment of $\mathcal{E}(t)$ about the zero-delay point, resulting in a second-moment estimate σ_{SM}:

$$\sigma_{SM}^2 = \frac{\int_{-\infty}^{\infty} t^2 \mathcal{E}(t)\, dt}{\int_{-\infty}^{\infty} \mathcal{E}(t)\, dt} \tag{1}$$

The motivation for (1) can be clarified by the example of a perfect Gaussian $G(t)$ of arbitrary amplitude and half-width σ:

$$G(t) = A \exp\left(-t^2/2\sigma^2\right) \tag{2}$$

When $\mathcal{E}(t) = G(t)$, the half-width is found correctly ($\sigma_{SM} = \sigma$) by application of (1). However, an interferometric measurement contains both additive noise and a random amplitude caused by speckle, whereas $G(t)$ does not. To accommodate the noise we specify a noise threshold and set the limits of integration of (1) equal to T_- and T_+, the points that bound the region in which $\mathcal{E}(t)$ exceeds the noise threshold (Fig. 1).

Integrating over the finite domain defined by the intersection of $\mathcal{E}(t)$ with the noise threshold, we obtain a biased estimate $\hat{\sigma}$ of the half-width:

$$\hat{\sigma}^2 = \frac{\int_{-T_-}^{T_+} t^2 \mathcal{E}(t)\, dt}{\int_{-T_-}^{T_+} \mathcal{E}(t)\, dt} \tag{3}$$

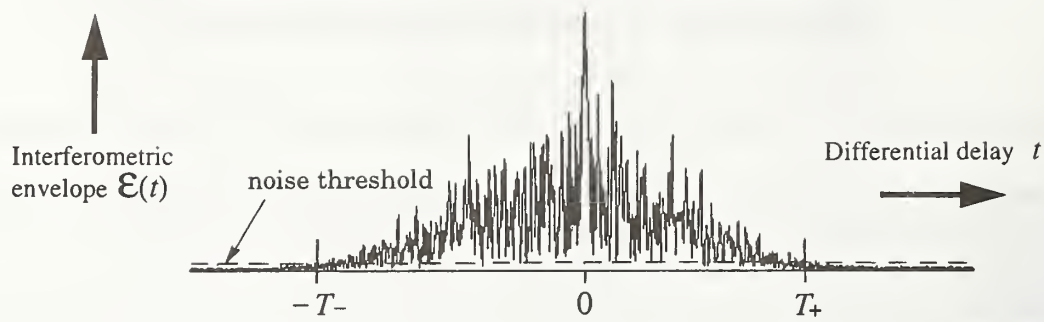

Fig. 1. a.c. photocurrent envelope resulting from an interferometric measurement of PMD. The second moment is calculated by integration over a central region where the noise does not dominate the signal. The bounds of this region can be defined by the furthest points of intersection between the envelope and a noise threshold.

We expect $T_- \approx T_+$ so for purposes of correction we'll use the mean value $T = (T_- + T_+)/2$. No attempt will be made to correct for errors induced by the central coherence peak, which can be suppressed. If we assume both the noise and the random amplitude are stationary, and assume the underlying envelope is truly Gaussian, then we can calculate a correction factor $z = \sigma/\hat{\sigma}$ which will allow the systematic bias caused by the noise threshold to be removed.

$$z = \frac{\sigma}{\hat{\sigma}} = \left(\frac{\int_{-x}^{x} t^2 G(t)\, dt}{\int_{-x}^{x} G(t)\, dt} \right)^{-\frac{1}{2}} = \left(1 - \frac{x\sqrt{\frac{2}{\pi}}}{\operatorname{erf}\left(\frac{x}{\sqrt{2}}\right) e^{x^2/2}} \right)^{-\frac{1}{2}} \tag{4}$$

$$\text{where} \quad x = \frac{T}{\sigma}$$

Once an envelope $\mathcal{E}(t)$ is measured, T is determined by the noise threshold and $\hat{\sigma}$ is calculated from (3). Given T and $\hat{\sigma}$, in principle (4) can be solved for σ or z, but the author is not aware of such a solution in closed form. Instead, consider the following approximation for z in terms of the measurable quantity $y \equiv \frac{T}{\hat{\sigma}} - \sqrt{3}$:

$$\frac{\sigma}{\hat{\sigma}} \approx \hat{z} = \begin{cases} 0.969 + \dfrac{0.0653543}{y} - \dfrac{0.00023788}{y^2} + 0.633438\,\mathrm{Exp}(-5.30178\,y + 1.09896\,y^2) & \text{for} \quad 1.743\,\hat{\sigma} < T < 3.85\,\hat{\sigma} \\ 1 \quad \text{for} \quad T \geq 3.85\,\hat{\sigma} & \text{where } y \equiv \dfrac{T}{\hat{\sigma}} - \sqrt{3} \end{cases} \tag{5}$$

The correction factor z and its approximation $\hat{z}$ are plotted in Fig. 2 as a function of T/σ, the number of corrected half-widths above the noise on either side of the zero delay point. The fractional error of the approximation (5) is $\delta z = (\hat{z} - z)/z$. This error is calculated from (4) and (5) for various values of $T/\hat{\sigma}$ (Fig. 3).

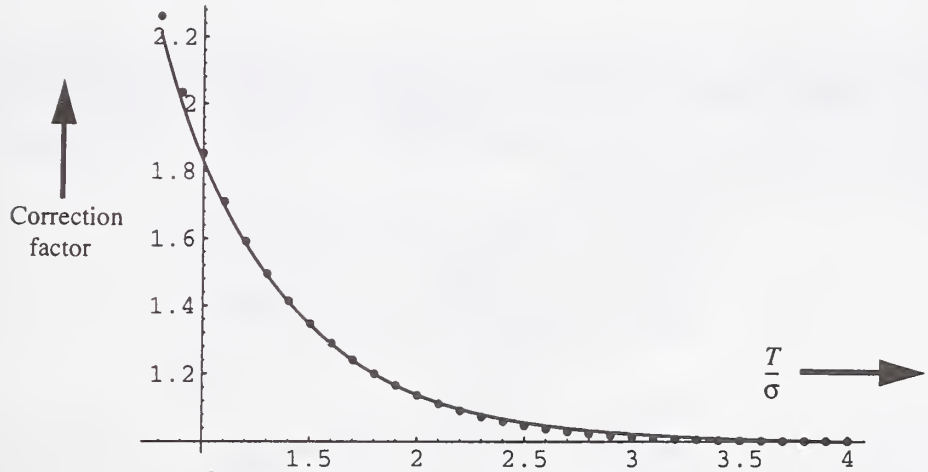

Fig. 2. Correction factor z and its approximation $\hat{z}$ as a function of T/σ. Points are exact corrections, solid line is the approximation.

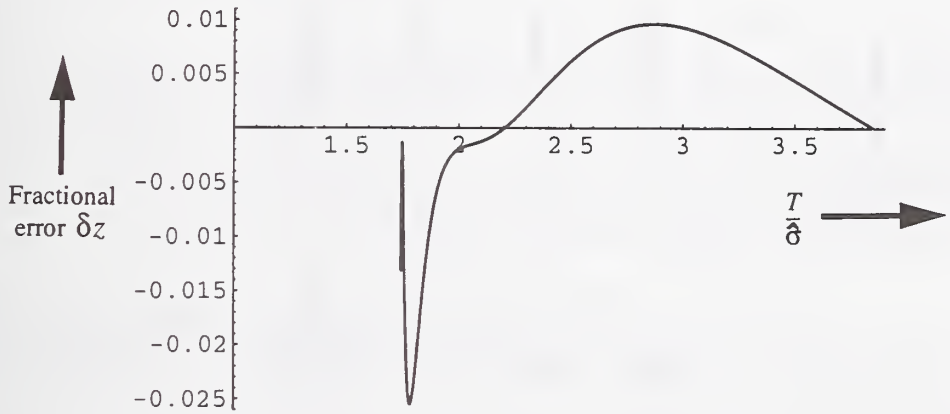

Fig. 3. Fractional error of the correction factor given by (5). Note the difference in the independent variable between Figs. 2 and 3. The ratio $T/\hat{\sigma}$ approaches a limit of $\sqrt{3} \approx 1.732$ for very small integration intervals, i.e. as T/σ approaches zero.

From Fig. 3, the factional error δz between (4) and (5) is seen to be given by

$$\begin{aligned} |\delta z| &< 0.01 \quad \text{for } T > 1.870\,\hat{\sigma} \\ |\delta z| &< 0.026 \quad \text{for } T > 1.743\,\hat{\sigma} \end{aligned} \tag{6}$$

Finally, we demonstrate the use of this correction factor with an ensemble of interferometric PMD measurements. A single 6.6-km single mode fiber, loosely wound on a spool, was measured 25 times using the block diagram of Fig. 3. Statistical independence of the 25 measurements was ensured by changing the temperature of the fiber in 8-K steps or by rearranging the layers of fiber on the spool between measurements. We assume the rearrangement and temperature changes had no systematic influence on the PMD of the fiber, and therefore consider the 25 half-width measurements to comprise a statistical ensemble. The mean of the ensemble distribution was estimated in terms of an 80% confidence interval, i.e. the mean of the

distribution lay within the interval with probability 0.8. Confidence intervals were calculated using noise thresholds 3 dB, 6 dB, 9 dB, and 12 dB above the measured rms shot noise. In each case, the resulting interval is shown in Fig. 5 with and without correction by the ratio given by (5).

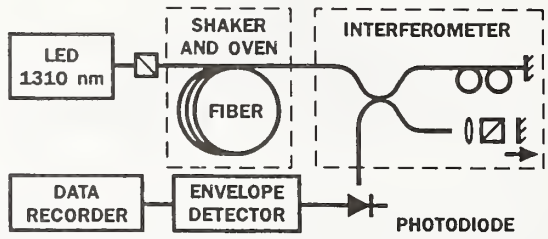

Fig. 4. Block diagram of interferometric PMD measurement.

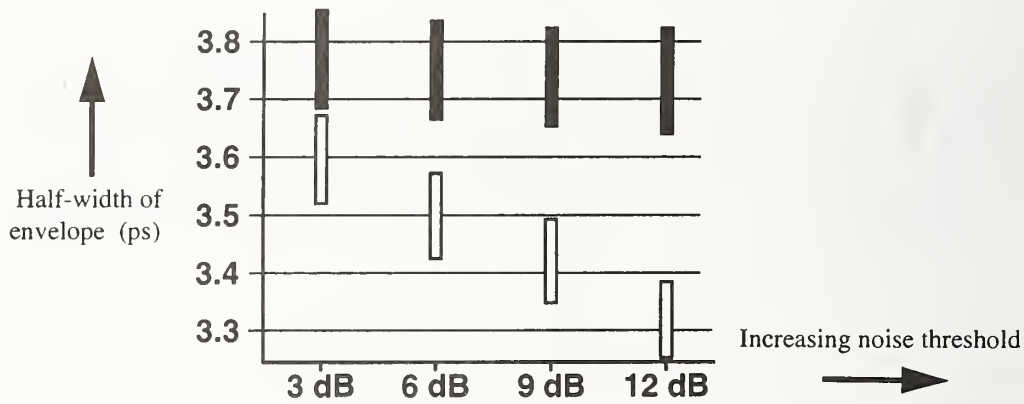

Fig. 5. 80% confidence intervals indicating the mean half-width of the interferometric Gaussian envelope, calculated using four different noise thresholds 3 dB, 6 dB, 9 dB, and 12 dB above the measured rms shot noise. Calculations for the filled intervals are corrected by (5); those for the open intervals are not corrected. Correction by (5) removes the influence of the noise threshold over the calculated PMD.

The signal level at the shoulder of the measured Gaussian envelope was approximately 38 dB above the rms shot noise level (a factor of 80 in photocurrent). Use of different noise thresholds is equivalent to use of a constant noise threshold coupled with differing amounts of optical loss in the measured fiber. The open intervals of Fig. 5 demonstrate the dependence of the calculated Gaussian half-width on the noise threshold. The filled intervals, calculated using the correction given by (5) are essentially independent of the noise threshold level.

Summary: Direct evaluation of the second moment of an interferometric PMD measurement leads to a bias in the calculated half-width $\hat{\sigma}$ of the Gaussian envelope. This bias can be removed by the correction factor given by (5). The true Gaussian half-width is given by $\sigma = \hat{\sigma}\hat{z}$. Efficacy of this correction is shown in Fig. 5, where uncorrected half-widths are seen to depend on the noise threshold, whereas the corrected half-widths are very nearly equal regardless of the noise threshold.

A practical comparison between two different PMD measurement methods

Bertil Arvidsson, Hans Mickelsson[1]
Ericsson Cables AB, Hudiksvall, Sweden

Kim Brising
TELIA, Farsta, Sweden

Abstract

A comparison between PMD measurements using the interferometric and the wavelength scanning technique is presented. The results, arising from measurements on fibres on shipping spools, fibres on spools with various diameters and on cabled fibres show a reliable relationship between the two methods. As a conclusion it can be said that a result obtained by one of the instruments is reproducible on the other.

Introduction

With increasing bit-rates in telecommunication networks PMD has become a more important subject in both installed cables and in cables under development. In order to investigate how different designs and installation techniques impact on the cable PMD a lot of field measurements as well as lab testing has to be carried out. Because we have used different instruments in lab environment and in field trials, an investigation of the accuracy between the two instruments were carried out. For a background of definitions and technique see (1).

Measurement set-up and choice of fibres and cables

The two instruments were one EG&G instrument, using the wavelength scanning technique (fixed analyzer) and one GAP instrument, using the interferometric technique. The main difference between the performance of these two instruments are the possible ranges. The actual EG&G instrument has a possible PMD-range between 0.05 to 1.6 ps, the wavelength can be choosen in different regions between 1165 and 1688 nm. The GAP-instrument is capable of measuring PMD from approximately 0.1 ps to 30 ps, the wavelength is chosen by using either the 1300 nm or 1550 nm LED.
For this comparison two 36-fibre ribbon cables and four bare fibres on shipping spools were chosen. Also five bare fibres wound on spools with different diameters, introducing different levels of PMD, were included in the comparison (see also 2).

Conditions and theory

All measurements were conducted in a clean room area with a controlled temperature, both the fibres and the cables were stored in that environment for at least 24 hours before any measurements took place. To obtain almost identical conditions for the comparative measurements they were performed in a sequence, first one and then the other instrument.
One problem in interpreting the results is the fact that different wavelength ranges gives slightly different results. The GAP-instrument uses two LED:s with unknown spectral widths and the EG&G-instrument uses two LED:s and a monochromator to control the spectral range. Since PMD has a slight wavelength dependence especially for short fibre lengths, this fact can have some impact on the results. Another matter to consider is the wavelength window where the measurements shall be performed.

---

[1] Now at Ericsson Telecom AB, Stockholm, Sweden.

Why can the PMD-value differ between measurements done by the interferometric and the wavelength scanning method?

1. The wavelength range in case of the EG&G instrument is well defined due to the monochromator and the two LED:s used. Uniform spectral weighting is achieved by normalising the polarimetric data for the source power and fiber loss (3). For the GAP instrument, the spectral range is determined by the shape of the LED spectrum (normally Gaussian), so this may lead to non-uniform spectral weighting.
2. The deployment conditions of the fibres/cables, the degree of mode coupling and intrinsic birefringence.
3. The statistical nature of PMD gives that the results between different measurements can vary significantly, up to 30-40% in some extreme cases.

Although the wavelength dependence typically only shows through in the second decimal point and all specifications seen so far specifies PMD to the first decimal point, the following methodology was used to amortise the effects of the wavelength dependence. For measurements with the wavelength scanning technique the best possible wavelength range was chosen. This means that sometimes in a series of measurements different ranges might have been used. However, the results are always treated as wavelength independent. For measurements using the interferometric technique at both wavelengths the results are averaged and taken as the fiber PMD value.

Results

Fibres on shipping spools

The four bare fibres on shipping spools, labelled A, B, C and D were measured 10 times with the GAP instrument at both 1310 nm and 1550 nm and 7 times with the EG&G instrument at different wavelength ranges to obtain a knowledge of the repeatability. The fibres were wound on standard shipping spools, diameter 150 mm, with a winding tension of approximately 30 grams. Table 1 shows the results. They consist of mean values between all wavelengths used on each instrument. As can be seen no significant differences are present.

Fibre	Instrument	PMD mean value		Length[km]
		[ps/√km]	[ps]	
A	GAP	0.04	0.20	19
	EG&G	0.06	0.25	
B	GAP	0.06	0.15	6
	EG&G	0.05	0.14	
C	GAP	0.07	0.15	4
	EG&G	0.07	0.11	
D	GAP	0.06	0.31	25
	EG&G	0.07	0.28	

Table 1. Repeatability measurements on fibres wound on shipping spools.

Fibres on spools with different bend radii

Five spools with radii ranging from 55 mm to 200 mm were chosen. These spools have been measured periodically for approximately 6 months with the wavelength scanning technique (ECA1-ECA6) to obtain a knowledge of the variation in PMD by time. The winding tension for all fibres were approximately 30 grams. The results are shown in Figure 1, ECA7 (representing the wavelength scanning technique) and TELIA (representing the interferometric technique)

were measurements carried out at the same time. The results show that ECA representing the wavelength scanning technique tends to measure a higher PMD-coefficient at higher PMD values than TELIA representing the interferometric technique does.

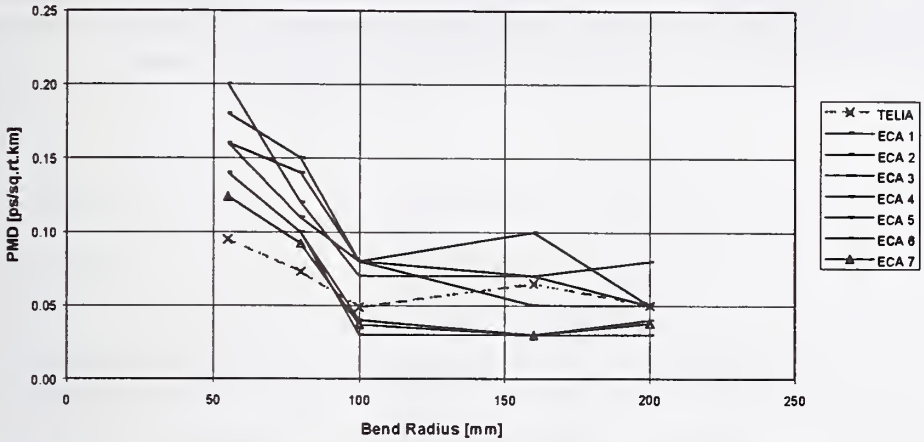

Figure 1 PMD measured at different bend radii with both techniques.

Cabled fibres

Two 36-fibres ribbon cables were wound on cable drums with a diameter of 950 mm, the winding tension was unknown but low enough to not impact on the results. Since the results are similar in both cables only PMD-coefficients from one of them are shown in Figure 2. The PMD-coefficients ranging from 0.03 to 0.36 ps/√km. This gives a quite broad PMD range and thereby a good indication of the relationship between the two methods. A statistical treatment, using the t-distribution gives the following results, averaged over all fibres.

Interferometric Method: PMD=0.12±0.16 ps/√km (95% significance level)

Wavelength scanning method: PMD=0.13±0.16 ps/√km (95% significance level)

This shows a good correlation between measurements performed with both techniques.

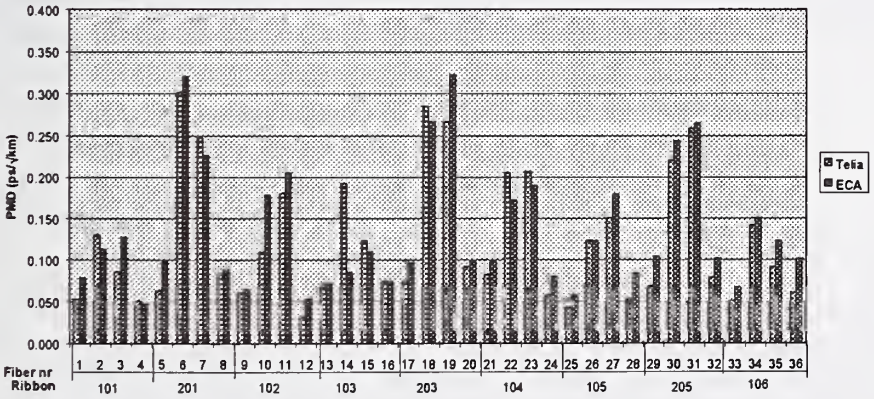

Figure 2 PMD measured on a cable, the high PMD on 3 of the ribbons is due to the cable design.

Summary

In Figure 3 a plot of ECA-values against TELIA-values is shown, PMD-coefficients measured in both cables and on the spools with different diameters are taken into consideration. In the plot a linear regression is also shown, giving a correlation coefficient, R, of 0.92. From a statistical point of view a R-value > 0.9 is indicating a reliable relationship. Further, a statistical treatment of the results by means of a two sided t-test with a significance level of 95% showing a reliable dependence between the two methods. Results from field measurements in Sweden are discussed in (4).

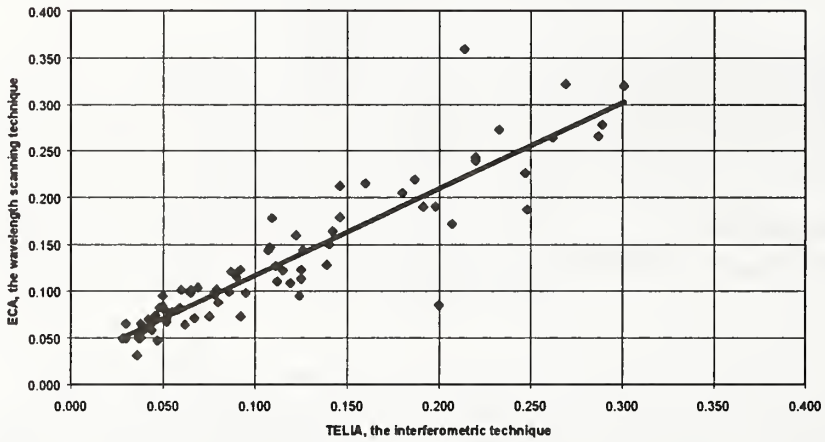

Figure 3

Acknowledgement

We thank Dr A. Barlow from EG&G for valuable technical discussions.

References

1 N. Gisin, "Polarization Mode Dispersion:Definitions, Measurements and Statistics", Symposium on Optical Fiber Measurements, 1994.

2 B. Arvidsson, H. Mickelsson, A. Barlow, "A PMD Study on Fibres in a Cable Factory", OFMC 95.

3 FOTP-113, TIA.

4 K. Brising, "Polarisation Mode Dispersion Field Measurements: Survey of the Swedish National Optical Network", to be published in IWCS 1996.

Interferometric Polarization Mode Dispersion Measurements with Femtoseconds Sensitivity

Ph. Oberson◊, K. Julliard◊, N. Gisin◊,
◊Group of Applied Physics
University of Geneva
1211 Geneva 4
Switzerland

R. Passy*, JP Von der Weid*
*Center for Telecommunications Studies
Pontifica Universidade Catolica
Rio de Janeiro 22453
Brasil

The standard interferometric measurement technique for Polarization Mode Dispersion (PMD) measures the cross correlation of the electro-magnetic field at the output of the fiber or optical device under test when a broad spectrum light source is used [1]. The sensitivity (smallest measurable PMD delay) of this well-established technique is limited by the coherence time of the light source. In this contribution we analyze critically extensions of the interferometric technique to lower values and present a new extension which provides a sensitivity of a few femtoseconds.

When the polarization mode delay is smaller or comparable to the coherence time of the source, the Fiber Under Test (FUT) behaves as a two mode fibers: the so-called principal states of polarization. For example, if the Differential Group Delay (DGD) is smaller than 0.1 ps, then the FUT behaves as a two mode fiber even when illuminated with an LED with 80 nm spectral width. In this case, in order to measure the DGD between these two principal states with the interferometric technique, the acquisition of the interferograms as well as their analysis and interpretation have to be changed.

A first possibility consists in using a birefringent Michelson interferometer based on a Polarization Beam Splitter (PBS) instead of the usual 50-50% beam splitter. The axes of this PBS are then adjusted to the "axes" of the FUT. In this way the two arms of the interferometers are extended by the two principal modes of the fiber. Hence the center of the interferogram is shifted with respect to its position in the absence of the FUT. This method is related to the cross-correlation interferometer describe in [2]. Note however that this method requires a full polarization controller to adjust the linear principal states of the birefringent Michelson interferometer to the principal states of the fiber under test. Indeed, the latter are generally elliptic. Hence, a simple polarization rotator (like the half-wave plate used in [2]) is insufficient. With such a half-wave plate the measured DGD underestimates the real DGD.

Below we present for the first time a new interferometric high sensitivity measurement technique based on a standard fiber interferometer with a 50-50% optical coupler (Patent applied for). In this technique a full polarization controller plus a polarization maintaining HiBi fiber of around 0.5 ps PMD delay are placed between the fiber under test and the interferometer, see Figure 1. The HiBi fiber produces two side-peaks on the interferogram, left and right from the central aurocorrelation peak. When the principal states of the FUT are aligned with the eigenmodes of the HiBi fiber, their delays add, whereas they subtract when the fast principal mode of the FUT is aligned to the slow mode of the HiBi fiber. Hence, by

measuring the displacement of the side-peaks when the orientation of the principal modes of the FUT are scanned relative to the axes of the HiBi fiber, the delay between them can be determined.

This measurement method is reminiscent of that presented in [3], since in both methods a HiBi fiber is inserted before the interferogram. An important difference, however, is that this reference [3] proposes to measure the spread of the interferogram (actually in [3] the interferogram is computed by Fourier transform a wavelength spectrum, but this does not change the argument). However, the determination of the position of an interferogram is much more accurate than the determination of its width. Indeed the position can be determined with a reproducibility of less than 3 fs [4], whereas it is difficult to determine the width with a reproducibility better than 50 fs. For example, in [4] a standard deviation of 2.14 fs was obtained for a thousand measurements of the position of interferograms at 1.55 micron. Moreover, without the polarization controller, the width of the satellite peaks do not contain the full information about the DGD of the FUT. For instance, if the principal states of the HiBi fiber and the FUT happen to be aligned, then the width of the satellite peak is determined only by the LED spectrum.

According to our experimental results the sensitivity of our setup is of a few femtoseconds (hence much lower than the source coherence time). The main limitation of this new measurement method lies in the birefringence of the pigtails and other components of the set-up. Note for example that three 1/4 wave plates can already produce a DGD of about 4 fs. Figure 2 presents three interferograms (around the position of one of the satellite peaks). They represent the three different alignment conditions between the FUT and the HiBi fiber: aligned, at 90 degrees and at 45 degrees, respectively. Clearly, the latter case corresponds to the larger width, as it should. The difference in position between the two extreme cases correspond to twice the DGD of the FUT. This result is in good agreement with other measurement methods. Figure 3 presents two complete interferograms, showing the central autocorrelation peak and the two satellite peaks for the two extreme alignments of the principal states. The 11 fs result illustrate the high resolution of this technique. In Figure 4 a graph of measurement results for various length of a HiBi fiber of known PMD (0.23 ps/m) is presented. The horizontal scale represents the expected DGD directly proportional to the fiber length. The vertical scale is the standard deviation of the distance between the two satellite peaks over 125 interferograms obtains for different alignment conditions.

In conclusion, the existing extensions of the interferometric measurement technique for PMD measurements to value lower than 0.1 ps are of limited use. A new extension has been developed and tested. It extends the measurement range down to about 10 fs.

Acknowledgments

This work has profited from stimulating discussions with Dr B. Perny from the Swiss Telecom PTT.

References

1. N. Gisin et al, IEEE J. Lightwave Technology 9, 821-827, 1991.
2. Y. Namihira et al. IEEE Photonics Technol. Lett. 1,329-331, 1989; see also OFMC'93, Torino, p. 189-192, 1993.
3. A.J. Barlow et al., Proceedings of the 3rd Optical Fiber Measurement Conference, Liège, Belgium, Edited by the European Action COST 241, p. II.4, 1995.
4. L. Thévenaz et al, IEEE J. Lightwave Technology 6, 1-7, 1988.

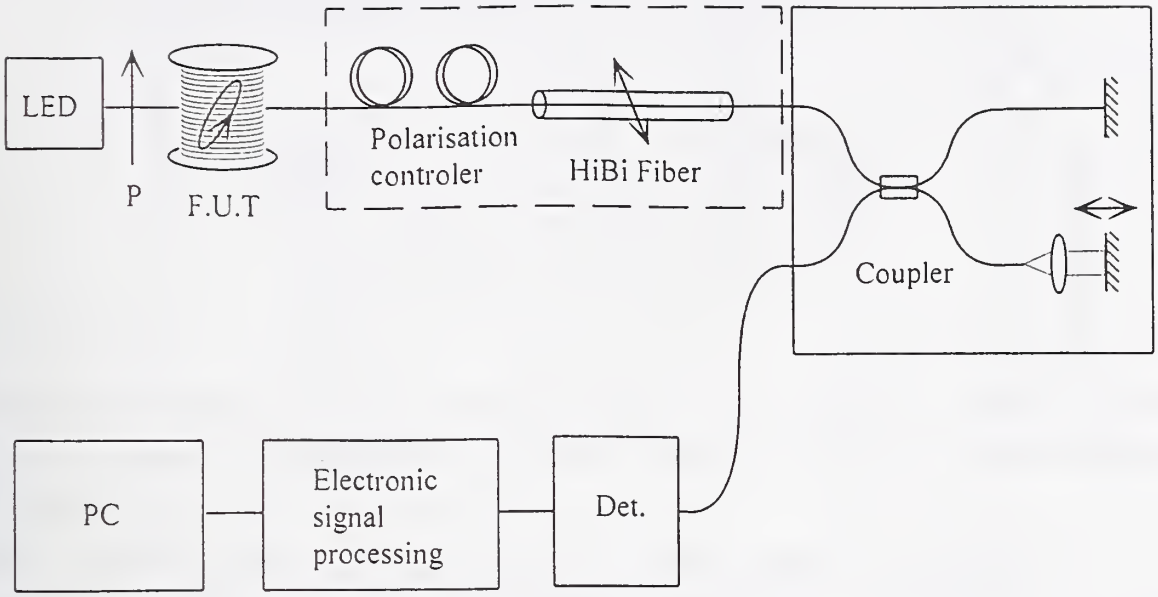

Figure 1: Schematic of the set-up. The ellipse on the Fiber Under Test (FUT) indicates that the principal polarization state are in general elliptic. The arrow on the HiBi fiber indicate the axes of such fiber that define linear polarization states. The polarization controller couples the two elliptic principal states of the FUT to the two linear eigenmodes of the HiBi fiber. The remaining of the set-up is identical to the instruments used for interferometric PMD measurements.

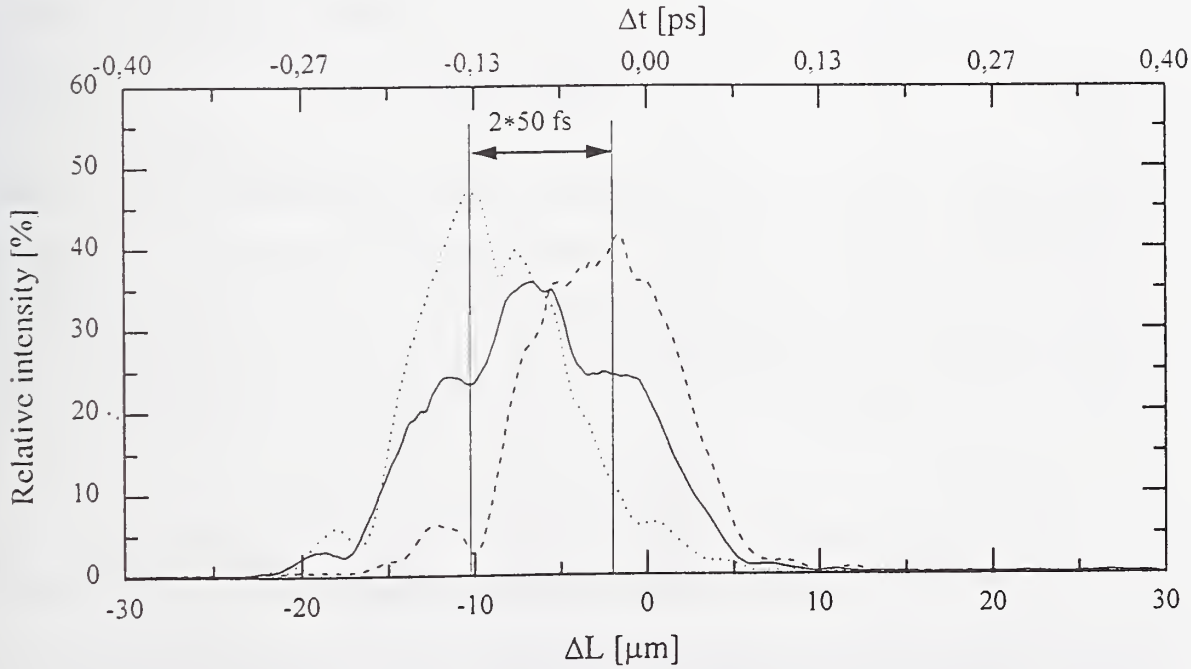

Figure 2: Example of interferograms obtained for a FUT with a relatively large PMD of 50 fs. Only the scan around one the side peaks produced by the HiBi fiber is shown. The full line corresponds to the case were the polarization controller is not aligned. The two side peaks can still be distinguished. The dotted and dashed lines correspond to the case were the fast principal polarization states of the FUT are aligned with the fast, slow eigenmode of the HiBi fiber, respectively.

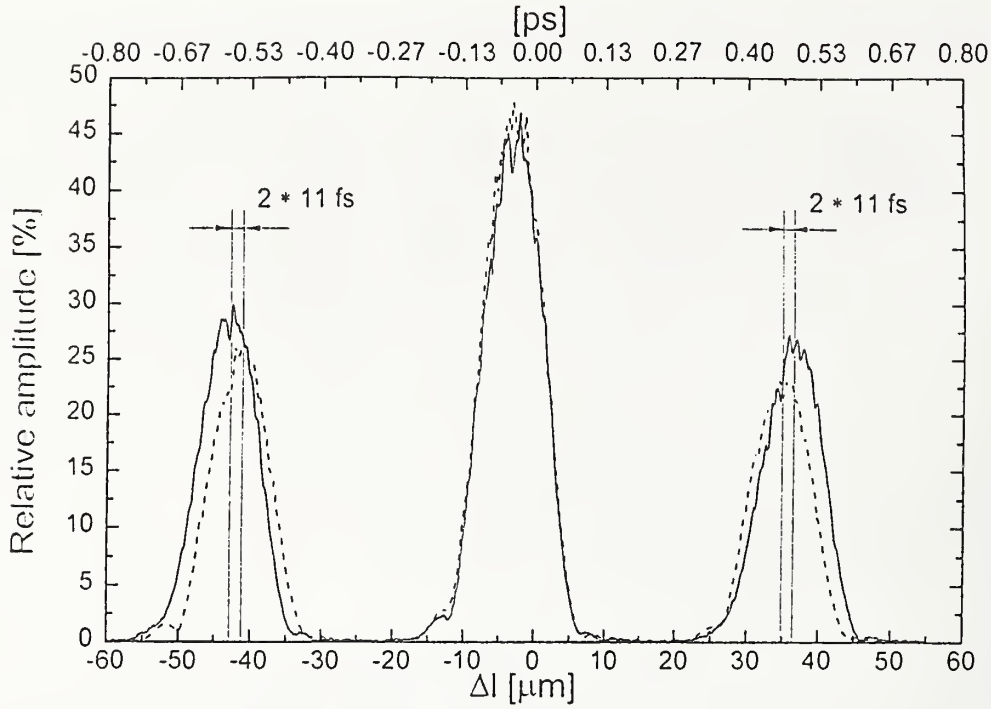

Figure 3: Example of interferograms obtained for a FUT with a DGD of about 10 fs. The scans through the central autocorrelation peak and the side peaks produced by the HiBi fiber are shown. The full and dashed lines correspond to the case were the fast principal polarization states of the FUT are aligned with the fast, slow eigenmode of the HiBi fiber, respectively.

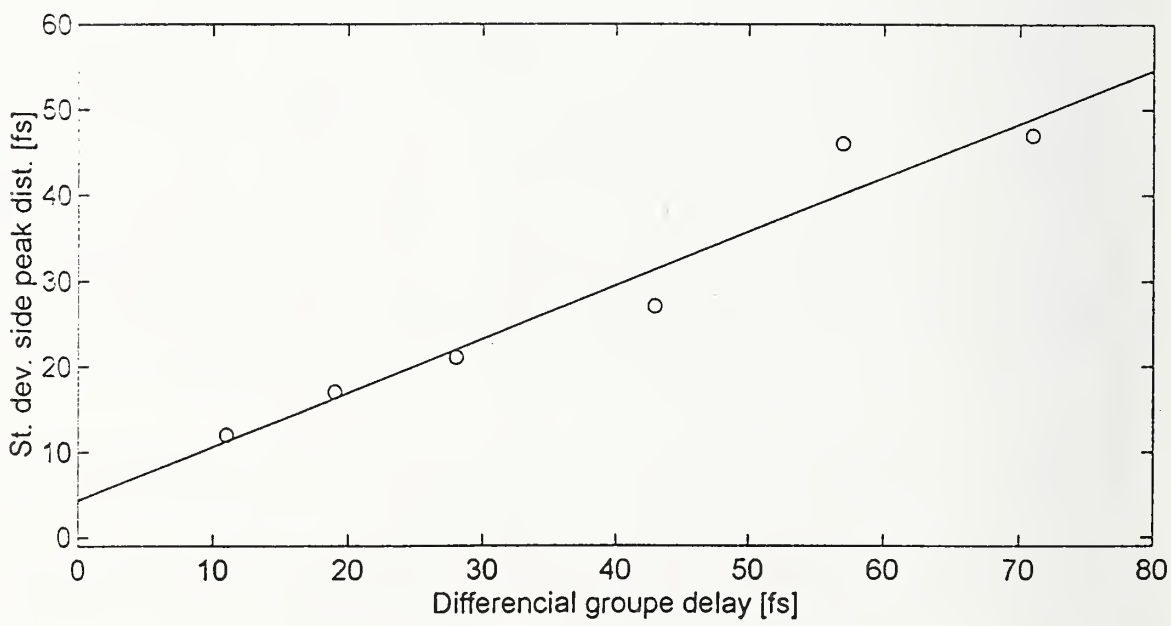

Figure 4: Measurement results versus expected PMD. The horizontal scale correspond to 230 fs/m times the fiber length, where the PMD of 230 fs/m was measured on a longer fiber sample with the standard interferometric measurement technique. The vertical scale corresponds to one standard deviation of the measured distance between the side peaks in 125 interferograms obtained for different relative orientations of the FUT and HiBi fiber axes. The standard deviation of the linear fit (full line) is of 5.5 fs. This illustrates the sensitivity of the measurement technique and its linearity.

A Novel PMD Estimation Technique with Wavelength Stepsize Optimization

Osamu Aso and Haruki Ogoshi

Opto-Technology Laboratory, Furukawa Electric Co., Ltd.

6, Yawata-Kaigandori, Ichihara, Chiba, 290 Japan

Tel. +81-436-42-1724, Fax. +81-436-42-9340

e-mail: aso@optec.ch.furukawa.co.jp

1. Introduction

The concept of the principal states of polarization(PSP) has been widely accepted and utilized in polarization analysis. PSP was introduced by Poole and Wagner[1] as the stable state of polarization(SOP) in the frequency(wavelength) domain.

In order to apply PSP theory to PMD analysis, the differential group delay(DGD) time of the two orthogonal PSPs is known to play an important role. According to Poole and Wagner, in the absence of polarization dependent losses, Jones matrix U of the optical transmission medium is represented as an element of the unimodular unitary matrices[2]:

$$U = \begin{bmatrix} u_1(\omega) & u_2(\omega) \\ -u_2^*(\omega) & u_1^*(\omega) \end{bmatrix}, \det U = +1 \tag{1}$$

DGD time $\Delta\tau$ of the PSPs is calculated as

$$\Delta\tau = 2\sqrt{\left(\frac{du_1}{d\omega}\right)^2 + \left(\frac{du_2}{d\omega}\right)^2} \tag{2}$$

At present, in order to estimate the above $\Delta\tau$ experimentally, two measurement techniques have been developed:Jones matrix eigenanalysis[3] and Poincare sphere method[4],[5]. With the Poincare sphere method, 3-dimensional real vector Ω is the essential parameter used to describe the polarization properties of the transmission medium. The vector is called as the PMD vector and its magnitude coincides with the DGD time of the PSPs:

$$|\Omega| = \Delta\tau = 2\sqrt{\left(\frac{du_1}{d\omega}\right)^2 + \left(\frac{du_2}{d\omega}\right)^2} \tag{3}$$

According to the geometrical interpretation, the Jones vector is understood as the Euclidian spinor quantity in Stokes space[2]. The transformation from the spinor field to the vector field makes it possible to prove the mathematical relation of eq.(3) explicitly[6]. In this report, based on the result of the above transformation, we will present a novel and direct PMD vector estimation technique through the Jones matrix measurements.

2. Wavelength Dependence of the SOP in the Stokes and Jones Vector Space

As discussed in the preceding section, PSP is defined as the stable state in the wavelength domain.

In this section, we will briefly review the basic equations which describe the wavelength dependence of the SOP both in the Stokes and Jones vector space.

2.1 Stokes Vector Representation

Stokes parameter representation of the wavelength dependence of a SOP has been discussed in ref.[5]. Discussions are summarized by the following equation of rotation[4],[5]:

$$\frac{d\,\mathbf{s}}{d\omega} = \Omega \times \mathbf{s}, \tag{4}$$

where $\mathbf{s}$ is the normalized Stokes vector and ω is the angular frequency of light. In eq.(4), Ω represents the rotational axis of the Stokes vector. The direction of the Ω vector indicates the PSP of the transmission medium, and the magnitude of the vector coincides with the DGD time of the PSPs[5].

2.2 Jones Vector Representation

Jones vector is understood as the spinor representation of the normalized Stokes vector field[2]. Thus any SOP points on the Poincare sphere are mapped into the spinor field. According to spinor analysis, eq.(4) can be represented as[6],[7]

$$i\frac{d\psi}{d\omega} = \frac{1}{2} H\,\psi, \tag{5}$$

where Ψ is the 2-dimensional complex Jones vector and H is the hermite matrix defined as

$$H \equiv \frac{2}{i} U \frac{dU^{+}}{d\omega} = \begin{bmatrix} h_1 & h_2 \\ -h_2^{*} & -h_1 \end{bmatrix}, \tag{6}$$

$$h_1 = \frac{2}{i}\left(u_1 \frac{du_1^{*}}{d\omega} + u_2 \frac{du_2^{*}}{d\omega}\right), \quad h_2 = \frac{2}{i}\left(u_2 \frac{du_1}{d\omega} - u_1 \frac{du_2}{d\omega}\right). \tag{7}$$

Using the unimodular unitary condition of the matrix U, it is easily shown that h_1 is the real and h_2 is the complex function. The physical meanings of eq.(4) and eq.(5) are essentially equivalent and both represents the rotational motion of the SOP around the PSP[6].

3. PMD Vector Estimation Based on the Jones Matrix Measurements

As shown in eq.(4) and (5), wavelength dependence of the SOP is described in the similar manner with rotation. The PMD vector is obtained from Stokes vector trajectory measurements with slight wavelength changes[4],[5].

Based on the spinor transformation discussed in section 2, the PMD vector can be derived as:

$$\Omega = \begin{bmatrix} h_1 \\ \mathrm{Im}\,(h_2) \\ \mathrm{Re}\,(h_2) \end{bmatrix}. \tag{8}$$

The magnitude of the Ω vector is easily calculated and satisfies eq.(3). Thus, direct estimation of the

PMD vector is possible to realize through the Jones matrix measurement[3].

In order to be able to apply the above method, we must assess the suitability of the frequency step size $\Delta\omega$. If the step size is larger than the upper limit from the first order approximation, the higher order effect[7] makes it difficult to estimate the PMD value accurately[5],[6]. For our discussions, a suitable $\Delta\omega$ ensures the hermiticity of the matrix H: the element h_1 must not have an imaginary component. It is expected that the estimation of the following quantity will lead us to a suitable step-size estimation

$$\Gamma(\Delta\omega) \equiv \left| \frac{\mathrm{Im}\left[h_1(\Delta\omega)\right]}{\mathrm{Re}\left[h_1(\Delta\omega)\right]} \right|. \tag{9}$$

If Γ is not negligible, the first order approximation is violated and the estimated Ω does not generally represent the PMD vector of the medium. So a suitable threshold Γ_{th} ($\Gamma_{th} \ll 1$) condition enables us to ensure accurate estimation.

We will now provide a summary of the discussions of this section. Jones matrix measurement by the sufficiently coherent light will enables us to determine the Jones matrix $U(\omega_0)$ and $U(\omega_0+\Delta\omega)$. Then one can apply finite differential approximation in order to estimate the matrix H and the quantity Γ.

4. Numerical Simulation

In order to confirm the discussions in the preceding section, we will perform a numerical simulation in this section. In order to show the availability of the scheme, we consider a transmission medium with polarization mode coupling. The medium consists of two PMFs with finite angular misalignment[9]. The specification of the two PMFs are as follows: they have the same linear birefringence and that birefringence is assumed to be independent of wavelength. The DGD of each fiber is set to be 3.00 ps and 2.00 ps respectively. Angular misalignment is set to be 30 deg..

Result of the simulation is shown in Fig. 1. It is understood that when the step-size $\Delta\omega$ decreases, $|\Omega|$ converges to the theoretical DGD time 4.36 ps. From this result, we can say that measurement feasibility is insured when we set $\Gamma_{th} = 0.10$ with accuracy 0.07ps.

5. Conclusion and Remarks

We have developed a direct PMD vector estimation technique. However, the technique strongly depends on the unitarity of the Jones matrix. On the other hand, at present, the practical Jones matrix measurement procedure is not expected to preserve the geometrical symmetry of the matrix[3]. As the exponential approximation scheme was introduced into the Jones matrix eigenanalysis by Heffner, it is necessary to consider some approximation scheme[6].

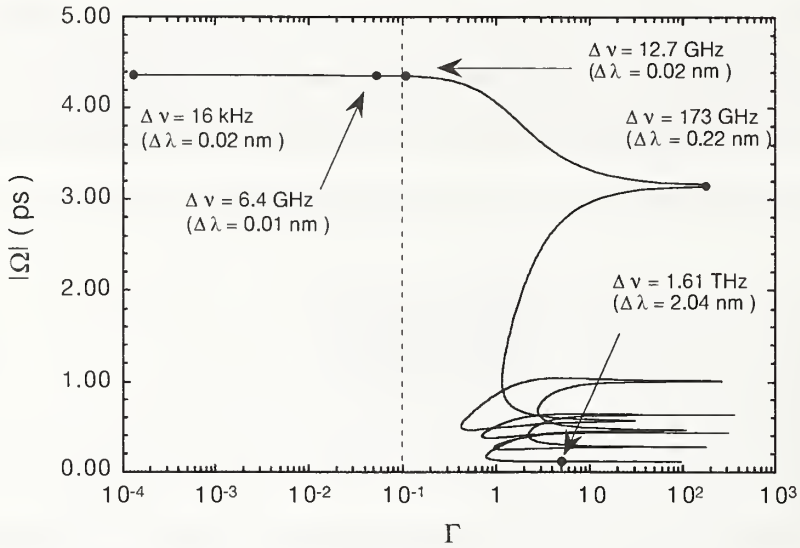

Fig. 1. Result of the numerical simulation. Horizontal axis shows Γ value and vertical axis is the magnitude of PMD vector.

Acknowledgment

The authors would like to thank Prof. T. Futamase and Mr. N. Jin of Tohoku University for their helpful discussions. O. A. would like to thank Mr. H. Nakamura for his reading of the manuscript and valuable comments. He also wishes to thank Mr. S. Yoon from the University of British Columbia for his reading of the manuscript and continuous encouragements.

References

[1] C. D. Poole and R. E. Wagner, *Electron. Lett.*, vol. 22, No. 19 (1986) pp. 1029 - 1030.

[2] H. Takenaka, *Nouv. Rev. Optique*, vol. 4, No. 1 (1973) pp. 37-41.

[3] B. L. Heffner, *Photon. Technol. Lett.*, vol. 4, No. 9 (1992) pp. 1066-1069.

[4]Y. Namihira and J. Maeda, *Symp. on Optical Fiber Measurements, Boulder, Co. USA* (1992) pp. 145-150.

[5] C. D. Poole, N. S. Bergano, R. E. Wagner and H. J. Shulte, *J. Lightwave Technol.*, vol. 6, No. 7 (1988) pp. 1185-1190, and references therein.

[6] O. Aso, I. Ohshima and H. Ogoshi, " Feasibility Study on A Jones Matrix Measurement Method Preserving A Geometrical Symmetry and Its Application to Polarization Mode Dispersion Analysis ", to be submitted.

[7] C. D. Poole and C. R. Giles, *Opt. Lett.*, vol. 13, No. 2 (1988) pp. 155-157.

[8] O. Aso, I. Ohshima and H. Ogoshi, *OEC'94, Makuhari, Japan* (1994) paper 14E - 2, pp. 238 - 239;*Symp. on OpticalFiber Measurement, Boulder Co, USA* (1994) pp. 159 - 160.

[9] O. Aso and H. Nakamura, *Electron. Lett.*, vol. 32, No. 6 (1996) pp. 578 - 579.

First Report of ITU-T PMD Round Robin Measurements for Optical Fibers and Component

Y. Namihira[*] and ITU-T PMD Round Robin Group[#]
[Asia (Japan)[#1], Europe[#2], USA[#3]]

[*] KDD R&D Laboratories (ITU-T Coordinator)
2-1-15, Ohara, Kamifukuoka, Saitama 356 Japan
Tel : +81-492-78-7801, Fax : +81-492-63-9328, E-mail: namihira@lab.kdd.co.jp

[#1] M.Ohashi (NTT), Y. Suetsugu (Sumitomo), M. Sawada (Fujikura), O. Aso (Furukawa), S. Suzuki (Hitachi Cable), M. Noguchi (OCC), M. Ichimura (Santec), H. Fujishima (Oyokoden LAB), T. Ozeki (Sophia University)
[#2] B. Perny (Swiss PTT, COST-241 Coordinator), N. Gisin (GAP), A. J. Barlow (EG&G)
[#3] P. A. Williams (NIST, TIA Coordinator), K. S. Kim (AT&T), A. F. Judy (Lucent)

1. Introduction

In high bit rate, long haul, WDM and analog transmission optical amplifier systems, the optical pulse broadening due to polarization mode dispersion (PMD) could impair the performance of the systems. Therefore, it is very important to measure accurately the PMD of the optical fibers and optical components.

At the ITU-T WP-4/15 (Optical fiber cables and Systems) meeting in May 1994, they have been decided to start the international PMD round robin measurements. It was agreed that the three running round robin measurements, one in Asia (Japan), organized by KDD (Y. Namihira), one in Europe, organized by COST 241 (B. Perny, Swiss Telecom PTT), and a third one in North America, organized by TIA (P. A. Williams, NIST) would be combined in the following ITU-T meeting. Recently, the PMD round robin result's reports were presented at ITU-T SG15 May/June 1996 meeting [1].

This paper is the first report of ITU-T PMD round robin measurements for single mode optical fibers and fiber optic component in Asian (Japan) region using KDD PMD specimens. The results of an extensive intercomparison of the ITU-T PMD round robin measurements on seven kinds of KDD PMD specimens, coordinated by KDD (Y. Namihira) are presented and discussed. Sixteen laboratories from all over the world participated the intercomparison of the PMD round robin measurements.

2. Classification and Definitions of PMD Measurement Methods

The PMD is the differential group delay (or PMD) $\Delta\tau$ between two orthogonal state of polarization (SOP). In the PMD measurements, several methods have been reported [2]. So far, the PMD has been measured by mainly two different procedures. One is the time domain measurement and the other is the frequency domain measurement. The former method is based on the Interferometric method {Air path - Crosscorrelation type (Int-X) [2,3] and Fiber reference-Autocorrelation type (Int-A) [4] } and Optical pulse method [2]. The latter method is based on the evolution of the states of polarization (SOP) as a function of the frequency (wavelength).

In the frequency domain, there are six methods (wavelength scanning method) such as the Fixed analyzer method with extrema counting (FAEC) method [5,6], the Fixed analyzer method with Fourier transformation analysis (FAFT) method [7], the Poincaré sphere (PS) method [2,8-10], the SOP method [2], the Jones matrix eigenanalysis (JME) method [11] and the Transfer function matrix (TFM) method [12]. The classification of the various PMD measurement methods are summarized in Table 1.

3. PMD Round Robin Measurements

Three block's ITU-T PMD round robin measurements coordinators of Asia (Japan), Europe (COST 241) and USA (TIA) are shown in Fig.1.

The photograph and specifications of KDD PMD specimens are shown in Fig.2 and Table 2, respectively. This KDD PMD specimens are still available.

The first results of ITU-T PMD round robin measurements of the KDD specimens KDD-#1, #2, #3,

#4, #5, #6 and #7 are summarized in Table 3. The dimensionless values (normalized PMD) in the Table 3 are experimentally measured values normalized to the average value measured by the all participants.

No (weak) mode coupling case of KDD-#1, #2 and #3, strong mode coupling case of #4 and #5, and weak (strong) mode coupling case #6 and #7 are shown in Fig. 3 (a), (b) and (c), respectively.

From Table 3 and Figs. 3 (a), (b) and (c), it was found that ;

1) Interferometric method using crosscorrelation definition (Int-X) [2,3] and Jones matrix eigenanalysis method (JME) [11] showed consistent results comparing with the other methods.
2) Interferometric method using autocorrelation definition (Int-A) [3] showed unstable results in the case of no(weak) (KDD-#1-3) and weak(strong) (#6,7) mode coupling cases, but in the strong mode coupl -ing case, stable results were obtained. Especially, one results of #1 showed extremely larger values.
3) Fixed analyzer method using extrema counting (FAEC) [5,6] showed a slightly larger values comparing with the Int-X and JME methods in the strong mode coupling case. Accordingly, in the strong mode coupling sample, FAEC method may require the mode coupling correction factor ($k \leq 1$).
4) FA method using Fourier transformation analysis (FAFT) [7] showed larger measurement results of KDD-#5 and #6 comparing with the other methods (Int-X and JME).
5) The PMD values of the Poincaré sphere (PS) [2,8-10] and SOP [2] methods were obtained from the same Stokes analyzer (Polarimeter), the both calculating algorisms were different. The both results were almost the same. But, the SOP method's measurement dynamic range was narrower than the other methods.
6) The PMD values of the JME [11] and Transfer function matrix (TFM) [12] methods were obtained from the same Stokes analyzer, the both calculatring algorisms were different. The TFM measurement results showed extremely smaller measurement results of #1 and #7 comparing with the other methods.

5. Conclusion

It was confirmed that the Interferometric method using crosscorrelation definition (Int-X), Poincaré sphere (PS) and Jones matrix eigenanalysis (JME) methods showed consistent results comparing with the other methods such as Autocorrelation type Interferometric method (Int-A), Fixed analyzer using extrema counting method (EAEC), Fixed analyzer using Fourier transformation analysis method (FAFT), SOP method and Transfer function matrix method (TFM), respectively.

References:

[1] COM 15-301 (KDD): "First report of ITU-T international PMD round robin measurements in Asia (Japan), Europe and USA", ITU-T SG15, May/June, Geneva, 1996.

[2] Y. Namihira et al.,: "Polarization mode dispersion measurements in optical fibers", (Invited papers), Symposium on Optical Fiber Measurements (SOFM'92), NIST, Boulder, Co., USA, p.145, 1992.

[3] Y. Namihira et al.,:"Comparison of various polarisation mode dispersion measurement methods in optical fibres", Electron. Lett., vol.28, no.25, p.2265, 1992.

[4] N. Gisin et al., :"Polarization mode dispersion of short and long single-mode fibers", IEEE, JLT,vol.9, no.7, pp.821-827, 1991.

[5] Y. Namihira et al.,:"PMD reduction of optical fiber cables for transoceanic optical amplifier submarine cable systems" (The Best Paper Award), IWCS'93, Session 14, pp.655-664, USA, 1993.

[6] C. D. Poole et al., :"Polarization -mode dispersion measurements based on transmission spectra through a polarizer", IEEE,JLT,vol.12, No.6, p.917, 1994.

[7] A. Barlow et al.,: "Polarization mode dispersion measurement using Fourier analysis: Investigation of mode coupling behaviour in fibers", SOFM'94, pp.167-170, NIST, Boulder, Co., USA. 1994.

[8] Y. Namihira et al.,:"Polarisation mode dispersion measurements in 1520 km EDFA system", Electron. Lett., vol.28, no.9, p.881-882, 1992.

[9] C. D. Poole et al., :"Polarization dispersion and principal states in a 147-km undersea lightwave cable", IEEE, JILT, vol.6, No.7, pp.1185-1189, 1988.

[10] D. Andreciani et al., ;"Measurement of the group-delay difference between the principal states of the polarization on a low-birefringence terrestrial fiber cable", Opt. Lett., vol.12, no.10, p.844, 1987.

[11] B. L. Heffner : "Automated measurement of polarization mode dispersion using Jones matrix eigenanalysis", Photonics Technol. Lett., vol.4, no.9, p.1066, 1992.

[12] T. Ozeki et al. :"Birefringence distribution along fiber length", OFC'96, FA4, p.295, USA, 1996.

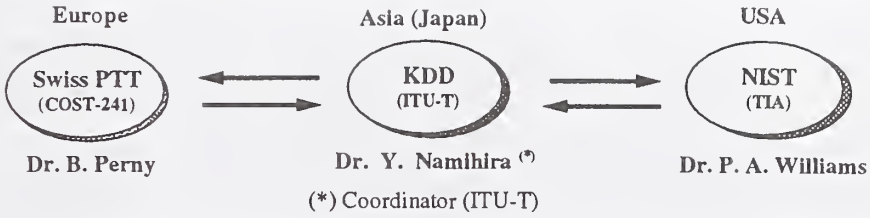

Fig.1 Coordinators of ITU-T International PMD round robin measurements

Table 1 Classification and definitions of various PMD measurement methods

	Time Domain			Frequency Domain (Wavelength Scanning)					
	Interferometric (Int)		Optical Pulse	Power		Principal State of Polarization (PSP)			
				Fixed Analyzer (FA)		Jones Matrix Eigenanalysis(JME)	Poincare' Sphere (PS)	State of Polarization (SOP)	Transfer Function Matrix (TFM)
	Crosscorrelation (Air Path Type) (Int-X)	Autocorrelation (Fibre Ref. Type) (Int-A)		Extrema Counting (FAEC)	Fourier Transformation Analysis (FAFT)				
Optical Source	Broadband Source (BS)	Broadband Source (BS)	Pulsed-LD	(#1) BS (#2) Tunable-LD (T-LD)	Broadband Source (BS)	Tunable-LD (T-LD)	Tunable-LD (T-LD)	(#1) T-LD (#2) BS & MON	Tunable-LD (T-LD)
Analyzer or Receiver	Michelson (or Mach Zehender) Interferometer	Michelson (or Mach Zehender) Interferometer	Streak Camera	(#1) Optical Spectrum Analyzer (OSA) (#2) Optical Power Meter (OPM)	Optical Spectrum Analyser (OSA)	Stokes Analyzer	Stokes Analyzer	(#1) Stokes Analyzer (#2) Rotatable Analyzer or Polarimeter	Stokes Analyzer
Basic Physical Measurement	Crosscorrelation between two orthogonal polarisation modes	Autocorrelation between two orthogonal polarization modes	A separation between two orthogonal polarization pulse	Transmission through an output polarizer at a series of wavelegnths	Transmission through an output polarizer at a series of optical frequency	Jones matrix at a series of wavelengths	Stokes vector arc on Poincare sphere at a series of wavelengths	SOP curve as a function of wavelength	Transfer function matrix at a series of wavelengths
Definition of PMD (or DGD)	(#1) A half Peak separation of two interferograms [Weak] (#2) Square root of the second moment of interferogram [Strong]	Square root of the second moment of interferogram	Peak separation of two optical pulses	Derive from number of extrema and wavelengths of first and last extremum	Square root of the second moment of Fourier transformed wavelength scanning data	Average of the DGD values computed from Jones matrix pairs	Derive from Poincare sphere rotation angle and frequency interval	Derive from a half number of extrema and wavelengths of first and last extremum of SOP curve	Average of the PMD values computed from Machraurin exapansion using Transfer matrix

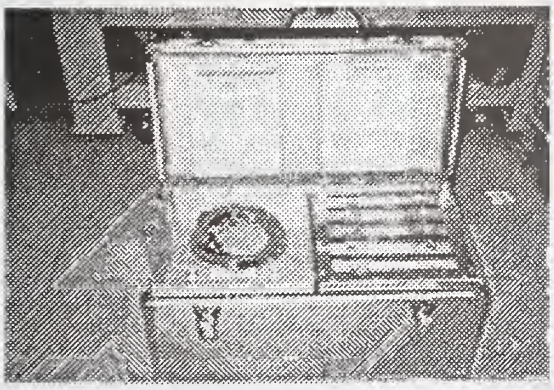

Fig. 2 Photograph of KDD PMD specimens

Table 2 Specifications of KDD PMD specimens

KDD PMD Test Specimens		Length [m]	Loss [dB]	PMD [ps]	Mode Coupling
Model	Contents				
KDD-#1	Optical Isolator	~ 0.04	~ 0.5	< 0.1	Weak
KDD-#2	No Spliced PMF	~ 0.646	~ 3.2	~ 0.1	No
KDD-#3	No Spliced PMF	~ 0.67	~ 1.3	~ 1.0	No (Weak)
KDD-#4	50 x PMFs (Randomly spliced)	~ 10.0	~ 9.9	~ 2.0	Strong
KDD-#5	6 x PMFs (Randomly spliced)	~ 8.708	~ 1.8	< 5.0	Strong
KDD-#6	G.654 Fiber Spool (CSF)	~ 13,991	~ 3.0	< 0.1	Weak
KDD-#7	G.653 Fiber Spool (DSF)	~ 13,673	~ 3.7	< 0.2	Weak (Strong)

PMF : Polarization Maintaining Fiber (Hi-Bi Fiber)
CSF : Cut-off Shifted Fiber (ITU-T G.654)
DSF : Dispersion Shifted Fiber (ITU-T G.653)

Table 3 Results of ITU-T PMD round robin measurements for optical fibers and component using KDD PMD specimens [The dimensionless values (normalized PMD) in the Table 3 are experimentally measured values normalized to the average value measured by the all participants]

PMD Method	KDD#1	KDD#2	KDD#3	KDD#4	KDD#5	KDD#6	KDD#7	Equipment	Algorism
Int-X (A)	0.789	0.970	1.006	#	#	#	#	C1(6)	C1(6)
Int-X (R)	1.014	0.992	1.005	1.035	1.068	0.751	0.941	C1(6)	C1(6)
Int-A (R)	1.177	0.879	3.098	1.101	1.072	1.402	1.029	C2(1),C3(1)	C2(1),C3(1)
FAEC (M)	1.027	1.038	1.002	1.036	0.833	1.165	1.112	C4(7),C5(7),C6(4)	C4(7),C5(7),C6(4)
FAFT (R)	1.014	1.015	0.992	1.075	1.384	1.323	0.965	C7(7)	C7(7)
JME (M)	0.989	1.023	1.000	0.885	0.935	0.859	0.882	C6(6)	C8(6)
JME (R)	0.989	1.023	1.002	0.956	0.992	0.859	0.900	C6(6)	C8(6)
PS (M)	0.989	1.008	0.999	0.907	0.933	0.849	0.924	P1(1),P2(1)	P1(1),P2(1)
SOP (M)	#	1.053	0.994	1.005	#	#	1.035	P1(1)	P1(1)
TFM (M)	0.675	1.152	1.004	0.609	0.813	0.790	0.412	C6(1)	H1(1)
Mode Coupling	Weak	No	No(weak)	Strong	Strong	Weak(Strong)	Weak(Strong)	Equipment	Algorism

(#) Not Measured C : Commercial P : Prototype H : Homemaid ( ) : Number

Int-X(A) ; Interferometric Crosscorrelation Air-path type (Peak)
Int-X(R) ; Interferometric Crosscorrelation Air-path type (RMS)
Int-A(R) ; Interferometric Autocorrelation Fiber reference type (RMS)
FAEC (M) ; Fixed Analyzer Extrema Counting. [Mean]
FAFT (R) ; Fixed Analyzer Fourier Ation Analysis. [RMS]
JME(M) ; Jones Matrix Eigenanalysis (Mean)
JME(R) ; Jones Matrix Eigenanalysis (RMS)
PS(M) ; Poincare Sphere (Mean)
SOP(M) ; State of Polarization (Mean)
TFM (M) ; Transfer Function Matrix (Mean)

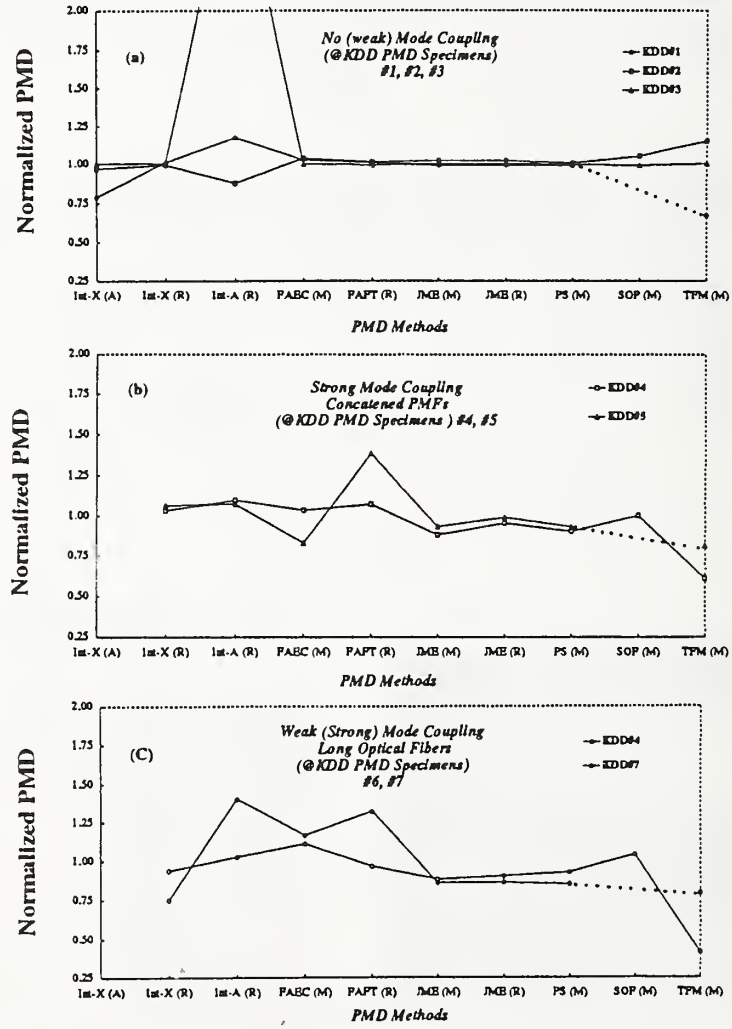

Fig.4 Results of ITU-T PMD round robin measurements (Normalized PMD) @ KDD PMD Specimens
(a) No (weak) mode coupling; Optical isolator & No spliced PMF
(b) Strong mode coupling ; Ramdomly spliced PMFs
(c) Weak (strong) mode coupling; Long optical fibers

TIA round robin for the measurement of PMD

P.A. Williams
Optoelectronics Division - National Institute of Standards and Technology
325 Broadway - Boulder CO 80303, U.S.A.

From 1994 to 1996, the National Institute of Standards and Technology (NIST) conducted a round robin for the measurement of polarization mode dispersion (PMD). This comparison was coordinated through the Telecommunications Industry Association (TIA) and involved participants from the United States as well as Europe and Japan measuring three PMD specimens. This paper will report the results of that round robin.

Three specimens were circulated to test various aspects of the measurement. These specimens were: Specimen 1, a pigtailed quartz waveplate with no polarization mode coupling; Specimen 2, a mode-coupled artifact composed of a stack of 12 quartz waveplates cemented together and pigtailed; and finally, Specimen 3, a 15 cm diameter spool of 25 km of typical communication fiber. All three specimens had a nominal PMD of a few tenths of one picosecond. This round robin included 16 participants from the United States, Europe, and Japan, and used up to four different measurement techniques: Jones matrix eigenanalysis (JME) – or equivalently the Stokes method, interferometry, and wavelength scanning, also known as fixed analyzer, with either extremum counting (WSEC) or Fourier transform analysis (WSFT) [1].

Specimen 1 (Stable, non-mode-coupled)
The single quartz waveplate has a theoretically predictable PMD which was calculated from the thickness of the waveplate and its wavelength dependent birefringence. However, the 2-3 m long fiber pigtails of the specimen have a non-negligible PMD which dominates the uncertainty of the device PMD. It is therefore possible to predict the measured PMD as the wavelength-averaged differential group delay DGD of the single waveplate device only to within ±2.5%, where the uncertainty is the maximum PMD variation seen experimentally when the fiber leads are arranged in various orientations.

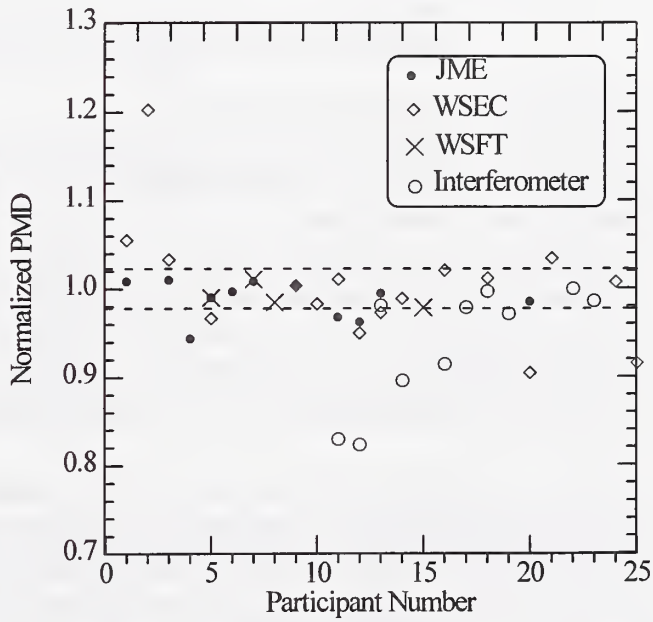

Figure 1 Single waveplate (Specimen 1).

Figure 1 shows the variation among participants' measurements of Specimen 1. The x-axis represents the participants, and the y-axis is their measured PMD normalized to the theoretically predicted value for the wavelength

at which the measurement was made. There are more participant numbers on the x-axis than participants because some participants made measurements on more than one similar system and consequently were assigned two participant numbers. Table I shows the measurement statistics. The agreement among participants is good, with most of the variation explainable by the PMD uncertainty due to the fiber leads (dashed lines of Figure 1). A few significant disagreements with theory can be seen. Some of these disagreements are explained by improper measurement techniques. One such disagreement is apparent in some of the interferometric results, where measurements were made by calculating the second moment of the double-peaked interferogram rather than measuring the time delay between the peaks. The existence of the autocorrelation peak in the interferogram might have led to incorrect results (yielding the smaller than theoretical values).

Table I Average / standard deviation of normalized measurements for each specimen. *One extreme data point was removed for interferometry (Int) statistics.

	Specimen 1	Specimen 2	Specimen 3
WSEC	1.00 / 0.067	1.02 / 0.119	1.08 / 0.28
WSFT	0.99 / 0.014	1.00 / 0.038	1.014 / 0.13
Int	0.94 / 0.068	0.99 / 0.051	0.96 / 0.21 *
JME	0.99 / 0.022	1.00 / 0.010	0.92 / 0.22
Total	0.98 / 0.060	1.00 / 0.076	n.a. / 0.24

Specimen 2 (Stable, mode-coupled)

The second specimen also has a theoretically predictable PMD. However, its application is not as straightforward. The DGD of the waveplate stack is derived from the measured thickness and known birefringence of each plate along with the known orientation angles of their optic axes with respect to each other. From this information, a Jones matrix for the 12-plate stack was calculated and DGD as a function of wavelength was derived. This information allows a theoretical prediction of PMD (as the average DGD over wavelength) with an accuracy similar to that of the single waveplate where the limit is a ± 2% uncertainty due to PMD of the fiber leads. This evaluation method allows accurate theoretical prediction of JME measurement results.

There is, however, a complication for other measurement techniques. A theoretical prediction of PMD is more difficult for techniques which do not measure DGD directly but rather measure PMD through some statistical parameter. Such techniques as interferometry and wavelength scanning with either extremum counting or Fourier analysis are subject to the fact that an exact theoretical prediction of the PMD of the mode-coupled artifact is possible only if the orientations of the measuring polarizer and analyzer are known with respect to the axes of the waveplate stack. This is not possible since the fiber pigtails randomly alter the polarization state before it impinges on the waveplate stack. In order to establish a theoretical prediction, participants made between 3 and 6

measurements with the polarizer and analyzer randomly rotated (or alternatively with the lay of the fiber leads randomized) between each measurement. The average of these measurements was normalized to a theoretical average derived from a computer simulation of 100 measurements over the same wavelength range using random polarizer and analyzer orientations.

Results are shown in Figure 2 and Table I. As expected, the best agreement came from the JME measurements where all of the data points fell within the uncertainty due to the PMD of the fiber leads (dashed lines). For the rest of the measurement techniques, most of the disagreements between experiment and theory are within the $2\sigma/N^{1/2}$ error bars, where σ is the standard deviation of the theoretical prediction and N is the number of measurements made by the participant. Uncertainties of the participant's measurement system are not included.

Specimen 3 (Spooled fiber)

Finally, for comparison Figure 3 and Table I show the results of measurements made on the spool of 25 km of single-mode fiber. Participants' results are plotted as the measured value divided by the average measured value of all the participants. There is no theoretical prediction with which to compare, but the standard deviation among participants gives an indication of the repeatability which can be expected on such a spooled fiber.

Conclusion

For measurements on the fiber spool (Specimen 3), the standard deviation σ was 24% with no statistically significant disagreements between measurement techniques.

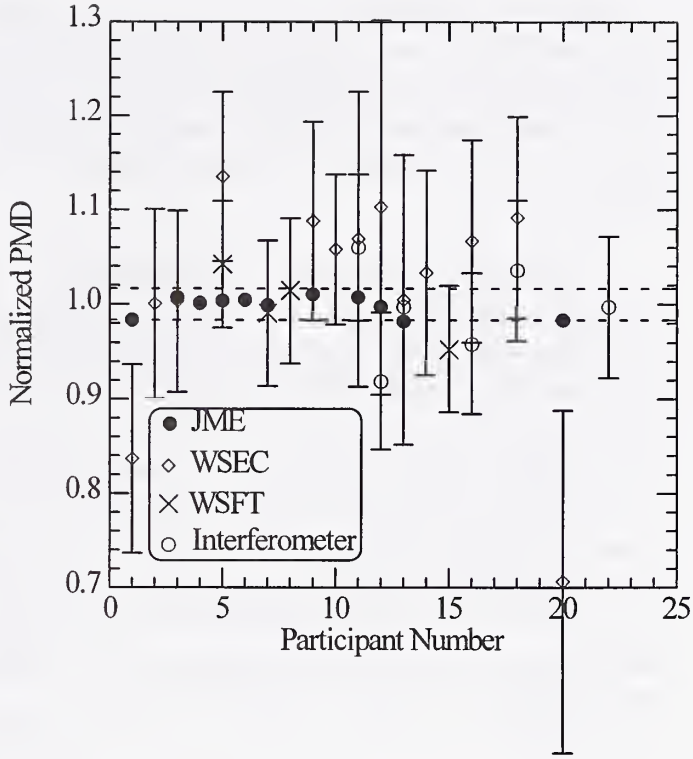

Figure 2 Waveplate stack (Specimen 2).

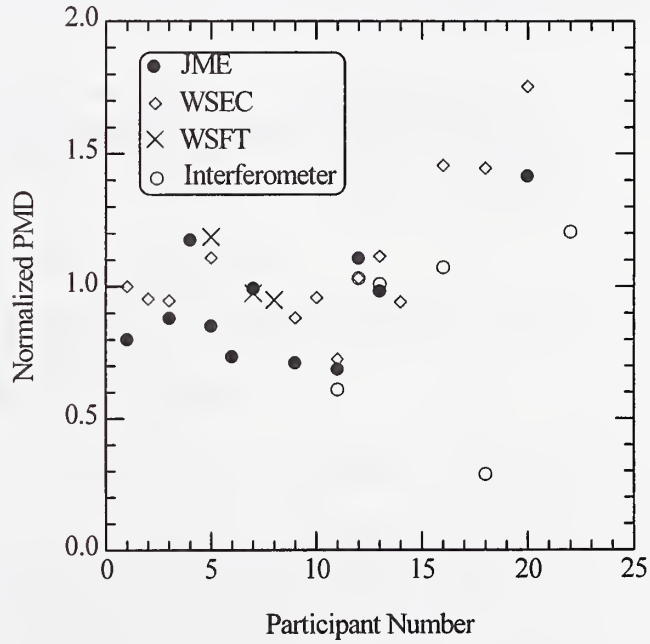

Figure 3 Spooled 25 km fiber (Specimen 3).

The non-mode-coupled Specimen 1 shows significant improvement over the fiber spool. With the

exception of interferometry, all of the measurement techniques yielded averages among the participants which were within 1% of theory. The overall uncertainty of specimen 1 is only 6%. The WSFT and JME techniques performed best with sigmas of only 1.4% and 2.2%, respectively (the WSFT result represents only 4 measurements). The poorer repeatability of WSEC and interferometry might be due to applying mode coupled measuring techniques to measuring the non-mode-coupled device.

For mode-coupled Specimen 2, each measurement technique's average value agrees within 2% of theory. The theory predicts only what the participant will measure using a given technique. It makes no statement as to whether different techniques should measure the same value. Indeed for this moderately mode-coupled 12-waveplate stack, all the techniques are not expected to measure the same value, but the normalized data does not illustrate these systematic measurement differences. With regard to standard deviation, the overall σ of 7.6% is only slightly higher than for Specimen 1 and is significantly lower than for the fiber spool. The JME technique shows the best stability among participants, with a σ of only 1%. This is as expected, since the JME technique is only weakly affected by birefringence in the fiber leads. Based on the results of this round robin, NIST is constructing a stack of 35 waveplates to increase mode-coupling and PMD. We anticipate that this new artifact will reduce the uncertainty due to PMD of fiber leads for all of the measurement techniques.

The author expresses thanks to the members of the TIA who helped in the organization of this round robin and also to all the participants from the United States, Japan, Switzerland, and the United Kingdom for taking part.

[1] For measurement methods using these techniques, see Fiber Optic Test Procedure (FOTP) 113, 122, and 124, Telecommunications Industry Association.

MEASUREMENT OF SOP EVOLUTION ALONG A LINEAR BIREFRINGENT FIBRE WITH TWIST USING POLARISATION OTDR

RE Schuh and AS Siddiqui
Department of Electronic Systems Engineering,
University of Essex,
Colchester, CO4 3SQ, UK

Abstract: We show how the state of polarisation (SOP) evolution along optical fibres can be measured using the non-destructive method of polarisation optical time domain reflectometry (POTDR). From the SOP evolution the linear birefringence and twist can be calculated along the fibre, thus identifying fibre sections with and without twist and sections with relatively high and low polarisation mode dispersion (PMD).

Introduction: POTDR, like OTDR, is a non-destructive method for measuring fibre parameters such as the birefringence characteristics [1] along the fibre with access to only one end. If the linear and circular birefringence distribution along a fibre is known, the fibre can be modelled. This would allow not just the PMD of the fibre to be calculated [2] but, as we show in this paper, also fibre sections with and without twist to be identified.

The POTDR fluctuation is a complicated function of the linear-circular birefringence distribution along the fibre. We recently showed that fibre twist significantly influences the periodicity of the observed signal from POTDR, and has to be taken into account when estimating PMD using this technique [3, 4]. In this paper we report a further result, namely that the SOP evolution obtained from a POTDR can be used to give the polarisation properties of the fibre. We believe this is the first report of experimental POTDR results showing the SOP evolution on the Poincaré sphere along a fibre with twist.

Theoretical Model: In [3, 4] it was shown that $\vec{\mathbf{S}}(l)$, the SOP observed at the input end of the fibre from the backscattered signal at the length l, along a uniformly twisted fibre, can be expressed as

$$\vec{\mathbf{S}}(l) = \mathbf{R}^T(\vec{\beta}l)\mathbf{A}_M\mathbf{R}(\vec{\beta}l)\vec{\mathbf{S}}(0) = \mathbf{M}(\vec{\beta}l)\vec{\mathbf{S}}(0) \qquad (1)$$

where $\mathbf{A}_M$ is the rotation invariant mirror matrix which changes the handedness of the SOP and $\mathbf{R}^T$ is the transpose of a rotation $\mathbf{R}$, given by

$$\mathbf{R} = \mathbf{I} + \sin(\beta l)\mathbf{B} + \left(1 - \cos(\beta l)\right)\mathbf{B}^2 \qquad (2)$$

where $\mathbf{I}$ is the 3x3 unit matrix, $\mathbf{B}_{ij} = \sum_{k=1}^{3} \varepsilon_{ijk}\hat{\beta}_k$ is a skew-symmetric matrix where ε_{ijk} is the permutation symbol which is 1 for cyclic, -1 for non-cyclic permutation of indices 1, 2, 3, and the unit vector $\hat{\beta}$ is determined in the rotating reference frame as $\hat{\beta} = \left(\beta_L \quad 0 \quad 2\gamma - g\gamma\right)^T / \beta$. Here, the magnitude, $\beta = \sqrt{\beta_L^2 + \left(2\gamma - g\gamma\right)^2}$ is the resultant birefringence due to the linear birefringence, β_L, the twist rate, γ, and the rotation coefficient, g. The occurrence of the rotation matrix $\mathbf{R}$ twice in Eq. 1 indicates that the matrix coefficients of $\mathbf{M}$ are quadratic in $\cos(\beta l)$ and $\sin(\beta l)$ and in general the intensity through an analyser may be expressed in the form of a Fourier series

$$I = a_0 + \sum_{n=1}^{2} a_n \cos(n\beta l) + b_n \sin(n\beta l) \qquad (3)$$

In the general case the evolution of the backscattered SOP is a self intersecting 'figure of eight' whose detailed shape depends on the incident SOP, linear birefringence and twist induced circular birefringence. For the simple case of zero twist the SOP trace is just a circle, a_1 and b_1 being zero, leading to just one component in the POTDR power spectrum. For backreflection from a section with twist, a_1 and b_1 are now not zero which, together with a_2 and b_2, lead to two components in the POTDR spectrum. This qualitative difference between the two POTDR spectra makes it possible to detect sections of fibre with twist. Measurement with simulation results using the power spectrum with the two frequencies will be presented. In this summary we show the full SOP evolution along the fibre obtained from POTDR.

Equation 1 may be extended to the SOP evolution as measured with the POTDR set-up shown in Fig. 1 by multiplying the backscattered SOP, $\bar{\mathbf{S}}(l)$, with a constant rotation matrix, $\mathbf{R}_C$ which is the transmission matrix of the 3dB coupler in backward direction, so that

$$\bar{\mathbf{S}}(l) = \mathbf{R}_C \mathbf{M}(\vec{\beta} l)\bar{\mathbf{S}}(0) \qquad (4)$$

$\mathbf{R}_C$ is just an overall rotation of the backscattered SOP trace on the Poincaré sphere.

Results and Discussion: A commercially available OTDR, with a spatial resolution of 2m, was modified with a computer controlled rotatable $\lambda/4$ waveplate-linear polariser combination, Fig. 1. A 56m length of fibre was freely suspended from either end, and twisted at the far end. The zero twist condition could be found by measuring the PMD at different twist rates [4]. The SOP from the backscattered intensity can be calculated by rotating the $\lambda/4$ plate to at least four independent positions. In our experiment we used 19 analyser positions from 0 to 180 degree for calculating the backscattered SOP, using a least square method. The SOP data was very reproducible over repeated measurements. Due to the dead zones at either end only 50 metres of the fibre could be resolved with our POTDR setup.

Fig. 2(a-e) shows the measurement and best fit simulation results at different twist rates for the backscattered SOP. The simulation is fitted to the measurements interactively on both the Poincaré sphere and on the azimuth and ellipticity variation of the SOP as a direct function of length using Eq. 4. Figure 2(a) shows the SOP evolution on the Poincaré sphere for the fibre in the zero twist condition, defined as that giving maximum PMD [4]. Now if the zero twist condition actually existed over the whole length of the fibre then the SOP trace would be just a repeated circle. However in the data of Fig. 2(a) only the last 31 metres of the fibre shows a repeated circular trace on the Poincaré sphere, the first 19 metres giving data points away from the circle. From this, and measuring the fibre with left and right hand twist using the POTDR, we could conclude that the first 19 metres of fibre has some small non-uniform linear birefringence and twist which may be frozen in during the fibre fabrication process. The last 31 metres of fibre was then modelled as a section with a nominally constant linear birefringence as the variable, to find the best fit to the measurements. The best fit simulation, indicated in Fig. 2(a), was obtained for β_L = 0.19rad/m for the last 31 metres of fibre. This value is within 34% of a value obtained by a direct PMD measurement over the whole 56 metre length of the fibre.

In Fig. 2(b-e) we again carry out the simulation for the last 31 metre section of the fibre. Applying a twist of 0.01 turns/m, Fig. 2(b), the backscattered SOP traces a figure of eight shape in accordance with Eq. 2 and 4. For the higher applied twist rate of 0.019 turns/m, Fig. 2(c), the area of the figure of eight decreases as predicted in [3, 4]. The simulated traces for the two applied twist rates, Fig. 2(b-e), again give β_L = 0.19rad/m and twist values of 0.012 and 0.021 turns/m respectively for the best fit. Fig. 2(d-e) show the azimuth and ellipticity variation of the SOP evolution for the applied twist of 0.019 turns/m as a function of length, where $L = 2\pi/\beta$ is the input SOP independent periodicity of the traces. Applying twist in the opposite direction also gave a figure of eight in the SOP evolution but with opposite direction as expected.

Conclusions: The SOP evolution along a fibre has been measured using POTDR and plotted on the Poincaré sphere. It has been shown that the linear birefringence and twist along the fibre can be evaluated using this data. Knowing the twist and linear birefringence along the fibre the PMD of the fibre can be calculated. This may be used during the manufacture of the fibre at different production stages to monitor the intrinsic PMD expectation of the fibre.

References

[1] A. J. Rogers, "Polarization-optical time domain reflectometry: a technique for the measurement of field distributions", *Applied Optics*, vol. 20, no. 6, pp 1060-1074, 1981.

[2] R.E. Schuh, E.S.R. Sikora, N.G. Walker, A.S. Siddiqui, L.M. Gleeson, D.H.O. Bebbington, "Theoretical analysis and measurement of the effects of fibre twist on the differential group delay of optical fibres", *Electron. Lett.* vol. 31, no. 20, pp 1772-1773, 1995.

[3] R.E. Schuh, JG Ellison, L.M. Gleeson, E.S.R. Sikora, A.S. Siddiqui, N.G. Walker, D.H.O. Bebbington, "Theoretical analysis and measurement of the effect of fibre twist on the polarisation OTDR of optical fibres", *OFC'96*, FA5, San Jose, 1996.

[4] R.E. Schuh, JG Ellison, AS Siddiqui, D.H.O. Bebbington, "Polarisation OTDR measurements and theoretical analysis on fibres with twist and their implications for estimation of PMD", *Electron. Lett.* vol. 32, no. 4, pp 387-388, 1996.

Acknowledgments: The authors wish to acknowledge X. Shan and J.G. Ellison for helping with the measurements and D.H.O. Bebbington for helpful discussion. This work was carried out under EPSRC Research Grant, number GR/K49454. The industrial partners are BT Laboratories, Martlesham Heath, Ipswich and Alcatel Submarine Networks, Greenwich, London.

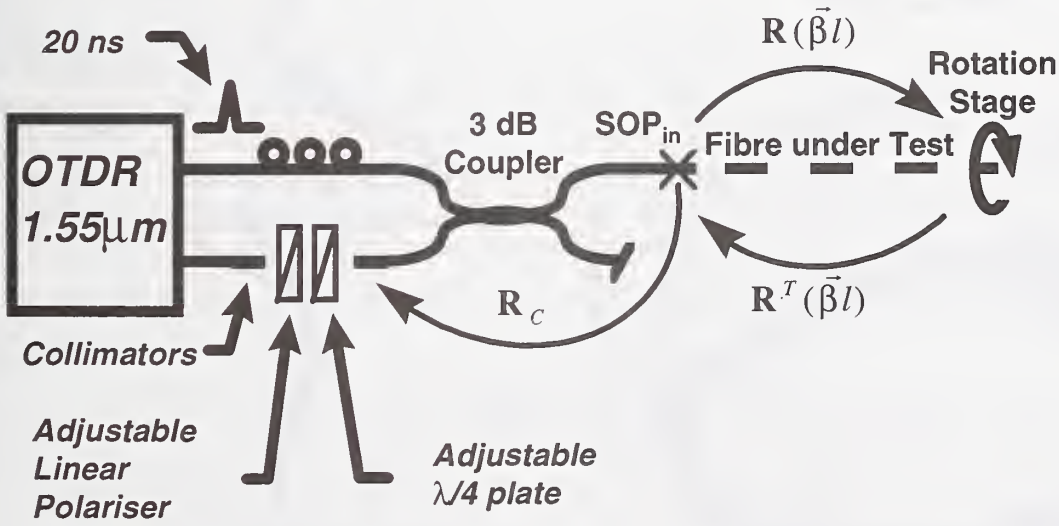

Fig. 1 Experimental POTDR setup.

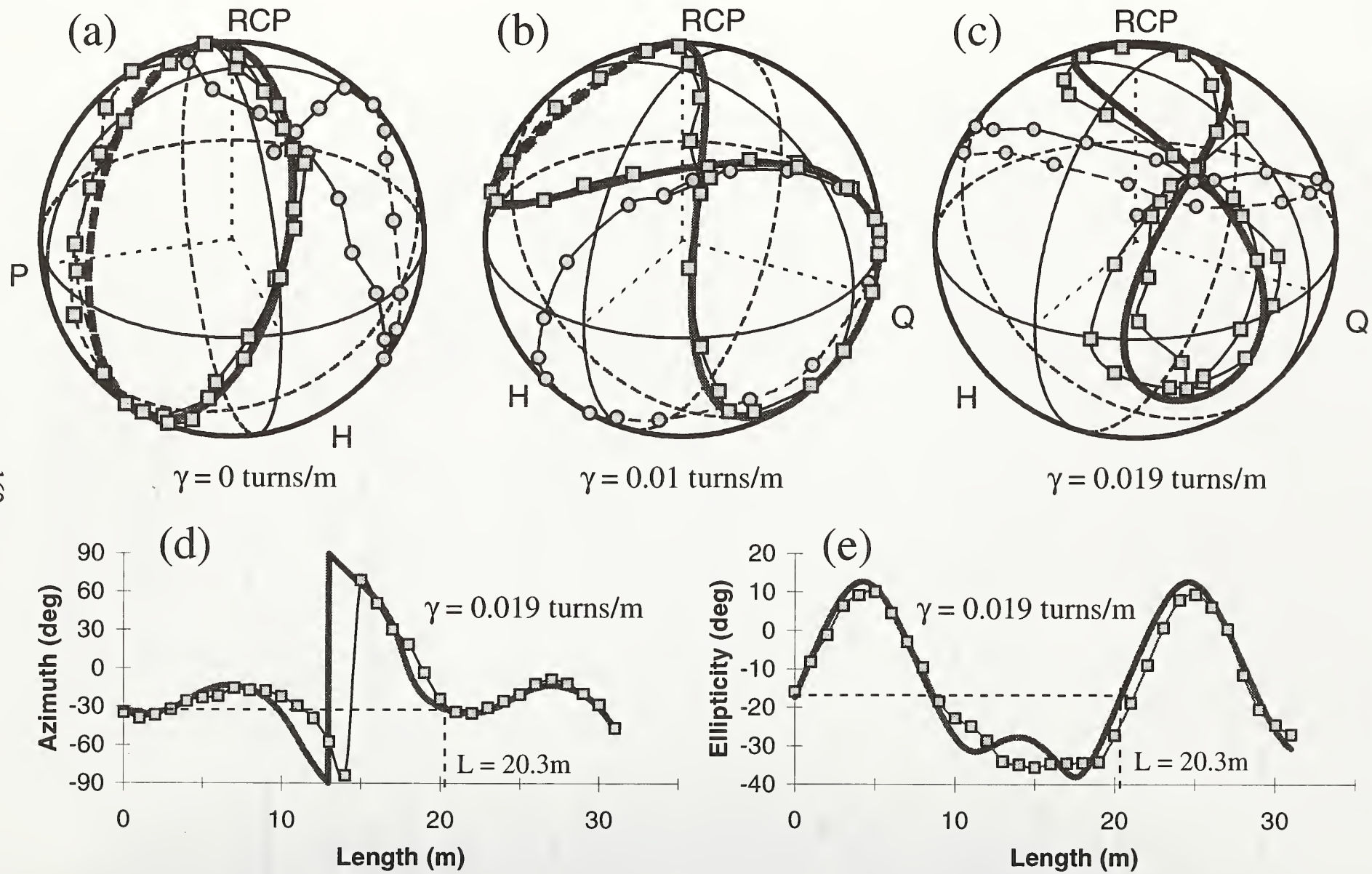

Fig. 2(a-e) Measurement and simulation of the SOP evolution along fibre with different twist rates using a POTDR.

○○○ Measurement from first 19m
□□□ Measurement from last 31m
—— Simulation

Polarisation Dependent Loss of Concatenated Passive Optical Components

A. ELAMARI[1], N. GISIN[1], B. PERNY[2], H. ZBINDEN[1], Ch. ZIMMER[2]

[1] University of Geneva, GAP/O, 20, rue de l'école de médecine, CH -1211, Geneva 4
[2] Swiss Telecom PTT, F&E 221, CH- 3000, Berne

Abstract
Global Polarisation dependent loss (**PDL**) of concatenated elements, each with some PDL, is difficult to predict since PDL can not be simply added. Moreover, if the fibre between the PDL elements has random effects on the polarisation state, then the global PDL is also random. We present simulations and measurements results of the corresponding statistics.

Introduction
In Passive Optical Networks (PONs), telecommunication optical fibres are usually combined with optical components like optical fibre couplers, wave length division multiplexers, isolators and other optical devices each of them may have an amount of polarisation dependent loss. Hence it is necessary to evaluate the global cumulated PDL of the concatenated elements. Contrarily to what one could expect, the total PDL is not simply the sum of the contribution of each PDL element. This is due to the fact that the global PDL depends on the relative orientations of the PDL axes at each connection (The PDL axis is defined as the axis on the Poincaré sphere corresponding to the polarisation state with minimum attenuation). Since the principal polarisation state of the single-mode fibres connecting the PDL elements fluctuates with time, the relative axes of the PDL elements do also fluctuate. Hence, a statistical description of the global PDL is important, since it allows to predict the statistics of the global attenuation.
In this contribution, we report the descriptions of the mean, the standard deviation and the probability of the global PDL of two or more concatenated PDL elements. Experimental results have been performed on polarising optical fibres used as PDL elements.

Theory
PDL is defined as the maximum change in insertion loss of an optical fibre component as the input polarisation is varied over all possible states. For completeness we recall some notations and results of ref [1]. Let T_{min} and T_{max} denote the minimum and the maximum transmission coefficient, respectively. Then $T_{depol} = (T_{max}+T_{min})/2$ is the transmission coefficient for depolarised light and $PDL_{dB} = 10 \log (T_{max}/T_{min})$ is the PDL expressed in dB. Since dB are not convenient "units" for fluctuating losses such as PDL, we prefer to represent PDL as a 3-dim vector $\vec{\Gamma}$ of length $\Gamma = (T_{max}-T_{min})/(T_{max}+T_{min})$ and direction corresponding to the polarisation state (as represented on the Poincaré sphere) of minimum attenuation. With such notations, the transmission coefficient for a polarisation state $\vec{M}_{in}$ is given by [1] : $T=T_{depol}(1+\vec{M}_{in}\vec{\Gamma})$. In [1] we showed that the PDL $\vec{\Gamma}_{12}$ of two concatenated elements each having a PDL of $\vec{\Gamma}_1$ and $\vec{\Gamma}_2$, is given by :

$$\vec{\Gamma}_{12} = \frac{\sqrt{1-\Gamma_2^2}}{1+\vec{\Gamma}_1\vec{\Gamma}_2}\vec{\Gamma}_1 + \frac{1+\vec{\Gamma}_1\vec{\Gamma}_2(1-\sqrt{1-\Gamma_2^2})/\Gamma_2^2}{1+\vec{\Gamma}_1\vec{\Gamma}_2}\vec{\Gamma}_2 \qquad (1)$$

From this equation one can derive the statistics of Γ_{12}. In particular the mean PDL $M(\Gamma_{12})$, assuming random relative orientations of $\vec{\Gamma}_1$ and $\vec{\Gamma}_2$, can be expressed with the following integral (where η represents the cosine of the angle between $\vec{\Gamma}_1$ and $\vec{\Gamma}_2$):

$$M(\Gamma_{12}) = \frac{1}{2}\int_{-1}^{1}\sqrt{\frac{\Gamma_1^2+\Gamma_2^2-\Gamma_1^2\Gamma_2^2+2\Gamma_1\Gamma_2\eta+\Gamma_1^2\Gamma_2^2\eta^2}{(1+\Gamma_1\Gamma_2\eta)^2}}\,d\eta \qquad (2)$$

Figure 2 shows theoretical plots of the mean of $M(\Gamma_{12})$, the mean plus and mean minus one standard deviation of Γ_{12}, the maximum of Γ_{12} and the minimum of Γ_{12} as function of Γ_2 for a fixed Γ_1. Note that the standard deviation is higher for Γ_2 close to Γ_1, and decreases when the difference Γ_2 - Γ_1 increases. Figure 3 shows analytical and numerical simulation of the probability distribution of Γ_{12}. Note that the unfavourable case of large values of Γ_{12} is more likely to happen than the favourable case of smaller values.
For more than 2 PDL elements, analytical computation becomes impractical. However, by using a simulation program one can calculate the global PDL and its statistics. In figure 4 the simulated probability distribution of the resultant PDL of five concatenated PDL elements as function of the global PDL $\Gamma_{1\text{-}5}$ is depicted.

Experiment
The measurement principle is based on searching the maximum and the minimum transmission through the device under test (**DUT**) while scanning all possible input polarisation states [2] (linear as well as circular or elliptical). The light coming from the 1300 nm Laser is launched in a 2 m long patchcord connected to an automatic polarisation controller, and then guided via a second patchcord to the DUT before entering a third patchcord connected with to the Power Meter. In the case of one PDL element (DUT 1) only one polarisation controller is needed. For the measurement of two concatenated PDL elements a second polarisation controller is needed (fig. 1). The DUT's used were polarising optical fibres of about 10 cm length .

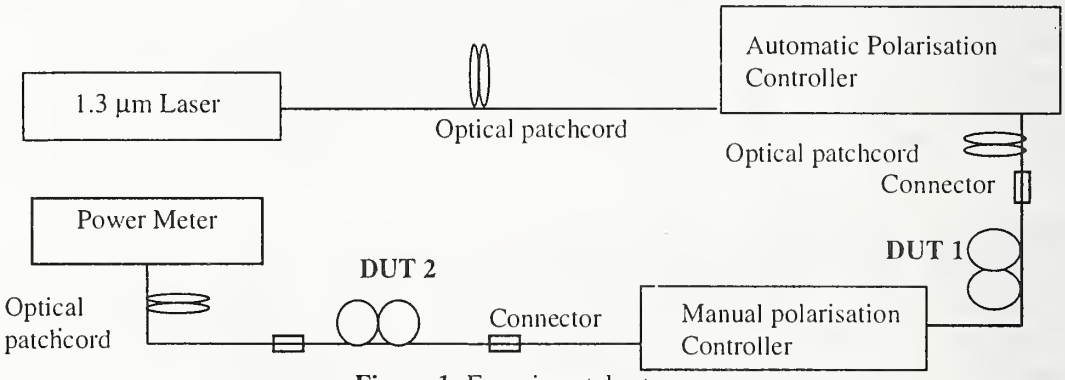

Figure 1: Experimental set-up

Results
Concatenation of two PDL elements
To determine the statistics of the PDL resultant from the concatenation of two PDL elements, it is necessary to introduce a second manual polarisation controller between the two PDL elements, this polarisation controller permits to rotate the axes of the second PDL element with respect to the first one. By rotating the manual polarisation controller between measurements, one may obtain the average and standard deviation corresponding to on all possible orientations between the two PDL vectors. (The PDL of all optical accessories are very low and have been neglected). Our results are summarised in table 1, the agreement with the theoretical formula (2) is excellent.

Γ_1	Γ_2	Theoretical Mean and Standard deviation of Γ_{12} Mean	Sd	Experimental Mean and Standard deviation of Γ_{12} Mean	Sd
0.102 (0.89 dB)	0.225 (1.99 dB)	0.239 (2.11 dB)	0.054	0.222 (1.96 dB)	0.053
0.184 (1.62 dB)	0.188 (1.65 dB)	0.244 (2.16 dB)	0.08	0.23 (2.03 dB)	0.076
0.744 (8.33 dB)	0.759 (8.63 dB)	0.833 (10.4 dB)	0.162	0.82 (10.04 dB)	0.150

Table 1: Theoretical and experimental results of the concatenation of two PDL elements.

Concatenation of five PDL elements

For the measurements of global PDL of 5 PDL elements, we maintained the same configuration than for the measurement of two PDL elements, except that the manual polarisation controllers were replaced by standard optical fibre patchcords. For each measurement, the layout of the patchcords was changed in order to rotate the polarisation and, hence to scan the relative axes of each PDL element. Our results on 65 experimental measurements are shown in table 2. For comparison we have developed a software simulation based of repeated application of formula (1). In figure 4 the results of 65 experimental measurements show good agreement with the theoretical fit, obtained by an iteration of 30000 simulations of formula (1) .

Γ_1	Γ_2	Γ_3	Γ_4	Γ_5	Global PDL $Mean^{th}$	$Mean^{Exp}$	Sd^{th}	Sd^{Exp}
0.19 (1.67 dB)	0.164 (1.43 dB)	0.178 (0.156 dB)	0.186 (0.163 dB)	0.164 (0.143 dB)	0.351 (3.18 dB)	0.350 (3.17 dB)	0.128	0.124

Table 2 : Theoretical and experimental results of global PDL resulting from the concatenation of five PDL elements, (th.: theoretical, Exp. : Experimental).

Figure 4 shows the experimental probability distribution of global PDL versus the global PDL of five PDL elements.

Simulation of 30 PDL elements

For large number N of devices with small PDL Γ_j, the global PDL derived in [2] is $\vec{\Gamma} = \sum_{i=1}^{N} \vec{\Gamma}_j + 0(\Gamma^2)$. Hence Γ becomes $\Gamma \approx M(\Gamma_j)\sqrt{N}$. A numerical simulation of the global PDL of up to 30 concatenated devices with 0.05 individual PDL was made. The simulated global PDL was drawn as function of the PDL number and was fitted to $\Gamma \approx M(\Gamma_j)\sqrt{N}$ in figure 5.

Conclusion

Statistical measurements of concatenated PDL elements have been presented and are in good agreement with the theory of referenece [1]. Regarding the difficulty of deriving an analytical expression for more than 2 PDL elements, a simulation program has been developed. Hence, we could compare our measurements of the concatenation of up to 5 PDL elements, and support an approximate formula valid for several elements with a low PDL.

Acknowledgement:

Thanks is due to F. Prieto for his collaboration.

References:

[1] N. Gisin, Statistics of polarisation dependent losses, Optics communication 114 (1995), p 399-405

[2] L. Ducos, R. Clin, P. Blanchard and F. Gauthier, Polarisation dependent loss of passive optical components, OFMC 95. 25-26 September 1995, Liège, Belgium.

Figure 2: Analytical global PDL Γ_{12} versus Γ_2 for a fixed Γ_1

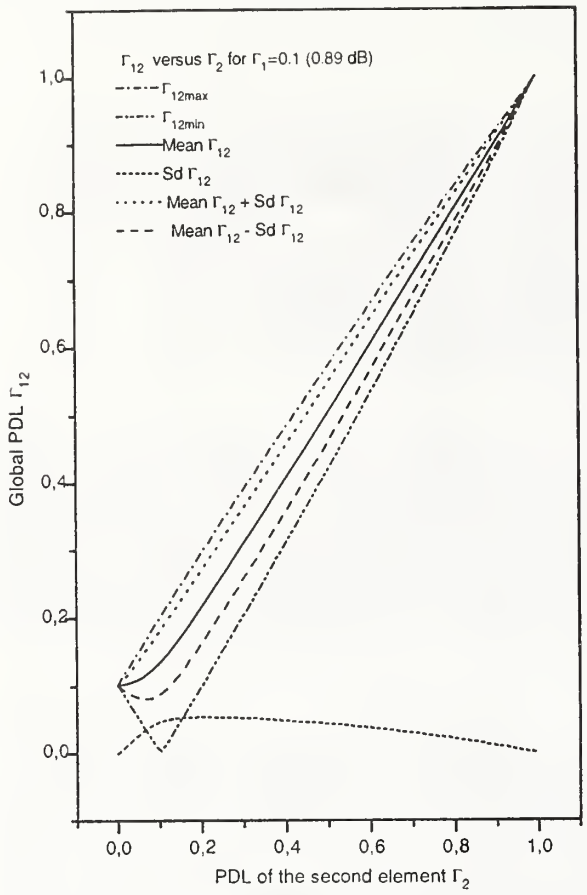

Figure 3: Analytical and numerical Probability of Γ_{12} versus Γ_{12} for Γ_1 = 0.1 (0.89 dB) and Γ_2= 0.225 (1.99 dB).

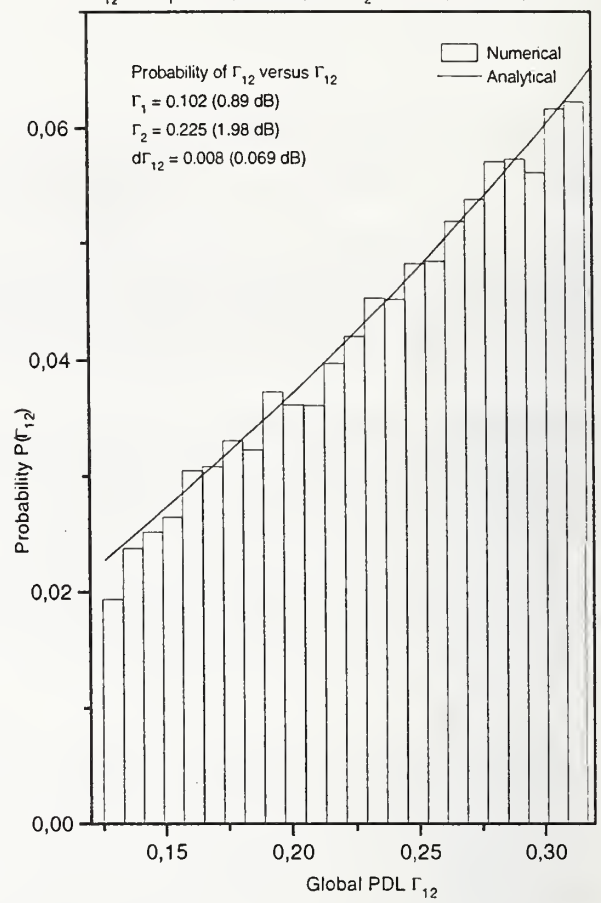

Figure 4: Experimental probability of the global PDL of 5 PDL elements

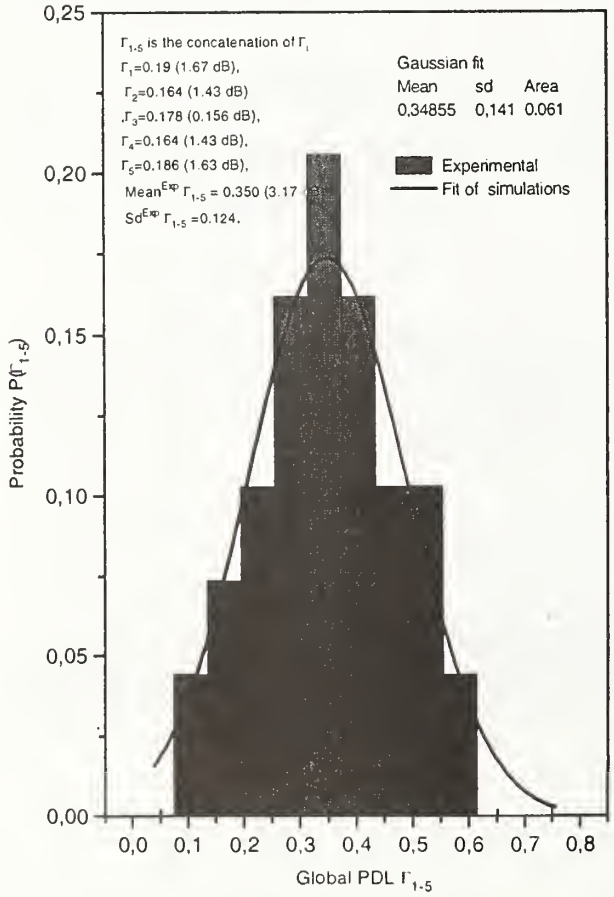

Figure 5: Global PDL versus PDL number for Γ_i = 0.05

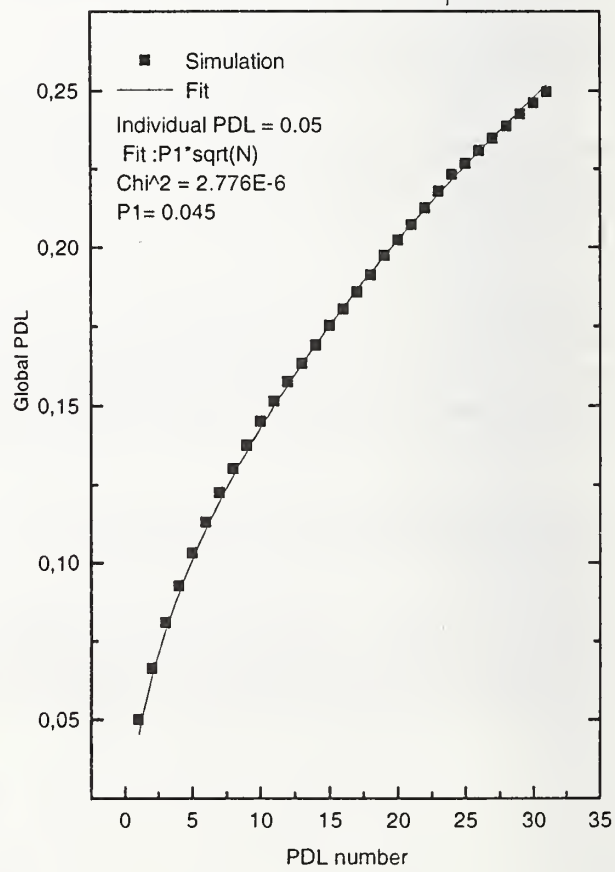

Novel Method for Polarization–maintaining Fiber Launch

Bernhard Scholl
Jens Rasmussen

Institute for High Frequency Technology
Aachen University of Technology

Abstract

A novel method is described to determine the principal axes of the polarization–maintaining fiber (PM–fiber). This technique is based on the measurement of the Mueller–matrix of the PM–fiber, but allows also a direct automatic alignment of the proper polarization.

1 Introduction

A polarization maintaining fiber is designed to deliver a linearly polarized lightwave signal at its output. Therefore linear polarized light has to be launched in the direction of one of the principal axes of the fiber. Finding this direction is tedious and time consuming. Several alignment methods have been reported, one using an elasto–optic modulation method, another using a tunable laser, both of which give an indication of misalignment of the polarization [1, 2]. In this paper, we describe a novel method which determines the direction of the principal axes of the fiber and which includes a polarization transformation setup to align the incident beam to the proper polarization.

2 Principle

The Mueller–matrix of a PM–fiber can be described as combination of a linear retarder with the Mueller–matrix M_{Ret} and a rotator with M_{Rot}

$$\mathrm{M}_{PM} = \mathrm{M}_{Rot}(\varphi_c) \cdot \mathrm{M}_{Ret}(\alpha, \varphi_l) \tag{1}$$

with

$$\mathrm{M}_{Ret}(\alpha, \varphi_l) = \begin{pmatrix} 1 & 0 & 0 & 0 \\ 0 & \cos\varphi_l + \cos^2 2\alpha\,(1-\cos\varphi_l) & \sin 2\alpha \cos 2\alpha\,(1-\cos\varphi_l) & -\sin 2\alpha \sin\varphi_l \\ 0 & \sin 2\alpha \cos 2\alpha\,(1-\cos\varphi_l) & \cos\varphi_l + \sin^2 2\alpha\,(1-\cos\varphi_l) & \cos 2\alpha \sin\varphi_l \\ 0 & \sin 2\alpha \sin\varphi_l & -\cos 2\alpha \sin\varphi_l & \cos\varphi_l \end{pmatrix} \tag{2}$$

and

$$\mathrm{M}_{Rot}(\varphi_c) = \begin{pmatrix} 1 & 0 & 0 & 0 \\ 0 & \cos\varphi_c & \sin\varphi_c & 0 \\ 0 & -\sin\varphi_c & \cos\varphi_c & 0 \\ 0 & 0 & 0 & 1 \end{pmatrix} \tag{3}$$

The angles α and φ_l correspond to the birefringence axis of the linear retarder and its phase delay, respectively, and the angle φ_c to the phase delay of the rotator. Simultaneously, α is equivalent to the angle of the principal axis at the input of the PM–fiber, and the principal axis at the output is given by $\alpha + \varphi_c$. Knowing the Mueller–matrix $\mathbf{M}_{PM}$ of the PM–fiber both angles can be calculated easily from its components by

$$\tan 2\alpha = -\frac{m_{42}}{m_{43}} \tag{4}$$

and

$$\tan 2\varphi_c = \frac{m_{34} \cdot m_{42} - m_{24} \cdot m_{43}}{m_{24} \cdot m_{43} - m_{34} \cdot m_{42}} \tag{5}$$

Thus, linear polarized light with an azimuth angle of α has to be launched into the PM–fiber. There are different ways for the determination of the Mueller–matrix of an optic device, the setup we used adjust any desired polarization state, too.

3 Realization

The setup to analyze the Mueller–Matrix of the PM–fiber consists of a feedback controlled polarization transformer and a standard polarization analyzer both controlled by a PC (s. Fig. 1).

The actual polarization transformation is done by three piezoelectric retarders [3]. The piezoelectric retarders consist of a PM–fiber wound around a piezoelectric cylinder. Applying a voltage to the cylinder lengthens the fiber and causes a phase delay between the two principal modes of the fiber. With three piezoelectric retarders every polarization state can be adjusted if the principal axes of the three PM–fibers pieces are tilted by 45° to each other. To control the polarization a standard 99:1–coupler follows the polarization transformer. At the low power output port of this coupler a standard four detector photo–polarimeter is used. Therefore the light is split into four different beams, which are analyzed by different polarization filters.

In a calibration process the standard polarization analyzer is placed at the high power output port. Thus, a 4x4 matrix can be found which connects the four detector signals of the low power port to the Stokes–vector of the light at the high power port [4]. Hence, the PC indicates the polarization at the high power output port after the calibration process.

To determine the principal axes of the unknown PM–fiber, the fiber is connected at the output of the feedback controlled polarization transformer and the standard polarization analyzer is placed at the output of the PM–fiber. Launching four different and known polarization states into the PM–fiber, adjusted by the piezoelectric retarders, the Mueller–matrix of the PM–fiber can be calculated by comparing the input and output polarization

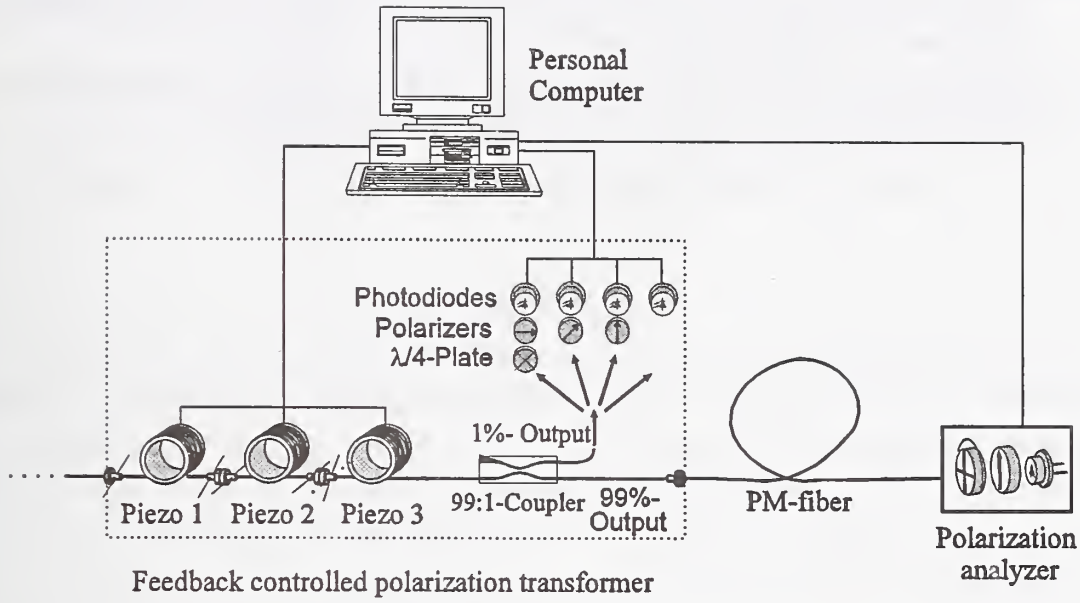

Figure 1: Setup for the determination of the principal axes of the PM–fiber

states of the PM–fiber. With eq. (4) the direction α of the principal axis can be calculated. In a second step the feedback controlled polarization transformer can be used to adjust the proper polarization into the PM–fiber. This can be done easily in comparing the current polarization state at the output of the feedback controlled polarization transformer with the desired polarization state. For the automatic alignment of the polarization the polarization transformer needs less than three seconds.

4 Conclusion

We have shown a possibility to determine the principal axes of a PM–fiber and to align automatically the proper polarization into the PM–fiber without changing the setup.

References

[1] S. L. A. Carrara, B. Y. Kim, H. J. Shaw, 'Elasto–optic alignment of birefringent axes in polarization–holding optical fiber', Optics Letters, Vol. 11, pp. 470-472, 1986

[2] A. Ebberg, R. Noe, 'Novel high precicion alignment technique for polarization maintaining fibres using a frequency modulated tunable laser', Electronics Letters, Vol. 26, pp. 2009-2010, 1990

[3] R. P. Tatam, C. N. Pannell, J. D. C. Jones, D. A. Jackson, 'Full polarization state control utilizing linearly birefringent monomode optical fiber', Journal of Lightwave Technology, Vol. 5, pp. 980-984, 1987

[4] B. Scholl, T. Stein, A. Neues, K. Mertens, 'In–line fiber optic polarimeter with a 99% coupler', Optical Engineering, Vol. 34, pp. 1669-1672, 1995

CHARACTERIZATION OF HIGH-SPEED AND LOW-LOSS POLYMER OPTICAL FIBERS

Yasuhiro Koike, Eisuke Nihei and Takaaki Ishigure

Faculty of Science and Technology, Keio University, Yokohama 223, Japan
Kanagawa Academy of Science and Technology, Yokohama 236, Japan

1. INTRODUCTION

The growing interests have been focused on high speed optical fiber communication in access and premises areas as well as long-distance communication. However, since the small core (5-10 μm diameter) of the single-mode fiber requires highly accurate connectors, serious increase of the cost of the whole system is expected in such access and premises areas. The large core (such as 300 μm or more) of the polymer optical fiber (POF) would make it possible to adopt injection-molded plastic connectors, which dramatically decreases the total cost of the system without any complicated lens alignment.

We have proposed a high bandwidth graded-index polymer optical fiber (GI POF), and have demonstrated several giga bit per second (Gbit/s) transmission in the 100 m GI POF link[1,2]. However, the transmission distance was limited to 100 m due to the intrinsic absorption loss. In this paper, the characterization of new GI POF with low attenuation even at 0.5 - 1.3-μm wavelength region is in detail described.

2. CHARACTERIZATION OF BIT RATE

In this paper, we focus on the possibility of high speed transmission by the fluorinated amorphous polymer base GI POF. The bandwidth of the GI POF was investigated by measuring the output pulse distortion by time domain measurement method[1]. As the light source, InGaAlP laser diode with 660-nm wavelength was used. Input pulse whose full width half maximum (FWHM) is 80 psec was coupled into 100-m length POF via objective lenses with 0.5 numerical aperture (NA) which is larger than that of NA of POF. Figure 1 shows the waveform of output pulse from the partially fluorinated polymer base GI POF[1,3] compared with the conventional step-index (SI) type POF with 0.5 NA. The bandwidth of the SI POF estimated by the result in Fig. 1 is less than 100 MHz for 100 m fiber, while in the case of the GI POF, the bandwidth is approximately 10 GHz. A low NA SI POF has been newly developed and 156 Mb/s transmission for 100 m link was demonstrated[4]. The GI POF will be required for higher bit rate and longer distance than those of the low NA SI POF.

Optimization of the refractive index profile of the GI POF should be the key technology in order to minimize the modal dispersion. The possible bit rate in GI POF link

was theoretically calculated considering both modal and material dispersions by using WKB method[5]. The material dispersion of the polymer matrix was estimated by measuring the wavelength dependence of the refractive index of polymer[6]. The results are shown in Fig. 2. It should be noted that the material dispersion of the perfluorinated (PF) polymer is much lower than that of silica in the range of 0.4 - 1.0-μm wavelength region, which indicates that the PF polymer base GI POF can have high bandwidth in the above wavelength region.

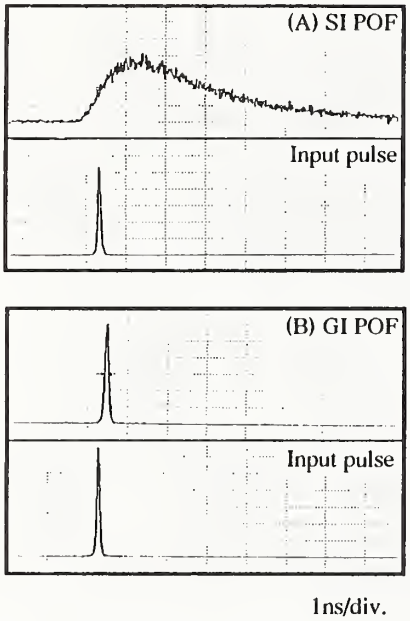

Fig. 1
Pulse broadening through GI and SI POFs.
Fiber length: 100m

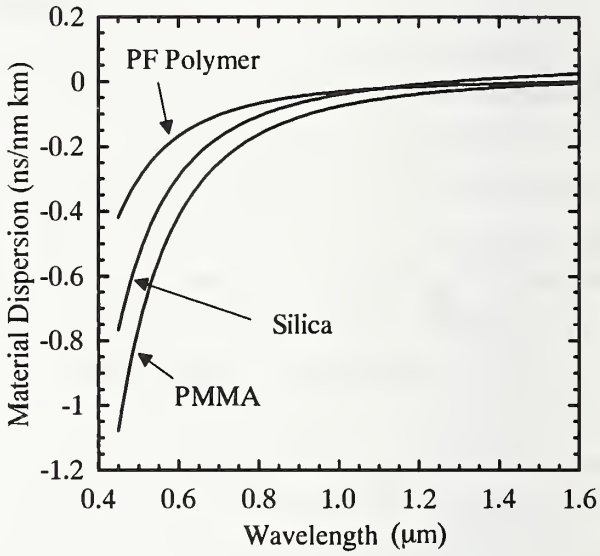

Fig. 2
Material dispersion of PF polymer compared with PMMA and silica[7]

3. CHARACTERIZATION OF TRANSMISSION ATTENUATION

The attenuation of transmission of the PMMA base GI POF is shown in Fig. 3. The minimum attenuation was about 150 dB/km at 0.65-μm wavelength which was almost the same as that of the step-index type POF commercially available.

However, the attenuation of PMMA base POF was abruptly increased from about 0.6-μm wavelength to the infrared region due to the absorption loss of overtones of carbon-hydrogen stretching vibration.

On the other hand, it is highly desirable to construct POF network system using commercially available LD and LED which operate in the range of 0.6 -1.5 μm of wavelength. Deuterated or fluorinated polymer base POF will be one of the promising candidates to eliminate the serious absorption loss in such wavelengths.

The attenuation spectra of perdeuterated (PD) and PF polymer GI POFs measured by conventional cut-back method are shown in Fig. 3. It is quite noteworthy that the PF polymer base GI POF has no serious absorption peak in the range of 0.5 - 1.3 μm wavelength and the attenuation even at 1.3-μm wavelength is about 50 dB/km.

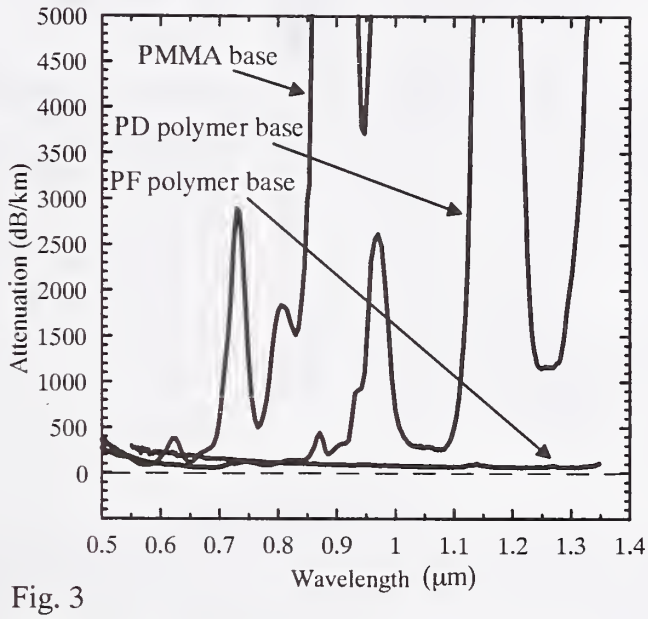

Fig. 3
Experimental attenuation spectra of GI POFs.

4. CHARACTERIZATION OF MODAL NOISE

It has been concerned that the modal noise degraded the bit error rate in the case of multi mode fiber with laser diode in the fiber-optic links. However, it is noteworthy that the large core (300 - 1000 μm diameter) of GI POF which transmits more than 30,000 modes causes no such degradation of bit error rate even if a laser diode with high coherency is used. We investigated the modal noise effect on the bit error rate in GI POF link as follows: a Fabry-Perot LD at 0.644 μm with 1 nm spectral width was used as the light source, and the bit error rate of 156 Mb/s system in which one fiber-to-fiber joint had been deliberately misaligned was measured.

Figure 4 shows the results of PMMA base GI POF with a 600-μm core diameter. Even when 200-μm misalignment was occurred, no significant degradation was observed. On the other hand, in the case of the conventional GI glass fiber whose core diameter was 62.5 μm, it was observed that a 10-μm of displacement caused large bit error rate degradation, and that it was impossible to obtain the accurate bit error rate curve in the case of 20-μm displacement because of a serious fluctuation of the output power from the fiber.

It is concluded that the large core of the GI POF offers low modal noise as well as

low coupling loss. The large core of GI POF enables the usage of inexpensive connector made by injection molding which tends to cause 20 to 50-μm misalignment.

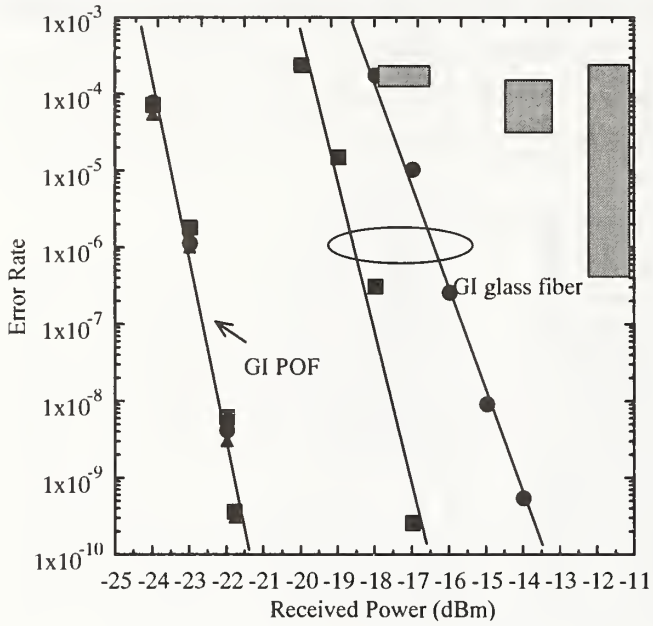

Fig. 4
Modal noise effect on bit error rate in PMMA base GI POF link.
Misalignment:
GI POF
■: 0 μm ●:100 μm ▲:200 μm
GI glass fiber
■: 0 μm ●:10 μm ▬ : 20 μm

5. CONCLUSION

The characterization of the POF in high-speed data communication is discussed. The perfluorinated polymer base GI POF has many advantages: one is no serious absorption peak in the range of 0.6-1.3-μm wavelength in its attenuation spectrum, and the attenuation at 1.3 μm where the LD for silica fiber operates is about 50 dB/km. Another is the low material dispersion compared with PMMA and silica, which allows more than 10 Gb/s transmission in 1 km link. In addition, no modal noise in the GI POF link is observed. Since the PF polymer is very flexible and stable for many chemicals and is not flammable, outdoor use of the PF polymer base GI POF will be possible as well as silica fiber. Therefore, we believe that these experimental and theoretical aspects suggest that the PF polymer base GI POF will be one of the promising candidates for "the last one mile".

REFERENCES

1. Y. Koike, T. Ishigure, E. Nihei, *IEEE J. Lightwave Technol.*, **13**, 1475 (1995)
2. T. Ishigure, E. Nihei, S. Yamazaki, K. Kobayashi, and Y. Koike, *Electron. Lett.*, **31**, 467 (1995)
3. T. Ishigure, E. Nihei, Y. Koike, C. E. Forbes, L. LaNieve, R. Straff, and H. A. Deckers, *IEEE Photon. Technol. Lett.*, **7**, 403 (1995)
4. S. Yamazaki, Proc. ECOC '95, **Tu. L.2.5**, 337 (1995)
5. R. Olshansky and D. B. Keck, *Appl. Opt.*, **15**, 483 (1976)
6. T. Ishigure, E. Nihei, and Y. Koike, *Appl. Opt.*, **35**, 2048 (1996)
7. J. W. Fleming, *J. Am. Ceram. Soc.*, **59**., 503 (1976)

A SINGLE DEVICE FOR BOTH ACCURATE MEASUREMENTS OF λ_c AND w_0 IN SINGLE-MODE FIBERS

D. PAGNOUX, J.-M. BLONDY, P. ROY, P. FACQ
Institut de Recherche en Communications Optiques et Microondes
Unité de Recherche Associée au CNRS
123, avenue A. Thomas - 87060 Limoges - FRANCE

The effective cutoff wavelength of the LP_{11} mode (λ_c) and the mode field radius (w_0) are two of the most important parameters for characterizing monomode optical fibers. For each measurement, many techniques have already been proposed. On the one hand, λ_c may be measured in particular by means of the near-field shape observation method [1], the mode interference technique [2], or the bend loss technique recommended by the ITU-T (CCITT) [3]. On the other hand, the main methods for measuring w_0 are the transverse offset method [4], the knife edge technique [5] and the far-field scan method whitch is recommended by the ITU [6].

In the recent years, we proposed a new technique based on the azimuthal analysis of the far-field to quickly and accurately measure λ_c [7]. In this paper, we show how this setup has been adapted to allow the measurement of w_0, while remaining as efficient as before for measuring λ_c. Only the source at the input of the fiber under test (FUT) and the software for analysing the detected signal at the output of the device have to be switched in order to get λ_c or w_0. The principle and the performances of this new dual characterization set up are presented.

First, let us remind that in the azimuthal far-field analysis technique, the part of the far-field pattern of the FUT which crosses a rotating slit is transmitted to a detector by means of a large core multimode fiber (Fig.1).

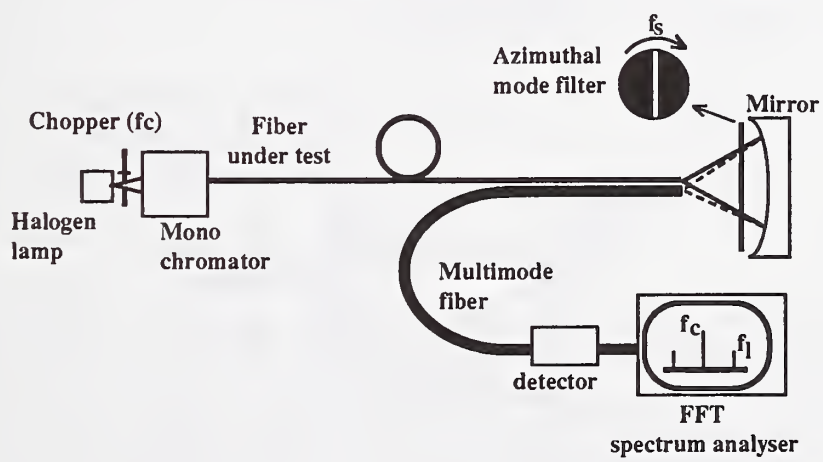

Fig. 1 : Setup for the measurement of λ_c by the azimuthal far-field analysis technique

The Fourier transform of the detected light gives a spectrum which analysis leads to the accurate determination of λ_c : indeed, as a matter of fact, A_c and A_l, the amplitudes of the lines at the f_c and $f_l = f_c \pm 2\ f_s$ frequencies respectively (with $f_c \approx 70$ Hz the frequency of the chopper at the input, and $fs \approx 4$ Hz the rotation frequency of the slit) are related to the powers P_{01} et P_{11} carried by the LP_{01} mode and the LP_{11} mode respectively, by :

$$D(\lambda) = 10\log\left(\frac{P_{11}}{P_{01}}\right) = 10\log\left(\frac{2A_1}{A_c - 2A_1}\right) \quad (1)$$

In the bend loss technique, λ_c is the wavelength for which the total transmitted power is 0.1 dB higher than the power transmitted by the pure LP_{01} mode. This criterion corresponds to a $D(\lambda_c)$ value equal to -16,4 dB. λ_c is then simply determined by scanning the wavelength domain until $D(\lambda_c)$ reaches -16,4 dB.

By this technique, the reliability of the measurements is typically better than 3 nm for 10 successive measures. The use of the concave mirror to concentrate light on to the multimode fiber through the slit is justified by the achromatism and the compactness of this configuration.

With regard to the measurement of w_0, it has already been demonstrated that [8] :

$$w_0 = \left[\frac{\int_{-\infty}^{+\infty} S(u)\,du}{4\pi^2 \int_{-\infty}^{+\infty} u^2\, S(u)\,du}\right]^{1/2} \quad (2)$$

with

$$S(u_0) = \Delta u \int_{-\infty}^{+\infty} |\phi\,(u,v)|^2\, dv \quad (3)$$

where

- $\phi(u,v)$ is the complex amplitude of the far-field at the output of the FUT,
- u and v are the coordinates in the spatial frequencies space corresponding to the Fourier conjugates of x and y respectively, which are the cartesian coordinates in the near field.

$S(u_0)$ is actually the autocorrelation function of the far-field pattern, equal to the power detected through a narrow slit of Δu width and set at the u_0 abscissa in the spatial frequencies space.

Thus, w_0 may be measured with the device shown on Fig.2.

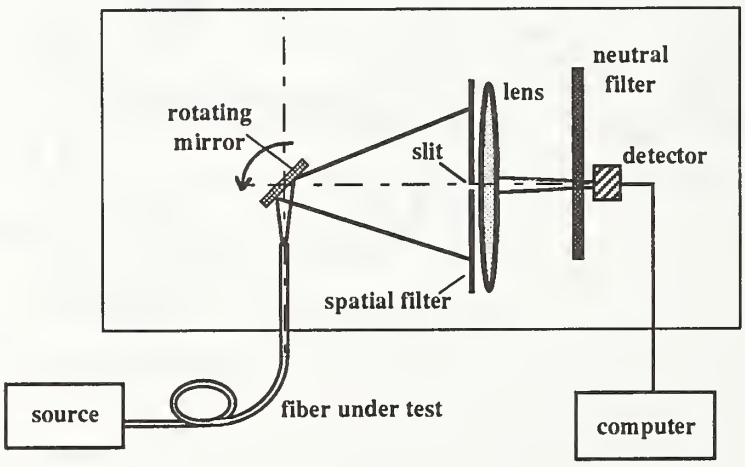

Fig. 2 : Setup for the measurement of w_0 using the analysis of the autocorrelation function of the far-field

For practical calculation of (2), the curve S(u) is sampled. In addition u_G, the abscissa of the center of gravity of S(u) must be introduced when S(u) is not centered in the u coordinates range of acquisition. Finally we obtain :

$$w_0 = \left[\frac{\sum_{i=0}^{n} S(u_i)}{4\pi^2 \sum_{i=0}^{n} (u_i - u_G^2)\, S(u_i)} \right]^{1/2} \quad (4) \qquad \text{with } u_G = \frac{\sum_{i=0}^{n} u_i\, S(u_i)}{\sum_{i=0}^{n} S(u_i)} \quad (5)$$

The principles of the devices of Fig.1 and Fig.2 have been combined in order to obtain a single set up allowing both λ_c and w_0 measurements (Fig.3). The arrangement of the device of Fig.1 essentially consists in :

- putting a lens behind the slit, to focuse the light on to a large area detector, in the place of the concave mirror and the large core multimode fiber,
- setting the FUT parallel to the spatial filter and reflecting the emerging light perpendicularly, towards this filter, by means of a mirror.

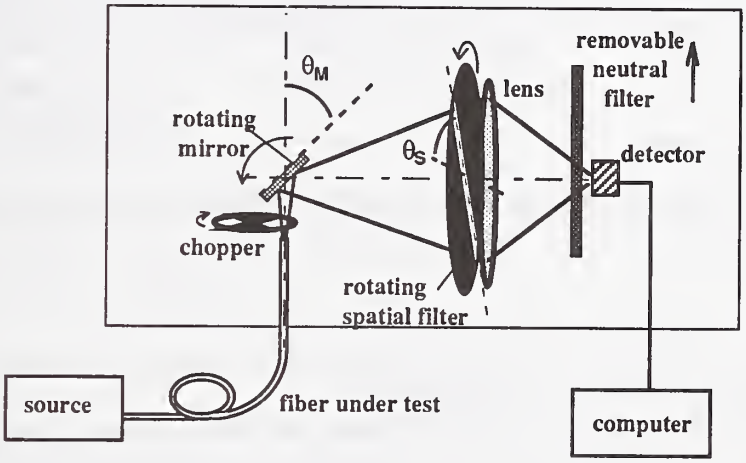

Fig. 3 : Dual measurement setup

The position or the motion of each component of the device are described in Table I. A large area detector is used in order to detect all the power transmitted through the slit of the spatial filter, taking into account the chromatic aberration of the lens. Let us notice that the neutral filter and the chopper may be removed from the device and set between the source and the FUT when they are necessary (respectively for attenuating the light from the laser diode when measuring w_0, and for chopping the light from the monochromator when measuring λ_c).

The performances of the dual measurement device are not degraded compared to those of each separated measurement setup. For all the tested fibers,the measurements of λ_c and w_0 are in very good agreement with those given by the methods recommended by the ITU. Owing to the very abrupt fall of the curve $D(\lambda)$, λ_c is determined with an accuracy better than 1 nm, and a repeatability within a range of only 3 nm for tens of successive measures. The technique does not require any reference measurement and is also unsensitive to source power level and detector sensivity drifts. It can be used for any length of fiber as well as for installed fiber links.

Concerning w_0, with the rotation frequency of the mirror equal to $f_m = 0.25$ Hz, a curve of S(u) is stored in 200 ms and 15 successive measurements can be realized in 1 minute. The very short duration of every measurement

largely reduces the effects of fluctuations of the launched power and of the sensitivity of the detector. The standard deviation over more than 100 measures remains smaller than 0.02 µm, i.e. 0,4%. The discrepancy between the mean value and the value given by the ITU method is typically lower than 0.03 µm for standard monomode fibers. More detailed results will be presented during the conference.

measured parameter	w_0	λ_c
source	laser diode at the working wavelength λ_0	monochromator
chopper	stopped	rotating at the f_c frequency
mirror	rotating at f_m	fixed at the position $\theta_M = 45°$
rotating spatial filter	fixed at the position $\theta_S = 0°$: the slit is set horizontal	rotating at the f_s frequency
lens	large enough to collect all the light transmitted through the slit	
neutral filter	set to avoid the saturation of the detector	removed
detector	large area detector	
computer	sampling of the signal and computation of relation (4)	spectral analysis of the signal and computation of relation (1) for determining $D(\lambda_c) = -16{,}4$ dB

Table I : Positions and motions of the different components of the proposed device, versus the measured parameter

References

[1] Y. MURAKAMI, K. KAWANA and H. TSUCHIYA : "Cutoff wavelength measurements for single-mode optical fibers", *Applied Optics*, 1979, **18**, pp. 1101-1105.

[2] K. ABE, Y. LACROIX, Y. CAI and L. BONNEL :"Determination of the LP_{11}mode cutoff wavelength from the modal interference pattern", *Proceedings of Symposium on Optical Fiber Measurements*, sept 15-17 1992, BOULDER (CO) USA, pp 221-224

[3] Y. KATSUYAMA, M. TOKUDA, N. UCHIDA and M. NAKAHARA : "New method for measuring V-value of a single-mode optical fibre", *Electronics Letters.*, 1976, **12**, pp. 669-670.

[4] J. STRECKERT, "New method for measuring the spot size of single mode fibers", *Optics Letters*, vol 5, n°12, 1980

[5] W.G. OTTEN, F.P. KAPRON, J.C. OLSEN, "Mode field diameter single-mode fibers by knife-edge scanning in the far-field", *Journal of Lightwave Technology*, Vol LT 4, n° 10, 1986

[6] W.T. ANDERSON, D.L. PHILEN, "Spot size measurements for single mode fibers - a comparison of four techniques", *Journal of Lightwave Technology*, Vol LT 1, n° 1, 1983

[7] D. PAGNOUX, J.-M. BLONDY, P. DI BIN, P. FAUGERAS, P. FACQ, "Azimuthal far-field analysis for the measurement of the effective cutoff wavelength in single-mode fibers - effects of curvature, length, and index profile", *Journal of Lightwave Technology*, Vol LT 12, n° 3, 1994

[8] B. GOULLEY, M. CLAPEAU, P. FACQ, "mode spot size measurements in non-circular optical waveguides", *Electronics Letters*, Vol 22, n°18, 1986

Wavelength Dependence of Correction Factor of Effective Area (A_{eff}) and Mode Field Diameter (MFD) in Various Optical Fibers

Yoshinori Namihira

KDD R&D Laboratories
2-1-15, Ohara, Kamifukuoka, Saitama 356 Japan

Tel : +81-492-78-7801, Fax : +81-492-63-9328, E-mail: namihira@lab.kdd.co.jp

1. Introduction

Optical nonlinearities limit the maximum power transmitted through the optical fibers and they have become a serious limitation in optically amplified ultralong transmissions spans [1]. The magnitude of the nonlinearity in the optical fiber depends on the nonlinear coefficient of the material, the power in the optical fibers and mode confinement.

Recently, the measurement of nonlinear coefficient (n_2/A_{eff}; n_2 is nonlinear refractive index, A_{eff} is effective area) have been measured by the shelf phase modulation (SPM) method [2-4], the cross phase modulation (XPM) method in the optical fibers [5], and the self-compensated interferometer method using 1064 nm Nd : YAG laser in the Er-doped fiber (EDF) [6] . In those methods, the nonlinear refractive index n_2 could not measured directly. Therefore if the A_{eff} can be expressed approximately from the mode field diameter (MFD), it is very useful for the nonlinear measurement.

In this paper, wavelength dependence of A_{eff} and MFD for the various single-mode optical fibers is first presented.

2. Effective Area (A_{eff})

Effective area (A_{eff}) is a parameter that is closely related to optical fiber nonlinearities that will affect the transmission quality of the optical fiber systems, especially in long-haul optically amplified systems. The effective area A_{eff} is given by [7]

$$A_{\mathrm{eff}} = \frac{2\pi\left[\int_0^\infty E(r)^2\, r\, dr\right]^2}{\int_0^\infty E(r)^4\, r\, dr} \qquad (1)$$

A_{eff} can be calculated from the measured refractive index profiles of the optical fibers [6-8] and using the refractive index profiles as the input to computer program that models the optical transmission properties of the fibers.

Here, E (r) is the electromagnetic field distribution of the fundamental mode of the fiber at radius r [7]. The integration is over the entire cross-sectional area of the fiber. For example, if we make a guassian approximation such that [8,9];

$$E(r) = \exp(-r^2/w^2) \qquad (2)$$

where $2w$ is the mode field diameter (MFD), then eq.(1) can be integrated and gives

$$A_{eff} = \pi w^2 \qquad (3)$$

The Gaussian approximation is accurate for 1.31 μm optimized single mode fiber (SMF; ITU-T G.652) and cut-off shifted fiber (CSF; ITU-T G.654) with step-index refractive profile near the LP_{11} cut-off wavelength, but for ITU-T G.652 and G.654 fibers at much longer wavelengths, and in the case of dispersion shifted fiber (DSF; ITU-T G.653) with non step-index refractive profile, A_{eff} can not be accurately estimated from eq.(3).

A more general but emprical relationship between A_{eff} and MFD (=2w) is [9];

$$A_{eff} \cong k\pi w^2 \quad (4)$$

where, k (≤ 1) is the correction factor of A_{eff} and w. The MFD (= $2w$) is defined by Petermann II definition as shown in Recommendation ITU-T G.650 (Definitons and test methods).

3. Wavelength Dependence ofCorrection Factor k of A_{eff} and MFD

In the experiment, the MFD was measured by the variable aperture test method. From the far field pattern (FFP) of the output optical power, it was then possible to calculate the near field pattern (NFP) using an inverse Hankel transformation. A_{eff} is then derived from the NFP by using eq.(1).

The correction factor k in eq.(4) depends on the wavelength and on fiber parameters such as refractive index profiles, MFD and zero-dispersion wavelength.

Fig.1, 2 and 3 show the examples of measured wavelength dependence of MFD, A_{eff} and correction factor k of the 1.31 μm optimized Single Mode Fiber (SMF: ITU-T G.652) and Dispersion Shifted Fiber (DSF: ITU-T G.653). Figs. 4 and 5 give examples of the calculated and measured results for a variety of fiber types {SMF, Cut-off Shifted Fiber (CSF: ITU-T G.654) and DSF). From Fig.5, it was found that the correction factor k was dependent of the refractive index profile caused by optical fiber fabrication techniques (such as VAD and MCVD etc.,). Accordingly, the summary of the measured correction factor k of A_{eff} and MFD (=$2w$) based on the examples of Fig. 5 are shown in Table 1.

4. Conclusion

The wavelength dependence of correction factor k of A_{eff} and MFD was first presented. It was found that the correction factor k was dependent of the refractive index profile caused by optical fiber fabrication techniques (such as VAD and MCVD etc.,). If the refractive index profile becomes step index profile, the correction factor k value approachs to nearly equal to 1.0.

Acknowledgement

The author wishes to thank Mr. M. Mori and Mr. H. Ochiai of Seiko Instrument Inc, (SII), Mr. A. Hallam of York Technology/PK Ltd., for their cooperation. Also, the author would like to thank Dr. H. Murakami and Dr. Y. Mimura of KDD R&D Labs. for their encouragement.

References:

[1] D. Marcuse, A. R. Charaplyvy, and R. W. Tkach :"Effect of fiber nonlinearity on long distance transmission", J. Lightwave Tech., 9, 9, pp.121-128, 1991.

[2] R. H. Stolen, W. A. Reed, K. S. Kim, and K. W. Quoi :"Measurement of optical nonlinearity of transmission fibers," SOFM'92, NIST, Boulder, USA, pp.71-75, 1992.

[3] K. S. Kim,W. A. Reed, R. H. Stolen, and K. W. Quoi. :"Measurement of the non-linear index of silica core and dispersion-shifted fibers," Optics Letters, vol.19, no.14, pp.257-259, 1994.

[4] Y. Namihira et al., :"Nonlinear coefficient measurements for dispersion shifted fibres using self-phase modulation method at 1.55 μm," Electron. Lett., vol.30, no.14, pp.1171-1172, 1994.

[5] A. Wada, T. O. Tsun, R. Yamauchi,:"Measurement of non-linear-index coefficients of optical fibers through the cross-phase modulation, using delayed-self-heterodyne technique," ECOC'92, P.42, 1992.

[6] J. E. Meier and W. E. Heinlein:" Improved self-compensated interferometer method to measure the effective nonlineality of an Er-doped fiber", OFMC'93, Sept. 21-22, Torino, Italy, 1993, pp.125-128.

[7] G. P. Agrawal :"Nonlinear Fiber Optics", Academic Press, 1989.

[8] J. V. Wright and E. S. R. Sikora ;"Determination of non-linear effective areas for dispersion shifted fibers," Symposium on Optical Fiber Measurements, NIST, Boulder, USA, pp.77-80, 1992.

[9] Y. Namihira:"Relationship between nonlinear effective area and mode field diameter for dispersion shifted fibers", Electron Lett., vol.30, no.3, pp.262-263, 1994.

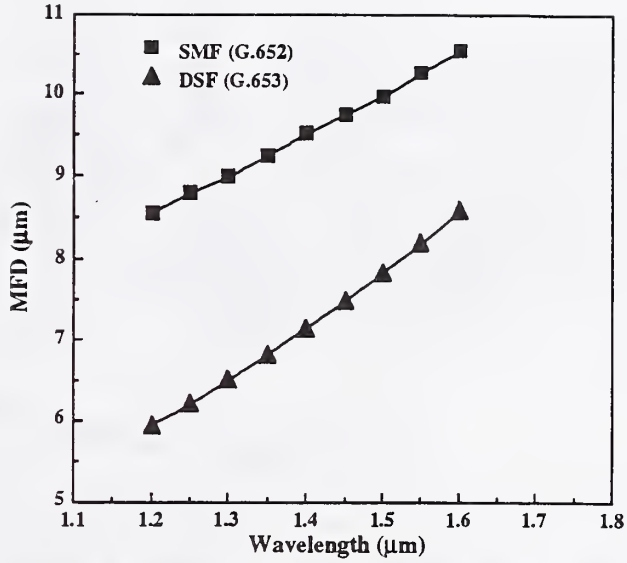

Fig.1 Example of measured wavelength dependence of MFD(=2w) of ITU-T G.652 and G.653 fibers

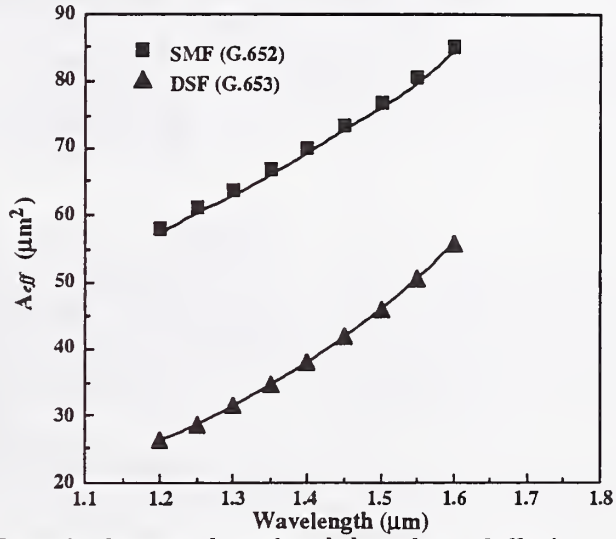

Fig.2 Example of measured wavelength dependence of effective area (A_{eff}) of ITU-T G.652 and G.653 fibers

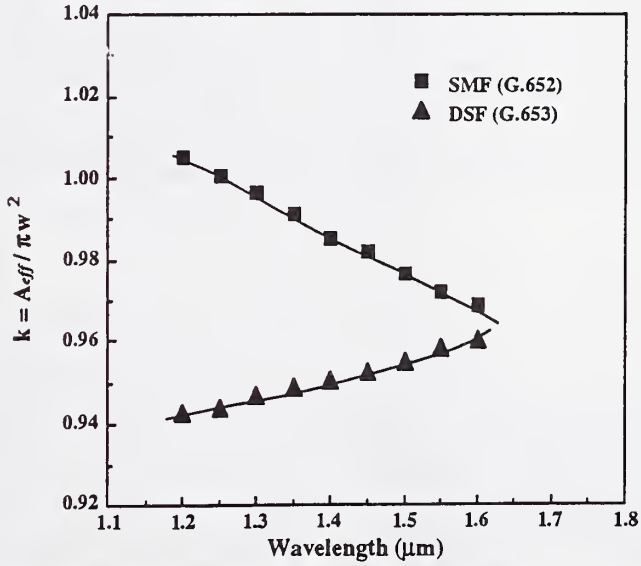

Fig.3 Example of measured wavelength dependence of correction factor k of A_{eff} and MFD(=2w) of ITU-T G.652 and G.653 fibers

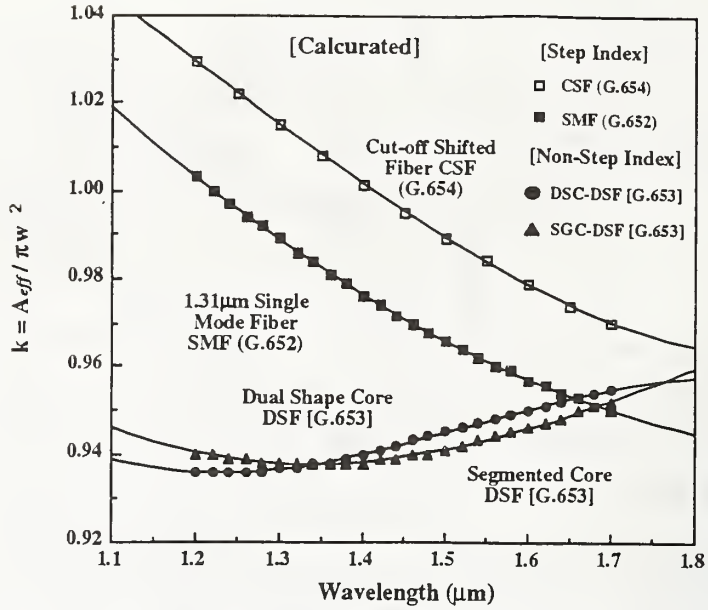

Fig.4 Example of calcurated wavelength dependence of correction factor k of A_{eff} and MFD(=2w) of ITU-T G.652, G.653 and G.654 fibers

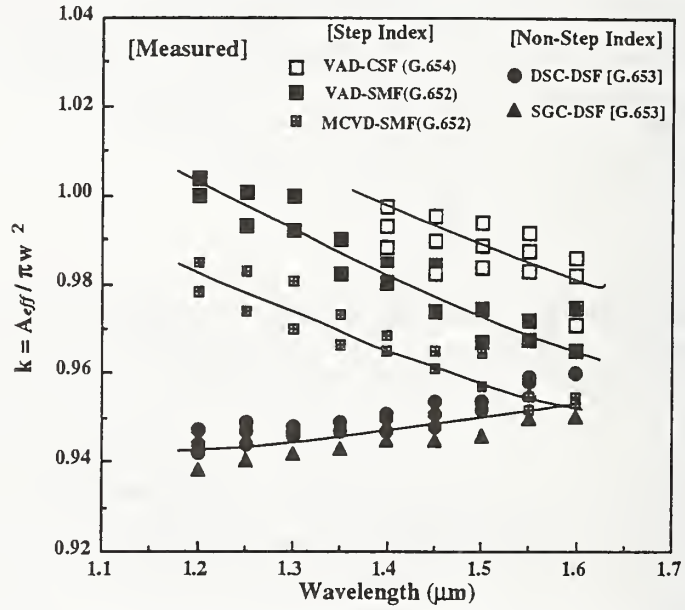

Fig.5 Example of measured wavelength dependence of correction factor k of A_{eff} and MFD(=2w) of ITU-T G.652, G.653 and G.654 fibers

Table 1 Summary of correction factor k of A_{eff} and MFD (= 2w) of ITU-T G.652, G.653 and G.654 fibers based on the examples in Fig. 5

Fiber types \ Wavelength λ		~ 1.31 μm	~ 1.55 μm
1.31μm Single Mode Fiber (SMF) [ITU-T G.652]	VAD	0.99 ~ 1.00 *	0.97 ~ 0.98
	MCVD	0.97 ~ 0.98 *	0.95 ~ 0.96
Cut-off Shifted Fiber (CSF) [ITU-T G.654]	VAD	----------	0.98 ~ 1.00 *
Dispersion Shifted Fiber (DSF) [ITU-T G.653]	VAD OVD etc.,	0.94 ~ 0.95	0.94 ~ 0.96 *

* : Optimum wavelength region

FIBER CUTOFF WAVELENGTH MEASUREMENT BY MODAL SPECTRUM MODULATION

P. DI BIN, C. SIMOS, D. PAGNOUX, P. FAUGERAS, P. FACQ

INSTITUT DE RECHERCHE EN COMMUNICATIONS OPTIQUES ET MICROONDES,
UNITE DE RECHERCHE ASSOCIEE AU CNRS
123, AVENUE ALBERT THOMAS, F-87060 LIMOGES CEDEX FRANCE

Introduction

The cutoff wavelength λ_c of a fiber is defined as the frontier between the single-mode and the bimode propagation regions. Many methods for measuring λ_c have already been presented, among which we can list : the near field shape observation method [1], the mode interference technique [2], the far-field azimuthal filtering technique [3] and the technique recomanded by the ITU-T [4]. Most of them either suffer of low speed measurement or need complex setups or information processing.

In this paper we propose a new simple method based on a spectral analysis of the light issued from the fiber under test when excited by alternate odd/even pattern configurations. A brief description of this method, its experimental validation and some typical results are presented in the following.

I Principle of the proposed method

The presented method is based on the fact that the LP_{11} mode launched into a fiber suffers a quite infinite attenuation in the single-mode wavelength domain, whereas its attenuation is comparable to that of the LP_{01} mode in the bimode regime. The principle brought into operation consists in alternately exciting the LP_{01} mode and the LP_{11} mode at the input of the fiber under test, and comparing the power carried by each mode at the output, versus the wavelength.

According to the criterion applied in the method recommended by the ITU-T, λ_c is the wavelength for which the suppression of the LP_{11} mode by means of a severe curvature induces a decrease of 0.1 dB of the transmitted power after propagation into a 2m tested fiber (the power launched into each mode at the input is assumed to be balanced).

The setup described on Fig.1 provides an easy alternate excitation of the two modes, together with the spectral analysis of the transmitted beam, leading to a very fast determination of λ_c. The light from a wide band source (LED or powerful lamp) is launched into a fiber F1 whose cutoff wavelength is appreciably lower than the one of the tested fiber : for example about 900 nm in order to characterize single-mode fibers in the 1300 nm region. The gaussian output pattern of this fiber is collimated by the lens L1. A rectangular glass plate with $\lambda/10$ polished surfaces and e=5mm thickness is set perpendicularly to the collimated beam, so to be crossed by exactly one half of this beam, inducing a phase difference with the other part equal to $\Delta\varphi$:

$$\Delta\varphi = \frac{2\pi}{\lambda} e\,(n-1) \qquad (1)$$

where n is the refractive index of the plate (n = 1.503 for BK7 when λ = 1300 nm).

The resulting beam is then focused on to the tested fiber by means of the lens L2. When $\Delta\varphi$ is equal to $2m\pi$, the launched pattern is of even type (as the LP_{01} mode is) and the injection efficiency is zero into the LP_{11} mode. On the opposite, when $\Delta\varphi$ is equal to $(2m+1)\pi$, the launched pattern is of odd type (as the LP_{11} mode is) and the injection efficiency becomes zero in the LP_{01} mode. The LP_{01} and LP_{11} modes are then alternately excited versus the wavelength.

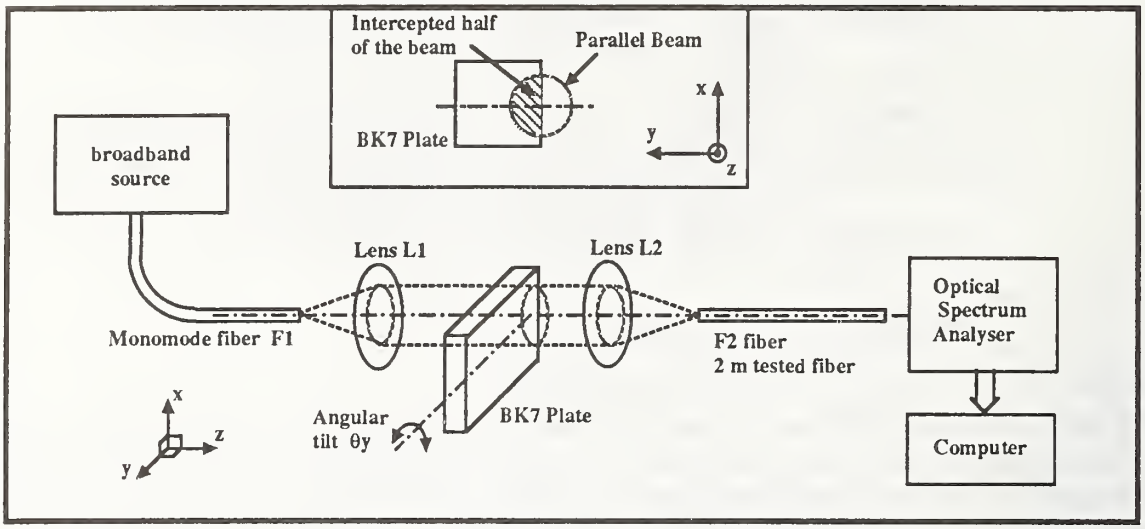

Fig. 1 : experimental setup

The switch from one mode to the other corresponds to a change in wavelength equal to $\Delta\lambda$:

$$\Delta\lambda = \frac{\lambda^2}{2\,e\,(n-1)} \quad . \qquad (2)$$

In the 1300nm region, $\Delta\lambda$ is approximatively equal to 0.34 nm. At the output end of the tested fiber, the transmitted spectrum is numerized and analysed by a computer. Let us define a modulation depth $M(\lambda)$ of the spectrum which is the local ratio P_{max} / P_{min} of the detected power level expressed in dB.

In an ideal case, in the bimode domain of the tested fiber, the transmitted spectrum is similar to the source spectrum, without oscillation, and M = 0 dB. On the opposite, in the single-mode region, the LP_{11} mode suffers an infinite attenuation which leads to grooves into the transmitted spectrum with a theoretically infinite depth, assuming a sufficiently narrow spectral bandwidth of analysis. Experimentally, as shown further, the modulation depth exhibits a finite maximum value, due to the partial coherence of the source, the spectrum analyser resolution and the residual setup alignment imperfections. Finally, in the cutoff region, λ_c is the wavelength corresponding to a 0.1dB decrease of the modulation depth measured in the single-mode domain.

II Characterization of the setup with a monochromatic source

The setup was characterized in the visible spectrum, using the monochromatic light of a 633 nm He-Ne laser. The mode pattern between the two lenses is supplied by a fiber F1 whose cutoff wavelength is now about 550 nm. The phase change $\Delta\varphi$ is obtained by an angular tilt of the plate around its θy axis modifying the optical path of the intercepted half of the beam.

A sample of the same single-mode fiber is set at the focus point of the lens L2 and the output power is measured versus the value of the plate tilt. The extinction ratio of the output power measured between two extreme excitation conditions (even or odd launched pattern) is higher than 30 dB. This very high contrast is due to the high coherence of the laser. This result clearly demonstrates that an odd selected pattern does not excite a significant amount of power into the LP_{01} mode of the fiber. It then purely excites the LP_{11} mode.

It is also of great importance to be sure that an even pattern does not significantly excite the LP_{11} mode. In order to verify this assumption, the output fiber was chosen to operate in the bimode regime at λ = 633 nm ($\lambda_c \approx 720$ nm) and the far-field pattern was analysed by means of a beam analyser.

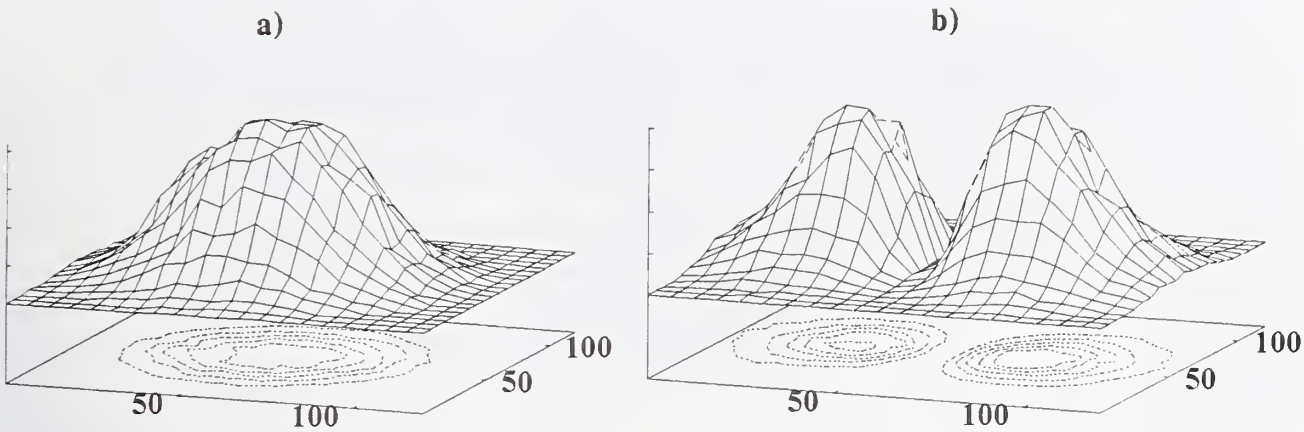

Fig 2: Experimental intensity profiles (Arbitrary units) of the far-field at the output of a bimode fiber (λ_c = 720 nm) versus the tilt of the plate (i.e. $\Delta\varphi$) : a) LP_{01} pattern (left); b) LP_{11} pattern (right).

Fig. 2 shows the far-field intensity pattern at the output of this fiber for different tilts of the plate, i.e. for various values of $\Delta\varphi$. It can be seen that, for suitable values of $\Delta\varphi$, modes with a very high purity are excited. In particular, an even launched pattern purely excites the LP_{01} mode and does not couple light into the LP_{11} mode, as shown on Fig 2-a. Fig 2-b confirms the previous conclusion about the pure selective excitation of the LP_{11} mode by a pattern of odd type. Between these two extreme situations, both LP_{01} mode and LP_{11} mode are excited. The optical power carried by each mode was measured, in order to verify theoretical calculations of LP_{01} and LP_{11} power excitation coefficients in the fiber F2. The LP_{11} injected power was measured to be about 2±0,2 dB lower than the LP_{01} within the optimal conditions. This result is in very good agreement with the value of 2 dB numerically calculated. This confirms that even in the bimode regime, the spectrum of a broadband light source will present residual modulation versus the wavelength of at least 2 dB. As this does not concern the monomode region, there is no effect on the criterion defined above for measuring λ_c.

III Experimental results with a broadband light source

The above proposed method was applied to the measurement of the cutoff wavelength of an ordinary 1300 nm single-mode commercial fiber. This one was first charaterized by the ITU-T recommended method giving a value of $\lambda_{c/ref}$= 1257±5 nm.

The setup of Fig.1 is now fitted out with an LED centered around 1290 nm, close to the expected λ_c value of the fiber under test. Its spectral width is 100 nm at -40 dB (observation is limited by the dynamic range of the spectrum analyser). The total emitted power is around -7 dBm.

Fig. 3 indicates the modulation depth M recorded at the output of the tested fiber, as a function of the wavelength. The bimode and single-mode regimes are clearly identified, described by a quite constant value of M (≈5dB and ≈15dB respectively). The transition between the two regions is characterized by an abrupt slope, indicating the cutoff region. Furthermore, this curve presents a great dynamic range extended up to 10 dB (against 3 dB for the ITU-T method), thus allowing a better accuracy in λ_c determination.

In the monomode region, the modulation depth should theoretically be constant, and the corresponding part of the curve should be an horizontal straight line. The slight slope experimentally obtained (straight line Δ) is attributed to the evolution of the ratio of the injection efficiencies of the two modes versus the wavelength. This slope is taken into account when applying the already defined criterion for λ_c determination : λ_c is the wavelength for which the parallel straight line Δ' plotted 0.1 dB below Δ crosses the experimental curve. In these conditions, the method leads to a value of λ_c equal to 1260 nm very close to the $\lambda_{c/ref}$ value (Fig. 3).

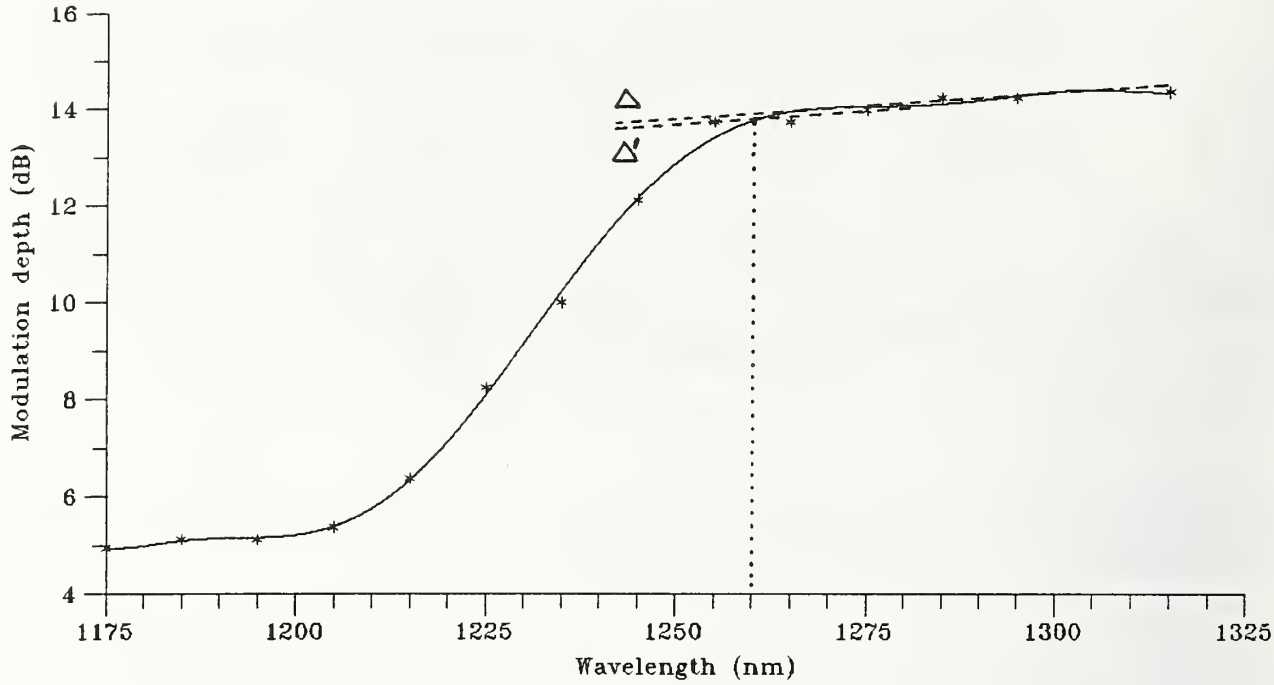

Fig. 3 : Modulation depth versus wavelength for the proposed method .

*** Experimental data

___ Fitted curve

- - - Δ and Δ'

Conclusion

We presented and validated experimentally a promising novel method for the measurement of the cutoff wavelength of a fiber. One of its basic advantages can be related to the controlled mode excitation conditions into the fiber, insuring accuracy and reliability of the measurements. The method is self referenced, the measured parameter M(λ) being insensitive to source power fluctuation. The accuracy of the proposed method is now as good as the ITU-T one. Further improvements should improve these first results.

The setup is small-sized, easy to utilize, has no moving parts and then permits very fast measurement (typically no more than few minutes, including the time spent for installing the fiber to test). This method is well adapted for both fast sytematic mass production control and precise laboratory measurements.

Acknowledgements

The authors are grateful to J.F. BAYON from French CNET Lannion for providing fibers used for the setup calibration.

REFERENCES

[1] Y. MURAKAMI, K. KAWANA and H. TSUCHIYA : "Cutoff wavelength measurements for single-mode optical fibers", *Appl. Opt.* , 1979, **18**, pp. 1101-1105.

[2] E. BRINKMEYER and S. HECKMANN : "Cutoff wavelength determination in single-mode fibers by mode interference", *Opt. Lett.*, 1984, **9**, pp. 28-30.

[3] J.M. BLONDY, A.M. BLANC, M. CLAPEAU and P. FACQ : "Azimuthal filtering technique for effective LP11 cutoff wavelength measurement in optical fibres", *Electron. Lett.*, 1987, **23**, n°10, pp. 522-523.

[4] Y. KATSUYAMA, M. TOKUDA, N. UCHIDA and M. NAKAHARA : "New method for measuring V-value of a single-mode optical fibre", *Electron. Lett.*, 1976, **12**, pp. 669-670.

A SIMPLE, FAST AND ACCURATE MEASUREMENT OF THE MODE FIELD RADIUS : THE AXIAL GAP METHOD

J.L. AUGUSTE, J.M. BLONDY, D. PAGNOUX, M. CLAPEAU, P. FACQ

Institut de Recherche en Communications Optiques et Microondes
URA CNRS N° 356
123, Avenue Albert Thomas
87060 - LIMOGES CEDEX - FRANCE

Abstract :

A simple set-up is developped to measure the mode field radius (MFR) of monomode fibers using the loss property of an axial gap.The measured MFR agrees with Petermann's definition. At least, only two measurement points along the axis are necessary, bringing a quick and simple tool. The results are in very good agreement with those obtained with the far-field scanning method recommended by the ITU-T.

Introduction :

Mode field radius is one of the most important parameters of monomode fibers. Its knowledge allows the theoretical evaluation of connection and microbending losses. It is also involved in the modelling of the chromatic dispersion. Recent experiments in the measurement of non linear effective area [1] have increased the necessity of an accurate determination of this parameter.

Many techniques have been developped to measure the MFR. The ITU-T recommendation uses the far-field angular scanning [2], coupled with the second definition of Petermann. The variable aperture method [3] and the transverse offset technique [4] give alternative ways to determine the MFR. But these techniques are time consuming specially when the field distribution deviates from the classical Gaussian form. This drawback increases when the MFR is measured versus the wavelength for chromatic dispersion evaluation. A faster and more accurate angular technique using a rotating mirror combined with the autocorrelation function of the far-field gives precise, quick and reproductible measurements of the MFR [5]. But, as the other techniques, it requires the acquisition of the whole transverse far-field.

The possibility of a measurement by an axial scanning of the far field had not yet been totally investigated. A technique has already been proposed by Saravanos *et al* [6], but it requires the acquisition of the far-field along the whole axis.

In this paper, we present an axial analysis of the far-field leading to the determination of MFR by a two points measurement. The theoretical assumptions are developped from the basis of the loss formula for an axially offset joint between two identical fibers. A complete exploitation of the technique shows that the MFR measured with this technique corresponds to Petermann's second definition in both cases of Gaussian and non-Gaussian fields.

Theoretical Assumptions:

In the case of a Gaussian mode propagating in the input fiber, the expression of the transmission factor for a longitudinal offset e is (ignoring Fresnel losses) :

$$T_D = \frac{1}{1+z^2} \qquad (1) \qquad \text{with} \qquad z = \frac{e}{k\,n\,w_o^2}$$

Where n is the cladding index and w_0 the MFR.

This formula is deduced from the following expression given by many authors [7], [8], [9] :

$$T_D = \frac{1+4\,z^2}{z^2 + \left(1+2\,z^2\right)^2} \qquad (2)$$

Eq(1) is obtained when noticing that : $(1+4\,z^2)\,(1+z^2) = z^2 + (1+2\,z^2)^2$

Therefore (1) is equivalent to : $$\frac{1}{T_D} = 1 + \frac{e^2}{k^2\,n^2\,w_o^4} \qquad (3)$$

The inverse of the power transmission factor is a linear function of the squared axial offset e^2 as depicted in figure 2. So, two points are sufficient to determine the MFR from the slope of the curve.

If Fresnel reflections at each endface of the fiber have to be taken into account, the new power transmission factor is given by the following expression.

$$\frac{1}{T} = \frac{(n+1)^4}{16\,n^2}\left[1 + \frac{e^2}{k^2\,n^2\,w_o^4}\right] \qquad (4)$$

Experimental set-up and results

In the experimental set-up shown in figure 1, the used light source can be a laser diode or a monochromator, or a tunable laser diode. An axial translation stage controlled by a precision stepper motor allows the variation of the axial gap e. At e = 0 position the two fibers are aligned in V grooves with a three axis precision translation stages. The detected power is collected by a small length of the tested fiber and carried out to the detector.

Two different procedures can be equally used :

- 2,5 m of tested fiber prealably stripped of its coating on some centimeters at a 2 meter length are set in the V grooves. The reference power is measured. Then the fiber is cut and the axial stage translates axially the tested fiber at different gap positions e. The mode field radius w_o is computed using eq. (4).
- the fiber is cut in two parts of 2 m for the tested one and some centimeters for the connection to the detector. The two fibers are aligned to obtain the maximum power and then translated to different gap position e. The MFR is computed using eq (3) because the Fresnel reflections are present for both reference and power measurements.

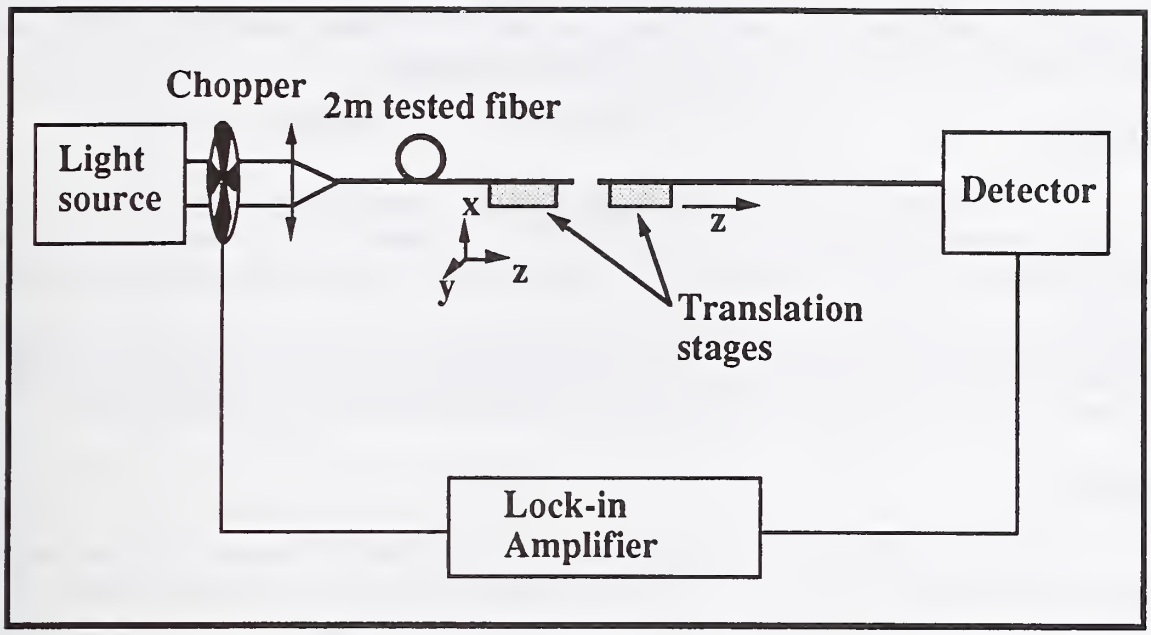

Figure1 : Experimental set-up

As shown in figure 2, the curve $1/_T$ versus e^2 is a straight line. In the first micrometers range, the measurement is perturbated by a Fabry-Perot cavity effect. That is why it is better to make the measurement with a wide gap between the two fibers (from 2 to 5 millimeters in our experiment).

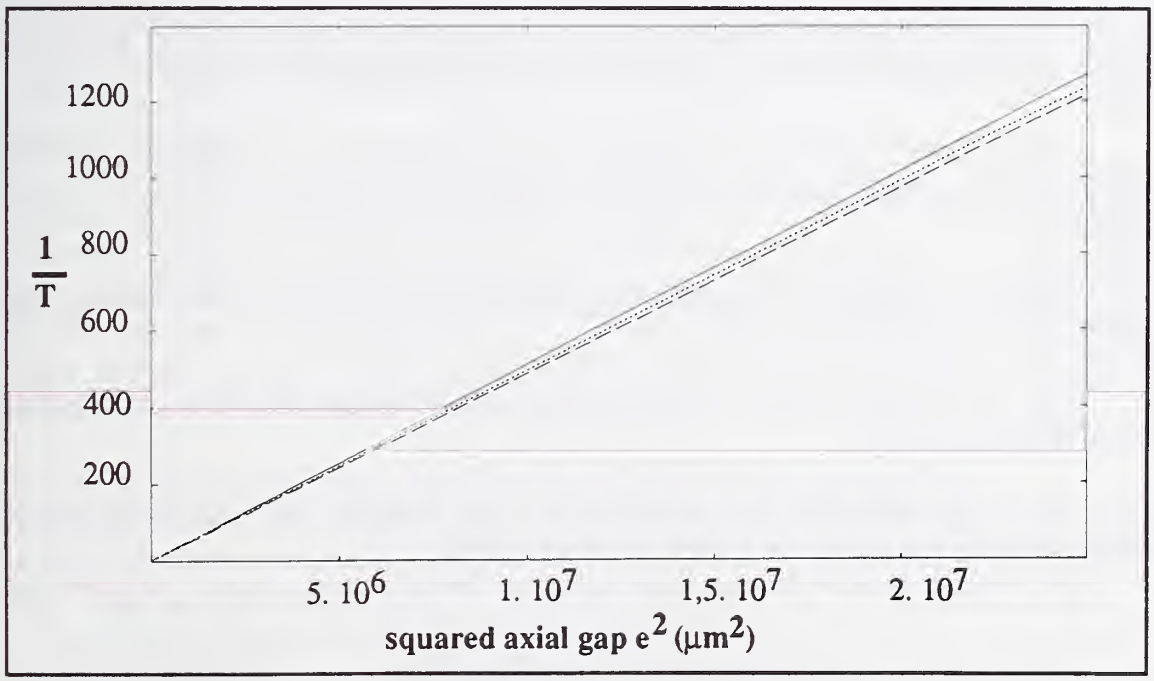

Figure 2 : Experimental curves of the measured inverse power transfer coefficient 1/T versus the squared axial gap e^2

The average value of MFR measured with the axial technique for a standard SMF 28 fiber is 4.54 µm very close to the value obtained with the ITU-T recommendation (4.55 µm).The discrepancy between ten successive measurements is less than 1%.

Conclusion :

The axial gap method gives a powerful tool for the measurement of the mode field radius. Two measurement points along the axis are sufficient. This leads to one of the fastest methods to obtain w_0. Our first experiments show a good agreement of the measured values with the ITU-T recommended far-field angular scanning method (within some 10^{-2} µm). The influence of different parameters such as precision on the gap e, power drifts of the source, small angular tilt of the fiber, uncertainties about the reference power, and linearity of the detector are being investigated.

References :

[1] Y. NAMIHARA, "Relationship between nonlinear effective area and mode field diameter for dispersion shifted fibers", Electronics Letters, Vol 30, n°3, pp 262-264, 1994.

[2] Recommendation of the CCITT n° G 652

[3] F. ALARD, L.B. JEUNHOMME, P. SANSONETTI, "Fundamental mode spot size measurement in single-mode optical fibres", Electronics Letters, vol 17., n°25, pp 958-960, 1981.

[4] J. STRECKERT, "New method for measuring the spot size of single mode fibers", Optics Letters, vol 5, n°12, pp 505-506, 1980.

[5] J.M. BLONDY, D. PAGNOUX, J. RIOUBLANC, P. ROY, P. FACQ, M. CLAPEAU, "Fast and accurate measurements of the mode field radius using the autocorrelation function of the far-field", Proceedings of OFMC'95, 25-26 septembre 1995, LIEGE (Belgique).

[6] C. SARAVANOS, R.S. LOWE, " The measurement of non-gaussian mode fields by the far field axial scanning technique" Journal of Ligthwave Technology, vol. LT4, n° 10, pp 1563-1566, 1986.

[7] D. MARCUSE, " Loss analysis of single mode fiber splices", Bell System Technical Journal, vol.56, n°5, pp 703-718, 1977.

[8] L. B. JEUNHOMME " Single mode fiber optics" 2nd edition Marcel Dekker inc., New-York and Basel, 1990.

[9] C. M. MILLER, S.C. METTLER, I. A. WHITE, "Optical fibers splices and connectors", Marcel Dekker inc., New-York and Basel, 1986.

Calibrated Test Fiber for Optical Time-Domain Reflectometers

Duwayne Anderson, Tektronix, inc.

Calibration of optical time-domain reflectometers (OTDRs) has traditionally involved calibration of the instrument's vertical and horizontal scales. For early OTDRs this level of instrument calibration was sufficient because these early machines provided only a waveform, with some cursors and zoom functions to assist the operator in making the actual measurements.

Modern OTDRs not only display the standard waveform, they also generate event tables that list the locations, losses, and reflectivities of components and anomalies located on the optical fiber. Mathematical algorithms, which interpret the OTDR's waveform and make measurements on it, generate these tables. Waveform characteristics such as noise, recovery from reflections, and digital filtering affect the accuracy of these algorithms. Tests show the system-level repeatability of many OTDRs is an order of magnitude less accurate than the hardware calibration of their subsystems [1]. Thus, it is no longer sufficient simply to calibrate the OTDR's hardware elements. We must also calibrate (or at least characterize) the OTDR's system performance, including absolute measurement errors arising from deficiencies in the interpretive algorithms.

A delay generator can be used, in conjunction with an optical-to-electrical converter and an optical transmitter, to calibrate the OTDR's time base and horizontal scale [2]. An optical transmitter and a variable attenuator can be used to calibrate the OTDR's vertical scale. Both of these subsystem-level calibration tasks involve non-fiber equipment that is easily calibrated to traceable standards. Calibration of the OTDR's system-level performance, however, requires a fully calibrated optical fiber with real components (events) such as connectors and splices, located along its length.

Three quantities describe each event on an optical fiber: distance from the OTDR, optical loss, and reflectivity. Ideally, the distance, loss, and reflectivity of each event on the test fiber should be calibrated and fully adjustable. We have developed such an optical-fiber test fixture that has three calibrated events. The first two events have calibrated distances, but not calibrated reflections or losses. The third event has calibrated distance, loss, and reflectivity, and the loss and reflectivity are both fully adjustable (see table 1).

Figure 1 illustrates the test fixture, which consists of the following components:

1. Four rolls of fiber. The lengths of the fibers are measured by the standard time-of-flight method, which gives a precise length for the fiber at a given (assumed) group index. The fiber loss is measured at 1310 and 1550 nm using the standard cut-back method [2].
2. Two calibrated optical attenuators with low insertion loss.
3. An optical coupler with measured split ratio at 1310 and 1550 nm.
4. A pigtailed mirror with measured reflectivity.
5. A device for bending the optical fiber and introducing loss.
6. A calibrated optical power meter.

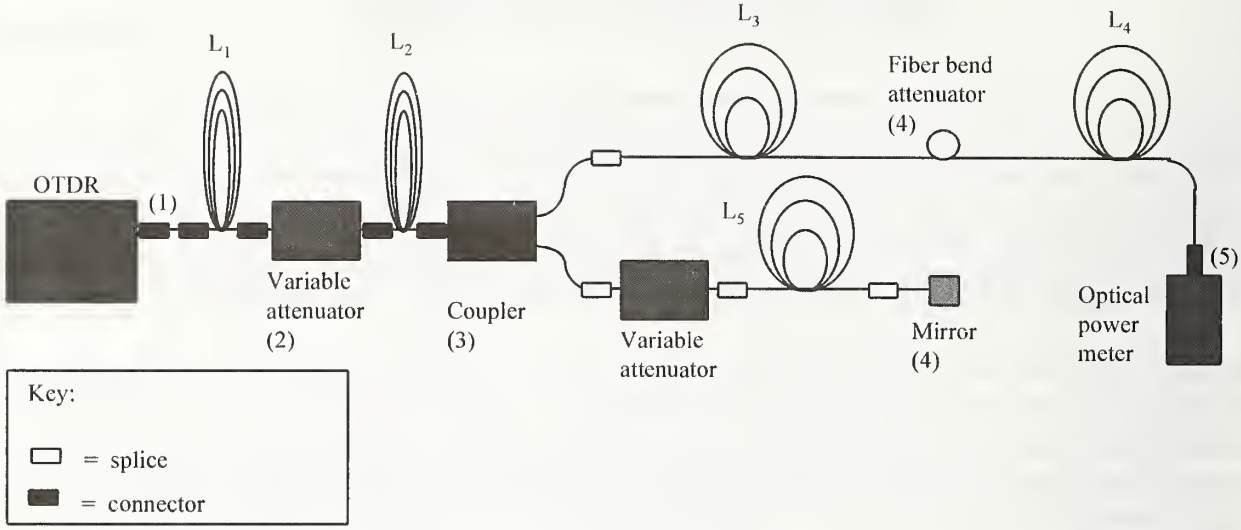

Figure 1. Configuration of the optical test fiber. The length of each section of fiber is measured with the time-of-flight method, and the insertion loss determined by the cut-back method.

Table 1
Approximate location, type, and calibration status of events

Event	Type of event	Event location	Event loss	Event reflectivity
1	Reflective	NA	NA	Uncalibrated
2	Low reflectance	Calibrated	Absolute loss uncalibrated Change in loss calibrated	Uncalibrated
3	Low reflectance	Calibrated	Uncalibrated	Uncalibrated
4	Adjustable: reflective or non-reflective	Calibrated	Calibrated and adjustable	Calibrated and adjustable
5	Reflective	Calibrated	NA	Uncontrolled

The first event on the test fiber is the reflection at the OTDR's front-panel connector. The second event is at distance L_1. The event's insertion loss is controlled by the variable attenuator, but is not calibrated because the losses of the connectors are unknown. However, the change in

loss (as a function of the attenuator loss) is calibrated. The attenuator is useful for raising or lowering the remaining events throughout the OTDR's dynamic range. This is important because the OTDR's performance on subsequent events can be altered depending on how close the events are to the noise floor. Together, the first and second attenuators may be used to move the reflection of the mirror through the OTDR's full vertical scale range. This is useful for characterizing and calibrating the OTDR's system linearity.

The second event is the coupler (the second attenuator is physically located less than 0.5 meter from the coupler, and is indistinguishable from it on the OTDR trace). The loss and reflectivity of this event are uncontrolled, but the distance is calibrated. The insertion losses of all the fiber spools are measured before assembly. Consequently, their link losses may be measured as the fiber is moved up and down through the OTDR's dynamic range by adjusting the loss of the first attenuator. This is one of the calibration procedures proposed by the IEC. The technique uses a reference fiber of known loss, moving it through the OTDR's vertical scale, and verifying that the fiber's link loss as measured by the OTDR remains constant [2].

The distance to the mirror (through one leg of the coupler) is exactly the same as the distance to the fiber bend (through the other leg of the coupler)[1]. The reflection from the mirror is overlaid on the OTDR's display with the non-reflective loss of the fiber bend. By adjusting the loss of the fiber bend, and the attenuator in the coupler leg with the mirror, the composite loss and reflectivity of the event, as seen on the OTDR's display, is fully adjustable and calibrated.

The true reflectivity of the mirror (as measured by the OTDR) is a function of the mirror's absolute reflectivity, the losses of fusion splices, the coupler split ratio, and the adjustable attenuator. The attenuator is calibrated, and the mirror's reflectivity characterized, before assembly. The splice losses are estimated from the fusion welder, and the coupler split ratio measured before assembly. Total uncertainty for the reflection is relatively high compared with tolerances for insertion loss, but well within tolerances specified by Bellcore [3].

The bend loss is calibrated from readings at the optical power meter, while the OTDR is in its laser-pulse mode. In the laser-pulse mode the laser fires at a constant rate, high above the power meter's bandwidth. With the OTDR in the laser-pulse mode, the optical power emanating from the far end of the test fiber is measured when the fiber is not bent (see figure 1). Next, the fiber is bent into a loop sufficient to attenuate the power meter's reading by a predetermined amount (0.25 dB, for example). The true calibrated loss that should be reported by the OTDR is:

$$Loss = -5\log\left(10^{\left(-\frac{Loss_{pm}}{5}\right)} + 10^{\left(-\frac{Q}{5}\right)}\right) \qquad [1]$$

[1] Precise assembly and calibration techniques are required to ensure the equality of these two distances.

In equation [1] $Loss_{pm}$ is the loss seen by the optical power meter (the difference in the power meter readings before and after the loop loss is introduced, in dB). The variable Q is a correction factor accounting for backscatter emanating from the coupler's second leg (the one with the mirror). If the event's reflectivity (as measured by the OTDR) is not too large, then ignoring Q results in an error of less than about 0.001 dB (assuming the mirror's absolute reflectivity is greater than about 85%).

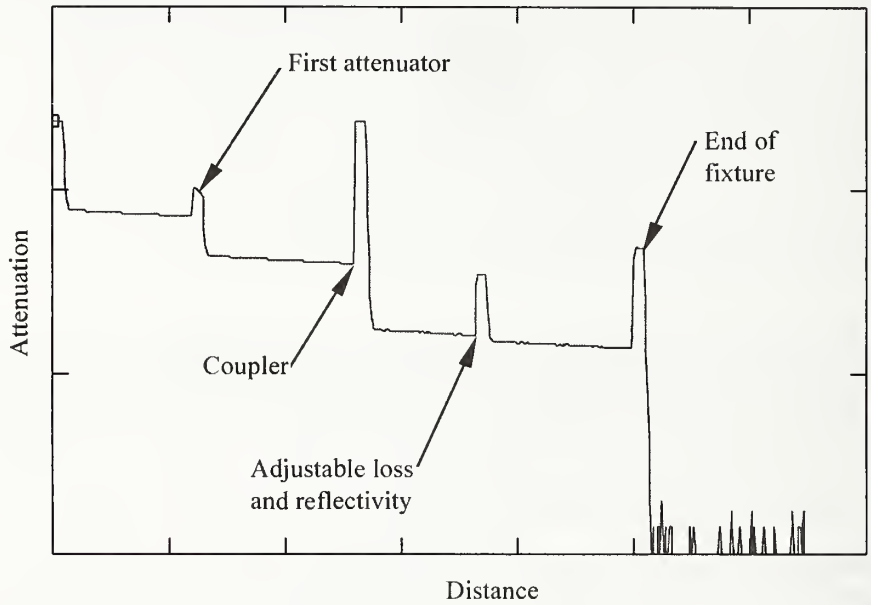

Figure 2. OTDR waveform of the test fiber.

We have found this test fixture to be an important tool for assessing the absolute accuracy of system-level measurements made with OTDRs. With this fixture, the OTDR's absolute accuracy for loss, distance, and reflectivity measurements can be tested and verified over the full width of the OTDR's vertical dynamic range. By attaching fibers of calibrated length to the fixture, the OTDR's performance can also be investigated over the instrument's distance-measurement range.

References:

[1] Duwayne Anderson and David Judge, *A Pattern Matching Algorithm for Remote Systems that Measures the Distance and Loss of Fusion Splices with High Precision*, National Fiber-Optics Conference, 1994.

[2] IEC TC 86 / WG4 / SWG2 *Calibration Of Optical Time-Domain Reflectometers.*

[3] Bellcore GR-196-CORE *Generic Requirements for Optical Time Domain Reflectometer (OTDR) Type Equipment.*

A Method for the Localisation and Quantization of Faults in Passive Tree-Structured Optical Networks using the OTDR technique

L. Wuilmart, V. Moeyaert, D. Daniaux, P. Mégret, M. Blondel

Service d'Electromagnétisme et de Télécommunications
Faculté Polytechnique de Mons
Boulevard Dolez 31 B-7000 MONS (BELGIUM)

ABSTRACT

A method for the detection, localisation and quantization of faults in tree-structured passive optical networks is presented. This method is based on the analysis of OTDR (Optical Time Domain Reflectometry) traces. Several kinds of faults have been generated in a 1X8 passive optical network to illustrate the effectiveness of this technique.

INTRODUCTION

The use of OTDR has proven to be very efficient for the maintenance of optical links. The access to only one extremity of the link is necessary; the OTDR signal wavelength and the data signal wavelength can be different so that the monitoring of the link involves no interruptions of the communications.
If a fault occurs in a point-to-point optical link, a simple comparison and analysis of OTDR traces leads to an accurate determination of its position, its kind and parameters such as its loss and return loss.
The problem is more complex in the case of a tree-structured network, since the trace acquired at the top of the network results in the combination of the reflected and backscattered light signals coming from the different optical paths. If a fault occurs in a branch of a tree-structured network, it can be easily detected comparing the trace acquired at the head of the failed network with a reference trace. However the affected branch and the fault's parameters (kind, loss, return loss) are more difficult to determine.
The method explained in this paper solves this problem. It is illustrated with the analysis of a 1X8 passive optical network. Several kinds of faults have been generated and the results obtained with a software implementing this method are presented.

METHOD

Fault detection and localisation

A fault in a point-to-multipoint optical link can be easily detected comparing an OTDR trace of the failed-supposed network with a faultless reference trace : a significative difference between these two traces is a failure sign. Moreover the failure is situated at the position where the trace difference becomes higher than a given threshold.
The problem lies in the determination of the failed branch on the basis of the analysis of an OTDR trace acquired at the network's head, since such a trace results in the combinations of all the backscattered and reflected signals.
Nevertheless as we can identify each branch on the trace with an end-reflection peak, we can determine the failed branch which is the one whose height's variation of the end-reflection peak is the more important (see examples in the experimental study). This assumes that significant and equivalent reflections are generated at the OTDR signal wavelength at the end of each branch and that the lengths of all theses branches are different.

Fault Quantization

The end-reflection peak's variation gives information about the kind of network failure: a left shift of a peak indicates a cut, a small height's variation can be caused by a small bend of the optical link, ... Other examples are given in the experimental study.
When a fault occurs in a point-to-point optical link, its loss can be directly measured on an OTDR trace. But this is not the case anymore for a tree-structured network, a simple analysis of an OTDR trace acquired at the network's head doesn't provide this parameter.
Actually to have an accurate fault loss estimation on the basis of a complex trace analysis, it is necessary to take into account the exact contribution to the complex trace of the reflected signals coming from each branch. One often thinks that this involves a previous knowledge of network's parameters [1][2] such as the splitter losses, the fibers attenuation, ... However we show below that the fault loss can be obtained using only OTDR traces informations.

Two traces informations are power levels (dB) measured by the OTDR at the top of the end-reflection peak associated to the fault branch, first on the reference trace (Pref) and second on the fault trace (Pfault).

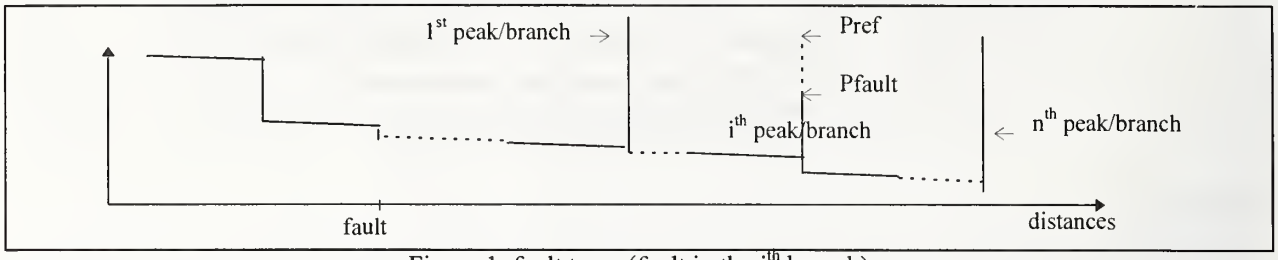

Figure 1: fault trace (fault in the ith branch)

Considering a fault in the ith branch, these power levels can be expressed as the sum of the reflected signals contributing to the trace at the ith peak position :

$$Pref = 5\log\left(\sum_{k=i}^{n} 10^{P(k)}\right) \tag{1}$$

$$Pfault = 5\log\left(10^{P(i)-Lf} + \sum_{k=i+1}^{n} 10^{P(k)}\right) \tag{2}$$

where P(k) is the power level (dB) at the ith peak's position of the reflected signal coming from the kth branch, Lf is the fault loss.

From (1) and (2) we can compute the fault loss (Lf) :

$$Lf = -5\log\left(\frac{10^{\frac{Pfault}{5}} - 10^{\frac{Pref}{5}}}{10^{\frac{P(i)}{5}}} + 1\right) \tag{3}$$

We see that the loss depends on P(i). Actually P(i) represents the power level that would be measured at the top of the fault branch's end-reflection peak if only the reflected signal from this branch contributes to the trace at the peak's position. In order to perform a fault loss determination, we must know this power level for each branch.

As we base on the fact that the part of a trace from the end of the penultimate branch to the end of the longest one is only composed of the reflected signal coming from the longest branch, it is possible to measure these power levels at the network's installation. The branches must be connected to the splitter in increasing length order and a trace must be acquired after each connection. So that, for each branch, we have a trace where it is the longest one, and therefore we can measure the wanted power level associated to each branch's end-reflection peak.

Advantages

- A main advantage of this method is its low cost compared with other reflectometric methods using active [3] or WDM [4] components inside the splitters.
- This method can apply to multistaged passive tree-structured optical networks.
- In order to estimate the fault loss, it is not necessary to previously define the network's parameters (splitter losses, fibers attenuations, ...).
- The presence of significative end-reflections at the OTDR wavelength increases the fault detection sensibility: in the case of a small loss, a more important modification of the trace will be observed with than without reflection peaks.

Drawbacks

- Since the trace is acquired at the network's head, the OTDR signal suffers the splitters losses. Therefore the OTDR dynamic -the maximum measurable loss-, becomes a limiting factor. The OTDR dynamic can be inproved in increasing the pulse duration but at the expense of the spatial resolution. However having a very accurate spatial resolution is not always needed as we suppose that faults generally appeared at well-known located connectors or splices or are created by external factors such as public works which can be accurately located.
- The branches must have different lengths in order to distinguish their end-reflection peak.

EXPERIMENTAL STUDY

Experimental Set Up

The effectiveness of this fault analysis method was demonstrated by acquiring and analyzing a 1X8 splitter's OTDR trace of a connected network build in our laboratory (see figure 2). The input fiber was about 2.50 km long and, behind the splitter, the length of the fibers was between 2.26 km and 6.10 km. All fibers were terminated on a 4% Fresnel reflection (right angle air/fiber interface).

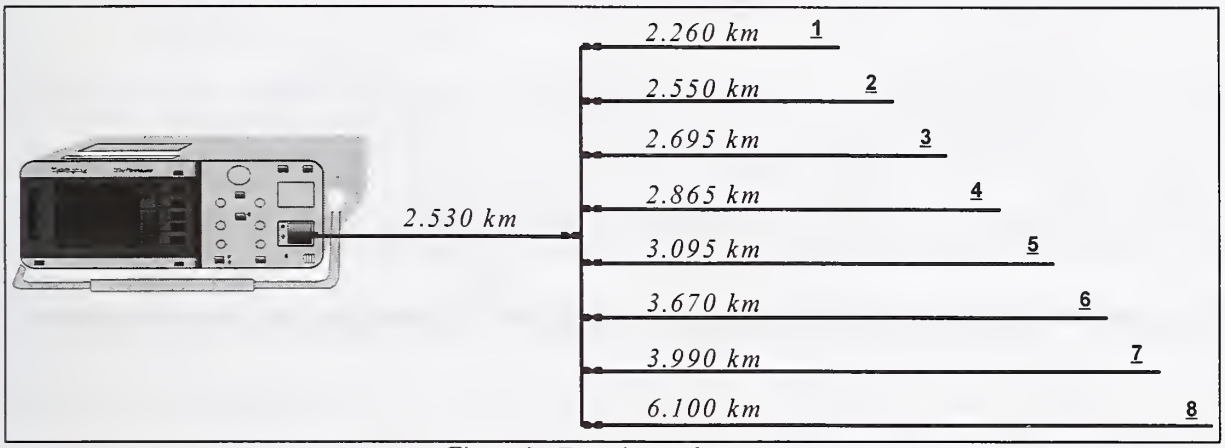

Figure 2 : Experimental set up.

An initial test was performed at 1550 nm using a 100 ns optical pulse. Figure 3 shows the 'installation' (reference) trace of our network on which one can easily see the large insertion loss characteristic of the 1X8 splitter and end-reflection peaks associated to each branch.

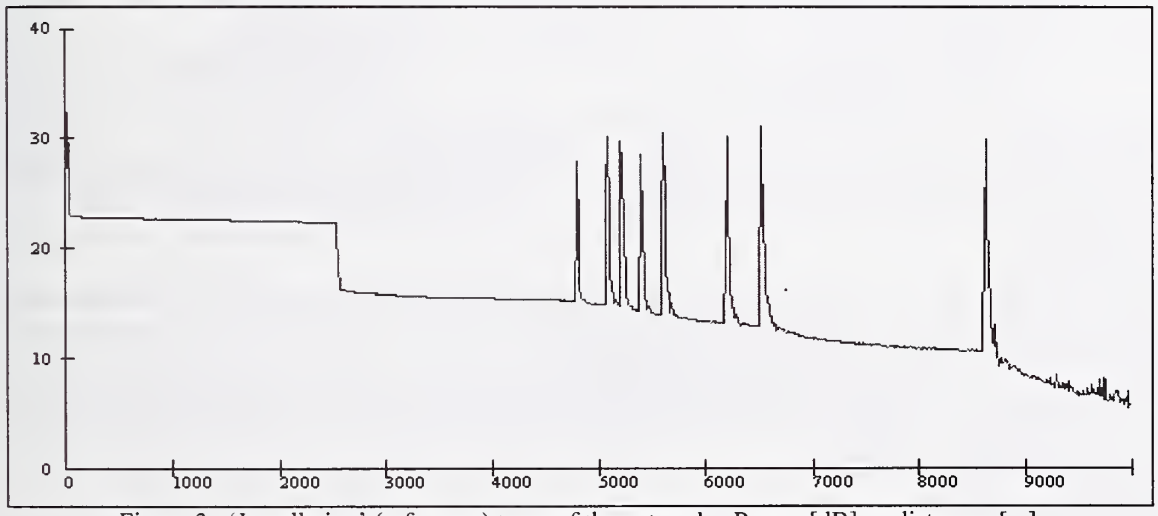

Figure 3 : 'Installation' (reference) trace of the network - Power [dB] vs distances [m].

Faults analysis

After this initial testing, some impairments were done to the network. Four are illustrated below:

1. a bend in the 3rd branch at 170m from the splitter (about 7dB loss).
2. a large bend in the 5th branch at 560m from the splitter
3. a break in the 3rd branch at 170m from the splitter
4. a break at the end of the 5th branch

For each impairment a new OTDR trace has been acquired and let to be analysed by our software in order to assess its quality in fault discrimination. Our software can display the reference trace, the fault trace and the difference between these traces (in the examples below, only the fault trace and the difference are displayed). A map of the network is drawn and a cross indicates the position of the fault. The fault loss, the fault position and a comment concerning the possible type of fault are also given.

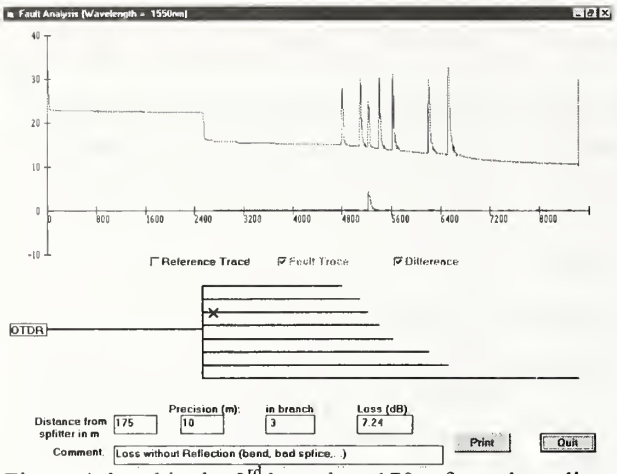

Figure 4: bend in the 3rd branch at 170m from the splitter

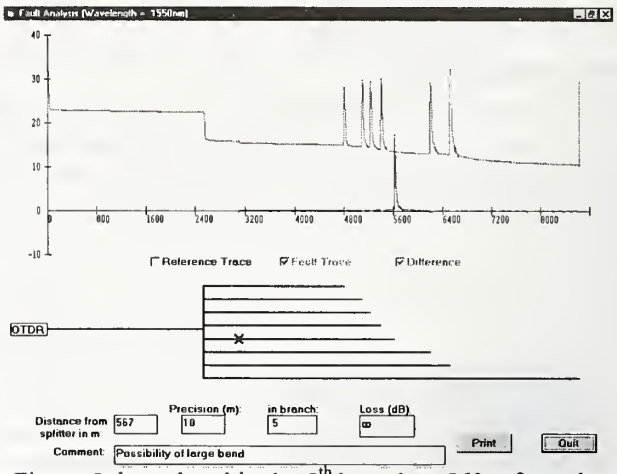

Figure 5: large bend in the 5th branch at 560m from the splitter.

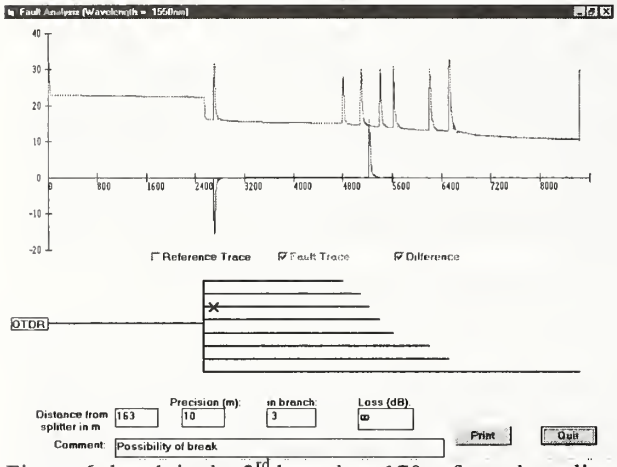

Figure 6: break in the 3rd branch at 170m from the splitter

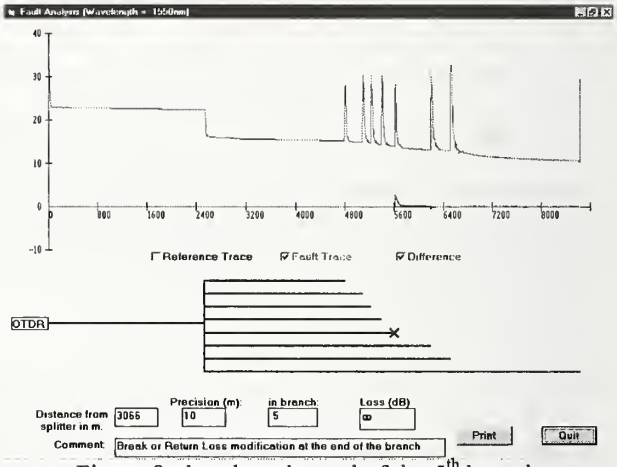

Figure 8 : break at the end of the 5th branch

CONLUSIONS

The method presented showed that the optical time domain reflectometry can be used to facilitate the maintenance of multistaged tree-structured passive optical networks at a low cost. This method has been implemented in a user-friendly software, and the results obtained proved its effectiveness.

We also showed that it is possible to estimate the loss of a fault only on the basis of OTDR traces acquired at the network's head despite the fact that such traces result in the combination of the reflected and backscattered signals coming from the different optical paths.

AKNOWLEDGMENTS

This work was funded by BELGACOM in the frame of RD/TR/UN/1 contract.

REFERENCES

[1] F. Kapron, J.D. Berardinelli, "OTDR Measurements Through Optical Splitters", proc. Optical Fiber Measurements Symposium, Boulder (USA) 1992.

[2] Caviglia et al., "OTDR analysis of tree-structured optical networks. Fiber test methods and field testing", proc. EFOC&N, 1994.

[3] Y-K. Chen et al., "Fault-Locating and Supervisory Technique for multistaged Branched Optical Networks", IEEE Photonics Technology Letters, Vol.6, n°7, July 1994.

[4] F. Yamamoto et al., "In-service Remote Access and Measurement Methods for Passive Double Star Networks", proc. 5th Conference on Optical/Hybrid Access Networks, Montréal (Canada) September 1993.

A COARSE RANGING MEASUREMENT METHOD FOR ACCESS SYSTEMS USING PASSIVE OPTICAL NETWORKS

A. FELLEGARA

ITALTEL -A Stet & Siemens Company - R & D Transmission Business Unit

20019 Castelletto di Settimo Milanese (Milano) - ITALY-

Abstract: A coarse ranging measurement method based on the use of an asymmetrical bidirectional system architecture is presented. The impact of the crosstalk on system performances is calculated and discussed.

In these years the deployment of fiber-optic cables is penetrating further to the local loop plant to bring broad band and/or narrow band directely to the customers. One candidate for this network is the Passive Optical Network (PON) which incorporates passive optical splitters, forming a point to multipoint network. In other words an Optical Line Termination (OLT) at the central office is connected by optical fibers to a plurality of substations called Optical Network Units (ONUs). The OLT centrally controls the data trafic to and from the various ONUs and, in particular, the information flow from the OLT to each ONU is called the *"downstream transmission"*, whereas the information that flows from each ONUs to the OLT is called the *" upstream transmission"*. Due to the peculiar character of this data trafic, it is essential to have a ranging procedure (that can be coarse or fine depending on the accuracy) which accounts for the distances between the main station and the substations allowing the transmitted data to arrive at the specified time slots for the substation with respect to the main station timing. This paper aims to investigate a coarse ranging method based on the use of low bite-rate optical signal traveling in downstream and upstream fibers always counterpropagating with respect to the data trafic. This method can be made clearer by the non exhaustive example reported in fig1: the OLT activates the ranging transmitter which sends a low bit-rate ranging signal counterpropagating with upstream data. The 'to-be-adjusted' ONU re-sends to the OLT the ranging, counterpropagating with the

downstream data. The measurement of the occurred round trip delay gives the desired ranging value. The coupling ratio of the optical splitters allows the transmission of the CW and BURST signals without any significant degradation of the power budget whereas the ranging losses are well compensated by the smaller value of the ranging sensitivity. A feasibility analysis of the system according to the proposed ranging measurement can be performed assuming the power budget given by [1]

$$\frac{P_t}{P_{r-data}} = A \cdot (k-\gamma)^2$$
$$\frac{P_t}{P_{r-rang}} = A \cdot (1-k-\gamma)^2 \qquad (1)$$

Where both couplers have a power splitting ratio of k:(1-k), γ is the coupler insertion loss, A is the fiber loss between the couplers, P_t and $P_{r\text{-}rang/data}$ are the optical transmitted and received powers for the ranging and data, respectively. The received powers (for $A=A_{max}$) vs coupling ratio are shown in fig.2. As an example, by using 10/90 couplers, the received powers are $P_{r\text{-}rang}$ =- 50.2 dBm (10 %) and $P_{r\text{-}data}$=-27.5 dBm (90 %), respectively. To evaluate the bit-rate let us impose that $P_{r\text{-}rang/data}$ satisfy also the following condition

$$P_{r-rang/data} \geq \frac{Q}{\rho}\left(\sqrt{< I^2_{therm} > + 2q\rho\, BP_{refl}}\right) \qquad (2)$$

where Q=6 , P_{refl} is the backreflected power that reaches the photoreceiver and both sides of eq.2 are equal when $P_{r\text{-}rang/data}$ are the receiver sensitivities, i.e the minima detectable average optical powers for a given BER. A simple calculation shows that 622 Mbit/s (data) and 2 Mbit/s (ranging) are solutions consistent with eqns. (1-2) at P_{refl} =0 since the correspondent baseline sensitivities are well below the received powers [1]. However, bidirectional direct-detection systems are sensitive to the crosstalk from Rayleigh backscattering and discrete reflections that, in PON systems, are mainly caused by the laser diode reflections at the ONU side [2]. The multipath interference and coherent Rayleigh noise [3], can be significantly reduced by using multimode Fabry-Perot semiconductor lasers, whereas a ranging bit-rate much lower than the data trafic bit-rate allows to filter out the crosstalk before the decision point on both receivers. On the other hand, the impact of the crosstalk-induced shot noise on

the system performances is evaluated with the help of eq. 2, by calculating the power penalty with respect to the baseline sensitivity. Fig. 3 reports the power penalty vs the crosstalk-receiver sensitivity ($CR = P_{refl}/P_{s\text{-}rang/data}$), showing a similar behaviour for both data and ranging curves. From this figure it can be concluded that for a wide range of reflection levels the increase of the sensitivities is well below the received power values corresponding to the 10/90 couplers. To understand these results, it is worth while to note how different is the role of the crosstalk played in the conventional bidirectional systems: in our case, in fact, the strong asymmetry in the operating bit-rates allows to filter out the signal-crosstalk before the decision point on both receivers. Thus, the crosstalk degradation is due to the crosstalk-induced shot noise which has a minor impact on the system performances.

In summary, a digital coarse ranging measurent method for PON systems is presented and the system penalties induced by the crosstalk are also calculated and discussed.

REFERENCES

[1] A. Fellegara - Electron. Letters, vol n.1, p.51 1996

[2] I. Van de Vorde, C. Sierens - ECOC '95-Brussels, paper Tu.P.19 p.449 , 1995

[3]R. Staubli, P.Gysel - J. Lightwave Tech., vol **9**, p.375 , 1991,

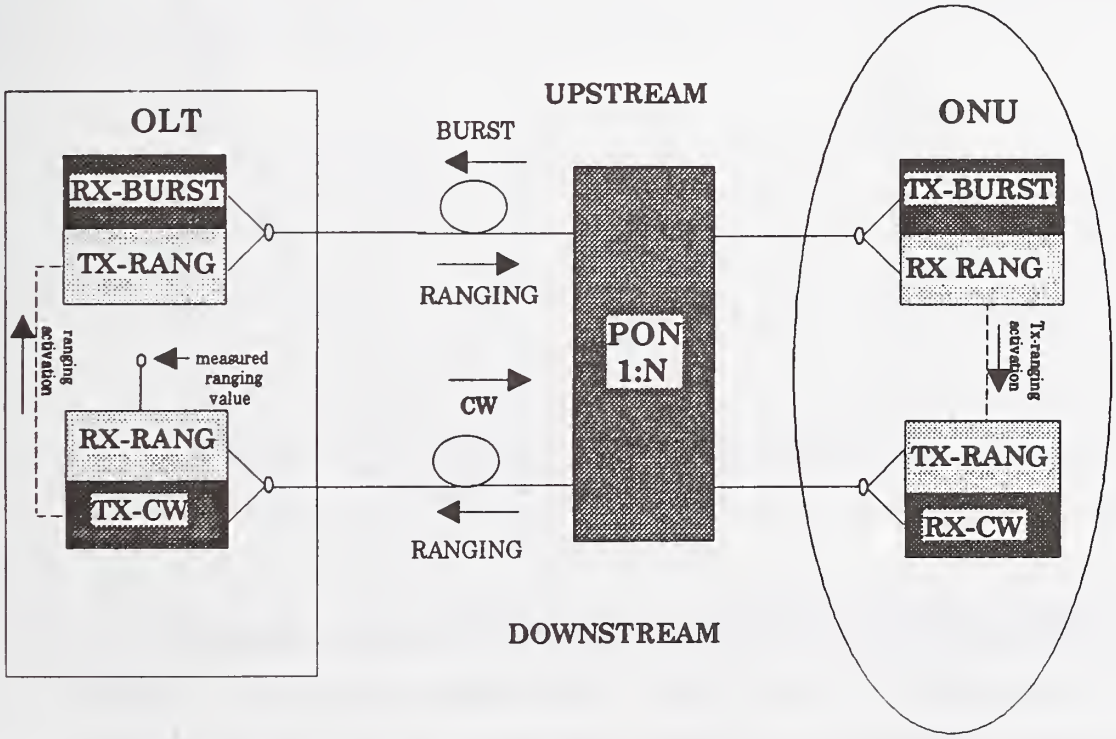

Fig.1 - Architecture of the optical link according to the proposed ranging procedure.

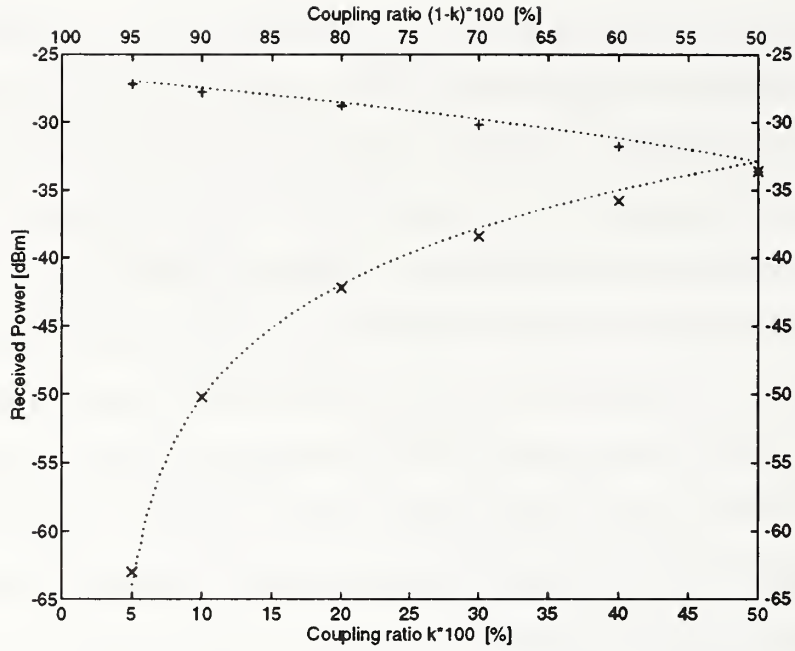

Fig. 2 - Received Power vs Coupling ratio. *Dotted lines*:theoretical calculations x, + = experimental data measuring power couplers with various splitting ratios. **Data**: A_{max}= 26 dB, Pt= 0 dBm, $\gamma = 0.04$.

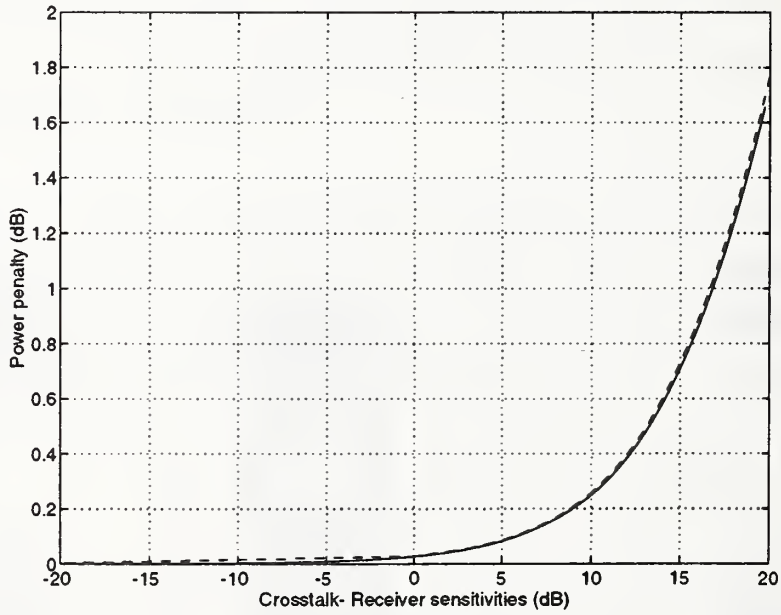

Fig.3 - Power Penalty vs Crosstalk power-receiver sensitivity. **Data**: ρ=0.73

Solid lines: 622Mbit/s, $P_{\tilde{S}}$= - 31.9 dBm, (data baseline sensitivity) , from [1]

Dotted lines: 2 Mbit/s, $P_{\tilde{S}}$= - 56.9 dBm, (ranging baseline sensitivity), from [1]

Spatial-resolution improvement in coherent optical frequency domain reflectometry for long optical fibers by reducing frequency-sweep nonlinearity

K. Tsuji, K. Shimizu, T. Horiguchi, and Y. Koyamada
NTT Access Network Systems Laboratories
Tokai-mura, Ibaraki-ken, 319-11, Japan

Abstract

We report long-range coherent optical frequency domain reflectometry (C-OFDR) with an auxiliary feedback-control circuit to suppress optical-frequency-sweep nonlinearity. We achieved spatial resolutions of 1 m and 50 m at the far ends of 1 km and 30 km optical fibers, respectively, without sacrificing the measurement time. These are the best results reported to date for C-OFDR.

1. Introduction

It is important to be able to measure loss and locate faults in optical fibers with high spatial resolution. For this purpose, coherent optical frequency domain reflectometry (C-OFDR) is very attractive because of its high spatial resolution and high sensitivity [1]-[6]. With this technique, the frequency of a lightwave is swept linearly with respect to time, and the frequency-swept lightwave is divided into probe and reference lightwaves. The probe lightwave is launched into an optical fiber under test, and the reflected-probe lightwave from the test fiber is mixed with the reference lightwave at an optical receiver. The resultant beat signal is analyzed in the frequency domain. The beat frequency f_b is in proportion to the optical-path difference ΔL between the reflected and reference lightwaves, as follows,

$$f_b = \gamma \Delta L / v_g \qquad (1),$$

where γ is the frequency sweep rate and v_g is the group velocity of light. Therefore, the reflection position can be identified uniquely from the beat frequency f_b as long as the frequency-sweep rate γ is kept constant. The spatial resolution is improved by narrowing the frequency-resolution bandwidth, and the achievable spatial resolution Δz_{min} is theoretically given by using the total frequency-sweep span ΔF, as follows,

$$\Delta z_{min} = v_g / 2\Delta F \qquad (2).$$

Therefore, a wide frequency-sweep span is required for high spatial resolution.

In previous reports, there have been a few experiments which employed C-OFDR for the measurement of long optical fibers [2]-[6]. In these measurements, frequency-sweep nonlinearity severely limits the spatial resolution. This is because it causes a fluctuation in the beat frequency f_b through the change in the frequency-sweep rate γ according to Eq. (1), which results in a broadening of the beat spectrum and degrades the spatial resolution. Since the beat-frequency fluctuation is more obvious when the optical-path difference ΔL is large, it becomes more difficult to achieve high spatial resolution as the length of the test fiber increases. In a previous study [6], we reduced the spectral broadening which results from the nonlinear-frequency sweep by using time-gated spectrum analysis, and improved the spatial resolution. With this technique, however, since a limited part of the frequency-sweep span and time are used, the achievable spatial resolution degrades according to Eq. (2) and the measurement time is considerably sacrificed depending on the degree of the frequency-sweep nonlinearity.

In this paper, we report a C-OFDR in which the frequency-sweep nonlinearity itself is suppressed by employing an auxiliary feedback-control circuit. We successfully improved the spatial resolution of C-OFDR without the substantial increase in measurement time reported in [6].

2. Experimental setup

Figure 1 shows the experimental setup, which consisted of the C-OFDR apparatus and an auxiliary feedback-control circuit to suppress the frequency-sweep nonlinearity. The lightwave source was an Er-Yb-glass laser operating at 1.55 μm with a linewidth of approximately 3 kHz. The lightwave was sinusoidally modulated with an external electro-optical (EO) phase modulator incorporating a Ti-diffused-$LiNbO_3$ waveguide. The EO phase modulator was driven by a synthesized-frequency sweeper. The lightwave frequencies of the modulation sidebands were swept by changing the modulation frequency linearly with respect to time. The frequency sweep rate γ was approximately 0.1 THz/s, where the frequency-sweep span was approximately 2 GHz and the sweep time was approximately 20 ms. Accordingly, the relation between the fiber length and the beat frequency was approximately 1 m/kHz. The frequency-modulated lightwave was divided into probe and reference lightwaves by using a directional coupler (DC1). The probe lightwave launched into an acousto-optical (AO) frequency shifter, which separated the beat spectra caused by the upper-modulation sidebands from those caused by the lower sidebands. The frequency-shifted-probe lightwave passed through an erbium-doped-fiber amplifier (EDFA), and was launched into an optical fiber under test by using a directional coupler (DC2), where the total optical power launched into the test fiber was 5.0 dBm. The reflected lightwave output from the test fiber was extracted through DC2, and was detected with an optical balanced-heterodyne receiver (OR1) by using the reference lightwave as a local oscillator (LO). The total LO power was -5.4 dBm. The photoelectric current from the optical receiver was analyzed with a spectrum analyzer. The signal-to-noise ratio was improved by averaging the beat spectrum 100 times. Time-gated spectrum analysis was used with a time-gate width of 5 ms.

By contrast, in the feedback-control circuit, the non-frequency-shifted lightwave from the AO was introduced directly into an optical balanced-heterodyne receiver (OR2). The frequency-shifted lightwave from the DC2 passed an isolator and an optical-fiber-delay line with a length of approximately 500 m, and was launched into OR2, where the beat signal between the two lightwaves was obtained from the photoelectric current. This beat signal was mixed with an RF signal and passed through a band-pass filter (BPF) to provide a reference signal. The frequency fluctuation of the reference signal, which was caused by the nonlinear-frequency sweep, was obtained by using a frequency discriminator (FD). The FD output, which passed through a low-pass filter (LPF) and an amplifier (AMP), was used for the frequency-sweep control. The control signal was fed into the FM-control terminal of the frequency sweeper.

3. Experimental results

Figure 2 shows the spectrum of the OR2 output. The center peak is the beat signal caused by the optical carrier and the other peaks are due to the modulation sidebands. We used the beat signal at a frequency of 80.29 MHz as the reference signal. The frequency change in the reference signal is obtained from the FD-output signal as shown in Fig. 3, where the signal-to-noise ratio was improved by averaging the signal 100 times. The solid and the dotted lines in Fig. 3 represent the frequency change with and without the frequency-sweep control, respectively. Consequently, we confirmed that the beat-frequency fluctuation was greatly reduced by using our modulation-frequency-sweep-control circuit.

Figure 4 shows OFDR waveforms for the vicinity of the far end of a 1-km-long optical fiber. The horizontal and the vertical axes correspond to fiber length and reflected-lightwave power, respectively. The resolution bandwidth of the spectrum analyzer was 300 Hz. The waveforms shown in Fig. 4(a) and (b) are beat spectra without and with frequency-sweep control, respectively. In Fig. 4(a), the peak due to the reflection at the far end of the test fiber broadened as a result of the frequency-sweep nonlinearity. Since the spectral width (3 dB below the peak) was approximately 4 kHz, the spatial resolution (3 dB) without the frequency-sweep control was approximately 4 m.

In Fig. 4(b), where the frequency sweep was controlled, there was an improvement in the spatial resolution for the far-end reflection. With the control, the spectral width (3 dB) was reduced to approximately 1 kHz, which gave a spatial resolution (3 dB) of 1 m for the far-end reflection. It was, however, 5 times as large as the theoretical value of 20 cm given by Eq. (2). This was due to the residual nonlinearity in the frequency sweep.

Furthermore, we measured a 30 km optical fiber. We have already shown that C-OFDR is possible, even for such a long optical fiber, by using the beat spectrum resulting from the mixing of phase-decorrelated lightwaves [6]. Figure 5 shows OFDR waveforms for the far-end of the test fiber. Here, (a) and (b) are beat spectra without and with frequency-sweep control, respectively. We set the resolution bandwidth of the spectrum analyzer to 10 kHz which was twice the linewidth of the lightwave, because the phase-correlated-beat signal for the far-end reflection disappeared and the beat-spectrum width broadened. By reducing the frequency-sweep nonlinearity, the spatial resolution (3 dB) for the far-end reflection was improved from approximately 200 m to 50 m. This is the same spatial resolution as that reported in our previous study under the same frequency-sweep rate γ [6], where we narrowed the time-gate width to less than 0.5 ms but sacrificed the measurement time. The ratio of the spatial resolutions to the fiber length were 1 m /1 km = 10^{-3} and 50 m /30 km = 1.7×10^{-3}, which are the best results to date for C-OFDR.

4. Conclusion

We demonstrated C-OFDR for long optical fibers using externally modulated lightwaves. By suppressing the frequency-sweep nonlinearity with an auxiliary feedback-control circuit, we achieved spatial resolutions of 1 m and 50 m for the far-end reflection from 1 km and 30 km optical fibers, respectively, without substantial narrowing of the time-gate width in the spectrum analysis.

References

[1] U. Glombitza and E. Brinkmeyer, "Coherent frequency-domain reflectometry for characterization of single-mode integrated-optical waveguides", *J. Lightwave Technol.*, vol. 11, pp. 1377-1384, 1993

[2] R. Passy, N. Gisin, J. P. von der Weid, and H. H. Gilgen, "Experimental and theoretical investigations of coherent OFDR with semiconductor laser sources", *J. Lightwave Technol.*, vol. 12, pp. 1622-1630, 1994

[3] W. V. Sorin, D. K. Donald, S. A. Newton, and M. Nazarathy, "Coherent FMCW reflectometry using a temperature tuned Nd:YAG ring laser", *IEEE Photon. Technol. Lett.*, vol. 2, pp. 902-904, 1990

[4] C. W. Lee, E. T. Peng, and C. B. Su, "Optical homodyne frequency domain reflectometer using an external cavity semiconductor laser", *IEEE Photon. Technol. Lett.*, vol. 7, pp. 664-666, 1995

[5] K. Tsuji, K. Shimizu, T. Horiguchi, and Y. Koyamada, "Coherent optical frequency domain reflectometry for a long single-mode optical fiber using a coherent lightwave source and an external phase modulator", *IEEE Photon. Technol. Lett.*, vol. 7, pp. 804-806, 1995

[6] K. Tsuji, K. Shimizu, T. Horiguchi, and Y. Koyamada, "Coherent OFDR using phase-decorrelated lightwaves for characterizing optical fiber transmission lines", *11th International Conference on Optical Fiber Sensors (OFS-11)*, pp. 804-806, 1996

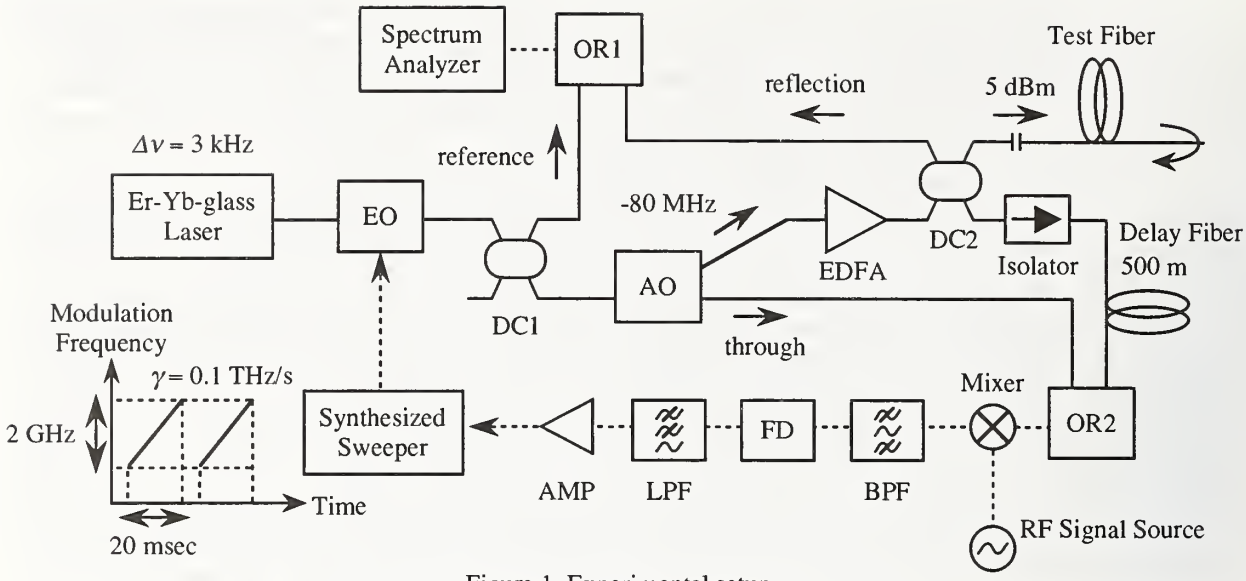

Figure 1. Experimental setup.

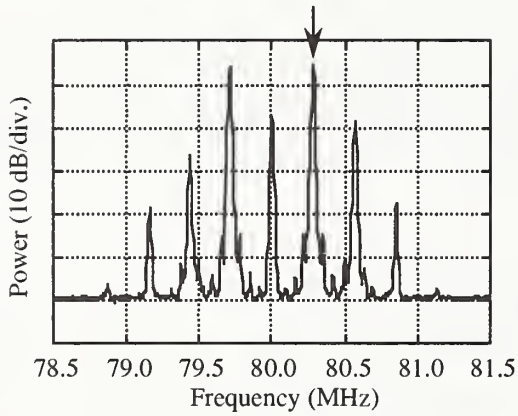

Figure 2. Spectrum of the beat signal from optical receiver 2 (OR2).

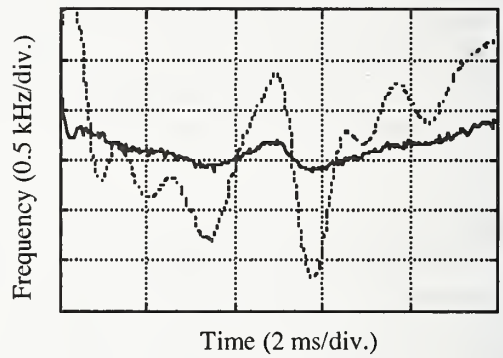

Figure 3. Frequency fluctuation of the reference signals . Solid and dotted lines correspond to the traces with and without the frequency-sweep control, respectively.

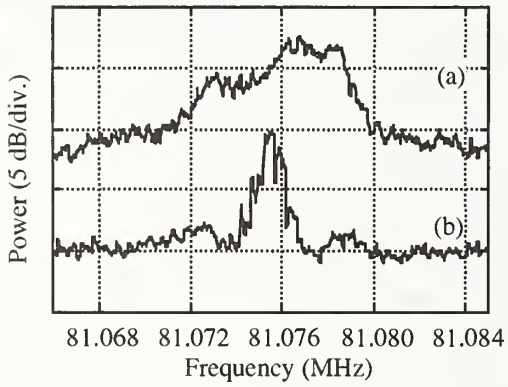

Figure 4. OFDR waveforms for the vicinity of the far end of the 1-km-test fiber (a) without, and (b) with the frequency-sweep control.

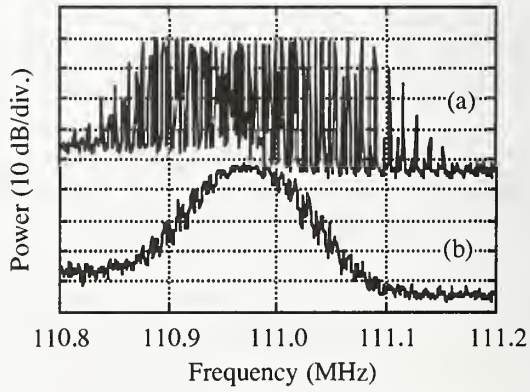

Figure 5. OFDR waveforms for the far end of the 30-km-test fiber (a) without, and (b) with the frequency-sweep control.

A NEW WIDE SCAN RANGE HIGH RESOLUTION OPTICAL LOW COHERENCE REFLECTOMETER

Mauro Bottanelli

SIRTI S.p.A., Cables and Optical Technologies
Via Manzoni 44, 20095 Cusano Milanino (MI), ITALY

Abstract

A transportable and easy to use optical low coherence reflectometer has been development for fault detection and optical component characterization. Up to 40 centimeters scan range, better than 80 μm spatial resolution and more than 100 dB dynamic range have been achieved by means of a new measurement configuration, without any polarization control elements or signal filtering technique.

Introduction

Optical Low Coherence Reflectometry (OLCR) has been already pointed out in the past as a suitable technique for high resolution fault detection and optical component characterization. Recently, the availability of erbium doped optical amplifiers as light sources and the growing interest in the development and testing of high technology optical components (couplers, WDMs, filters, attenuators, isolators...) have emphasized OLCR potentiality with respect to traditional measurement method. Commercially available Optical Domain Reflectometers (OTDR), for instance, are limited both in resolution and in dynamic range when a centimetric or a sub-centimetric fault location is needed, or when a very low back-reflection component has to be analysed. On the contrary, OLCR systems offer suitable features for those goals.

This paper describes the design, the development and the first characterization of a new transportable and easy to use OLCR set-up, which has been conceived both for field fault detection and for optical component analysis and quality control applications. The new OLCR set-up has been developed by SIRTI R&D laboratories in cooperation with the Polytechnic of Milan during the last year.

Theory and background

Fig. 1 reports the basic scheme of a generic OLCR set-up. The continuous wave low coherence radiation from the light source is parted into a measurement and a reference beam by means of a beam splitter. After reflections, respectively inside the Device Under Test (DUT) and from the variable length reference path mirror, the beams are combined by the splitter, giving interference patterns on the detector. The set-up therefore reproduces a Michelson interferometer, but, due to the source low coherence time, interference can rise only for very limited difference between the measurement and the reference path, that is: discrimination among different back-scattering points inside the DUT can be obtained with a very high spatial resolution, simply moving the reference mirror by means of a micropositioning stage. The larger the source optical power, the higher the OLCR set-up dynamic range; the narrower the source autocorrelation function, the higher the OLCR set-up resolution. In the past, only Light Emitting Diodes (LEDs) or Super-Luminescent Diodes (SLDs) constituted suitable sources for OLCR set-ups, but better performances can be achieved nowadays by means of the Amplified Spontaneous Emission (ASE) of an erbium doped Optical Fiber Amplifier (OFA).

Let us now review the main features of OLCR systems:

- *Spatial resolution*: the shortest spatial distance between two contiguous scattering points that can be distinguished by the system. It can be proved to be:

$$\Delta z = \frac{\lambda^2}{2n\Delta\lambda} \qquad (1)$$

  where λ and $\Delta\lambda$ are respectively the wavelength and the spectral width of the source, and n is the material refraction index of the DUT.

- *Sensitivity*: the lowest back-scattered signal that can be detected by the system. It can be proved to be:

$$(2)\quad \begin{cases} \text{a)} \quad R_{min} = \dfrac{qB}{\gamma I_{dc}} & \text{(shot noise limited case)} \\ \text{b)} \quad R_{min} = \dfrac{B}{2\gamma \cdot \delta\nu} & \text{(excess noise limited case)} \end{cases}$$

being B the detection band of the optical signal, q the elementary charge, γ the DUT insertion loss, I_{dc} the photodetector direct current offset and $\delta\nu$ a sort of equivalent source band width defined by the source power spectrum $G(\nu)$ as:

$$\delta\nu \equiv \frac{\left[\int_0^{+\infty} G(\nu)d\nu\right]^2}{\int_0^{+\infty} G^2(\nu)d\nu}$$

In the first case, the system sensitivity is mainly limited by the photodetector characteristics; in the second, it is limited by the light source intensity fluctuations.

- *Blind space*: the spatial width of some areas inside the DUT where the system can not perform a good measurement, due to the presence of minor lobes in the source autocorrelation function. Those areas are typically adjoining intense light back-scattering centers in the DUT. Their spatial extension can range from 20 mm (multimode LD source) to 5 mm (LED, SLD source) or to 0.5 mm (ASE source) considering the source FW60dB (Full Width at 60 dB from the top of the autocorrelation function).

- *Scan range*: the largest continuous spatial range that can be scanned by the system, typically about 20 centimeters more or less, depending on the system design and purpose.

A new OLCR configuration

Fig. 2 sketches the main features of our new OLCR configuration. The light source is the amplified spontaneous emission of an erbium doped optical amplifier, having 6 dBm optical output power at 1530 nm, about 8 mm FWHM spectral width, a 1 ps FWHM autocorrelation function width (see figure 3) and a very low polarization degree. Light is launched into a traditional SMR type optical fiber without any particular kind of polarization control, and is parted into measurement and reference beams by means of a 50:50 fusion coupler. A sawtooth ramped piezoelectric cylinder (PZT) as phase modulator (PM) has been inserted on the OLCR reference arm in order to improve the sensitivity by means of a lock-in amplifier detection. A particular micropositioning motorized stage (up to 0.2 micron step resolution) can adapt the reference path to the measurement one, in order to scan up to 40 cm DUT length. Other two 50:50 fusion couplers and two InGaAs PIN detectors have been inserted into the configuration in order to implement the so-called "balanced detection" technique, that is a subtraction between photocurrents deleting the source intensity fluctuation excess noise. In ideal conditions (coupler splitting ratio k=0.5, equal detector responsivities, identical detection pigtail paths) the system can be considered shot noise limited only, with even up to a 40 dB sensitivity improvement with respect to the single PIN detection. The opto-mechanical set-up is completely controlled by a personal computer by means of a C language developed program.

A comparison among our new set-up and the most effective traditional OLCR configurations [1, 2, 3] (fig. 4/a, /b and /c) is summarized in the following points:

- in the case of a perfectly balanced detection, /b configuration sensitivity can be proved to be theoretically the highest; our configuration and the c/ one have a theoretical sensitivity 3 dB worse than for /b. /a configuration can not be considered balanced in any case (it is the worst one). However the real sensitivity also depends on the PZT position: due to macrobending losses, it can be proved that the PZT placed on the

measurement arm can make sensitivity worse, while, as in our configuration, the PZT placed on the reference arm does not influence the sensitivity;

- our and /a configurations have the highest scan range, because they double the moving stage mechanical scan range. Moreover, as far as we know, a 40 cm scan range has never been reported in the literature till now;

- our and /a configurations delete the influence of possible light reflections at the fiber-air interfaces, because in these two configurations unwanted reflected light and the reference light travel along the same physical paths.

New OLCR set-up characterization and first experimental results

Table 1 reports our OLCR set-up main features, as measured according to several trial experimental results. It is interesting to point out the fact that these such remarkable performances are however still under the maximum configuration theoretical potentialities (the maximum theoretical sensitivity level, for instance, has been calculated to be 142 dB), and that they have been achieved without any kind of particular optical component selection, polarization control systems or hardware end software filtering technique. Those present features can be considered to be sufficient for every practical measurement purposes, a part from fiber Rayleigh scattering level evaluation, which would require an higher sensitivity and, in general, a very long measurement time.

Sensitivity	107 dB
Repeatability	0,86 dB
Reproducibility	0,89 dB
Spatial resolution (FWHM)	75 μm
Blind space	FW20dB = 260 μm FW40dB = 550 μm FW60dB = 1,04 mm
Scan range in the air	60 cm
Scan range in the fiber	40 cm
Measurement mean time (for a 2 cm long DUT)	5 minutes (at the finest scan step)

Table 1 - New OLCR set-up mean features

By means of an experimental report, fig. 5 illustrates the capability of the new OLCR system to be used as fault detector. Other measurement examples will be shown during the paper presentation, especially concerning component characterization.

Conclusions

A new OLCR set-up for fault detection and high resolution component characterization has been developed and described. Up to 40 centimeters scan range, better than 80 μm spatial resolution and more than 100 dB dynamic range have been achieved.

Acknowledgements

This work has been developed by the author and by Adolfo Ottonello during a one year stage in SIRTI's laboratories. We would like to thank Mario Martinelli (Polytechnic of Milan) for his invaluable help in theoretical question deepening.

References

[1] H.H. Gilgen, G. Bodmer, C. Zimmer, *"Optical coherence domain reflectometry as a test method for integrated optics devices"*, 2nd Optical Fibre Measurements Conference, Turin, p. 143-146, 1993.

[2] W.V. Sorin, D.M. Baney, *"Measurement of Rayleigh backscattering at 1.55 μm with 32 μm spatial resolution"*, Photonics Technology Letters, vol. 4, p. 374-376, 1992.

[3] K. Takada, T.Kitagawa, M. Shinizu, M. Horiguchi, *"High-sensitivity low coherence reflectometer using erbium-doped superfluorescent fibre source and erbium-doped power amplifier"*, Electronics letters, vol. 29, p. 365-367, 1993.

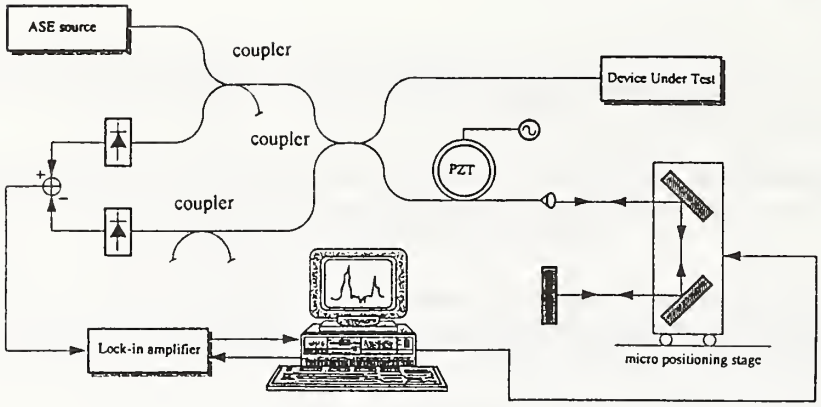

Fig. 2 - Sketch of the new OLCR set-up

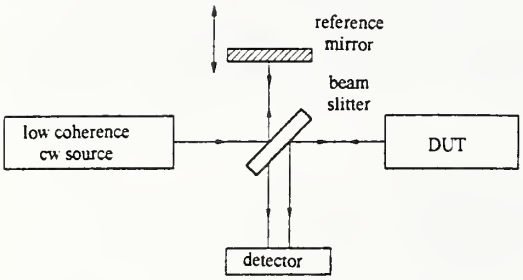

Fig. 1 - Basic scheme of a generic OLCR set-up

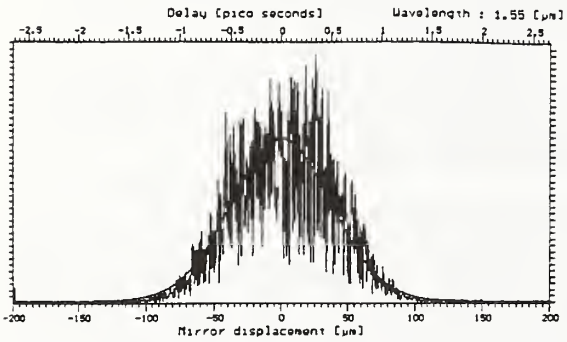

Fig. 3 - ASE source autocorrelation function

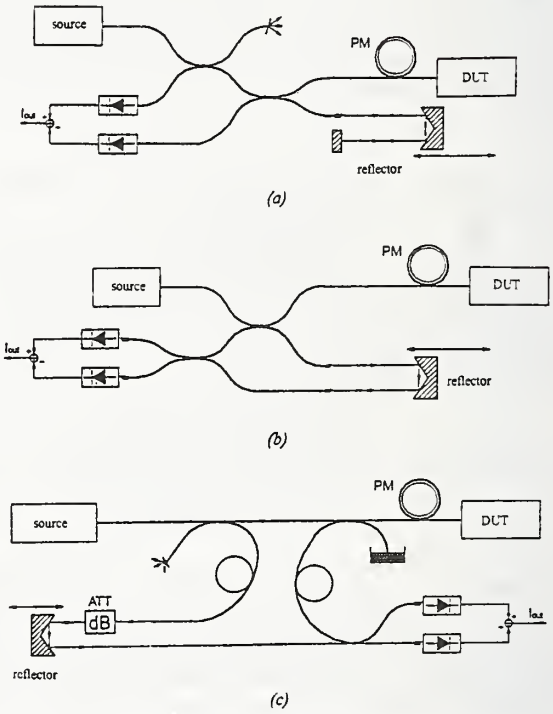

Fig. 4 - Most effective traditional OLCR set-ups

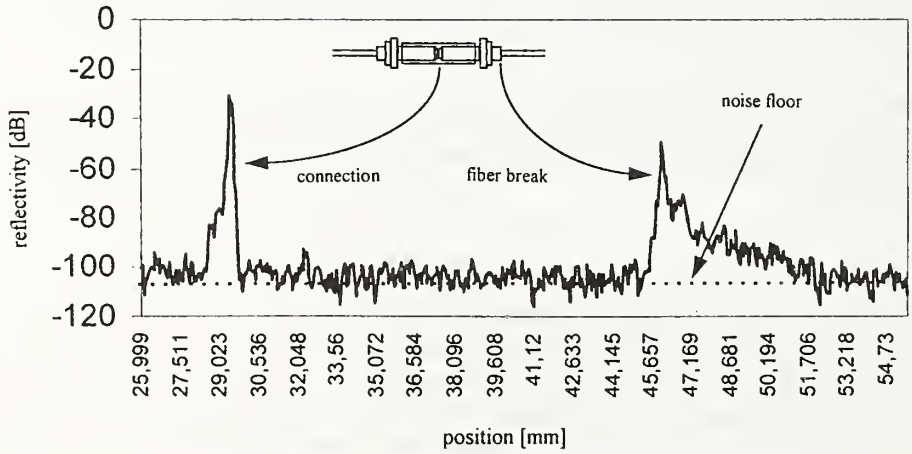

Fig. 5 - Measurement report example: fiber break identification

Interferometric noise in fiber transmission systems incorporating birefringent substances

Michael A. Bukhshtab

Corning Incorporated, Opto-Electronic Components, Corning, NY 14831

The impact of interferometric noise terms on the bit-error-rate floors of a transmission system with a DFB laser degrades its performance due to the conversion of laser phase noise into signal dependent intensity noise [1]. Measurement systems evaluating optical amplifiers, dispersion compensation fibers and WDM elements often contain birefringent components. Transmission of a coherent and polarized laser beam through a birefringent substance between potential refractive index discontinuities creates a complex interference pattern contributing to auxiliary intensity noise of the measurement system itself.

This paper presents a computation of interference noise in a distributed birefringent substance by summing interference patterns created by components with equal and different numbers of reflections along each birefringent axis, and then within any selected polarization direction. The optimum phase settings for measurements under low auxiliary noise conditions are identified by computing the phase retardance of a total system that is required to establish its performance as a noise filter. This approach assumes the similar frequency dependence and probability distribution of interferometric noise as in [1].

The multiple-path interference in a birefringent substance can be represented as two processes for waves with equal and different numbers of passes through it: the comparative and the cross-reference events [2]. Only light modes that contribute to the comparative interference have identical amplitudes. Presuming that the products of both surface reflections of this substance are $(\rho_{o1}\rho_{o2})^2$, $(\rho_{e1}\rho_{e2})^2 \ll 1$ only the interference of waves separated by at least two dual-reflection circles is not counted. Such a second-order approximation, computing interference among all components diverted by any dual pass, gives:

$$I_{\tau,\Sigma} = I_0\left[\frac{1-\rho_o}{\sqrt{(1-\rho_o)^2+4\rho_o\sin^2\delta_o}}\cos\varphi\cos(\varphi-\gamma)+\frac{1-\rho_e}{\sqrt{(1-\rho_e)^2+4\rho_e\sin^2\delta_e}}\sin\varphi\sin(\varphi-\gamma)\right]^2 - \tag{1}$$

$$-I_0\tau_o\tau_e\sum_{i=1}^{m}\left\{\rho_o^{m-1}\rho_e^{m-1}\sin^2\left[\frac{(2m-1)\delta}{2}\right]+\rho_o^{m}\rho_e^{m-1}\sin^2\left(m\delta_o+\frac{\delta}{2}\right)+\rho_o^{m-1}\rho_e^{m}\sin^2\left(m\delta_e+\frac{\delta}{2}\right)\right\}\sin 2\varphi\sin[2(\varphi-\gamma)].$$

here $\delta = (2\pi/\lambda)(n_e - n_o)h$; h is thickness of the substance; ρ_o, ρ_e are its reflectances along the ordinary and extraordinary axes; $\delta_m = (2m + 1)(\delta_e - \delta_o)$; $\delta_o = (2\pi/\lambda)(hn_o)$, $\delta_e = (2\pi/\lambda)(hn_e)$; $m = 1, 2, 3...$ is the integer.

The first term in equation (1) accounts for the comparative interference patterns along the ordinary and extraordinary axes of the birefringent substance. The second term includes some infinite number of components with different amplitudes, which participate in the cross-reference interference between the ordinary and extraordinary directions while having m_o and m_e reflections, respectively. Let us omit interference of waves separated by more than one dual-reflection circle inside the retarder. This means that squared surface reflection factors: $(\rho_{o1}\rho_{o2})^2$, $(\rho_{e1}\rho_{e2})^2$ are negligible compared to unity. For identical front and back surface reflections this is equal to $(\rho_o^2)^2 << 1$, $(\rho_e^2)^2 << 1$. Equation (1) thus transforms to:

$$I_{\tau,\Sigma,dual} = I_0\left[\frac{1-\rho_o}{\sqrt{(1-\rho_o)^2 + 4\rho_o \sin^2\delta_o}}\cos\varphi\cos(\varphi-\gamma) + \frac{1-\rho_e}{\sqrt{(1-\rho_e)^2 + 4\rho_e \sin^2\delta_e}}\sin\varphi\sin(\varphi-\gamma)\right]^2 -$$
$$- I_0\tau_o\tau_e\left\{\begin{array}{l}\sin^2\left(\frac{\delta}{2}\right) + \rho_o\rho_e\sin^2\left(\frac{3\delta}{2}\right) + \rho_o\sin^2\left(\delta_o + \frac{\delta}{2}\right) + \rho_e\sin^2\left(\delta_e + \frac{\delta}{2}\right) + \\ + \rho_o^2\rho_e\sin^2\left(2\delta_o + \frac{\delta}{2}\right) + \rho_o\rho_e^2\sin^2\left(2\delta_e + \frac{\delta}{2}\right)\end{array}\right\}\sin 2\varphi\sin[2(\varphi-\gamma)]. \quad (2)$$

Equation (2) still counts many multiple reflections. When boundary reflectances are low, the number of accepting terms could be reduced by the approximation of $\rho_{o1}\rho_{o2} << 1$, $\rho_{e1}\rho_{e2} << 1$ or $\rho_o^2 << 1$, $\rho_e^2 << 1$:

$$I_{\tau,\Sigma,sgl} = I_0\left[\frac{1-\rho_o}{\sqrt{(1-\rho_o)^2 + 4\rho_o \sin^2\delta_o}}\cos\varphi\cos(\varphi-\gamma) + \frac{1-\rho_e}{\sqrt{(1-\rho_e)^2 + 4\rho_e \sin^2\delta_e}}\sin\varphi\sin(\varphi-\gamma)\right]^2 -$$
$$- I_0\tau_o\tau_e\left\{\sin^2\left(\frac{\delta}{2}\right) + \rho_o\rho_e\sin^2\left(\frac{3\delta}{2}\right) + \rho_o\sin^2\left(\delta_o + \frac{\delta}{2}\right) + \rho_e\sin^2\left(\delta_e + \frac{\delta}{2}\right)\right\}\sin 2\varphi\sin[2(\varphi-\gamma)]. \quad (3)$$

Assuming a limited coherence length, when wave components with phase shifts δ_o, δ_e do not interfere:

$$I_{\tau,\Sigma,sgl,uncoher} = I_0\left[\sqrt{\frac{1-\rho_o}{1+\rho_o}}\cos\varphi\cos(\varphi-\gamma) + \sqrt{\frac{1-\rho_e}{1+\rho_e}}\sin\varphi\sin(\varphi-\gamma)\right]^2 -$$
$$- I_0(1-\rho_o)(1-\rho_e)\left\{\sin^2\left(\frac{\delta}{2}\right) + \rho_o\rho_e\sin^2\left(\frac{3\delta}{2}\right)\right\}\sin 2\varphi\sin[2(\varphi-\gamma)]. \quad (4)$$

Fig. 1 depicts a quarter-wave retarder for λ=1555 nm with spectral attributes similar to quartz whose optical axis is oriented at 30° to parallel input and output polarization directions, so $\gamma = 0°$; $\varphi = 30°$. These

computations are based on a presumption of six percent reflections for polished fiber endfaces as in [1]. Effects are computed by equations (2) – (4) (curves 1 – 3) versus an ideal case of no reflections (curve 4). Although the character of each curve is similar, the equations compute different intensity noise, seen as oscillations of mean intensities. Since at low reflectances equations (2), (3) give similar results (curves 1, 2), there is no need to consider all multiple reflections. However, the reduced amount of determined by equation (4) terms (curve 3) predicts an incorrect light transmission. It also is seen that interference noise is elevated at high and low intensities of transmitted light, related to multiples of $\pi/2$ phase retardance. It is different near the 0.5 intensity regions matching ideally optimal $\delta_{opt} = \pi/4$. Counting all reflections the actual δ_{opt} point changes, since dual-path phase shifts for each optical axis are not multiples of $\pi/4$.

Fig. 1. Transmission of the quarter-wave retarder for 1555 nm between two air gaps: 1 - all effects are counted; 2 - only first two dual-reflection cycles are included; 3 - only two-beam interference is considered, 4 - ideal case assuming no reflections

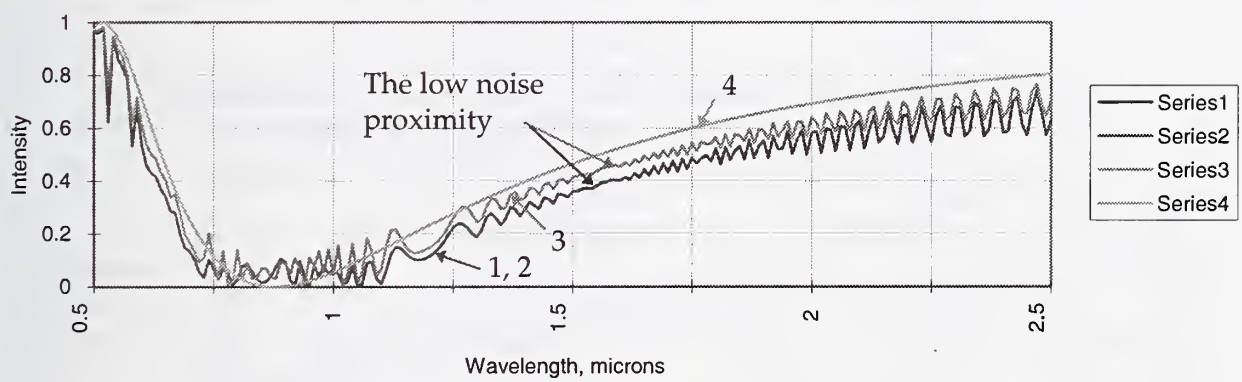

Let us thus define that optimal phase shift δ_{opt}, which is needed to obtain the minimum influence of spectral changes of incident light, and correspondingly the lowest interference noise in transmission:

$$\frac{\partial\left(I_{\tau,\Sigma,dual}/I_0\right)}{\partial\delta} = -\frac{\tau_o\tau_e}{2}\left\{\begin{matrix}\sin\delta + 3\rho_o\rho_e\sin 3\delta + \rho_o\sin(2\delta_o+\delta) + \rho_e\sin(2\delta_e+\delta) + \\ + \rho_o^2\rho_e\sin(4\delta_o+\delta) + \rho_o\rho_e^2\sin(4\delta_e+\delta)\end{matrix}\right\}\sin 2\varphi\sin[2(\varphi-\gamma)] \quad (5)$$

$$\frac{\partial\left(I_{\tau,\Sigma,sgl}/I_0\right)}{\partial\delta} = -\frac{\tau_o\tau_e}{2}\left\{\sin\delta + 3\rho_o\rho_e\sin 3\delta + \rho_o\sin(2\delta_o+\delta) + \rho_e\sin(2\delta_e+\delta)\right\}\sin 2\varphi\sin[2(\varphi-\gamma)] \quad (6)$$

$$\frac{\partial\left(I_{\tau,\Sigma,sgl,uncoher}/I_0\right)}{\partial\delta} = -\frac{(1-\rho_o)(1-\rho_e)}{2}\left\{\sin\delta + 3\rho_o\rho_e\sin 3\delta\right\}\sin 2\varphi\sin[2(\varphi-\gamma)] \quad (7)$$

The potential points of the lowest interference changes of the observing intensity, and thus minimal interference noise, are corresponding to zero of the second derivatives. These second derivatives are:

$$\frac{\partial^2\left(I_{\tau,\Sigma,dual}/I_0\right)}{\partial^2\delta}=-\frac{\tau_o\tau_e}{2}\left\{\begin{matrix}\cos\delta+9\rho_o\rho_e\cos 3\delta+\rho_o\cos(2\delta_o+\delta)+\rho_e\cos(2\delta_e+\delta)+\\+\rho_o^2\rho_e\cos(4\delta_o+\delta)+\rho_o\rho_e^2\cos(4\delta_e+\delta)\end{matrix}\right\}\sin 2\varphi\sin[2(\varphi-\gamma)]. \quad (8)$$

$$\frac{\partial^2\left(I_{\tau,\Sigma,sgl}/I_0\right)}{\partial^2\delta}=-\frac{\tau_o\tau_e}{2}\left\{\cos\delta+9\rho_o\rho_e\cos 3\delta+\rho_o\cos(2\delta_o+\delta)+\rho_e\cos(2\delta_e+\delta)\right\}\sin 2\varphi\sin[2(\varphi-\gamma)]. \quad (9)$$

$$\frac{\partial^2\left(I_{\tau,\Sigma,sgl,uncoher}/I_0\right)}{\partial^2\delta}=-\frac{(1-\rho_o)(1-\rho_e)}{2}\left\{\cos\delta+9\rho_o\rho_e\cos 3\delta\right\}\sin 2\varphi\sin[2(\varphi-\gamma)]. \quad (10)$$

The first and second derivatives of transmission given by equations (5) – (10) are depicted by Fig. 2, 3.

Fig. 2. Intensity changes in transmission at the quarter-wave retardance at 1555 nm existing between refractive index discontinuities: curves 1 - 3 are computed to equations (5) - (7)

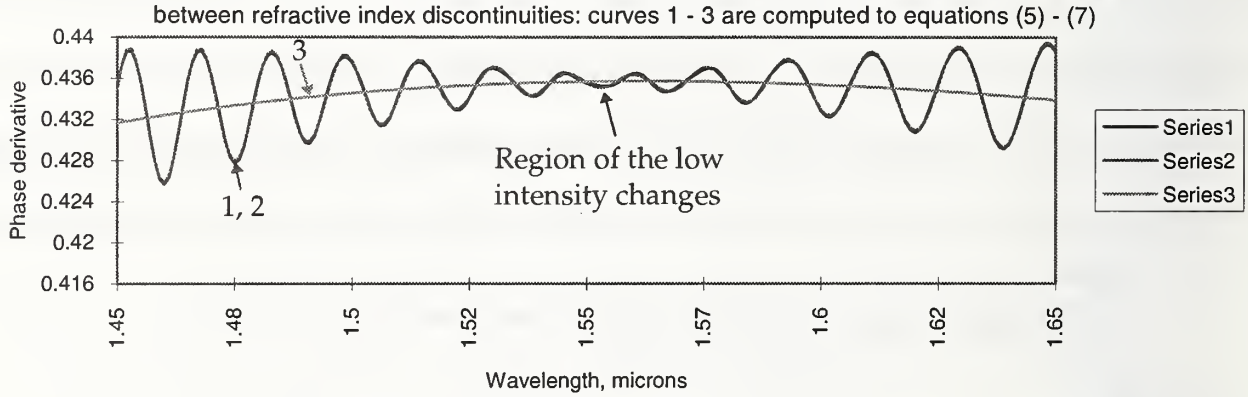

Fig. 3. Finding the optimal wavelength that matches the optimal phase retardance and the lowest excessive noise: curves 1 - 3 are computed by equations (8) - (10)

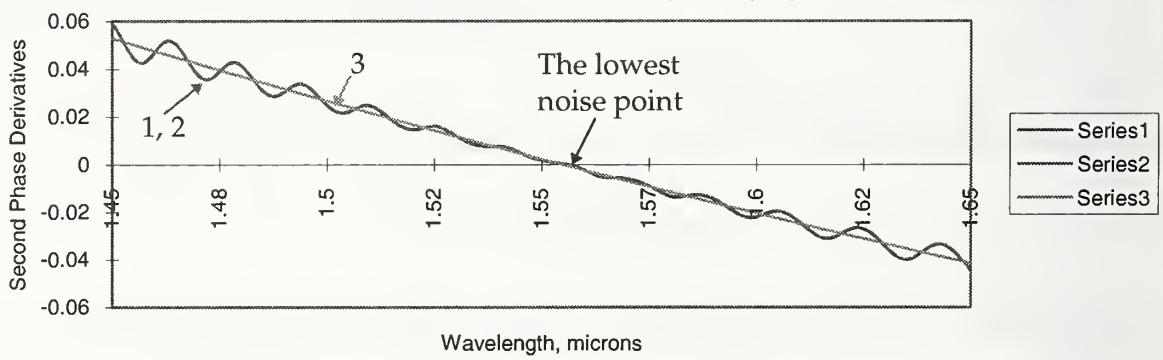

The proposed reduction of birefringence-induced multiple-path interference noise terms can expand design of transmission and measurement systems by incorporating fibers with the optimal birefringence.

Reference:

[1] J. L. Gimlett, N. K. Cheung, Effects of phase-to-intensity noise conversion by multiple reflections on gigabit-per-second DFB laser transmission systems, J. Lightwave Technol., 1989, Vol. 7, No. 6, pp. 888–895

[2] M. Bukhshtab, The influence of surface reflections on computation and measurement of retardance, Meas. Sci. Technol., 1995, Vol. 6, No. 7, pp. 910 – 920

AUTHOR INDEX

Anderson, Duwayne . . . 191
Antos, A.J. 61
Artiglia, M. 31
Arvidsson, Bertil 139
Aso, Osamu 147, 151
Auguste, J.L. 187
Barlow, A.J. 151
Bartelt, H. 27
Berkey, G.E. 61
Blondel, M. 195
Blondy, J.M.. . . . . 175, 187
Boness, R. 75
Bottanelli, Mauro. 207
Brising, Kim 139
Bukhshtab, Michael A. 211
Chia, Shin-Lo 57
Clapeau, M. 187
Clayton, J.B. 105
da Silva, Valéria L. 61
Daniaux, D. 195
Del Core, Andrea 67
Dell, J.M. 35
Di Bin, P. 183
Dultz, W. 71
Dupre, J. 1
Elamari, A. 163
Ertmer, A. 27
Eiselt, M. 115
Facq, P. 175, 183, 187
Faugeras, P. 183
Fellegara, A. 67, 199
Franzen, D.L. 121
Fujishima, H. 151
Fuss, M. 13
George, G. 89
Gisin, B. 131
Gisin, N. 131, 143, 151, 163
Hackert, Michael J. 79
Headley, Clifford 105
Heens, B. 31
Heffner, B.L. 135
Herchenröder, G. . . . 71, 93
Horiguchi, T. 203
Humphreys, D.A. 97
Ichimura, M. 151
Ishigure, Takaaki 171
Jopson, R.M. 115
Judy, A.F. 151
Julliard, K. 143
Kashyap, Raman 7
Keenan, Darryl A. 49
Kim, K.S. 151
Kirchhof, J. 75
Klein, K.-F. 75
Koike, Yashuhiro 171
Koyamada, Y. 203
Krusius, J.P. 89
Larsen, C. 31
Li, Xaioyu 49, 101
Liu, Y. 61
Martinelli, Mario 67
Mechels, S.E. 121
Mégret, P. 195
Melloni, Andrea 67
Mickelsson, Hans 139
Mitachi, S. 53
Moeyaert, V. 195
Mörl, K. 93
Müller, H.-R. 27
Nagase, R. 53
Namihira, Yoshinori151, 179
Newhouse, M.A. 61
Nihei, Eisuke 171
Niklès, Marc 111
Noguchi, M. 151
Oberson, Ph. 143
Ogoshi, Haruki 147
Ohashi, M. 151
Ozeki, T. 151
Pagnoux, D. . 175, 183, 187
Passy, R. 131, 143
Perny, B. 151, 163
Potenza, Marcello 23
Rasmussen, Jens 167
Reed, W.A. 105
Reichel, V. 27
Reith, L.A. 39
Robert, Philippe A. . . . 111
Rothhardt, M. 27
Roy, P. 175
Salina, Pascal 111
Saravanos, Costas 45
Schlager, J.B. 121
Scholl, Bernhard 167
Schuh, R.E. 159
Scott, Thomas R. . . 49, 101
Shimizu, K. 203
Siddiqui, A.S. 159
Siliquini, J.F. 35
Simos, C. 183
Smith, David 83
Soccolich, C. 31
Suetsugu, Y. 151
Sutherland, J. 89
Suzuki, S. 151
Sawada, M. 151
Tambosso, Tiziana 23
Thévenaz, Luc 111
Townley-Smith, Paul . . 45
Tsuji, K. 203
Unger, S. 75
Vayshenker, Igor . . 49, 101
Vobian, J. 71, 75, 93
Von der Weid, J.P. 131, 143
Willems, F.W. 17, 31
Williams, P.A. 125, 151, 155
Wittl, F. 71, 75
Wuilmart, L. 195
Xu, M.G. 35
Yang, Shao 101
Zainul, M.Ajaaz 79
Zbinden, H. 163
Zimmer, Ch. 163

•U.S. GOVERNMENT PRINTING OFFICE: 1996-404-525/67902

NIST Technical Publications

Periodical

Journal of Research of the National Institute of Standards and Technology—Reports NIST research and development in those disciplines of the physical and engineering sciences in which the Institute is active. These include physics, chemistry, engineering, mathematics, and computer sciences. Papers cover a broad range of subjects, with major emphasis on measurement methodology and the basic technology underlying standardization. Also included from time to time are survey articles on topics closely related to the Institute's technical and scientific programs. Issued six times a year.

Nonperiodicals

Monographs—Major contributions to the technical literature on various subjects related to the Institute's scientific and technical activities.

Handbooks—Recommended codes of engineering and industrial practice (including safety codes) developed in cooperation with interested industries, professional organizations, and regulatory bodies.

Special Publications—Include proceedings of conferences sponsored by NIST, NIST annual reports, and other special publications appropriate to this grouping such as wall charts, pocket cards, and bibliographies

Applied Mathematics Series—Mathematical tables, manuals, and studies of special interest to physicists, engineers, chemists, biologists, mathematicians, computer programmers, and others engaged in scientific and technical work.

National Standard Reference Data Series—Provides quantitative data on the physical and chemical properties of materials, compiled from the world's literature and critically evaluated. Developed under a worldwide program coordinated by NIST under the authority of the National Standard Data Act (Public Law 90-396). NOTE. The Journal of Physical and Chemical Reference Data (JPCRD) is published bimonthly for NIST by the American Chemical Society (ACS) and the American Institute of Physics (AIP). Subscriptions, reprints, and supplements are available from ACS, 1155 Sixteenth St., NW, Washington, DC 20056.

Building Science Series—Disseminates technical information developed at the Institute on building materials, components, systems, and whole structures. The series presents research results, test methods, and performance criteria related to the structural and environmental functions and the durability and safety characteristics of building elements and systems.

Technical Notes—Studies or reports which are complete in themselves but restrictive in their treatment of a subject. Analogous to monographs but not so comprehensive in scope or definitive in treatment of the subject area Often serve as a vehicle for final reports of work performed at NIST under the sponsorship of other government agencies.

Voluntary Product Standards—Developed under procedures published by the Department of Commerce in Part 10, Title 15, of the Code of Federal Regulations. The standards establish nationally recognized requirements for products, and provide all concerned interests with a basis for common understanding of the characteristics of the products. NIST administers this program in support of the efforts of private-sector standardizing organizations.

Consumer Information Series—Practical information, based on NIST research and experience, covering areas of interest to the consumer. Easily understandable language and illustrations provide useful background knowledge for shopping in today's technological marketplace.

Order the **above** *NIST publications from: Superintendent of Documents, Government Printing Office, Washington, DC 20402.*

Order the **following** *NIST publications—FIPS and NISTIRs—from the National Technical Information Service Springfield, VA 22161.*

Federal Information Processing Standards Publications (FIPS PUB)—Publications in this series collectively constitute the Federal Information Processing Standards Register. The Register serves as the official source of information in the Federal Government regarding standards issued by NIST pursuant to the Federal Property and Administrative Services Act of 1949 as amended, Public Law 89-306 (79 Stat. 1127), and as implemented by Executive Order 11717 (38 FR 12315, dated May 11, 1973) and Part 6 of Title 15 CFR (Code of Federal Regulations).

NIST Interagency Reports (NISTIR)—A special series of interim or final reports on work performed by NIST for outside sponsors (both government and non-government). In general, initial distribution is handled by the sponsor; public distribution is by the National Technical Information Service, Springfield, VA 22161, in paper copy or microfiche form.

U.S. Department of Commerce
National Institute of Standards and Technology
325 Broadway
Boulder, Colorado 80303-3328

Official Business
Penalty for Private Use, $300